

THE HYBRID PANEL-TRUSS ELEMENT:
DEVELOPING A NOVEL FINITE ELEMENT FOR THE NONLINEAR ANALYSIS OF
REINFORCED CONCRETE BEAMS AND SHELLS

by

Edvard P.G. Bruun

A thesis submitted in conformity with the requirements
for the degree of Master of Applied Science
Graduate Department of Civil Engineering
University of Toronto

© Copyright 2017 by Edvard P.G. Bruun

Abstract

The Hybrid Panel-Truss Element:

Developing a Novel Finite Element for the Nonlinear Analysis of Reinforced Concrete Beams and Shells

Edvard P.G. Bruun

Master of Applied Science

Graduate Department of Civil Engineering

University of Toronto

2017

This research thesis presents a finite element for the nonlinear analysis of reinforced concrete beams and shells. The Hybrid Panel-Truss (HyPT) element overcomes the computational limitations that exist when working with current analysis paradigms implemented in commercial software. Instead of explicit shape functions, the element utilizes the combined actions of simpler subcomponents to capture the coupled axial, flexural and shear deformations associated with reinforced concrete structures. The finite element formulation itself is robust as only one element is required through the depth of a member, and efficient since the global degrees of freedom necessary in a structural analysis model are reduced. The predictive accuracy of the HyPT element was verified using the American Concrete Institute database of shear critical reinforced concrete beam tests. In addition, the element was used to successfully model the experimental component of this research - the first documented pure torsion tests on reinforced concrete shells.

Acknowledgements

I would like to thank my supervisors, Professor Evan C. Bentz and Professor Oh-Sung Kwon, for providing guidance throughout this graduate degree. The large scope and open-ended nature of the work was daunting at times, but in retrospect helped me to mature as a structural engineer and academic.

The overall research project was funded by an NSERC Collaborative Research and Development (CRD) grant, with additional support from an NSERC Canada Graduate Scholarship (CGS-M) and Ontario Graduate Scholarship (OGS).

A special acknowledgment goes to Professor Michael P. Collins, whose lectures on the combined actions of shear and torsion in reinforced concrete were crucial in helping me formulate the finite element presented in this thesis. His advice and suggestions throughout the experimental program were also invaluable. I will fondly carry his saying - "To find the answer, you must know the answer" - with me throughout my career.

Without the University of Toronto's structural laboratory staff none of the experimental work would have been possible. The help from: Renzo Basset, John MacDonald, Giovanni Buzzeo, Michel Fiss, Bryant Cook, and Xiaoming Sun made the construction, installation and execution of the world's first pure torsion tests a reality. I count myself lucky to have been working in the laboratory in the final year before both Giovanni and John's retirement, it is a shame that future generations of graduate students will not have them around.

I would also like to thank all of my graduate student peers in the Civil Engineering Department for making this a wonderful environment to work in. I would like to especially acknowledge the following individuals: Jeff Salmon, for the countless coffees and company during the long days in the lab; Allan Kuan, for the hours spent discussing all research-related topics; Giorgio Proestos, for the time spent training me to use the Shell Element Tester (SET) and for being an inspiring academic.

Most importantly, I would like to thank my mother, father, sister, and Felix for their support.

Contents

1	Introduction	1
1.1	Background and Research Motivation	2
1.2	Research Objectives and Overview	4
1.3	Literature Review	5
1.3.1	Elasticity-Based Finite Element Models for Shells	5
1.3.2	Multi-Component Models	8
1.3.3	Previous Work Related to the 2d-HyPT Element	11
1.4	Thesis Organization	11
2	A Finite Element for the Analysis of Reinforced Concrete Beams	12
2.1	Description of 2d-HyPT Element	13
2.2	Flexural & Axial Truss Stiffness Terms	15
2.2.1	Deformation Patterns	15
2.2.2	Truss Bar Stiffness Matrix - Diagonal Terms	16
2.2.3	Truss Bar Stiffness Matrix - Off-Diagonal Terms	17
2.2.4	Truss Bar Stiffness Terms - Calculations	19
2.3	Shear Panel Stiffness Terms	25
2.3.1	Deformation Patterns	25
2.3.2	Expressing Nodal Forces in Term of Applied Shear Stress	26
2.3.3	Expressing Shear Strain in Terms of Nodal Displacements	27
2.3.4	Shear Panel Stiffness Matrix	29
2.4	Post-Cracking Interaction Terms	30
2.4.1	Uncracked Concrete	30
2.4.2	Cracked Concrete	30
2.4.3	Post-Cracking Chord Forces	31
2.4.4	Post-Cracking Interaction Stiffness Matrix	32
2.5	Element Verification	33
2.5.1	Methodology	33
2.5.2	Shear Critical Beam Database Analysis	34
2.5.3	Large-Scale Structural Analysis	38
2.5.4	Augustus-II Convergence Study	42
3	Description of Experimental Program	44
3.1	Specimen Design and Construction	45
3.1.1	Reinforcement Schematic	45
3.1.2	Specimen Construction	47

3.2	Material Properties	49
3.2.1	Concrete Cylinder Tests	49
3.2.2	Steel Coupon Tests	51
3.3	Experimental Set-up	52
3.3.1	Actuator Configuration	52
3.3.2	Coordinate System	54
3.3.3	Loading Protocol	54
3.4	Instrumentation	58
3.4.1	Built-in Actuator Sensors	58
3.4.2	Linear Variable Differential Transformers (LVDTs)	58
3.4.3	Three-Dimensional Coordinate Measurement System	59
3.4.4	Linear Potentiometers (LPs)	60
3.4.5	Embedded Concrete Strain Gauges (EGs)	62
3.4.6	Reinforcement Strain Gauges (SGs)	64
4	Experimental Results	65
4.1	Actuator Load Cell Measurements	66
4.2	In-Plane LVDT Measurements	67
4.2.1	Specimen ES1	71
4.2.2	Specimen ES2	74
4.3	In-Plane LED Measurements	77
4.3.1	Specimen ES1	79
4.3.2	Specimen ES2	85
4.4	Out-of-Plane LP & EG Measurements	91
4.4.1	Specimen ES1	94
4.4.2	Specimen ES2	99
4.5	Reinforcement SG Measurements	104
4.5.1	Specimen ES1	105
4.5.2	Specimen ES2	106
5	Discussion of Experimental Results and Observations	107
5.1	Experimental Progression	108
5.1.1	Specimen ES1 Load Stage Photographs	109
5.1.2	Specimen ES2 Load Stage Photographs	111
5.2	Specimen Deformation and Damage	113
5.2.1	Surface Deformation Pattern	113
5.2.2	Spalling of Cover Concrete	115
5.2.3	Additional Observations	116
5.3	In-Plane Experimental Data Comparison	117
5.3.1	Torque-Twist	117
5.3.2	In-Plane Shear Strain	118
5.3.3	Principal Tensile & Compressive Strain	118
5.3.4	Strain Gauges	120
5.4	Out-of-Plane Experimental Data Comparison	121
5.4.1	Out-of-Plane Shear Strain	121
5.4.2	Through the Thickness Strain (Z-dir)	122

6	A Finite Element for the Analysis of Reinforced Concrete Shells	124
6.1	Preliminary Modelling Considerations	125
6.1.1	Shell-2000 Prediction	125
6.1.2	Lessons Learned	126
6.2	Description of 3d-HyPT Element	127
6.2.1	Two-Dimensional Vizualization	128
6.2.2	Full Member Representation	129
6.3	Derivation of Stiffness Matrix	131
6.3.1	Horizontal Truss Stiffness Terms	131
6.3.2	Vertical Truss Stiffness Terms	136
6.3.3	Shear Panel Stiffness Terms	137
6.4	Explanation of Analysis Program	141
6.4.1	MATLAB Main File	141
6.4.2	Input Files and Structure Generation	142
6.4.3	Structural Analysis and Program Output	147
6.5	Element Verification	149
6.5.1	Deformations	150
6.5.2	Analysis Comparison	150
7	Conclusions and Recommendations	153
7.1	Summary of Thesis Objectives	154
7.2	Summary of Results and Conclusions	155
7.2.1	Experimental	155
7.2.2	Analytical	155
7.3	Recommendations for Future Work	156
7.3.1	Experimental	156
7.3.2	Analytical	156
	References	157
	Appendix	158
A.	Shear Critical Beam Databases	159
A.1	No Stirrups - Point Loads	160
A.2	No Stirrups - Distributed Load	171
A.3	Stirrups - Point Loads	172
B.	AeroPro Experimental Data	174
B.1	Specimen ES1	175
B.2	Specimen ES2	183
C.	LED Load Stage Grids	192
C.1	Specimen ES1	193
C.2	Specimen ES2	199
D.	Analysis Program: Main Code Structure	205
E.	Analysis Program: Input/Output Files	208
E.1	Input Text Files for Shell Torsion Analysis	208
E.2	Analysis Summary Output Files for Torsion Specimen ES2	211
E.3	Sample Load Stage Output Files for Torsion Specimen ES2	214

List of Tables

2.1	Database Summary	35
2.2	Important Structural Observations at Load Stages	39
3.1	Summary of Specimen Properties	44
3.2	Summary of Specimen Reinforcement	45
3.3	Average Test Day Concrete Properties	50
3.4	Average Reinforcement Steel Properties	51
3.5	Loading Actuator Summary	53
3.6	LP Summary Information	61
4.1	Applied Torsion at Load Stages	65
4.2	Applied Forces and Resulting Moments	66
4.3	LVDT Data at Load Stages	70
4.4	LED Data at Load Stages	78
4.5	LP & EG Data in XZ-Plane at Load Stages	92
4.6	LP & EG Data in YZ-Plane at Load Stages	93
4.7	SG Data at Load Stages	104
5.1	North Face Crack Width Summary at Load Stages	108

List of Figures

CHAPTER 1: Introduction

Section 1.1

1.1 The Growth of Processing Power in the Context of a Sectional Analysis	2
---	---

Section 1.3

1.2 Degeneration of Three-Dimensional Solid Element	6
1.3 Spurious Deformation Mode with A Single Integration Point	6
1.4 Summary of Degenerated Shell Elements	7
1.5 Multi-Layered Shell Model and Sectional Forces	8
1.6 Space Truss Model and Force Equilibrium	9
1.7 Stringer Panel Element Schematic	10
1.8 Cantilever Constructed from Stringer Panel Elements	10

CHAPTER 2: A Finite Element for the Analysis of Reinforced Concrete Beams

Section 2.1

2.1 HyPT Element Numbering Convention	13
2.2 Beam Modelled with HyPT Elements Placed in Series	13
2.3 Element Stiffness Defined by Cross-Section	14
2.4 Visualization of HyPT Element Subcomponents	14

Section 2.2

2.5 A Representation of Axial Compression and Tension in the Element	15
2.6 A Representation of Positive and Negative Flexure in the Element	15
2.7 Generic Truss Bar	16
2.8 Element DOFs and Connecting Truss Bars	16
2.9 Forces Developed in a Non-Linked Truss System	17
2.10 Forces Developed in a Linked Truss System	17
2.11 Equivalent Nodal Forces Due to a Triangular Stress Block	18
2.12 Vertical Trusses Based on the Gross Cross-Section	19
2.13 Nodal Displacements to Calculate Horizontal Truss Strains	20
2.14 Resulting Sectional Concrete and Steel Stresses	20
2.15 Concrete Section Expressed as Discrete Slices	21
2.16 Concrete and Steel Secant Stiffness Formulation	21
2.17 Incrementing Top or Bottom Truss Strain	22

Section 2.3

2.18 Shear Stresses Related to Shear Deformations	25
2.19 A Representation of Positive and Negative Shear Stresses in the Element	25
2.20 Positive Shear Stress and Resulting Nodal Forces	26
2.21 Shear Stresses Acting on the Effective Shear Panel	26
2.22 Arbitrary Deformation Pattern - Relative Vertical Displacements	27
2.23 Vertical Displacement of the Right Side due to Rigid Body Displacement	27
2.24 Vertical Displacement of the Right Side due to Curvature Displacement	28
2.25 Vertical Displacement of the Right Side due to Shear Strain.	29

Section 2.4

2.26 Force Equilibrium and Stress State for Shear in Uncracked Reinforced Concrete	30
2.27 Force Equilibrium and Stress State for Shear in Cracked Reinforced Concrete	30
2.28 Simplified Force and Stress State for Shear in Cracked Reinforced Concrete	31
2.29 Additional Horizontal Force Carried in the Section Chords	31
2.30 Post-Cracking Forces Independent of the Applied Shear Direction	32

Section 2.5

2.31 HyPT Element Implemented with Response-2000 and Augustus-II	33
2.32 Full Dataset Analysis Results - Shear Critical Beams (No Stirrups)	34
2.33 Full Dataset Analysis Results - Shear Critical Beams (Stirrups)	35
2.34 Analysis Distribution of Under-Reinforced Shear Critical Rectangular Beams	36
2.35 Cumulative Density of Analysis Distribution	36
2.36 Analysis Distribution of Large Shear Critical Rectangular Beams	37
2.37 Cumulative Density of Analysis Distribution	37
2.38 Geometry of Two-Storey Frame Tested at the University of Toronto	38
2.39 Duong Frame - Model Mesh and Deformed Shape Before Failure	38
2.40 Duong Frame - Pushover Analysis vs. Experimental Results	39
2.41 Salmon Frame - Model Mesh and Deformed Shape Before Failure	40
2.42 Salmon Frame - Pushover Analysis Results	40
2.43 Coupled Shear Wall Modelled with Augustus-II	41
2.44 Individual Coupling Beam Model	41
2.45 VecTor2 Beam Meshes	42
2.46 Convergence Analysis	43
2.47 Runtime Analysis	43

CHAPTER 3: Description of Experimental Program

Section 3.1

3.1 ES1 North Face Cage	46
3.2 ES2 North Face Cage	46
3.3 Welded Reinforcement Cage	47
3.4 Casting Reinforced Concrete Specimen	48
3.5 Completed Shell Specimen	48

Section 3.2

3.6 Concrete Compressive Strength Gain	49
3.7 Cylinder Stress-Strain Curve at 28 Days	50
3.8 Cylinder Stress-Strain on Test Day	50
3.9 Steel (XY) Coupon Stress-Strain Curve	51
3.10 Steel (Z) Coupon Stress-Strain Curve	51

Section 3.3

3.11 Shell Element Tester Schematic	52
3.12 Actuator Placement and Numbering	53
3.13 Shell Element Coordinate System	54
3.14 In-Plane Actuator Forces During Test	55
3.15 Actuator Forces on North/South Face	56
3.16 External Moments Applied to the Specimen	56
3.17 Pure Torsion Applied to the Test Region	57
3.18 Torsion Represented as In-Plane Shear Forces	57

Section 3.4

3.19 In-Plane LVDT Locations	59
3.20 In-Plane LED Locations	60
3.21 LP Through-Thickness Placement	60
3.22 Out-of-Plane LP Locations	61
3.23 LP Placement on Specimen ES1	61
3.24 Embedded Strain Gauge Rosette	62
3.25 EG Through-Thickness Placement	62
3.26 Out-of-Plane EG Locations	63
3.27 Out-of-Plane Instrumentation in Reinforcement Cage	63
3.28 Longitudinal Bar SG Locations	64
3.29 T-Head Bar SG Locations in ES2	64

CHAPTER 4: Experimental Results

Section 4.2

4.1 Calculating Experimental Twist Strain	67
4.2 Calculating Shear Strain from Two Linear Strains	68
4.3 Fully Defined Mohr's Circles	69
4.4 ES1 Applied Torsion vs. Twist Strain	71
4.5 ES1 Applied Torsion vs. In-Plane (XY) Shear Strain	72
4.6 ES1 Applied Torsion vs. X-Direction Strain	72
4.7 ES1 Applied Torsion vs. Y-Direction Strain	72
4.8 ES1 Applied Torsion vs. Principal Tensile Strain	73
4.9 ES1 Applied Torsion vs. Principal Compressive Strain	73
4.10 ES1 Applied Torsion vs. Angle of Principal Strain (CCW+)	73
4.11 ES2 Applied Torsion vs. Twist Strain	74
4.12 ES2 Applied Torsion vs. In-Plane (XY) Shear Strain	75
4.13 ES2 Applied Torsion vs. X-Direction Strain	75
4.14 ES2 Applied Torsion vs. Y-Direction Strain	75
4.15 ES2 Applied Torsion vs. Principal Tensile Strain	76
4.16 ES2 Applied Torsion vs. Principal Compressive Strain	76
4.17 ES2 Applied Torsion vs. Angle of Principal Strain (CCW+)	76

Section 4.3

4.18 LED Element Strains	77
4.19 ES1 Applied Torsion vs. In-Plane (XY) Shear Strain	79
4.20 ES1 In-Plane (XY) Shear Strain at 'Peak' Torsion	79
4.21 ES1 Applied Torsion vs. X-Direction Strain	80

4.22	ES1 X-Direction Strain at 'Peak' Torsion	80
4.23	ES1 Applied Torsion vs. Y-Direction Strain	81
4.24	ES1 Y-Direction Strain at 'Peak' Torsion	81
4.25	ES1 Applied Torsion vs. Principal Tensile Strain	82
4.26	ES1 Principal Tensile Strain at 'Peak' Torsion	82
4.27	ES1 Applied Torsion vs. Principal Compressive Strain	83
4.28	ES1 Principal Compressive Strain at 'Peak' Torsion	83
4.29	ES1 Applied Torsion vs. Angle of Principal Strain (CCW+)	84
4.30	ES1 Angle of Principal Strain (CCW+) at 'Peak' Torsion	84
4.31	ES2 Applied Torsion vs. In-Plane (XY) Shear Strain	85
4.32	ES2 In-Plane (XY) Shear Strain at 'Peak' Torsion	85
4.33	ES2 Applied Torsion vs. X-Direction Strain	86
4.34	ES2 X-Direction Strain at 'Peak' Torsion	86
4.35	ES2 Applied Torsion vs. Y-Direction Strain	87
4.36	ES2 Y-Direction Strain at 'Peak' Torsion	87
4.37	ES2 Applied Torsion vs. Principal Tensile Strain	88
4.38	ES2 Principal Tensile Strain at 'Peak' Torsion	88
4.39	ES2 Applied Torsion vs. Compressive Tensile Strain	89
4.40	ES2 Principal Compressive Strain at 'Peak' Torsion	89
4.41	ES2 Applied Torsion vs. Angle of Principal Strain (CCW+)	90
4.42	ES2 Angle of Principal Strain (CCW+) at 'Peak' Torsion	90

Section 4.4

4.43	Example of LP arrangement in XZ and YZ Planes	91
4.44	ES1 Applied Torsion vs. Out-of-Plane (XZ) Shear Strain	94
4.45	ES1 Applied Torsion vs. X-Direction Strain	94
4.46	ES1 Applied Torsion vs. Principal Tensile Strain	95
4.47	ES1 Applied Torsion vs. Principal Compressive Strain	95
4.48	ES1 Applied Torsion vs. Principal Angle	95
4.49	ES1 Applied Torsion vs. Out-of-Plane (YZ) Shear Strain	96
4.50	ES1 Applied Torsion vs. Y-Direction Strain	96
4.51	ES1 Applied Torsion vs. Principal Tensile Strain	97
4.52	ES1 Applied Torsion vs. Principal Compressive Strain	97
4.53	ES1 Applied Torsion vs. Principal Angle	97
4.54	ES1 Applied Torsion vs. Through the Thickness (Z) Strain	98
4.55	ES2 Applied Torsion vs. Out-of-Plane (XZ) Shear Strain	99
4.56	ES2 Applied Torsion vs. X-Direction Strain	99
4.57	ES2 Applied Torsion vs. Principal Tensile Strain	100
4.58	ES2 Applied Torsion vs. Principal Compressive Strain	100
4.59	ES2 Applied Torsion vs. Principal Angle	100
4.60	ES2 Applied Torsion vs. Out-of-Plane (YZ) Shear Strain	101
4.61	ES2 Applied Torsion vs. Y-Direction Strain	101
4.62	ES2 Applied Torsion vs. Principal Tensile Strain	102
4.63	ES2 Applied Torsion vs. Principal Compressive Strain	102
4.64	ES2 Applied Torsion vs. Principal Angle	102
4.65	ES2 Applied Torsion vs. Through the Thickness (Z) Strain	103

Section 4.5

4.66	ES1 Applied Torsion vs. X-Reinforcement Strain	105
4.67	ES1 Applied Torsion vs. Y-Reinforcement Strain	105

4.68	ES2 Applied Torsion vs. X-Reinforcement Strain	106
4.69	ES2 Applied Torsion vs. Y-Reinforcement Strain	106
4.70	ES2 Applied Torsion vs. Z-Reinforcement Strain	106

CHAPTER 5: Discussion of Experimental Results and Observations

Section 5.1

5.1	ES1 Applied Torsion-Twist at Load Stages	109
5.2	ES1 at Failure	109
5.3	ES1 Load Stage Photographs	110
5.4	ES2 Applied Torsion-Twist at Load Stages	111
5.5	ES2 at Failure	111
5.6	ES2 Load Stage Photographs	112

Section 5.2

5.7	ES1 Surface Deformations Measured by LED Targets	113
5.8	ES2 Surface Deformations Measured by LED Targets	114
5.9	Visible Cover Spalling at Specimen Edge	115
5.10	Visible Cover Spalling at Cored Locations	115
5.11	Crack Slip in Failed ES1 Specimen	116
5.12	Bulging Cover and Residual Curvature in Failed ES1 Specimen	116

Section 5.3

5.13	Applied Torsion-Twist Comparison	117
5.14	In-Plane Shear Strain Comparison	118
5.15	In-Plane Principal Strain Comparison	119
5.16	Membrane Representation of ES1 and Results at Peak Shear Stress	119
5.17	In-Plane Reinforcement Strain Comparison	120
5.18	Membrane Vital Signs for ES1 at Peak Shear Stress	120

Section 5.4

5.19	Out-of-Plane Shear Strain Comparison	122
5.20	Out-of-Plane Concrete Expansion Comparison	122
5.21	Out-of-Plane T-Head Reinforcement Strain	123

CHAPTER 6: A Finite Element for the Analysis of Reinforced Concrete Shells

Section 6.1

6.1	Shell-2000 Models of Experimental Specimens	125
6.2	Shell-2000 In-Plane Shear Strain and Torque-Twist Behaviour	126
6.3	Shell-2000 Torque-Twist Compared to Experimental Results	126

Section 6.2

6.4	3d-HyPT Element Numbering Convention	127
6.5	Vizualization of 3d-HyPT Element Subcomponents	127
6.6	Six Faces Representing the 3d-HyPT Element	128
6.7	Simply Supported Beam Modelled with 3d-HyPT Elements Placed in Series	129
6.8	Simply Supported Beam with Complex Loading	129
6.9	Simply Supported Slab Modelled with 3d-HyPT Elements Placed in a Grid	130
6.10	Cantilevered Slab Modelled with 3d-HyPT Elements	130

Section 6.3

6.11 Relative Deformations of Trusses in XZ-Plane Faces	131
6.12 Interpolated Strains Between Parallel Faces	132
6.13 Unit Increments at Right Side of Element	133
6.14 Equivalent Nodal Forces Based on Strain Increment at DOF #7	134
6.15 Vertical Trusses in the 3d-HyPT Element	136
6.16 Axial Strain in Vertical Direction Based on Twist Strain	136
6.17 Z-Direction Strain Applied to Vertical Trusses	137
6.18 XZ-Plane Panel Stiffness Matrix (Equal In-Plane Shear Strains)	140
6.19 XZ-Plane Panel Stiffness Matrix (Unequal In-Plane Shear Strains)	140

Section 6.4

6.20 Preliminary Program Operational Flowchart	142
6.21 Sample Global Input File for Fixed Slab Model	143
6.22 Sample Section Input File for Fixed Slab Model	144
6.23 Program Output from Structural Analysis Input Files (Slab)	145
6.24 Program Output from Structural Analysis Input Files (Beam)	146
6.25 Analysis Program Operational Flowchart	147
6.26 Deformation and Cracking Output at Load Stage for Fixed Slab Model	148
6.27 Deformation and Cracking Output at Load Stage for Cantilevered Beam Model	148

Section 6.5

6.28 Finite Element Mesh for Torsion Shell Experiments	149
6.29 Analysis Element Geometry	149
6.30 Typical Deformed Shape During the Analysis of a Torsion Shell	150
6.31 Analysis Program Results: Torque-Twist	151
6.32 Analysis Program Results: Out-of-Plane Shear Strain	152

APPENDIX

A.1 Shear Critical Beam Database (No Stirrups - Part 1/11)	160
A.2 Shear Critical Beam Database (No Stirrups - Part 2/11)	161
A.3 Shear Critical Beam Database (No Stirrups - Part 3/11)	162
A.4 Shear Critical Beam Database (No Stirrups - Part 4/11)	163
A.5 Shear Critical Beam Database (No Stirrups - Part 5/11)	164
A.6 Shear Critical Beam Database (No Stirrups - Part 6/11)	165
A.7 Shear Critical Beam Database (No Stirrups - Part 7/11)	166
A.8 Shear Critical Beam Database (No Stirrups - Part 8/11)	167
A.9 Shear Critical Beam Database (No Stirrups - Part 9/11)	168
A.10 Shear Critical Beam Database (No Stirrups - Part 10/11)	169
A.11 Shear Critical Beam Database (No Stirrups - Part 11/11)	170
A.12 Shear Critical Beam Database (No Stirrups & Distributed Load)	171
A.13 Shear Critical Beam Database (Stirrups - Part 1/2)	172
A.14 Shear Critical Beam Database (Stirrups - Part 2/2)	173
B.1 ES1 Experimental Data (Forces)	175
B.2 ES1 Experimental Data (LVDTs)	176
B.3 ES1 Experimental Data (LPs - Part 1/2)	177
B.4 ES1 Experimental Data (LPs - Part 2/2)	178

B.5	ES1 Experimental Data (EGs - Part 1/2)	179
B.6	ES1 Experimental Data (EGs - Part 2/2)	180
B.7	ES1 Experimental Data (North SGs)	181
B.8	ES1 Experimental Data (South SGs)	182
B.9	ES2 Experimental Data (Forces)	183
B.10	ES2 Experimental Data (LVDTs)	184
B.11	ES2 Experimental Data (LPs - Part 1/2)	185
B.12	ES2 Experimental Data (LPs - Part 2/2)	186
B.13	ES2 Experimental Data (EGs - Part 1/2)	187
B.14	ES2 Experimental Data (EGs - Part 2/2)	188
B.15	ES2 Experimental Data (North SGs)	189
B.16	ES2 Experimental Data (South SGs)	190
B.17	ES2 Experimental Data (T-Head SGs)	191
C.1	ES1 In-Plane (XY) Shear Strain at Load Stages	193
C.2	ES1 X-Direction Strain at Load Stages	194
C.3	ES1 Y-Direction Strain at Load Stages	195
C.4	ES1 Principal Tensile Strain at Load Stages	196
C.5	ES1 Principal Compressive Strain at Load Stages	197
C.6	ES1 Angle of Principal Strain (CCW+) at Load Stages	198
C.7	ES2 In-Plane (XY) Shear Strain at Load Stages	199
C.8	ES2 X-Direction Strain at Load Stages	200
C.9	ES2 Y-Direction Strain at Load Stages	201
C.10	ES2 Principal Tensile Strain at Load Stages	202
C.11	ES2 Principal Compressive Strain at Load Stages	203
C.12	ES2 Angle of Principal Strain (CCW+) at Load Stages	204
D.1	MATLAB Main File Code (Part 1/3)	205
D.2	MATLAB Main File Code (Part 2/3)	206
D.3	MATLAB Main File Code (Part 3/3)	207
E.1	Global Input File for Specimen ES1 and ES2 Models	208
E.2	Section Input File for Specimen ES1	209
E.3	Section Input File for Specimen ES2	210
E.4	Global Summary Output File for Specimen ES2 (Part 1/2)	211
E.5	Global Summary Output File for Specimen ES2 (Part 2/2)	212
E.6	Section Summary Output File for Specimen ES2	213
E.7	Load Stage Iteration File (Excerpt) for Specimen ES2 (Part 1/2)	214
E.8	Load Stage Iteration File (Excerpt) for Specimen ES2 (Part 2/2)	215
E.9	Load Stage Summary File (Reduced) for Specimen ES2	216

Chapter 1

Introduction

The following chapter will present an overview of the research program presented in this thesis. The growth of nonlinear finite element analysis in structural engineering is first presented in the context of the parallel technological development in computing. This discussion is followed by the justification for this specific research, which is primarily motivated by the need to overcome certain challenges associated with modern finite element modelling paradigms when applied to the analysis of complex three dimensional reinforced concrete structures.

This is followed by an outline of the specific experimental and numerical objectives that were defined at the outset of the project, and how these are presented in the thesis document structure. A summary of key research documents and existing research literature is also included for readers that wish to delve into the main influences for the finite elements presented in this thesis.

1.1 Background and Research Motivation

Over the last 40 years, two factors have contributed to major advancements in the fields of reinforced concrete design and analysis. First, the exponential increase in computational power has allowed for structural engineering problems with geometric complexity and material nonlinearity to be efficiently handled by computer-based solution procedures. The ubiquitous presence of nonlinear finite element analysis (NLFEA) in all aspects of structural analysis work is a testament to the success of this approach. Second, the 1986 publication of Modified Compression Field Theory (MCFT) has introduced a general and rational solution to the complex shear problem in reinforced concrete [1]. In 1996, this theory was further developed into a design procedure [2], which has subsequently become the basis for the shear provisions in the Canadian reinforced concrete design code [3, 4] and numerous other codes worldwide.

The predictive accuracy of the MCFT can be coupled with the speed of computer-based analysis - examples of this are the VecTor2 [5, 6] and Response-2000 [7] software packages developed at the University of Toronto. For a member level analysis, VecTor2 functions by representing a reinforced concrete structure as a mesh of triangular or rectangular membrane elements based on the MCFT formulation [8]. For a sectional analysis, Response-2000 functions by representing a reinforced concrete cross-section as the summation of several discrete slices through the thickness [9]. Figure 1.1 depicts the growth in the computing power of commercially available IntelTM processors [10] in the context of a sectional analysis of a complex pretensioned highway girder with Response-2000.

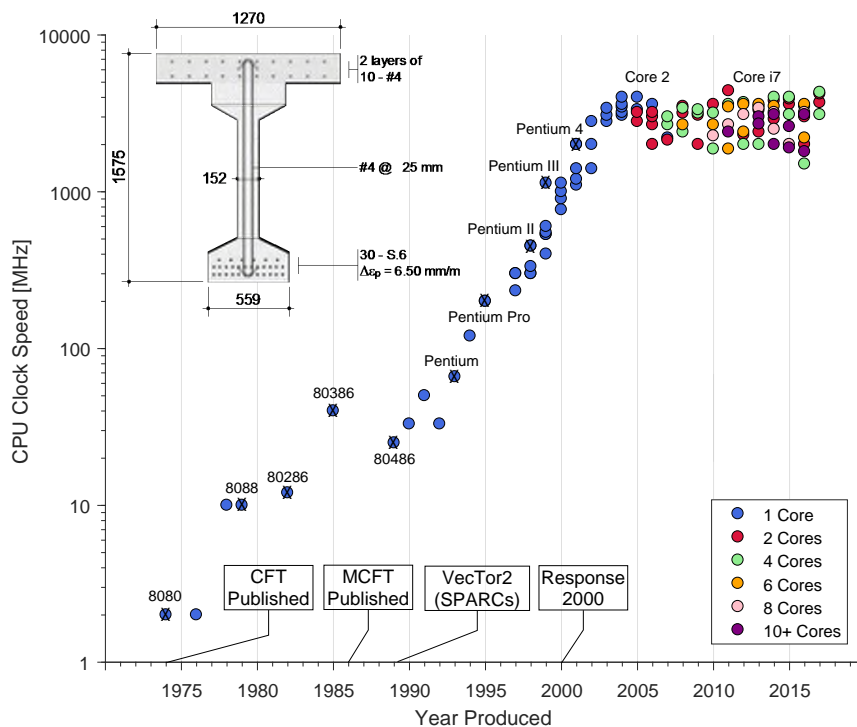


Figure 1.1: *The Growth of Processing Power in the Context of a Sectional Analysis*

The dramatic improvement in computer processors has made it possible to solve reinforced concrete sectional analysis problems that were previously unwieldy; a task that would take several hours two decades ago can now be completed in mere seconds. Yet a detailed non-linear analysis of a whole structure, as opposed to a cross-section, is in many ways still considered a challenging task. While cross-sectional and single member analyses can tell us much about specific sub-components of a structure, there are also complex effects (e.g. torsion) that can result from three-dimensional loading, complex geometry, or general global behaviour that will not necessarily be captured by a local analysis. It is therefore more desirable to model as much of a structure as realistically as possible - the trade-off is that adding modelling complexity leads to a more computationally demanding analysis. Depending on the geometry, models with thousands of elements and degrees of freedom (DOFs) could be necessary to represent the complete structure. While rigorous academic software (i.e. The VecTor Suite) can be extended to the macro-level analysis of structures, the execution time often becomes excessive at such large scales. Figure 1.1 underscores the fact that relying on increasing processor speeds is also not a viable long-term strategy for large-scale structural analysis. The growth of single processor speeds has essentially plateaued, and in the last decade emphasis has instead been placed on the development of multi-core processors. While this development helps speed up certain computational tasks, not all structural analysis algorithms and solution methods can currently be run in parallel to take advantage of multiple cores.

The main computational demand associated with NLFEA comes from simultaneously solving a large system of equations, which represents the relationship between the forces and displacements at DOFs (i.e. the stiffness method). When formulated as a finite element problem this relationship falls under two distinct paradigms - either using many low-powered elements, or using few high-powered elements to represent the structure. The term *power* refers to the number of DOFs and the complexity of the underlying shape functions defining the element. The highly non-linear nature of reinforced concrete has typically precluded the use of the later approach; it is difficult to develop a high-powered general element based on shape functions that can accurately cover large volumes and still capture phenomenon such as localized cracking, yielding, and shear failure. Therefore, successful reinforced concrete analysis programs such as VecTor2 have adopted the first approach by using numerous low-powered elements instead [11]. These elements are based on simple linear shape functions, and can be used to approximate a highly nonlinear strain field when distributed in a sufficiently fine mesh. Yet this means that the analysis results can be highly sensitive to modelling parameters, and relying on a large quantity of elements to represent a structure becomes exponentially more computationally expensive as the size of the structure being modelled increases. Therefore, a novel finite element paradigm is necessary, one that is both simply formulated and robust with respect to the number of elements - resulting in a finite element analysis that is less reliant on computational capacity, but still able to accurately capture the nonlinear behaviour of reinforced concrete.

1.2 Research Objectives and Overview

This thesis will present the mathematical formulation of the Hybrid Panel-Truss (HyPT) element, which has been created in an attempt to deal with the analysis time and model complexity challenges arising from current reinforced concrete NLFEA paradigms. The overall research program can be subdivided into the following set of objectives:

1. To consolidate the work done to date on the two-dimensional version of the element, and to expand the derivation to include a rigorous membrane formulation based on the MCFT.
2. To validate the two-dimensional element against a series of experimental results.
3. To construct two shell specimens, with and without shear reinforcement, and to load them under pure torsion with a displacement-controlled loading protocol.
4. To derive and validate the three-dimensional version of the element against the torsion experiments.

The **first objective** is to present an updated derivation of the two-dimensional Hybrid Panel-Truss (2d-HyPT) element, which is intended for the full-member analysis of reinforced concrete beams and columns. The element is derived with a specific focus on the ability to predict shear failure, therefore expanding the derivation to include a shear panel based on an MCFT formulation is a significant improvement to previous approaches.

The **second objective** is to determine the speed and accuracy of the 2d-HyPT element when utilized in the analysis of reinforced concrete structures. The derivation of the single element stiffness matrix is accompanied by an extensive member-level validation study against a database of shear critical reinforced concrete beams, followed by a large-scale structure validation exercise against two previously tested frames.

The **third objective** is to design, construct and carry-out a testing program for two reinforced concrete shells under pure torsion, with the goal of determining the influence of T-head shear reinforcement on the ultimate strength and ductility of the specimens. The testing procedures and the data for these experiments are meticulously presented as they represent the first tests of this nature. These results are also integral to the derivation of the three-dimensional version of the HyPT element - there were certain assumptions regarding the out-of-plane strains that were inherent in the 2d-HyPT formulation and could only be clarified with experimental data.

The **fourth objective** is to extend the 2d-HyPT element formulation for use in three dimensions. The 3d-HyPT element is based on many of the same principles as its two dimensional counterpart, but takes added steps to account for additional connectivity and out-of-plane effects in the element. The experimental data from the two torsion shell tests is also built into certain assumptions included in the model.

1.3 Literature Review

The proposed element is unique in that it combines the computational simplicity of a low-powered element with the ability to capture complex deformation patterns typical of a high-powered element. With both the 2d and 3d-HyPT formulations, only one element is necessary through the thickness of a member, thereby significantly reducing the number of global DOFs present in a problem. The element uses a multi-component approach where the axial, flexure and shear deformations inherent in reinforced concrete are captured by specific internal components. The relative deformations of one-dimensional axial trusses, that each connect two nodes, are used to represent axial and flexural deformations; two-dimensional shear panels, that each connect the four nodes of a face, are used to represent shear deformations. These deformation patterns can be defined through simple translational DOFs, while more complex effects are explicitly accounted for in the resulting deformation patterns associated with the element. In contrast, more complex finite elements attempt to account for things like rotational deformations through explicit DOFs and require numerical integration schemes to solve, which will add an additional computational demand to the analysis. The following section briefly reviews some of the standard approaches for modelling shell elements, and then introduces some of the previous research dealing with multi-component models and how these ideas have influenced the derivation of the HyPT element.

1.3.1 Elasticity-Based Finite Element Models for Shells

Standard shell elements are formulated based on either the Kirchoff plate bending or the Mindlin theory, which are appropriate for modelling thin or thick shells respectively. Thin shells are a special case, where the finite element formulation is simplified by neglecting out-of-plane effects. On the other hand, the thick shell formulation takes a more generalized form and can be applied to all cases, and is therefore a more complex finite element to derive [12]. The following section will focus on the strengths and weaknesses of standard shell finite elements that have been derived from three-dimensional elasticity.

Degenerated Shells

A discussion of various shell modelling techniques is presented by Figueiras and Owen [13], where the most practical approach is using what are called degenerated elements. These elements are developed from the equations of three-dimensional elasticity, which are implemented in the form of isoparametric elements that use independent displacement and rotational DOFs. Essentially a generalized three-dimensional solid element is collapsed to a shell element, which relies on the deformation of fewer nodes. Figure 1.2 shows the degeneration of a 20-noded and 60-DOF solid element into a 8-noded and 40-DOF shell element [14]. In this example, each node has three translational and two rotational DOFs.

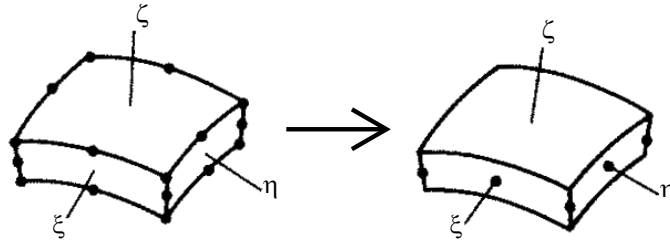


Figure 1.2: *Degeneration of Three-Dimensional Solid Element (Adapted from Cook et. al. [14])*

The Heterosis Shell Element

The Heterosis shell is a type of degenerated element that has been shown to perform well when implemented with a rotating crack model for the analysis of both thin and thick reinforced concrete shells [15, 16]. The element is a 9-noded quadratic element with a total of 42 DOFs, where the three translational DOFs of the central node are removed. Yet while this element is considered a good compromise between the less complex Serendipity and more complex Lagrange quadratic elements [17], it still suffers from some of the same drawbacks. The Heterosis element relies on complex numerical integration to determine the stiffness matrix of the element while minimizing spurious deformation modes - the reduced numerical integration scheme used is a 3x3 Gaussian grid for the bending and membrane energy, and a 2x2 Gaussian grid for the out-of-plane shear energy [13]. This particular reduced integration scheme is used to achieve optimal computational performance while removing what are known as "zero-energy" deformation modes, which are mathematical artifacts that are in reality physically impossible as they occur in the element without changes to the the internal energy. For example, if the number of integration points is reduced in an attempt to speed up the calculation process, the finite element formulation becomes more prone to these unrealistic deformations. Figure 1.3 illustrates a spurious deformation mode that would exist if the stiffness of a two-dimensional element was being calculated with just one integration point at the center. The dotted line shows a hypothetical deformation in the element, which a numerical integration based on the central point would suggest requires no change to the internal energy, as represented by the constant vertical and horizontal strains measured at the point (i.e. no change in length of the red lines).

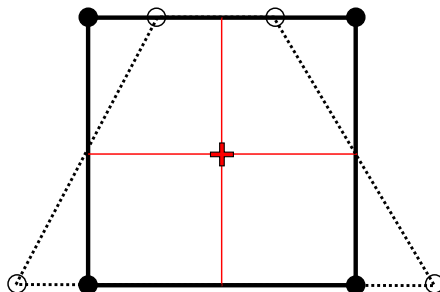


Figure 1.3: *Spurious Deformation Mode with A Single Integration Point*

Even with a complex integration scheme, the Heterosis element still has one spurious deformation mode, while the Serendipity and Lagrange elements have two and four respectively [13]. Although the severity of certain modes is somewhat reduced as they would not be communicable in a mesh of elements. There also exist other methods that attempt to control the "zero-energy" modes in simpler reduced integration schemes, such as one-point quadrature [18]. Yet such methods become exceedingly difficult to apply to reinforced concrete, where a high degree of nonlinearity often means that sampling only one point is not enough to characterize the complex strain field.

To summarize, while the Heterosis element is both mathematically rigorous and proven to work for the analysis of thin and thick reinforced concrete shells, its reliance on a complicated integration scheme results in a large computational demand - at each iteration, and for each element, several numerical integrations must be performed to determine the element stiffness matrix. It is also difficult to improve on this formulation, since reducing the number of integration points to improve the speed will lead to either spurious deformation modes, or an incorrect representation of the nonlinearity in reinforced concrete. For reference, information on the three degenerated shell models mentioned in this section is presented in Figure 1.4, which is taken from the work by Trevor Hrynyk [16].

	SERENDIPITY	HETEROSIS	LAGRANGE
u, v, w shape functions	Serendipity	Serendipity	Lagrange
θ_1, θ_2 shape functions	Serendipity	Lagrange	Lagrange
integration scheme	bending: 2 x 2 – Gauss shear: 2 x 2 – Gauss	bending: 3 x 3 – Gauss shear: 2 x 2 – Gauss	bending: 3 x 3 – Gauss shear: 2 x 2 – Gauss
number of spurious zero-energy modes	bending: 1* membrane: 1*	bending: 0 membrane: 1*	bending: 1 membrane: 2+1*
constraint index	1	3	4

¹ from Figueiras and Owen (1984)

* not communicable in a mesh of two or more elements

● - $u, v, w, \theta_1, \theta_2$ degrees of freedom considered

○ - θ_1, θ_2 degrees of freedom considered

Figure 1.4: Summary of Degenerated Shell Elements (Hrynyk [16, p. 164], Adapted from Hughes[17])

1.3.2 Multi-Component Models

The HyPT element takes a different approach to the modelling of reinforced concrete, relying on the aggregate action of simpler subcomponents, instead of using element-level shape functions derived from three-dimensional elasticity. The stiffness matrices of the various components are calculated by relating the nodal displacements of the element to a combination of flexural, axial, and shear deformations. The truss bar subcomponents that carry axial and flexural deformations are calculated based on a fiber-model approach, while the shear panel subcomponents are calculated using an in-plane MCFT analysis.

The idea to represent the complex interactions in reinforced concrete by summing the contributions of several more simple subcomponents is not a new concept - the HyPT element draws inspiration from some notable multi-component examples that are presented in this section.

Multi-Layer Model

The stacked membrane, or multi-layer model, is a generalized sectional method where a shell is assumed to be made up of several in-plane membrane elements (Figure 1.5). Variations in stiffness through the thickness of the shell are explicitly accounted for as unique stress-strain relationships are calculated for each membrane. The force resultants (N_x, N_y, N_{xy}) and moment resultants (M_x, M_y, M_{xy}) can then be summed across the whole shell to determine the overall sectional behaviour. The analytical process is improved since a two-dimensional membrane is a relatively simple problem to solve, although the downside is that out-of-plane shear effects are neglected. The idea of using multiple in-plane membranes to represent global behaviour is reflected in the derivation of the shear panel subcomponent for the 3d-HyPT element.

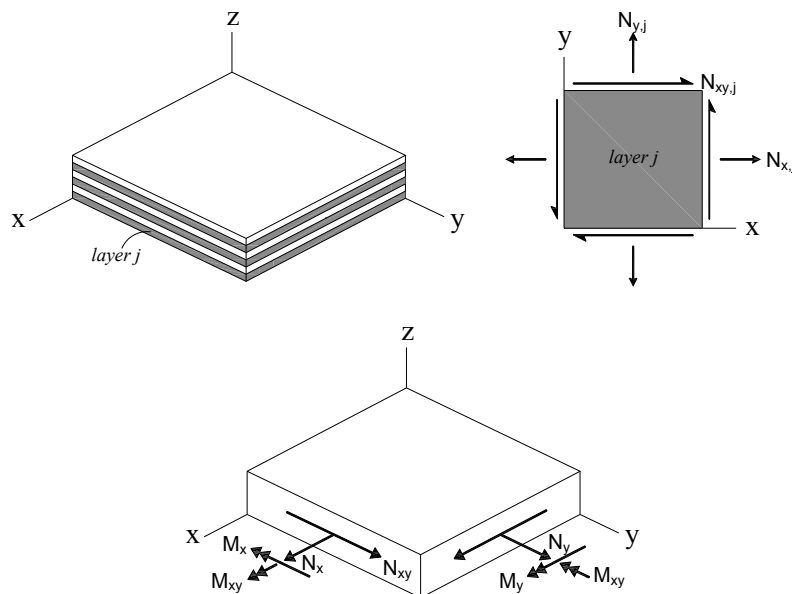


Figure 1.5: *Multi-Layered Model and Sectional Forces (Hrynyk [16, p. 8], Adapted from Collins [19]*

Space Truss Model

The internal load-carrying mechanism in a cracked reinforced concrete member subjected to torsion can be described with the three-dimensional Space Truss model. After cracking, a reinforced concrete beam is idealized as a truss with longitudinal chords, diagonal concrete struts, and transverse steel ties [20]. In the horizontal direction, each chord consists of the passive and active longitudinal steel area and any concrete that is in compression. While in the vertical direction, the concrete forms a diagonal compressive strut held together by the stirrups. Looking at the section, the compression in the strut is balanced by a tension in the chords and a shear flow along the perimeter, while at the corner the vertical component is carried by a tension in the stirrups and an additional force in the chord [21].

If the geometry of the space truss is known, the force resultants in each of these components can be calculated from statics. Moments and axial forces can be resolved into chord forces, while shears and torsions will result in diagonal compressions that can be resolved into shear flows along the faces of the section and additional chord forces [20]. Figure 1.6 is taken from the work by Collins and Mitchell, which shows how an applied torsion is carried through the different components in a cracked reinforced concrete section. The idea of resolving the sectional resultants into longitudinal and vertical force demands that are carried by different components is also used in the formulation of the HyPT element.

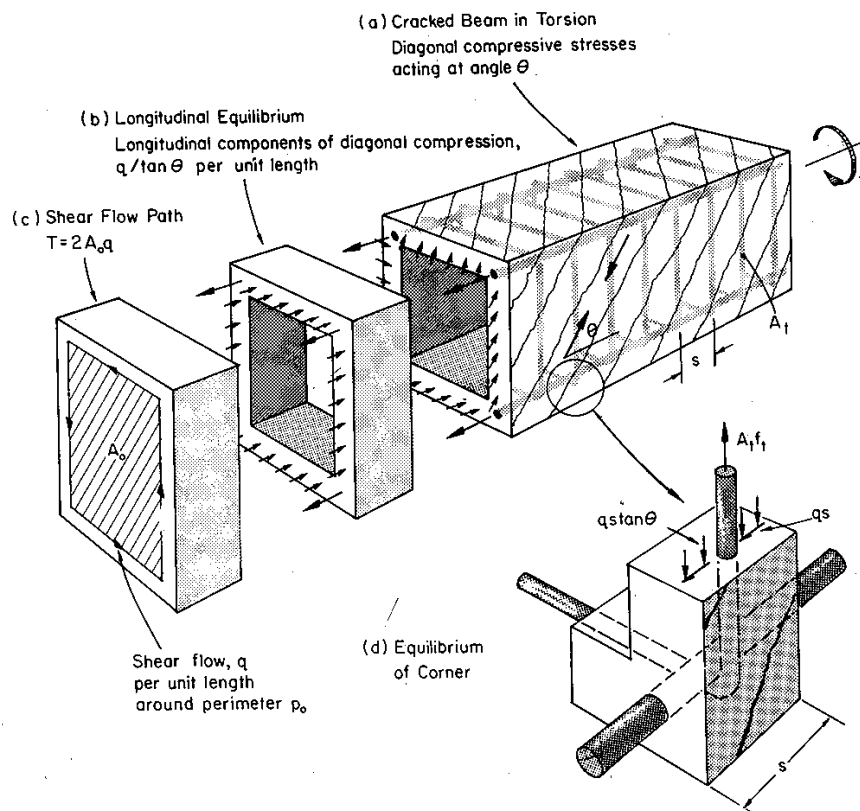


Figure 1.6: *Space Truss Model and Force Equilibrium (Collins and Mitchell [21])*

Stringer Panel Model

The Stringer Panel model is similar to the Space Truss model since it distributes the different internal forces in a reinforced concrete member to specific components. For example, the four stringers transfer normal forces, and border a flat plate that can only transfer shear forces [22]. The top and bottom stringers are analogous to the top and bottom chords defined in the Space Truss model. A schematic of the element is shown in Figure 1.7.

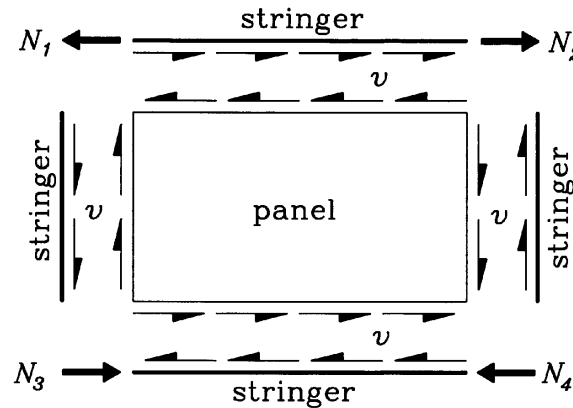


Figure 1.7: *Stringer Panel Element Schematic (Blaauwendraad [22])*

An important feature of the Stringer Panel model is that it was specifically formulated as a finite element, and is hence closely related to the research objectives of this thesis. By contrast, the Space Truss model is an excellent general design tool, but it is not directly applicable to a finite element procedure. The Stringer Panel elements are assembled to construct a two dimensional member, such as the cantilever beam that is shown in Figure 1.8. Once the element mesh is defined, the structure is subjected to external loads. The global behaviour is then determined based on the relationship between the load and displacement defined by the sum of all the individual element stiffnesses and connections between DOFs. There are many similarities between the Stringer Panel and the HyPT formulation, although the 2d-HyPT element accounts for reinforced concrete nonlinearity through the constitutive relationships of the MCFT, and improves the robustness of the analysis by requiring only one element through the thickness of the member.

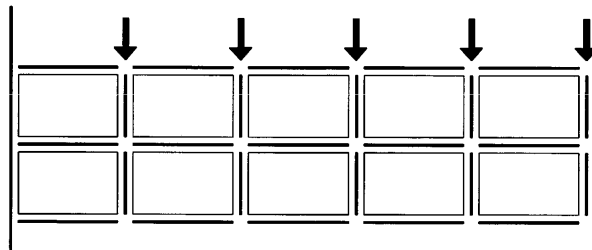


Figure 1.8: *Cantilever Constructed from Stringer Panel Elements (Blaauwendraad [22])*

1.3.3 Previous Work Related to the 2d-HyPT Element

There exists some specific research on the derivation and implementation of the 2d-HyPT element, which has until this thesis remained unnamed. Several students at the University of Toronto, supervised by Professor Bentz, have over recent years worked with the element, to varying degrees, as implemented in the analysis program Augustus-II. There has yet to be an official peer-reviewed publication related to the development of the element.

For those interested in reading about further applications and case studies using the 2d-HyPT element the following thesis documents could be useful: Yeung (2008, [23]), Cheung (2012, [24]), Zaeem (2013, [25]), Yap (2016, [26]). But note that the current thesis presents the most up-to-date derivation of the element, and consolidates all of the previous derivations while simultaneously improving the element formulation significantly. To avoid confusion, the derivation work in these previous theses should be considered superseded by the work presented herein.

1.4 Thesis Organization

The main body of this thesis is organized into seven main chapters, plus an appendix for additional information. Each of these chapters accomplishes the following:

- Chapter 1: Provides an introduction to the topic of finite element analysis in the context of reinforced concrete shells. Outlines the high-level focus and organization of the thesis.
- Chapter 2: Presents a mathematical derivation of the stiffness terms for the various subcomponents in the two-dimensional Hybrid Panel Truss (2d-HyPT) element. Presents the results of an extensive validation study against a database of shear critical beams and two experimental frames.
- Chapter 3: Describes the experimental program. Focuses on the material properties, construction procedures, instrumentation types, and experimental loading protocol for both shell specimens.
- Chapter 4: Presents the relevant data from the two pure torsion shell experiments, and explains how the instrumentation data streams were processed and manipulated.
- Chapter 5: Discusses the results of the shell tests and draws conclusions that will be implemented when deriving the finite element for the analysis of shell structures.
- Chapter 6: Extends the mathematical derivation of the 2d-HyPT into three dimensions for the use in the analysis of complex structures. Presents the implementation of the 3d-HyPT element in an original computer program and compares the analysis results to the experimental data.
- Chapter 7: Summarizes the main contributions of this research and recommends future research tasks.

Chapter 2

A Finite Element for the Analysis of Reinforced Concrete Beams: Derivation and Verification

The following chapter will present the numerical derivation and verification of a finite element for the nonlinear structural analysis of reinforced concrete beams subjected to in-plane loading. The finite element will be referred to as the Hybrid Panel-Truss (2d-HyPT) element - the prefix is meant to distinguish it from the three-dimensional implementation of the element used for the analysis of reinforced concrete shells, which is derived in Chapter 6 of this thesis. If no prefix is used, a reference to the two-dimensional implementation is to be assumed.

The derivation is divided into sections corresponding to the individual components that make up the complete stiffness matrix for a single element. The verification study is then meant to test the element's ability to accurately predict the failure loads for a database of reinforced concrete beam tests, along with two large-scale frames tested at the University of Toronto. In this thesis, the HyPT element is used to construct finite element models of the verified specimens and experiments reported in the ACI shear critical beam databases, for beams with and without shear reinforcement [27, 28].

2.1 Description of 2d-HyPT Element

The Hybrid Panel-Truss (HyPT) element is a two-dimensional rectangular element with a total of four nodes and eight degrees of freedom (DOFs) - two orthogonal translational DOFs per node oriented in the plane of the member (Figure 2.1).

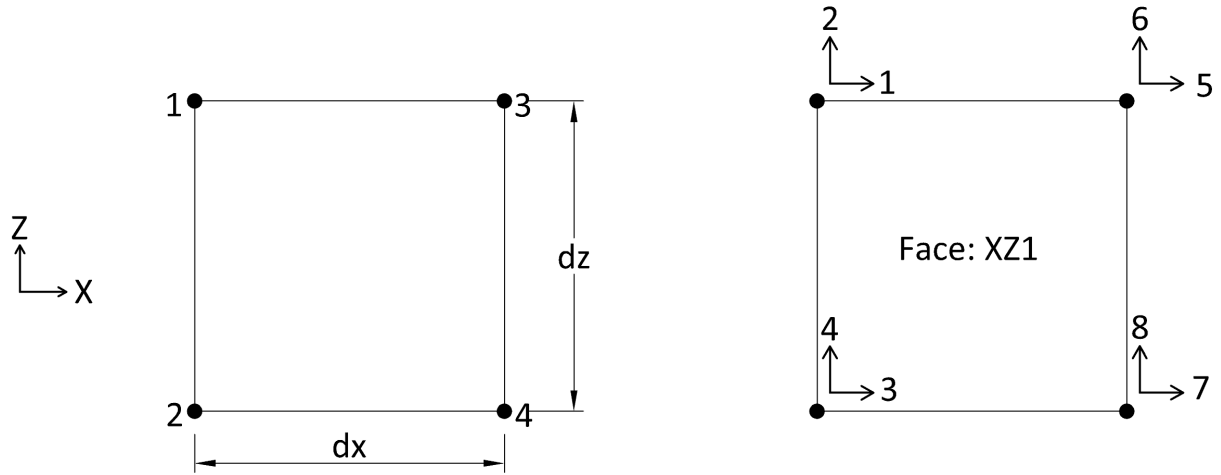


Figure 2.1: *HyPT Element Numbering Convention: Nodes (Left) & DOFs (Right)*

A reinforced concrete beam or column member can be represented with several individual elements placed in series along the longitudinal axis (defined by the direction of the flexural reinforcement). The unconventional node numbering shown in Figure 2.1 reflects the fact that elements are always linked through both nodes on either their left or right face, reminiscent of the plane-sections concept used to describe flexure. Loading and restraint conditions are only applied at the nodes. Figure 2.2 shows a schematic of a simply-supported beam with a double point load, represented by nine elements over the total span.

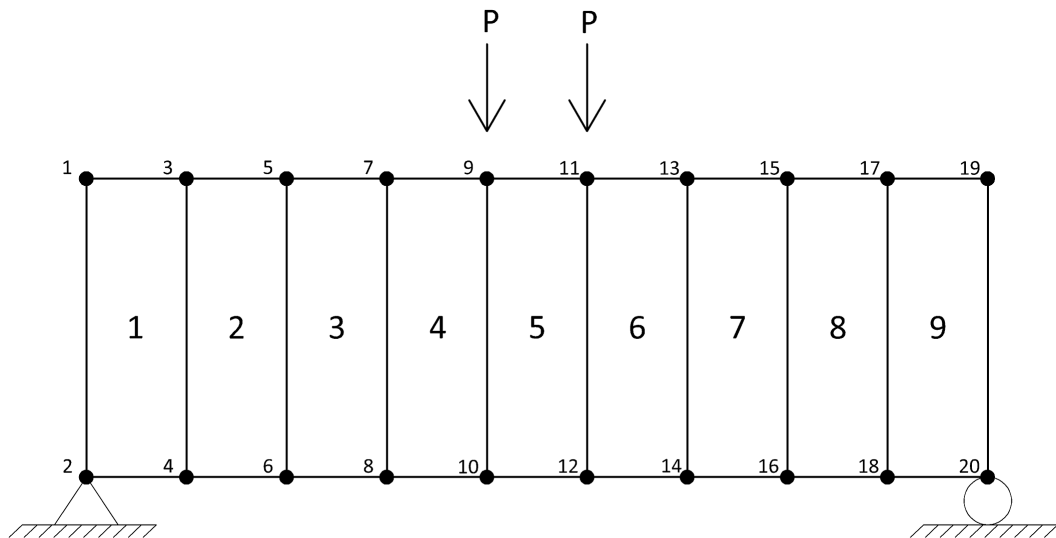


Figure 2.2: *Beam Modelled with HyPT Elements Placed in Series*

The full height of the member is represented by only one element - the material properties of the cross-section (the plane into the page) are used to define the stiffness of the individual elements (Figure 2.3) spaced along the length. The cross-sectional dimensions (d_y & d_z) are set by the structural geometry, while the length/size of the element (d_x) is set by the user.

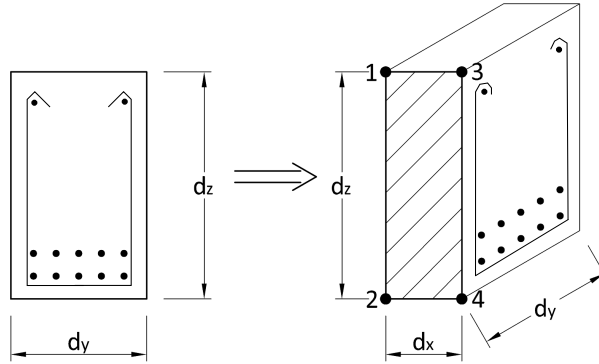


Figure 2.3: *Element Stiffness Defined by Cross-Section*

The efficiency of the HyPT element, with respect to the number of DOFs needed, is due to the unique combination of three separate subcomponents that together are able to represent the internal actions inherent in reinforced concrete: flexure/axial, shear, and post-cracking shear-flexure interaction. The HyPT element can be idealized as a two-dimensional panel that provides shear stiffness, linking two vertical and horizontal one-dimensional truss bars that provide flexural and axial stiffness (Figure 2.4). Similar multi-component models have been proposed in the past, an early example being the Space Truss model developed in the context of torsion design [20], or the Stringer Panel developed in the context of finite element analysis [22]. More details on these models can be found in the literature review section, but as a summary both models idealize reinforced concrete as a system composed of truss and panel elements.

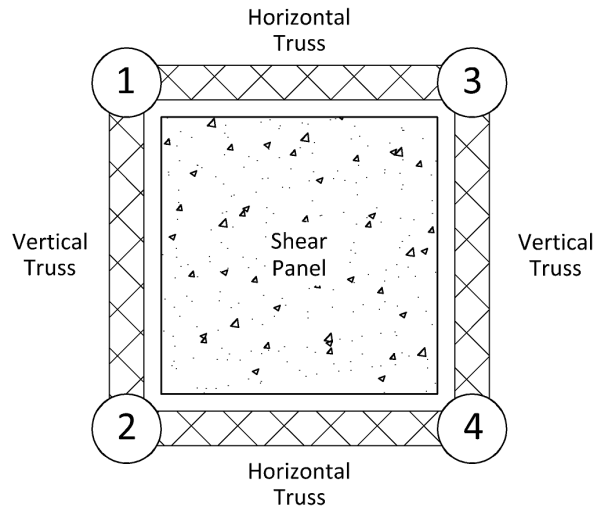


Figure 2.4: *Visualization of HyPT Element Subcomponents*

2.2 Flexural & Axial Truss Stiffness Terms

The flexural and axial stiffness of the HyPT element is defined by a series of one-dimensional truss bars, which can only carry axial force, linking two adjacent nodes. The top and bottom truss bars connect nodes 1-3 and 2-4 respectively, and the left and right truss bars connect nodes 1-2 and 3-4 respectively.

2.2.1 Deformation Patterns

The combined action of the horizontal truss bars is used to represent complex deformation patterns. For example, Figure 2.5 illustrates how axial compression and tension in the element can be represented by the uniform shortening or lengthening of the top and bottom truss bars.

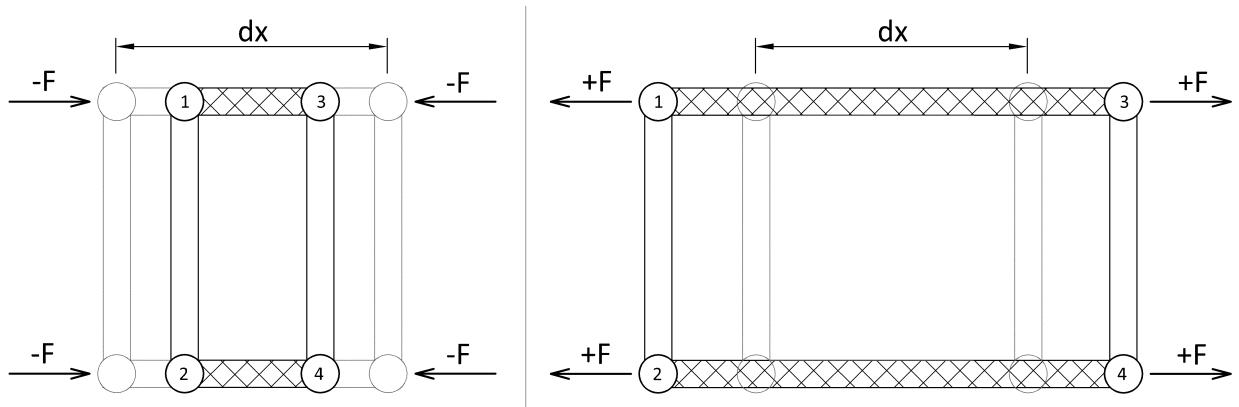


Figure 2.5: A Representation of Axial Compression (Left) and Tension (Right) in the Element

Flexural deformations are represented by the relative deformation of the horizontal truss bars, while retaining rotational equilibrium in the element. For example, positive flexure is seen as the relative contraction of the top truss bar and elongation of the bottom truss bar, and reverse for negative flexure (Figure 2.6).

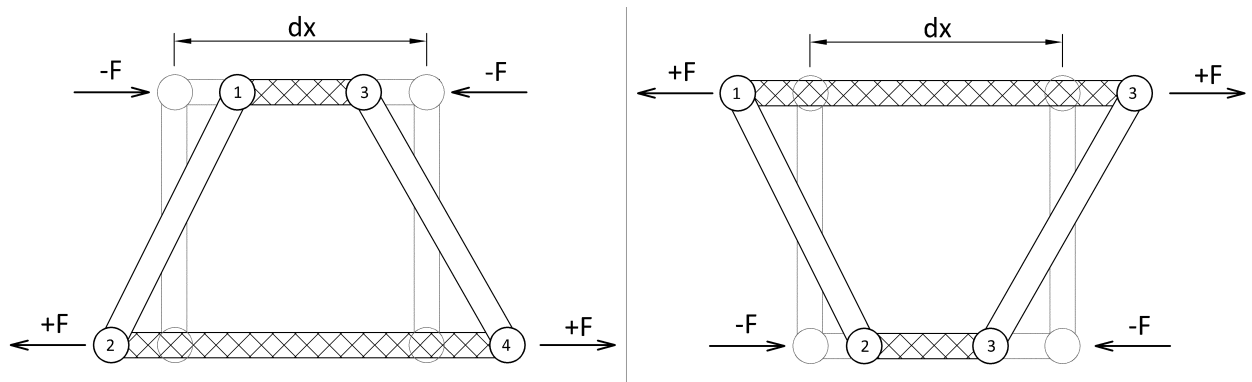


Figure 2.6: A Representation of Positive (Left) and Negative (Right) Flexure in the Element

2.2.2 Truss Bar Stiffness Matrix - Diagonal Terms

A stiffness matrix is used to relate the axial and flexural deformation patterns described in the previous section to the applied forces on the four nodes of the HyPT element. The deformation of a generic truss bar is shown in Figure 2.7, which can also be expressed in matrix form (Equation 2.1).

$$\begin{bmatrix} K_{bar} & -K_{bar} \\ -K_{bar} & K_{bar} \end{bmatrix} \begin{Bmatrix} u_1 \\ u_2 \end{Bmatrix} = \begin{Bmatrix} F_1 \\ F_2 \end{Bmatrix} \quad \text{where: } K_{bar} = \frac{EA}{L} \quad (2.1)$$

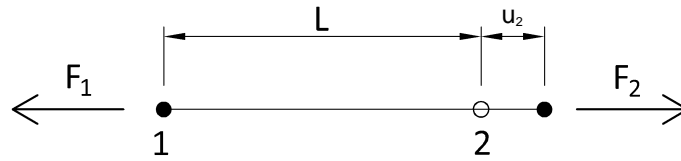
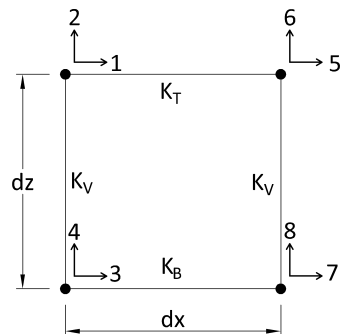


Figure 2.7: Generic Truss Bar

This concept, when applied to all four truss bars in the HyPT element, results in the linear system represented by Equation 2.2. The location of individual stiffness terms is determined based on which DOFs are being linked by that particular truss bar - the DOFs and truss bar notations are reiterated in Figure 2.8.

$$\begin{bmatrix} K_T & 0 & 0 & 0 & -K_T & 0 & 0 & 0 \\ 0 & K_{V,L} & 0 & -K_V & 0 & 0 & 0 & 0 \\ 0 & 0 & K_B & 0 & 0 & 0 & -K_B & 0 \\ 0 & -K_V & 0 & K_V & 0 & 0 & 0 & 0 \\ -K_T & 0 & 0 & 0 & K_T & 0 & 0 & 0 \\ 0 & 0 & 0 & 0 & 0 & K_V & 0 & -K_V \\ 0 & 0 & -K_B & 0 & 0 & 0 & K_B & 0 \\ 0 & 0 & 0 & 0 & 0 & -K_V & 0 & K_V \end{bmatrix} \begin{Bmatrix} u_1 \\ u_2 \\ u_3 \\ u_4 \\ u_5 \\ u_6 \\ u_7 \\ u_8 \end{Bmatrix} = \begin{Bmatrix} F_1 \\ F_2 \\ F_3 \\ F_4 \\ F_5 \\ F_6 \\ F_7 \\ F_8 \end{Bmatrix} \quad (2.2)$$



where:

K_T = Top Truss Bar Stiffness

K_B = Bottom Truss Bar Stiffness

K_V = Left or Right Truss Bar Stiffness

Figure 2.8: Element DOFs and Connecting Truss Bars

2.2.3 Truss Bar Stiffness Matrix - Off-Diagonal Terms

The formulation of the stiffness matrix presented in the previous section implies that the top and bottom faces of the element behave independently. For example, if a unit displacement is applied at DOF #1, only the top truss bar will develop force while the bottom truss bar is unaffected as shown in Figure 2.9.

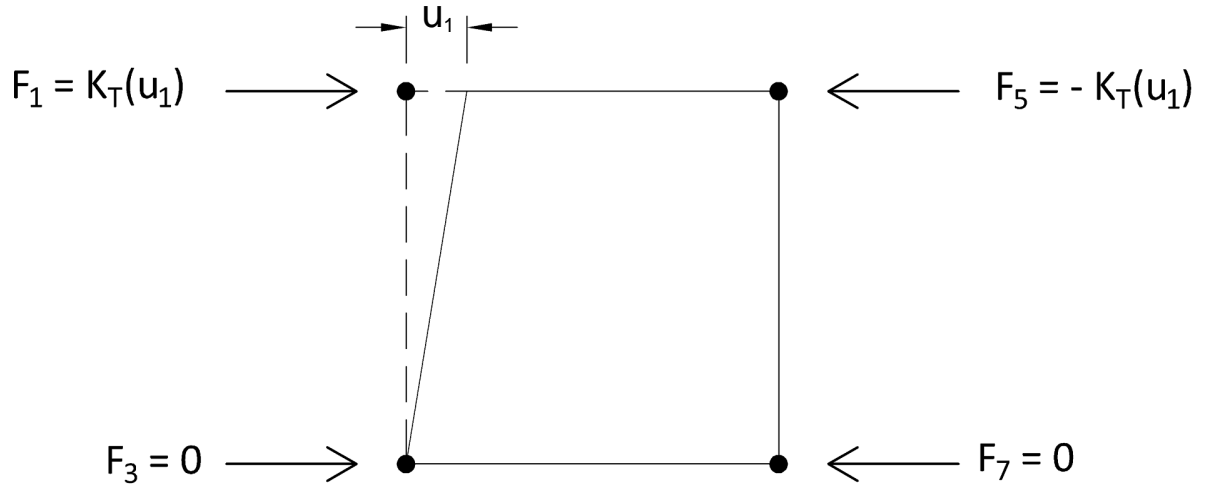


Figure 2.9: Forces Developed in a Non-Linked Truss System

Yet this is not a realistic scenario, as the bottom of the element is inherently linked to the top through the material (steel reinforcement bars and concrete) found over the depth of the section. Looking at it from the perspective of plane-sections, pushing on the top node of the element will result in a linearly varying strain over the whole section, which must result in some force transferred to the bottom node as well (Figure 2.10). Off-diagonal terms are required in the stiffness matrix to reflect this relationship, thereby linking the top and bottom truss bars on both the left and right side of the element.

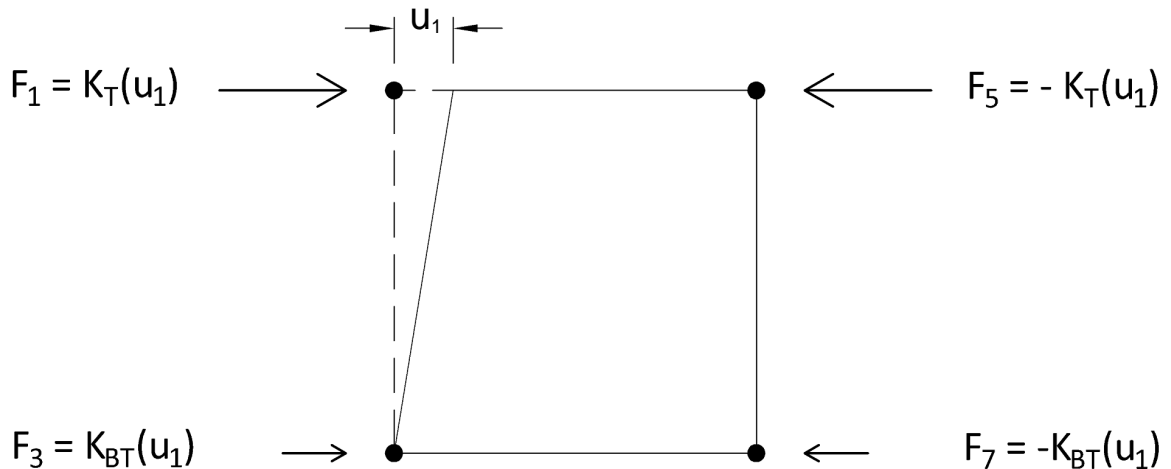


Figure 2.10: Forces Developed in a Linked Truss System

This concept can be further explained by examining the force equilibrium on the face of a homogeneous and linear elastic block with a unit displacement applied at the corner. A linear strain results in a triangular stress block, which can be transformed to equivalent forces at the nodes by maintaining rotational equilibrium in the system. These resultants are the F_1 and F_3 forces as shown in Figure 2.10 and 2.11.

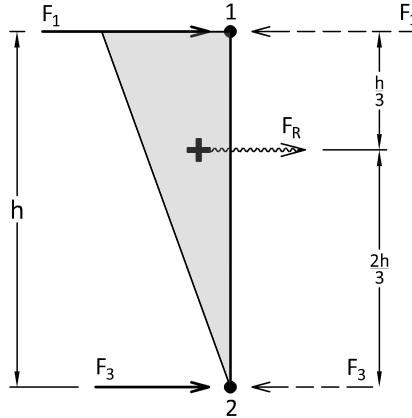


Figure 2.11: *Equivalent Nodal Forces Due to a Triangular Stress Block*

Equation 2.3 shows the relationship between the top and bottom truss bars (where $K_{BT} = K_{TB}$), as represented by a unit displacement on the left side of the element (Figure 2.10). The rest of the off-diagonal terms can be derived through the same exercise, simply applying a unit displacement on the right face.

$$\begin{bmatrix} K_T & K_{TB} \\ K_{BT} & K_B \\ -K_T & -K_{TB} \\ -K_{BT} & -K_B \end{bmatrix} \begin{Bmatrix} u_1 \\ u_3 \end{Bmatrix} = \begin{Bmatrix} F_1 \\ F_3 \\ F_5 \\ F_7 \end{Bmatrix} \quad (2.3)$$

Combining the diagonal and off-diagonal truss terms leads to system of equations represented by Equation 2.4. Note that the off-diagonal terms only exist for the horizontal truss bars, the vertical truss bars are not linked in the same manner (the reasoning behind this will be explained in the following section).

$$\begin{bmatrix} K_T & 0 & K_{TB} & 0 & -K_T & 0 & -K_{TB} & 0 \\ 0 & K_V & 0 & -K_V & 0 & 0 & 0 & 0 \\ K_{BT} & 0 & K_B & 0 & -K_{BT} & 0 & -K_B & 0 \\ 0 & -K_V & 0 & K_V & 0 & 0 & 0 & 0 \\ -K_T & 0 & -K_{TB} & 0 & K_T & 0 & K_{TB} & 0 \\ 0 & 0 & 0 & 0 & 0 & K_V & 0 & -K_V \\ -K_{BT} & 0 & -K_B & 0 & K_{BT} & 0 & K_B & 0 \\ 0 & 0 & 0 & 0 & 0 & -K_V & 0 & K_V \end{bmatrix} \begin{Bmatrix} u_1 \\ u_2 \\ u_3 \\ u_4 \\ u_5 \\ u_6 \\ u_7 \\ u_8 \end{Bmatrix} = \begin{Bmatrix} F_1 \\ F_2 \\ F_3 \\ F_4 \\ F_5 \\ F_6 \\ F_7 \\ F_8 \end{Bmatrix} \quad (2.4)$$

2.2.4 Truss Bar Stiffness Terms - Calculations

Vertical Truss Bars

The two vertical truss bars provide stiffness in the transverse direction, which is only required for numerical stability. Since the HyPT element is formulated to span the whole height of the section, it does not explicitly rely on the vertical trusses to capture axial or flexural deformations, and assumes that clamping stresses are negligible. Therefore, to simplify these vertical truss terms a constant stiffness is assigned to them based on the gross area of concrete, element height, and uncracked concrete elastic modulus. This calculation is expressed in Equation 2.5 and Figure 2.12.

$$K_v = \frac{E_c (d_x d_y)}{2d_z} \quad (2.5)$$

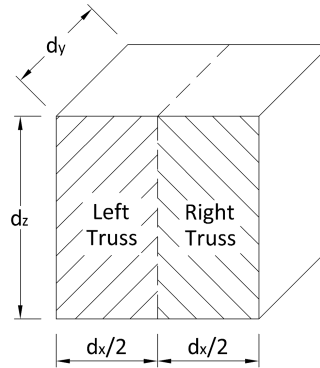


Figure 2.12: *Vertical Trusses Based on the Gross Cross-Section*

Horizontal Truss Bars

Axial and flexural deformations are represented by the elongation and contraction of the top and bottom truss bars. The stiffness terms of these components must therefore be calculated in a way that captures the nonlinear behaviour of reinforced concrete in both tension and compression. The goal is to relate an increasing strain state (based on the relative displacement of the four nodes of the element) to a degradation of the truss bar stiffness as both the steel and concrete reach their nonlinear ranges.

The HyPT element uses a "fiber model" model approach, whereby the section is divided into discrete components (concrete and steel layers), to calculate the separate stiffness terms. The procedure is as follows:

1. Find linear strain over height of section (based on nodal displacements)
2. Find axial force resultants in discrete components (secant stiffness method)
3. Increment strain at DOF of interest (stiffness method approach)
4. Calculate sectional forces due to strain increment
5. Transform to equivalent nodal forces (moment equilibrium)
6. Calculate stiffness terms

Step 1.

Based on the displacement of the four nodes (Figure 2.13) the strain in the horizontal trusses can be calculated through Equations 2.6. Assuming that plane-sections remain plane, the strain will vary linearly from the top to the bottom of the section. Displacements are taken as positive to the right and negative to the left, and compressive strains are negative and tensile strains are positive.

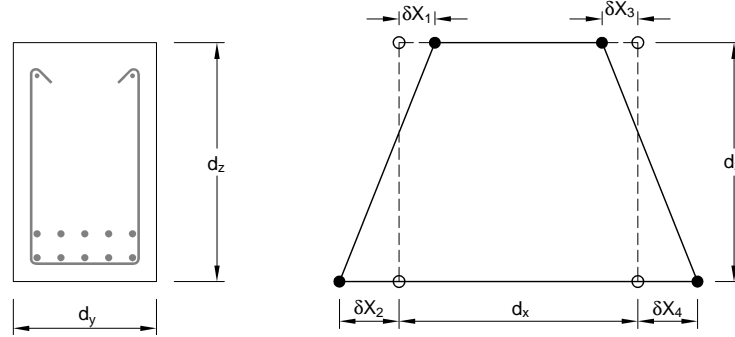


Figure 2.13: Nodal Displacements to Calculate Horizontal Truss Strains

$$\mathcal{E}_{top} = \frac{\delta X_3 - \delta X_1}{d_x} \quad (2.6)$$

$$\mathcal{E}_{bot} = \frac{\delta X_4 - \delta X_2}{d_x}$$

Step 2.

The internal forces in the cross-section can be found by integrating and summing the resulting stresses over the whole depth (Figure 2.14). The concrete stress is a continuous function over the depth (d), while the steel stress is expressed at discrete points ($d_{s,i}$) (Equation 2.7).

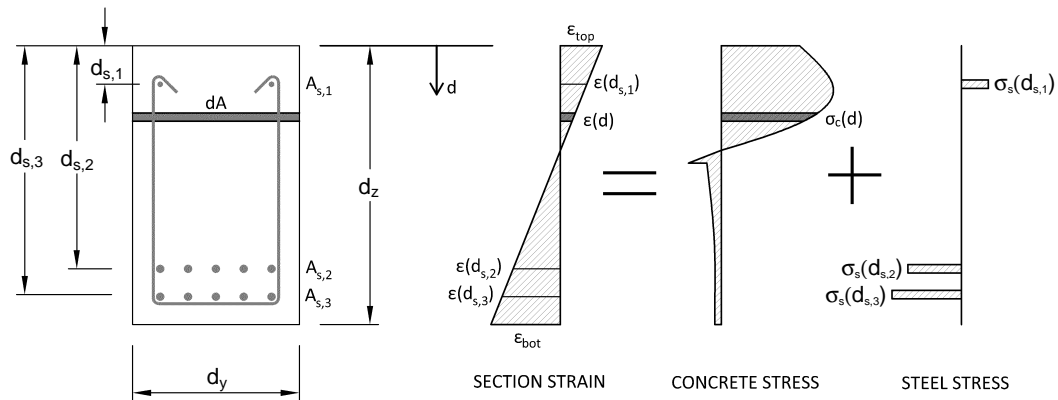


Figure 2.14: Resulting Sectional Concrete and Steel Stresses

$$F_c = \int_0^d \sigma_c(d) \cdot dA \quad (2.7)$$

$$F_s = \sum_{i=1}^{\#Layers} \sigma_s(d_{s,i}) \cdot A_{s,i}$$

The concrete expression can be simplified if the total force is expressed as the contribution from discrete slices, with a constant strain (Figure 2.15) and corresponding stress calculated at the center of the slice ($d_{c,i}$). The number of slices needed to accurately represent the integral depends on the degree of nonlinearity in the concrete function, although from experience using 10-20 layers results in a reasonable approximation. For a rectangular cross-section with a constant width, the integral can be reduced to Equation 2.8.

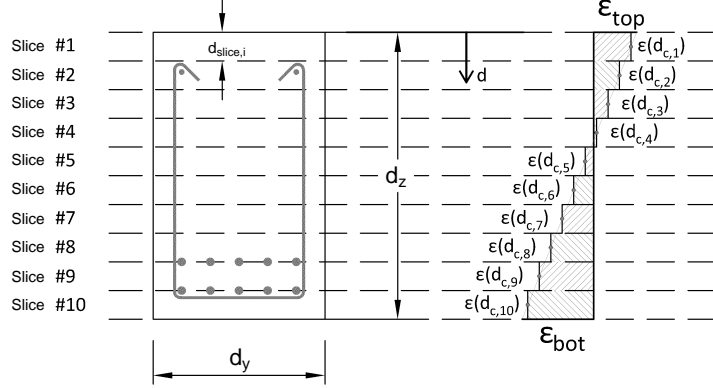


Figure 2.15: Concrete Section Expressed as Discrete Slices

$$F_c = d_y \cdot \sum_{i=1}^{\#Slices} \sigma_c(d_{c,i}) \cdot d_{slice,i} \quad (2.8)$$

To account for the concrete and steel material nonlinearity, the strains are mapped to their corresponding points on the material stress/strain curve (Figure 2.16). The forces can then be calculated in terms of the secant stiffness (Equation 2.9). Using the modular ratio (n) the steel stiffness is expressed in terms of the concrete stiffness in the corresponding slice (subtracting the area of concrete displaced by the steel).

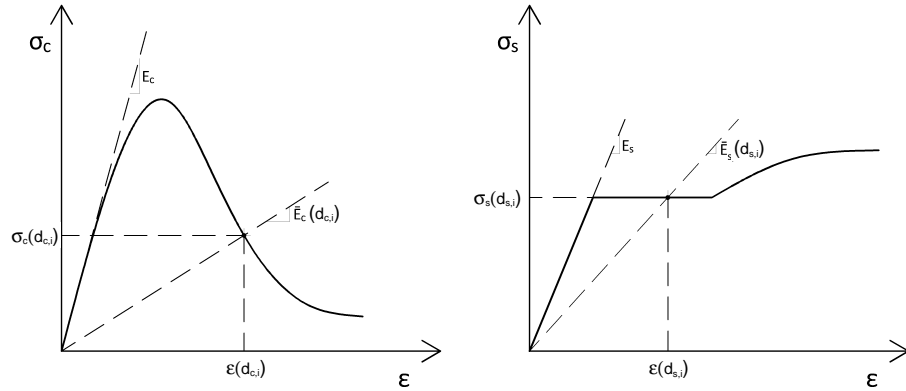


Figure 2.16: Concrete (Left) and Steel (Right) Secant Stiffness Formulation

$$F_c = d_y \cdot \sum_{i=1}^{\#Slices} \bar{E}_c(d_{c,i}) \cdot \varepsilon(d_{c,i}) \cdot d_{slice,i} \quad (2.9)$$

$$F_s = \sum_{i=1}^{\#Layers} \bar{E}_c(d_{s,i}) \cdot (n_i - 1) \cdot \varepsilon(d_{s,i}) \cdot A_{s,i}$$

Step 3.

Recall the definition of stiffness (force per unit displacement) as it applies to the stiffness method. Where $K_{i,j}$ is the term that corresponds to the force at DOF j resulting from a unit displacement at DOF i , while keeping all other displacements at zero (Equation 2.10).

$$K_{i,j} = \frac{F_j}{\Delta_i} \quad (2.10)$$

For example, the truss stiffness matrix for the left face of the HyPT element is expressed in Equation 2.11.

$$\begin{bmatrix} K_{1,1} & K_{1,3} \\ K_{3,1} & K_{3,3} \end{bmatrix} \begin{Bmatrix} \Delta_1 \\ \Delta_3 \end{Bmatrix} = \begin{bmatrix} K_T & K_{TB} \\ K_{BT} & K_B \end{bmatrix} \begin{Bmatrix} \Delta_T \\ \Delta_B \end{Bmatrix} = \begin{Bmatrix} F_T \\ F_B \end{Bmatrix} \quad (2.11)$$

where:

$$\Delta_T = \mathcal{E}_{top} \cdot d_x$$

$$\Delta_B = \mathcal{E}_{bot} \cdot d_x$$

Using the stiffness method definition, the individual terms can be derived by applying an infinitesimal strain to the existing strain condition ($d\epsilon_{top}$ in Figure 2.17). Calculating $K_{1,1}$ and $K_{1,3}$ requires an increment in DOF 1 (top), while calculating $K_{3,3}$ and $K_{3,1}$ requires an increment in DOF 3 (bottom) (Equation 2.12).

$$\begin{aligned} K_{1,1} &= \frac{dF_T}{d\Delta_T} = \frac{dF_T}{d\mathcal{E}_{top} \cdot d_x} \\ K_{1,3} &= \frac{dF_B}{d\Delta_T} = \frac{dF_B}{d\mathcal{E}_{top} \cdot d_x} \\ K_{3,3} &= \frac{dF_B}{d\Delta_B} = \frac{dF_B}{d\mathcal{E}_{bot} \cdot d_x} \\ K_{3,1} &= \frac{dF_T}{d\Delta_B} = \frac{dF_T}{d\mathcal{E}_{bot} \cdot d_x} \end{aligned} \quad (2.12)$$

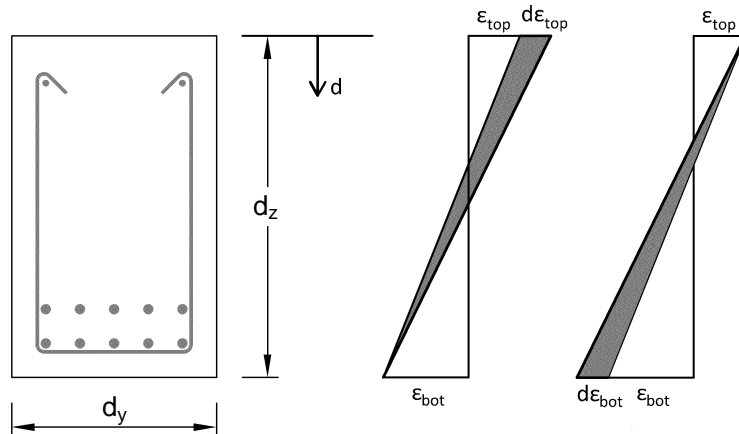


Figure 2.17: Incrementing Top (Left) or Bottom (Right) Truss Strain

Step 4.

Applying the same rationale used to explain the off-diagonal terms (Section 2.2.3) means that a unit displacement (or infinitesimal strain) that is applied at either the top or bottom truss must result in a linearly decreasing strain increment - shown in Equation 2.13, where d is measured from the top of the section.

$$\begin{aligned}\varepsilon(d) &= \frac{d_z - d}{d_z} \cdot d\mathcal{E}_{top} \\ \varepsilon(d) &= \frac{d}{d_z} \cdot d\mathcal{E}_{bot}\end{aligned}\tag{2.13}$$

The incremental force contribution from the various cross-sectional layers is then found by substituting the appropriate incremented strain expression into the material force summation, which results in Equation 2.14 and 2.15. The strain term based on the nodal coordinates is replaced by the incremented strain expression, since only the additional force contribution is of interest when calculating the stiffness term. For example, when calculating the $K_{1,1}$ term a strain increment is applied to the top truss - the concrete slices closer to the top of the section would have a larger incremented strain and force contribution than the slices closer to the bottom. This leads to the intuitive result that the top slices contribute more to the stiffness of the top truss than the bottom truss.

$$d\mathcal{E}_{top} \rightarrow \begin{cases} dF_c = \frac{d_y \cdot d\mathcal{E}_{top}}{d_z} \cdot \sum_{i=1}^{\#Slices} (d_z - d_{c,i}) \cdot \bar{E}_c(d_{c,i}) \cdot d_{slice,i} \\ dF_s = \frac{d\mathcal{E}_{top}}{d_z} \cdot \sum_{i=1}^{\#Layers} (d_z - d_{s,i}) \cdot \bar{E}_c(d_{s,i}) \cdot (n_i - 1) \cdot A_{s,i} \end{cases}\tag{2.14}$$

$$d\mathcal{E}_{bot} \rightarrow \begin{cases} dF_c = \frac{d_y \cdot d\mathcal{E}_{bot}}{d_z} \cdot \sum_{i=1}^{\#Slices} (d_{c,i}) \cdot \bar{E}_c(d_{c,i}) \cdot d_{slice,i} \\ dF_s = \frac{d\mathcal{E}_{bot}}{d_z} \cdot \sum_{i=1}^{\#Layers} (d_{s,i}) \cdot \bar{E}_c(d_{s,i}) \cdot (n_i - 1) \cdot A_{s,i} \end{cases}\tag{2.15}$$

Step 5.

The incremental sectional forces are now transformed to equivalent nodal forces by solving moment equilibrium across the section. The top or bottom nodal forces are calculated as the sum of the concrete and steel moment contributions about the bottom or top truss respectively, divided by the lever arm (Equation 2.16).

$$\begin{aligned}dF_T &= \frac{dM_{c,bot} + dM_{s,bot}}{d_z} \\ dF_B &= \frac{dM_{c,top} + dM_{s,top}}{d_z}\end{aligned}\tag{2.16}$$

Equations 2.17 and 2.18 show the incremental moment equations resulting from a top or bottom strain increment respectively. The first term in the subscript refers to the material type, and the second term refers to the moment axis.

$$d\mathcal{E}_{top} \rightarrow \left\{ \begin{array}{l} dM_{c,bot} = \frac{d_y \cdot d\mathcal{E}_{top}}{d_z} \cdot \sum_{i=1}^{\#Slices} (d_z - d_{c,i})^2 \cdot \bar{E}_c(d_{c,i}) \cdot d_{slice,i} \\ dM_{c,top} = \frac{d_y \cdot d\mathcal{E}_{top}}{d_z} \cdot \sum_{i=1}^{\#Slices} (d_z - d_{c,i})(d_{c,i}) \cdot \bar{E}_c(d_{c,i}) \cdot d_{slice,i} \\ dM_{s,bot} = \frac{d\mathcal{E}_{top}}{d_z} \cdot \sum_{i=1}^{\#Layers} (d_z - d_{s,i})^2 \cdot \bar{E}_c(d_{s,i}) \cdot (n_i - 1) \cdot A_{s,i} \\ dM_{s,top} = \frac{d\mathcal{E}_{top}}{d_z} \cdot \sum_{i=1}^{\#Layers} (d_z - d_{s,i})(d_{s,i}) \cdot \bar{E}_c(d_{s,i}) \cdot (n_i - 1) \cdot A_{s,i} \end{array} \right. \quad (2.17)$$

$$d\mathcal{E}_{bot} \rightarrow \left\{ \begin{array}{l} dM_{c,bot} = \frac{d_y \cdot d\mathcal{E}_{bot}}{d_z} \cdot \sum_{i=1}^{\#Slices} (d_{c,i})(d_z - d_{c,i}) \cdot \bar{E}_c(d_{c,i}) \cdot d_{slice,i} \\ dM_{c,top} = \frac{d_y \cdot d\mathcal{E}_{bot}}{d_z} \cdot \sum_{i=1}^{\#Slices} (d_{c,i})^2 \cdot \bar{E}_c(d_{c,i}) \cdot d_{slice,i} \\ dM_{s,bot} = \frac{d\mathcal{E}_{bot}}{d_z} \cdot \sum_{i=1}^{\#Layers} (d_{s,i})(d_z - d_{s,i}) \cdot \bar{E}_c(d_{s,i}) \cdot (n_i - 1) \cdot A_{s,i} \\ dM_{s,top} = \frac{d\mathcal{E}_{bot}}{d_z} \cdot \sum_{i=1}^{\#Layers} (d_{s,i})^2 \cdot \bar{E}_c(d_{s,i}) \cdot (n_i - 1) \cdot A_{s,i} \end{array} \right. \quad (2.18)$$

Step 6.

The separate stiffness terms can now be calculated as previously shown (Equation 2.12), by dividing the transformed nodal force by either $d\mathcal{E}_{top} \cdot d_x$ or $d\mathcal{E}_{bot} \cdot d_x$. Note that the stiffness matrix is symmetric across the diagonal (e.g. $K_{1,3} = K_{3,1}$ etc.).

2.3 Shear Panel Stiffness Terms

Shear stiffness of the HyPT element is provided by a two-dimensional panel at the center of the element, which connects all four nodes. The shear stresses and strains are related by the secant shear stiffness (\bar{G}) as shown in Equation 2.19 and Figure 2.18, where the secant shear stiffness term can be calculated from an MCFT analysis of the panel [1, 11]. The following section will explain how the shear stiffness is represented in the HyPT element formulation.

$$\tau_{xz} = \tau_{zx} = \bar{G} \cdot \gamma_{xz} \tag{2.19}$$

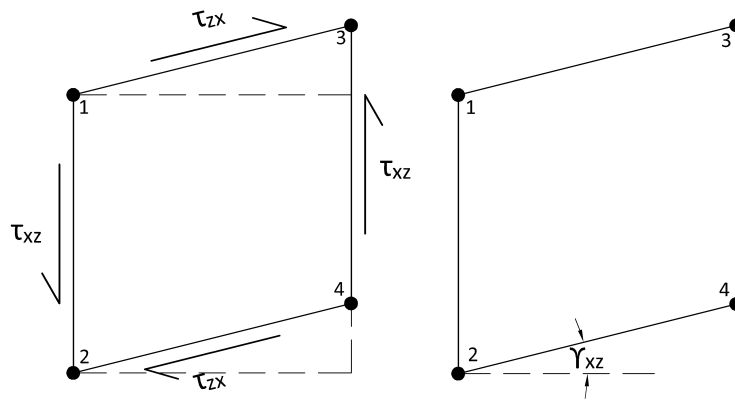


Figure 2.18: Shear Stresses (Left) Related to Shear Deformations (Right)

2.3.1 Deformation Patterns

Shear strain is a measure of angular deviation, which cannot be explicitly captured by the system of one-dimensional truss bars that are used for flexural and axial deformations. Therefore, the shear panel is necessary to represent the deformation patterns shown in Figure 2.19. While positive and negative shear are arbitrary definitions with respect to the shear stiffness, for the derivation of the stiffness matrix the sign convention shown below will be used.

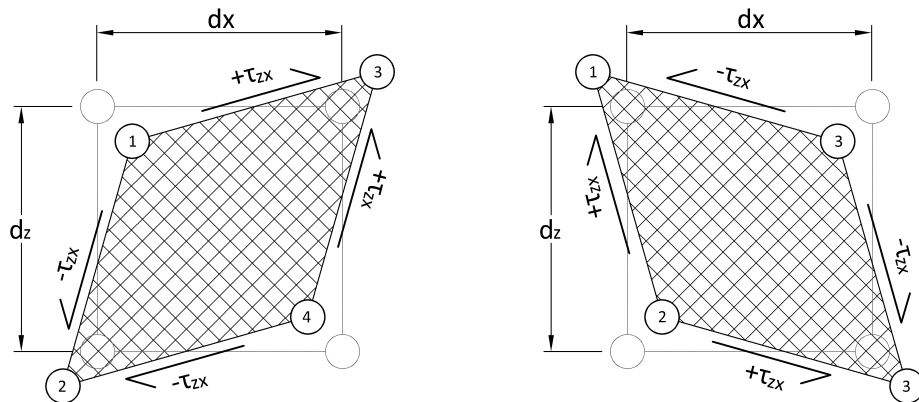


Figure 2.19: A Representation of Positive (Left) and Negative (Right) Shear Stresses in the Element

2.3.2 Expressing Nodal Forces in Term of Applied Shear Stress

The shear stress acting on a plane is assumed to be distributed equally between adjacent nodes (i.e. τ_{xz} is constant in Figure 2.20). The resulting nodal forces are expressed in Equation 2.20.

$$F'_x = \frac{1}{2}\tau_{xz} \cdot A_{face} = \frac{1}{2}\bar{G}\gamma_{xz} \cdot d_y d_x \tag{2.20}$$

$$F'_z = \frac{1}{2}\tau_{xz} \cdot A_{face} = \frac{1}{2}\bar{G}\gamma_{xz} \cdot d_y d_z$$

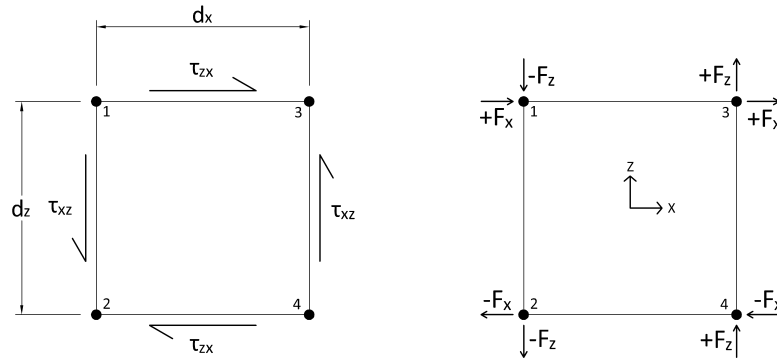


Figure 2.20: Positive Shear Stress (Left) and Resulting Nodal Forces (Right)

The forces calculated in Equation 2.20 do not reflect the fact that the effective shear zone in a reinforced concrete section does not span the whole height. A more accurate representation of the panel stresses is shown in Figure 2.21, where the effective shear zone is defined by the location of the resultant tension and compression axial forces in the section. The forces in the effective zone must still be consistent with the location of the nodes, and must be transformed to equivalent nodal forces. This is done by modifying Equation 2.20 while keeping rotational and force equilibrium, which leads to Equation 2.21.

$$F_x = F'_x \cdot \frac{d_v}{d_z} \tag{2.21}$$

$$F_z = F'_z \cdot \frac{d_v}{d_z}$$

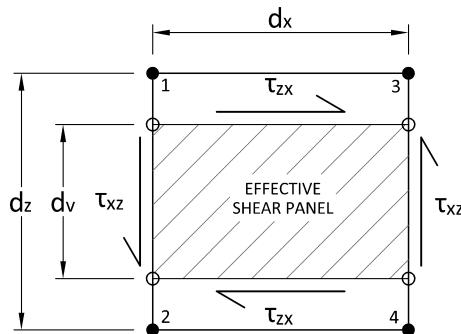


Figure 2.21: Shear Stresses Acting on the Effective Shear Panel

2.3.3 Expressing Shear Strain in Terms of Nodal Displacements

Shear strains in the panel are only a component of the total potential deformation, therefore it is necessary to find an expression to extract the shear strain from an arbitrary deformation pattern. This is done by visualizing the relative vertical displacement of the right side of the element (Figure 2.22) as being composed of three different types of displacements: rigid body, curvature and shear. This relationship is expressed in Equation 2.22, where the sign convention is based on the axis defined in Figure 2.20 (i.e. up & right = +).

$$\underbrace{\frac{\Delta z_3 + \Delta z_4}{2}}_{\text{Avg. Right}} - \underbrace{\frac{\Delta z_1 + \Delta z_2}{2}}_{\text{Avg. Left}} = \underbrace{\theta_L \cdot d_x}_{\text{Rigid Body}} + \underbrace{\phi d_x \cdot \frac{d_x}{2}}_{\text{Curvature}} + \underbrace{\gamma_{xz} \cdot d_x}_{\text{Shear}} \quad (2.22)$$

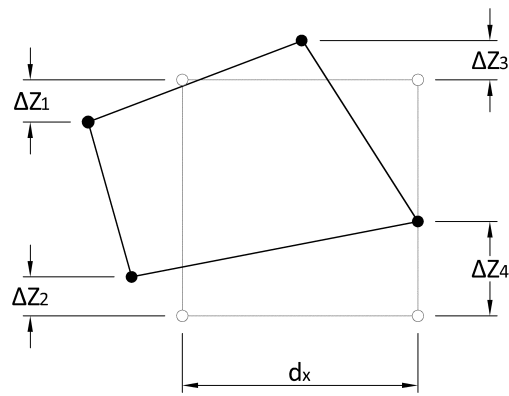


Figure 2.22: Arbitrary Deformation Pattern - Relative Vertical Displacements

Rigid body displacement is defined as a rotation of the panel. Assuming that the left corner is fixed, as shown in Figure 2.23, the relative vertical displacement of the right side is expressed by Equation 2.23.

$$\frac{\Delta z_3 + \Delta z_4}{2} = \theta_L \cdot d_x \quad (2.23)$$

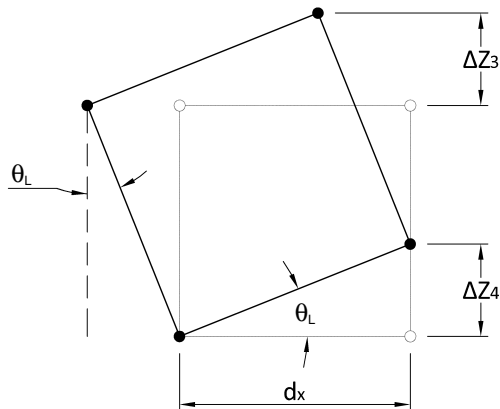


Figure 2.23: Vertical Displacement of the Right Side due to Rigid Body Displacement

The rotation of the left or right side is expressed in Equation 2.24 (counter-clockwise rotation is positive).

$$\theta_L = \frac{\Delta x_2 - \Delta x_1}{d_z} \quad (2.24)$$

$$\theta_R = \frac{\Delta x_4 - \Delta x_2}{d_z}$$

Curvature displacement is determined by fixing the left face, then assuming that only the right face displaces (Figure 2.24). By formulation, the curvature is constant over the length of a HyPT element so applying the Moment Area Theorem #2 results in 2.25.

$$\frac{\Delta z_3 + \Delta z_4}{2} = \phi d_x \cdot \frac{d_x}{2} \quad (2.25)$$

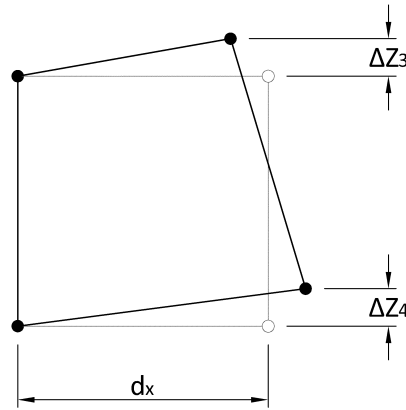


Figure 2.24: *Vertical Displacement of the Right Side due to Curvature Displacement*

Moment Area Theorem #1 states that the change in rotation between two points is equal to the area under the curvature diagram, which for a constant curvature region leads to Equation 2.26.

$$\phi d_x = \theta_R - \theta_L \quad (2.26)$$

Substitute Equation 2.24 into 2.26 and rearranging to solve for the curvature results in Equation 2.27).

$$\phi = \frac{(\Delta x_4 - \Delta x_3) - (\Delta x_2 - \Delta x_1)}{d_z d_x} \quad (2.27)$$

Shear displacement is determined by fixing the left face and assuming that the right face displaces due to shear (small angle assumption). The relative displacement is shown in Figure 2.25 and expressed by Equation 2.28.

$$\frac{\Delta z_3 + \Delta z_4}{2} = \gamma_{xz} d_x \quad (2.28)$$

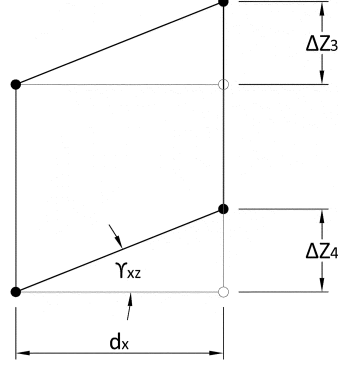


Figure 2.25: Vertical Displacement of the Right Side due to Shear Strain.

The final result is shown in Equation 2.29, where the shear strain can be expressed in terms of nodal displacements. The expression is found by substituting Equation 2.24, 2.27 & 2.28 into Equation 2.22 and solving for the shear term.

$$\gamma_{xz} = \frac{\Delta x_1}{2d_z} - \frac{\Delta z_1}{2d_x} - \frac{\Delta x_2}{2d_z} - \frac{\Delta z_2}{2d_x} + \frac{\Delta x_3}{2d_z} + \frac{\Delta z_3}{2d_x} - \frac{\Delta x_4}{2d_z} + \frac{\Delta z_4}{2d_x} \quad (2.29)$$

2.3.4 Shear Panel Stiffness Matrix

Substituting the shear strain expression (Equation 2.29) into the expressions for the nodal forces (Equation 2.20) results in the stiffness matrix and system of linear equations represented by Equation 2.30.

$$\frac{\bar{G}d_yd_v}{4d_z} \begin{bmatrix} \frac{d_x}{d_z} & -\frac{d_x}{d_x} & -\frac{d_x}{d_z} & -\frac{d_x}{d_x} & \frac{d_x}{d_z} & \frac{d_x}{d_x} & -\frac{d_x}{d_z} & \frac{d_x}{d_x} \\ -\frac{d_z}{d_z} & \frac{d_z}{d_x} & \frac{d_z}{d_z} & \frac{d_z}{d_x} & -\frac{d_z}{d_z} & -\frac{d_z}{d_x} & \frac{d_z}{d_z} & -\frac{d_z}{d_x} \\ -\frac{d_x}{d_z} & \frac{d_x}{d_x} & \frac{d_x}{d_z} & \frac{d_x}{d_x} & -\frac{d_x}{d_z} & -\frac{d_x}{d_x} & \frac{d_x}{d_z} & -\frac{d_x}{d_x} \\ -\frac{d_z}{d_z} & \frac{d_z}{d_x} & \frac{d_z}{d_z} & \frac{d_z}{d_x} & -\frac{d_z}{d_z} & -\frac{d_z}{d_x} & \frac{d_z}{d_z} & -\frac{d_z}{d_x} \\ \frac{d_x}{d_z} & -\frac{d_x}{d_x} & -\frac{d_x}{d_z} & -\frac{d_x}{d_x} & \frac{d_x}{d_z} & \frac{d_x}{d_x} & -\frac{d_x}{d_z} & \frac{d_x}{d_x} \\ \frac{d_z}{d_z} & -\frac{d_z}{d_x} & -\frac{d_z}{d_z} & -\frac{d_z}{d_x} & \frac{d_z}{d_z} & \frac{d_z}{d_x} & -\frac{d_z}{d_z} & \frac{d_z}{d_x} \\ -\frac{d_x}{d_z} & \frac{d_x}{d_x} & \frac{d_x}{d_z} & \frac{d_x}{d_x} & -\frac{d_x}{d_z} & -\frac{d_x}{d_x} & \frac{d_x}{d_z} & -\frac{d_x}{d_x} \\ \frac{d_z}{d_z} & -\frac{d_z}{d_x} & -\frac{d_z}{d_z} & -\frac{d_z}{d_x} & \frac{d_z}{d_z} & \frac{d_z}{d_x} & -\frac{d_z}{d_z} & \frac{d_z}{d_x} \end{bmatrix} \begin{Bmatrix} \Delta x_1 \\ \Delta z_1 \\ \Delta x_2 \\ \Delta z_2 \\ \Delta x_3 \\ \Delta z_3 \\ \Delta x_4 \\ \Delta z_4 \end{Bmatrix} = \begin{Bmatrix} F_{x1} \\ F_{z1} \\ F_{x2} \\ F_{z2} \\ F_{x3} \\ F_{z3} \\ F_{x4} \\ F_{z4} \end{Bmatrix} \quad (2.30)$$

The secant shear stiffness must be determined at each iteration through an MCFT analysis, following the same principles outlined in the membrane element formulations published by Professor Vecchio [11]. The HyPT shear panel follows a displacement-based procedure, where the input strains to the MCFT (ϵ_x & γ_{xz}) are based on the nodal displacements of the element from the previous iteration, while the transverse/clamping stress (σ_z) is assumed to be 0. The outputs from this calculation are: σ_x , τ_{xz} , and ϵ_z .

2.4 Post-Cracking Interaction Terms

When the concrete cracks in shear, additional tensile forces must be transferred into the longitudinal bars to satisfy equilibrium [4]. Additional terms must be added to the HyPT element stiffness matrix to reflect the additional forces that exist at the nodes post-cracking. The structural mechanics underlying these terms is explained in the following section.

2.4.1 Uncracked Concrete

Uncracked reinforced concrete can be treated as an isotropic material, where the force equilibrium for a pure shear element is shown in Figure 2.26. The horizontal component of the principal compression and tension balance perfectly at the section, while the vertical resultant is equal to the applied shear

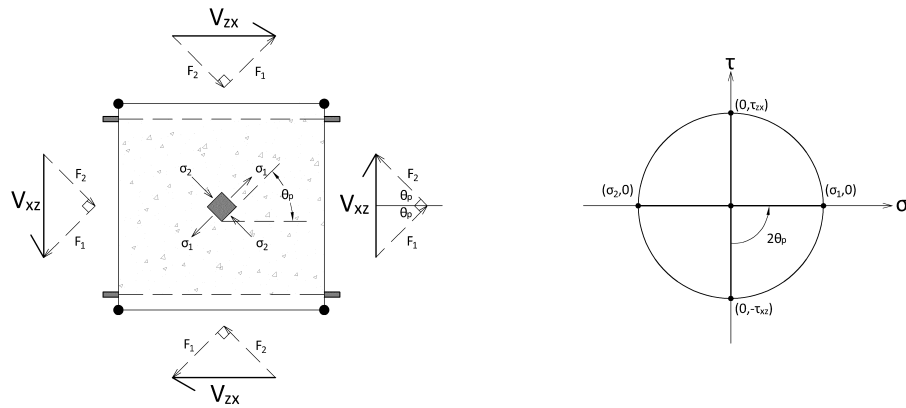


Figure 2.26: Force Equilibrium (Left) and Stress State (Right) for Shear in Uncracked Reinforced Concrete

2.4.2 Cracked Concrete

When concrete cracks the tensile capacity is significantly reduced, but due to tension stiffening the average principal tensile stress in the concrete does not go to zero (MCFT formulation [1]). The horizontal components of the compression and tension forces no longer balance, therefore an additional axial force (F_x) is necessary to balance the internal force polygon as shown in Figure 2.27. The F_1 force corresponds to the post-cracking tensile capacity in the concrete.

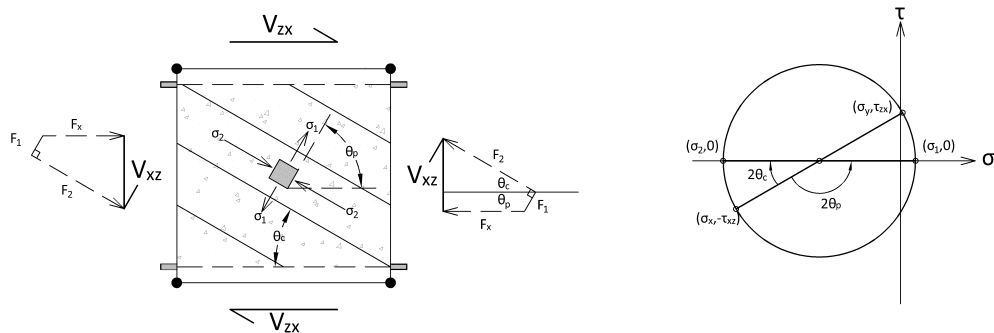


Figure 2.27: Force Equilibrium (Left) and Stress State (Right) for Shear in Cracked Reinforced Concrete

For the purpose of this derivation, a conservative assumption is made that there is no post-cracking tensile capacity (CFT formulation [21]). The simplified force polygon and stress state are shown in Figure 2.28.

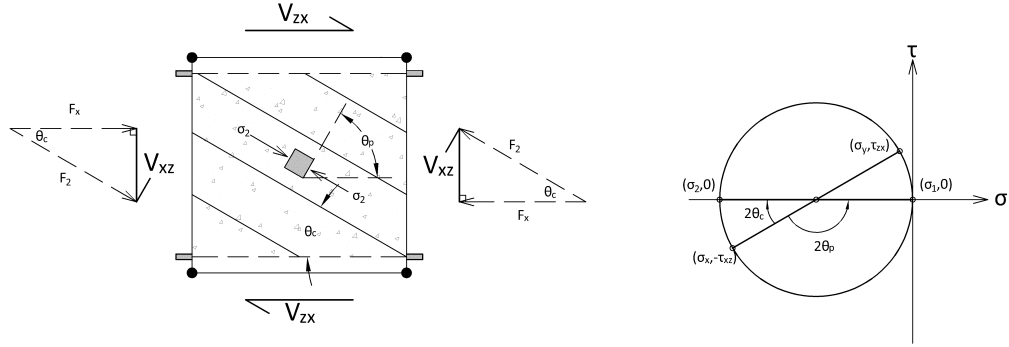


Figure 2.28: *Simplified Force (Left) and Stress State (Right) for Shear in Cracked Reinforced Concrete*

2.4.3 Post-Cracking Chord Forces

The axial force required to balance the horizontal component of the compression struts is carried as an additional tensile force (F'_h) in the longitudinal reinforcement. The net axial force on the section is zero, therefore the sum of the additional tension in the reinforcement must be equal to the horizontal component of the compression struts as shown in Figure 2.29. The load is assumed to be evenly distributed between the top and bottom chords, because the tension is uniform over the section.

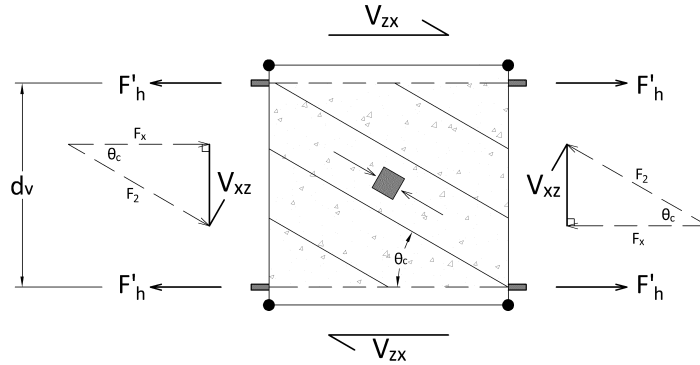


Figure 2.29: *Additional Horizontal Force Carried in the Section Chords*

Assuming a uniformly applied shear stress over the effective depth, the horizontal component of the strut can be expressed by Equation 2.31.

$$F_x = \tau_{xz} d_v d_y \cdot \cot(\theta_c) \quad (2.31)$$

Substituting Equation 2.19 for the shear stress and distributing the force equally to the top and bottom chord results in Equation 2.32.

$$F'_h = \frac{F_x}{2} = \frac{\bar{G} \gamma_{xz} d_v d_y}{2} \cdot \cot(\theta_c) \quad (2.32)$$

Transforming the forces on the longitudinal bars to the nodal coordinates, similar to the procedure discussed in the derivation of the truss bar stiffness terms (Section 2.2.4), results in Equation 2.33.

$$F_h = F'_h \cdot \frac{d_v}{d_z} = \frac{\bar{G}\gamma_{xz}d_v^2d_y}{2d_z} \cdot \cot(\theta_c) \quad (2.33)$$

2.4.4 Post-Cracking Interaction Stiffness Matrix

Regardless of the sign of the shear that causes cracking, the direction of the resulting additional forces on the nodes is always tensile, as shown in Figure 2.30.

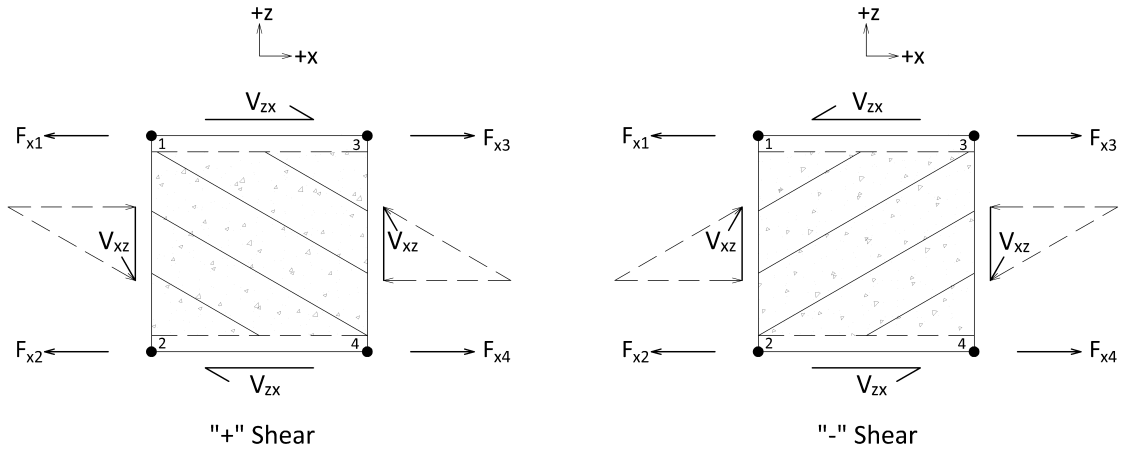


Figure 2.30: *Post-Cracking Forces Independent of the Applied Shear Direction*

Substituting the shear strain expression (Equation 2.29) into the additional horizontal force expression (Equation 2.33) results in the system of equations shown in Equation 2.34. Note that the top sign is for positive shear strains, while the bottom sign is for negative shear strains. The unidirectionality of the post-cracking forces leads to the non-symmetry of the matrix, which is not typical for a traditional finite element formulation.

$$\begin{bmatrix} \mp a & \pm b & \pm a & \pm b & \mp a & \mp b & \pm a & \mp b \\ 0 & 0 & 0 & 0 & 0 & 0 & 0 & 0 \\ \mp a & \pm b & \pm a & \pm b & \mp a & \mp b & \pm a & \mp b \\ 0 & 0 & 0 & 0 & 0 & 0 & 0 & 0 \\ \pm a & \mp b & \mp a & \mp b & \pm a & \pm b & \mp a & \pm b \\ 0 & 0 & 0 & 0 & 0 & 0 & 0 & 0 \\ \pm a & \mp b & \mp a & \mp b & \pm a & \pm b & \mp a & \pm b \\ 0 & 0 & 0 & 0 & 0 & 0 & 0 & 0 \end{bmatrix} \begin{Bmatrix} \Delta x_1 \\ \Delta z_1 \\ \Delta x_2 \\ \Delta z_2 \\ \Delta x_3 \\ \Delta z_3 \\ \Delta x_4 \\ \Delta z_4 \end{Bmatrix} = \begin{Bmatrix} F_{x1} \\ 0 \\ F_{x2} \\ 0 \\ F_{x3} \\ 0 \\ F_{x4} \\ 0 \end{Bmatrix} \quad (2.34)$$

The constants (a & b) are represented by Equations 2.35, where the secant shear stiffness is the only unknown variable, and is found in the same way discussed in Section 2.3.4.

$$a = \frac{\bar{G}d_v^2d_y}{4d_z^2} \cdot \cot(\theta_c)$$

$$b = \frac{\bar{G}d_v^2d_y}{4d_zd_x} \cdot \cot(\theta_c)$$
(2.35)

The axial forces that are developed in the z-direction in a cracked element are not of interest, hence the 0-terms in Equation 2.34. These terms could be derived with same procedure just described, looking at the top and bottom instead of the left and right faces. But these terms can be neglected since the HyPT element effectively neglects clamping stresses and assumes a large and constant stiffness in the vertical truss bars; modifying the corresponding vertical stiffness terms would have a negligible impact. Recall that the calculation of the secant shear stiffness is also based on the conservative assumption of zero clamping stress.

2.5 Element Verification

An extensive verification study was performed to determine the accuracy of the 2d-HyPT element in the context of predicting the load-deformation response of reinforced concrete structures. The 2d-HyPT element was implemented in the analysis program Augustus-II, which was used for the member level analysis of slender shear critical beams published in the ACI-DAfStb Databases [27, 28], followed by the large-scale analysis of reinforced concrete frames previously tested at the University of Toronto [29, 30].

2.5.1 Methodology

Reinforced concrete cross-sections are defined with Response-2000 [7], and then referenced in a specially formatted global structural geometry text file. This serves as the input file for the Augustus-II program, which formulates the global stiffness matrix (based on the HyPT element formulation) and then solves the linear system of equations. The process is summarized in Figure 2.31, and a detailed description of this methodology can be found in Section 4.3 of the thesis written by Zaeem [25].

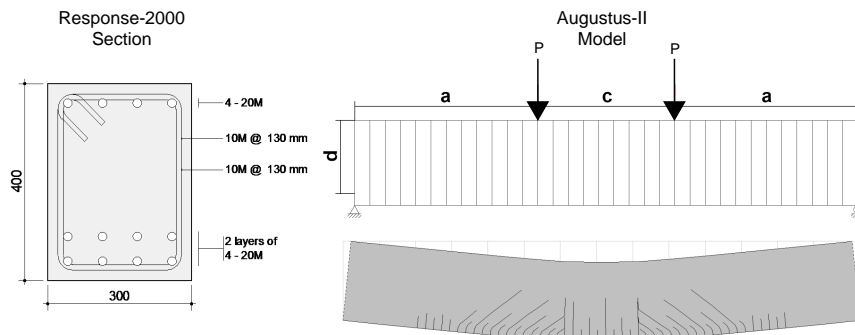


Figure 2.31: *HyPT Element Implemented with Response-2000 (Left) and Augustus-II (Right)*

2.5.2 Shear Critical Beam Database Analysis

An Augustus-II analysis was run for each of the reinforced concrete beams found in the ACI database for shear critical tests - the predicted failure load from this analysis was then compared to the recorded experimental failure load (Exp./Pred.). A ratio greater than 1.0 implied that the analysis was conservative and under-predicted the actual failure load, which in theory is a desirable outcome from a design perspective since the safety of the structure is guaranteed. Conservative results are especially important in shear critical cases, since the failure mechanism of such structures is brittle and occurs without much warning. Shear failure is also difficult to capture accurately, therefore the ability of the HyPT element to consistently and conservatively estimate the failure of the database beams is a significant achievement. The databases are summarized in Appendix A.

Full Dataset

The database results are divided between beams with [28] and without [27] stirrups, presented in Figures 2.32 & 2.33 respectively. The results were further subdivided into point or uniformly loaded rectangular beams, and point-loaded T-beams. To determine whether there is any significant relationship between the predictive capabilities of the element and geometric properties of the beams being tested, each figure shows the same data plotted against four different parameters. For beams without stirrups (Figure 2.32) the trend indicated that predictions improve for deeper cross-sections (top left), more lightly reinforced cross-sections (bottom left), and more slender beams (top right). The dataset for beams with stirrups (Figure 2.33) is much smaller, and hence these trends are not as easily determined.

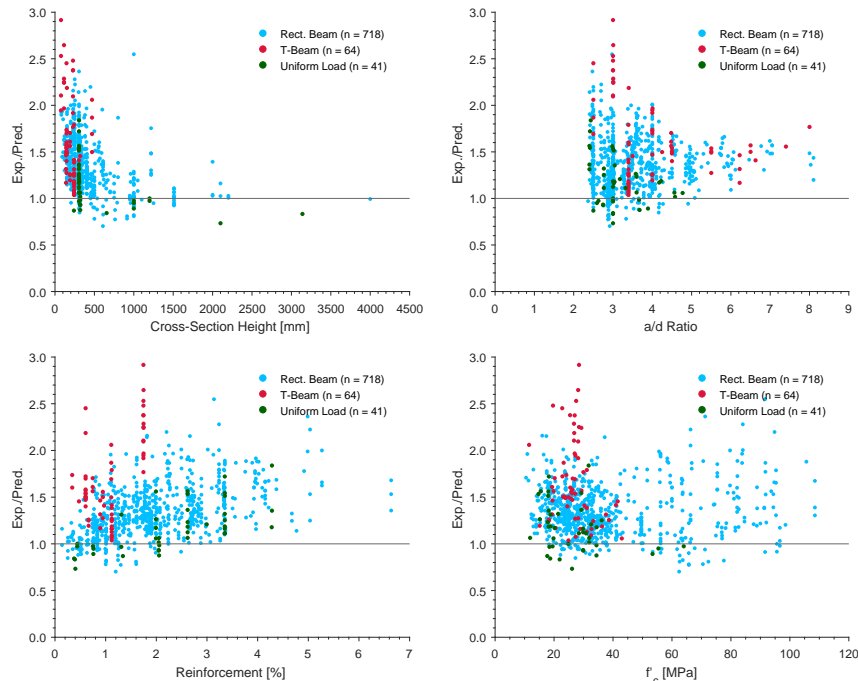


Figure 2.32: Full Dataset Analysis Results - Shear Critical Beams (No Stirrups)

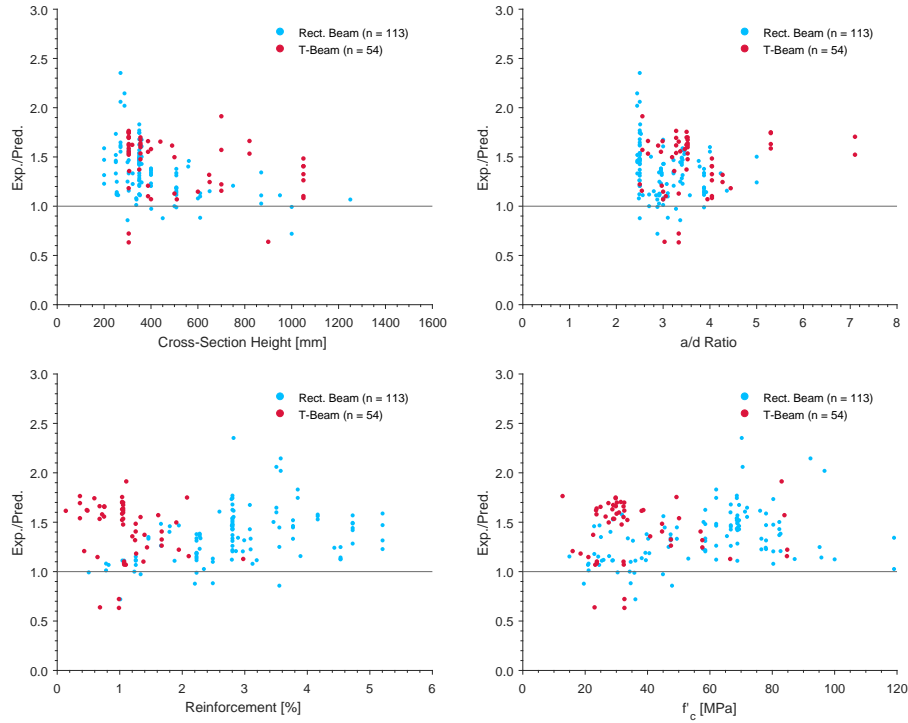


Figure 2.33: Full Dataset Analysis Results - Shear Critical Beams (Stirrups)

Table 2.1 presents the statistics of the full database analysis performed in Augustus-II compared to the American (ACI), European (EC) and Canadian (CSA) design codes. The code results are taken from a previous study [31] using the 2013 version of the database, which has since been updated leading to a different number of beams examined in the current study.

The Augustus-II results are represented with a normal curve that has the properties listed in the table. The 5th percentile value indicates the Exp./Pred. ratio under which 5% of the total tests fall (a value close to 1.0 is desirable). The Augustus-II analysis is shown to provide good results - the averages fall within the ranges of the codes, with an improved coefficient of variation. The rectangular beams with both point and distributed loads are much better represented than the T-beams.

Table 2.1: Database Summary

<i>Type</i> *	<i>No Stirrups</i>				<i>Stirrups</i>			
	n	μ	COV	5 th %	n	μ	COV	5 th %
ACI 318-11	784	1.42	38.3 %	-	170	1.52	22.3 %	-
EC-2	784	1.10	27.9 %	-	170	1.44	17.9 %	-
CSA A23.3-14	784	1.22	22.3 %	-	170	1.29	29.8 %	-
Augustus-II	823	1.30	15.8 %	0.96	167	1.37	19.5 %	0.93
Rect. Beam	718	1.30	15.2 %	0.97	113	1.33	16.6 %	0.96
T-Beam	64	1.51	16.5%	1.10	54	1.53	26.1 %	0.87
Uniform Load	41	1.09	15.0%	0.82	0	-	-	-

* Code analyses based on the 2013 version of databases [31]

Reduced Datasets

Due to the small quantity of T-beams and distributed load tests there was less certainty regarding their statistical representation. Also, a number of rectangular beams listed in the database were deemed unrealistic from a constructibility standpoint - excessively reinforced or with a small cross-sectional height. Therefore, to show how Augustus-II performed in analyzing more realistic beams that are also more statistically significant (i.e. larger number of entries), an analysis of certain database subsets is presented next.

Figure 2.34 shows a histogram of the analysis results for point-loaded rectangular beams with and without stirrups, where the level of flexural tension reinforcement falls below the balanced level as specified by the Canadian Code (Clause 13.4 in [3]). Figure 2.35 shows the CDF of these results, compared to that of a normal curve with the values listed on the figure. The average and coefficient of variation for this subset are improved, while good agreement with the normal curve are shown for the lower half of the results.

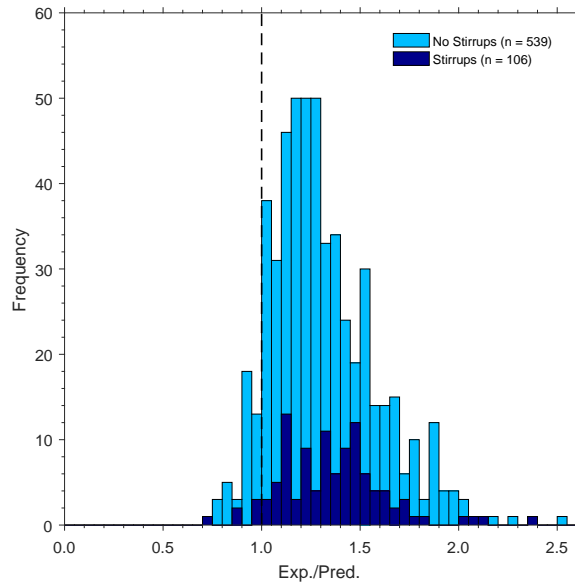


Figure 2.34: Analysis Distribution of Under-Reinforced ($\rho \leq \rho_{bal}$) Shear Critical Rectangular Beams

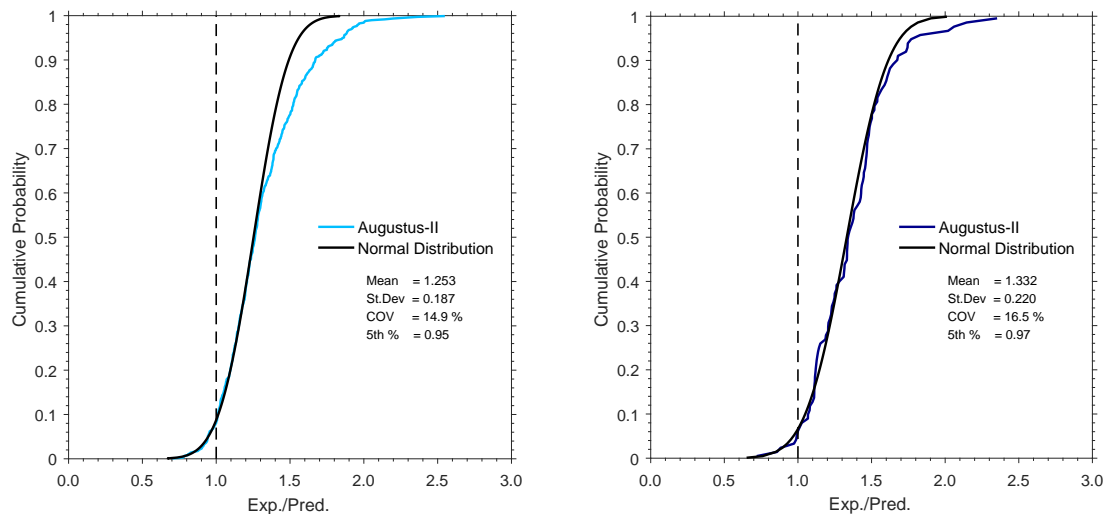


Figure 2.35: Cumulative Density of Analysis Distribution: No Stirrups (Left), Stirrups (Right)

Figure 2.36 shows a histogram of the analysis results for point-loaded rectangular beams with and without stirrups, where the previous subset is further filtered so that the height of the rectangular cross-section is greater than 350 mm. The total number of beams is significantly reduced, with only 218 beams without stirrups and 41 beams with stirrups meeting the criteria. Figure 2.37 shows that the average and coefficient of variation for this subset are further improved: averages of 1.199 and 1.173, and COVs of 15.8% and 14.9%, for beams with and without stirrups respectively. Once again the normal curve shows excellent agreement with the lower half of the data, which implies that there is no systematic error in Augustus-II when predicting beams that fall into the lower range.

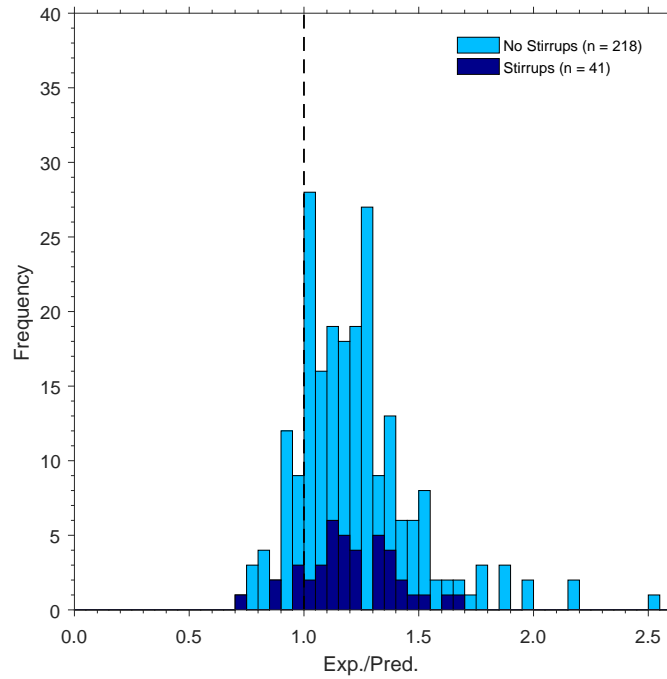


Figure 2.36: Analysis Distribution of Large ($h \geq 350$ mm) Shear Critical Rectangular Beams

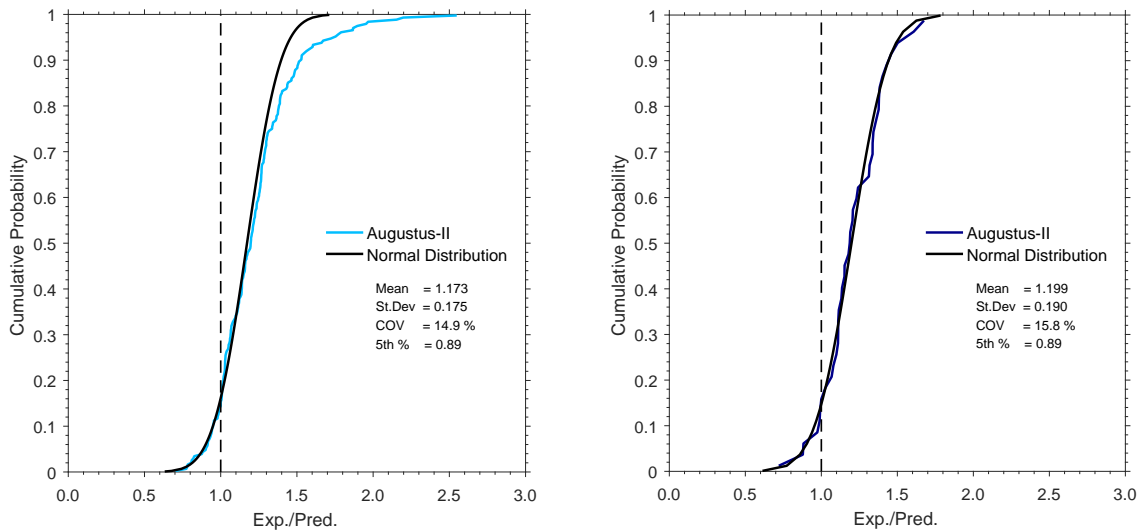


Figure 2.37: Cumulative Density of Analysis Distribution: No Stirrups (Left), Stirrups (Right)

2.5.3 Large-Scale Structural Analysis

The Augustus-II framework is not limited to just member-level analysis, it can also be extended to large-scale structures (e.g. frames and coupled shear walls). These models use HyPT elements for the beams and columns, and a mesh of two-dimensional membrane elements, defined in the program Membrane-2000 [32], for the joint regions.

Duong Frame (2006)

Figure 2.38 shows the geometry and structural detailing of a two-storey frame that was tested at the University of Toronto in 2006. These images are taken directly from Duong's doctoral thesis [33, p. 34-35].

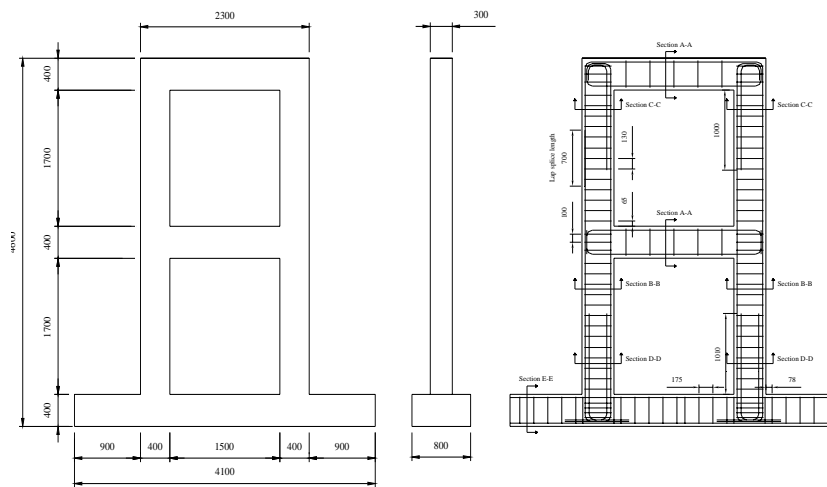


Figure 2.38: *Geometry of Two-Storey Frame Tested at the University of Toronto (Duong, [33, 29])*

Figure 2.39 shows the frame modelled in Augustus-II. The various colours in the left image correspond to the different sections defined in Response-2000 and Membrane-2000. The right image is the post-processed output of the frame just before failure, where the deformed shape and crack pattern is consistent with a load being applied at the top beam and shear failure in the first floor beam about to occur.

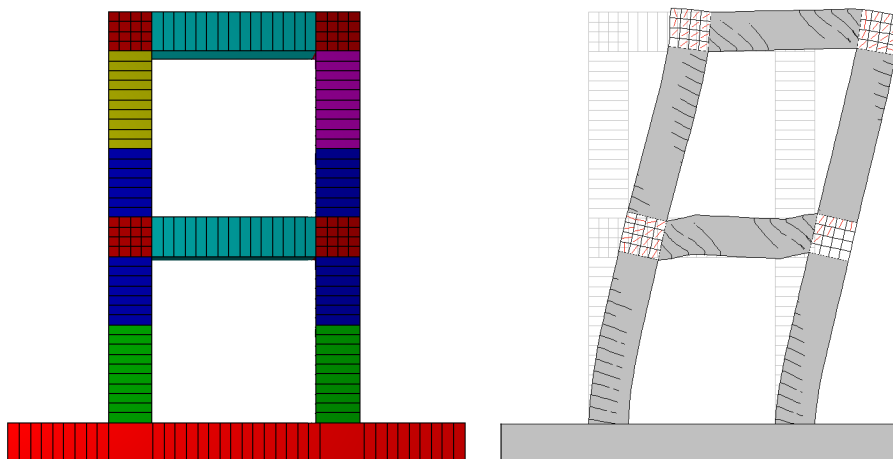


Figure 2.39: *Duong Frame - Model Mesh and Deformed Shape Before Failure*

The full experimental protocol for the Duong Frame was complex, involving reverse cyclic loading and the structural retrofitting of the damaged beam. The HyPT element has not been derived to capture cyclic behaviour, therefore only the initial first forward loading cycle of the test is being compared in Figure 2.40.

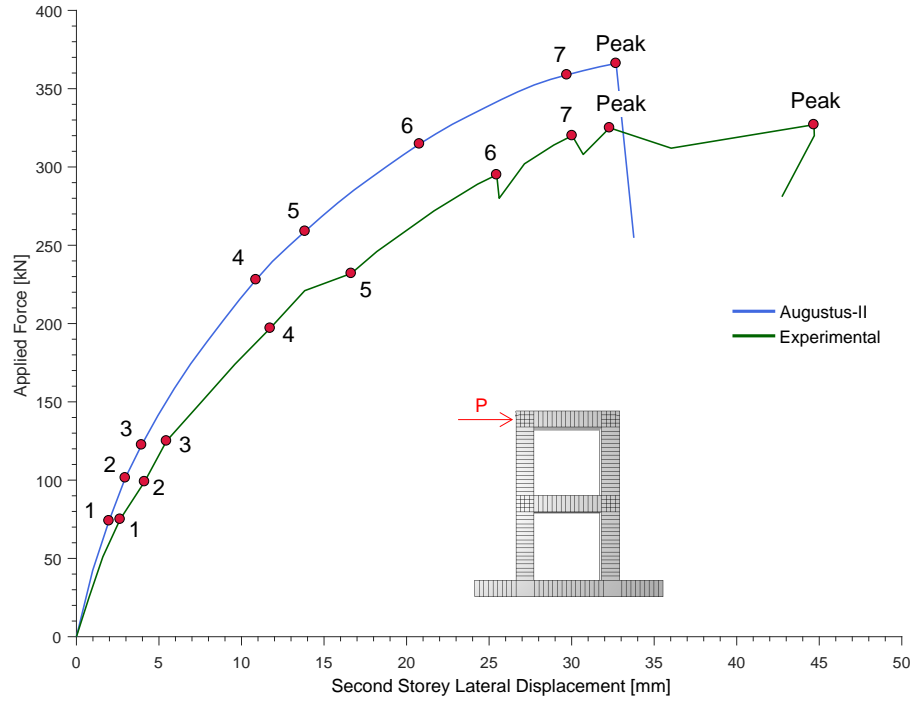


Figure 2.40: *Duong Frame - Pushover Analysis vs. Experimental Results*

The Augustus-II analysis slightly over-predicts the strength and stiffness of the frame and fails suddenly by shear failure in the first storey beam (this is the correct mode of failure), while the actual specimen exhibited significantly more ductility at its peak load. Yet the structural observations (Table 2.2) show good agreement between the experiment and model - the initial peak loading occurs at roughly the same second storey displacement, although the experimental specimen is able to sustain an additional 12 mm of displacement before unloading.

Table 2.2: Important Structural Observations at Load Stages [33, p. 112,132]

<i>Point</i>	<i>Description</i>	<i>Experimental</i>		<i>Augustus – II</i>	
		<i>P [kN]</i>	Δ [mm]	<i>P [kN]</i>	Δ [mm]
1	1 st Floor Beam - First Flexural Crack	75	2.65	74	1.98
2	Left Column - First Flexural Crack	99	4.13	101	2.96
3	1 st Floor Beam - First Shear Crack	123	5.46	122	3.95
4	2 nd Floor Beam - First Shear Crack	197	11.74	228	10.88
5	1 st Floor Beam - First Flexural Yield	232	16.65	259	13.85
6	1 st Floor Beam - Full Flexural Yield	295	25.46	315	20.79
7	2 nd Floor Beam - First Flexural Yield	320	30.03	359	29.72
Peak*	Significant Stiffness/Load Drop	325	32.30	366	32.69

* The frame was unloaded and cycled following this forward loading cycle

Salmon Frame (2017)

A single-storey frame recently tested at the University of Toronto was also modelled in Augustus-II - the mesh and deformed shape are shown in Figure 2.41. This experimental study has yet to be presented in a peer-reviewed publication, therefore the structural geometry and detailing are not shown here.

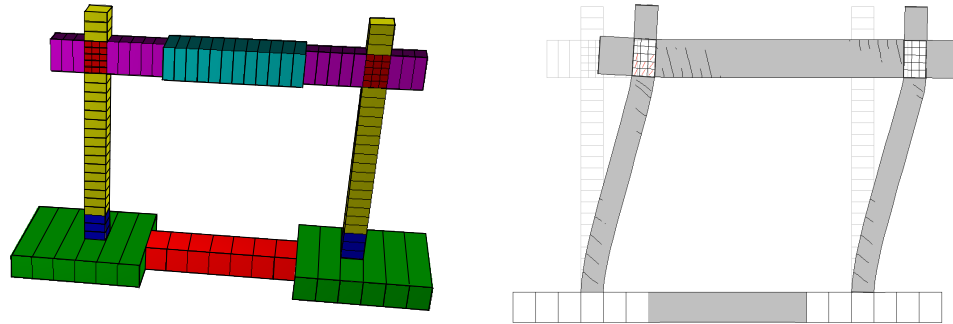


Figure 2.41: *Salmon Frame - Model Mesh and Deformed Shape Before Failure*

The researchers responsible for this test have requested that the detailed experimental hysteresis of the frame also be omitted from the current discussion. This explains why only the Augustus-II results, with important points annotated, are shown in Figure 2.42. Based on this pushover analysis, the peak load was 164 kN and occurred at a lateral displacement of 26 mm. Subsequent failure was initiated by complete yielding of the longitudinal steel at the top of the right column - this observation is reflected in photos of the failed specimen [30]. It is important to note that a direct comparison to the experimental results is not warranted since the cyclic nature of the tests would affect the ductility of the frame, although a backbone curve based on the peaks of the later forward cycles appears to closely match the reported Augustus-II peak value.

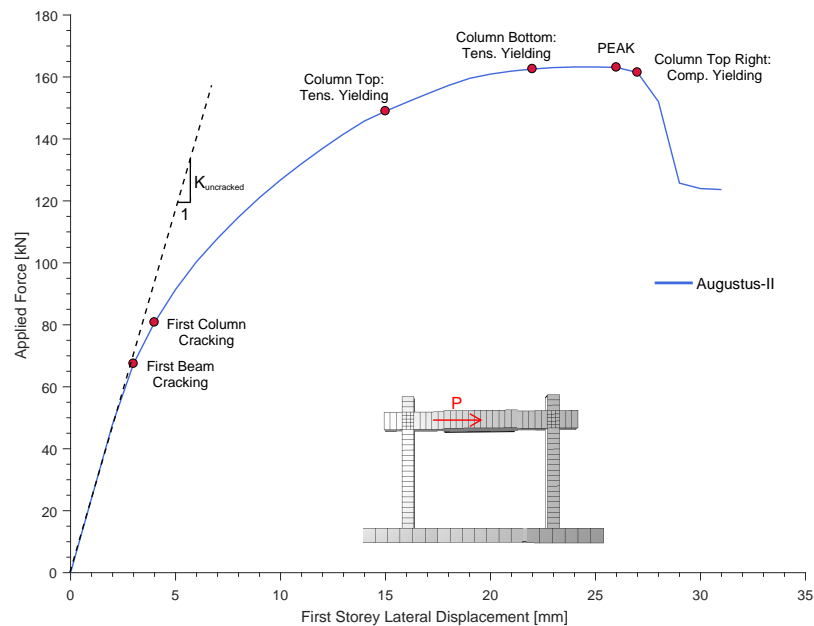


Figure 2.42: *Salmon Frame - Pushover Analysis Results*

Coupled Shear Wall

Augustus-II also has the ability to analyze full-scale structures that would typically be too large to build and test in a laboratory setting, and too cumbersome to analyze in traditional FEM programs. Figure 2.43 shows the mesh and deformed shape of a 10-storey coupled shear wall, where the coupling beams are modelled with HyPT elements and the walls with membrane elements. A detailed discussion of these models and results can be found in the thesis written by Yap [26]. The input nodal displacements for the membrane elements are determined by linear interpolation between the 2d-HyPT nodes at interface locations where the nodes do not coincide.

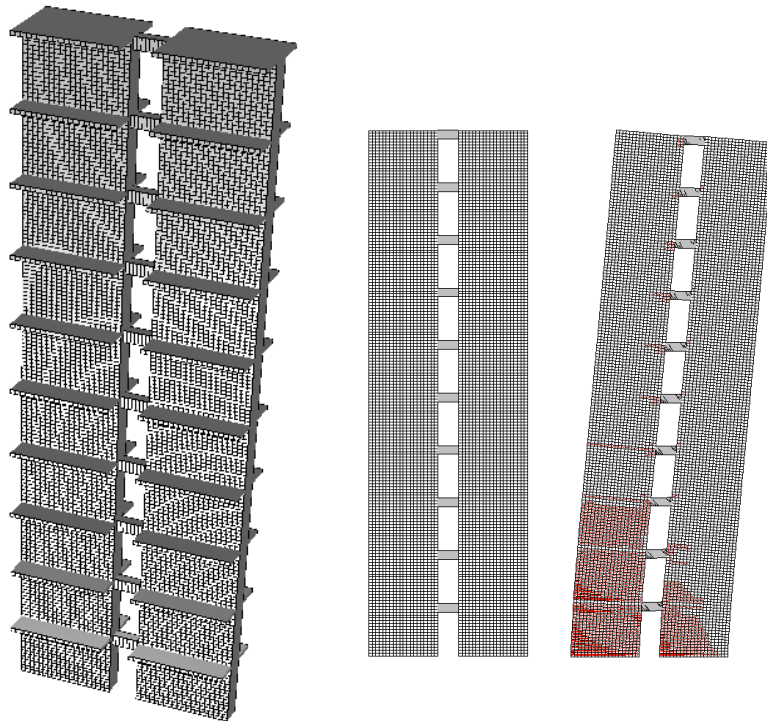


Figure 2.43: *Coupled Shear Wall Modelled with Augustus-II (Yap [26])*

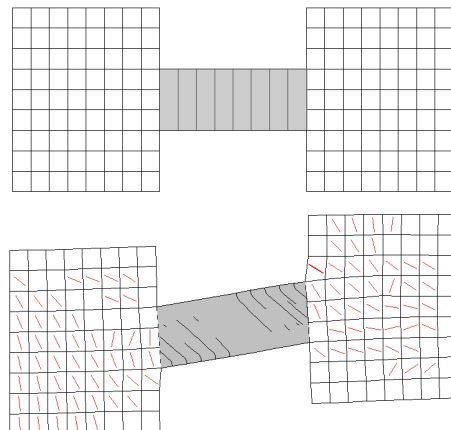


Figure 2.44: *Individual Coupling Beam Model*

2.5.4 Augustus-II Convergence Study

To determine the relative performance of Augustus-II, two beams from the ACI database (#131 (Aster, 1974) & #1356 (Sneed, 2007)) were selected and also analyzed with VecTor2, which is a successful program for the nonlinear finite element analysis of reinforced concrete developed at the University of Toronto [6]. Figure 2.45 shows the VecTor2 finite element meshes for both beams - in contrast to Augustus-II, the mathematical formulation of the elements used in VecTor2 is such that several are required through the thickness of a member to accurately represent the structural mechanics of reinforced concrete.

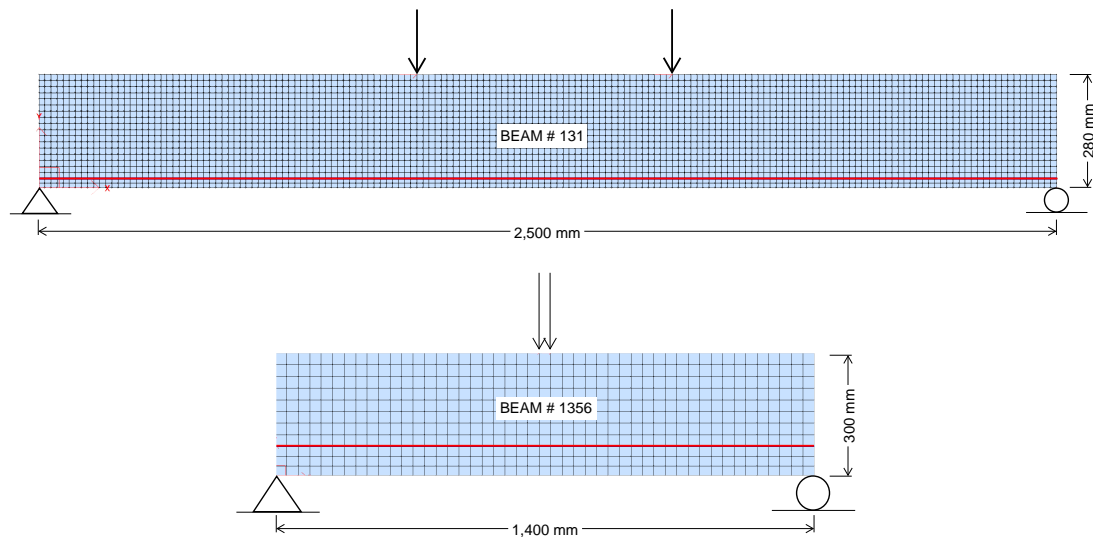


Figure 2.45: *VecTor2 Beam Meshes*

The two programs are assumed to be performing satisfactorily since shear failure occurs in both beams at similar converged Exp./Pred. ratios (~ 1.2 for Beam #131, ~ 1.5 for Beam #1356). The purpose of this study is determine the number of elements that are needed in each program to achieve convergence (i.e. when the failure load stops changing with the addition of more elements) and how the analysis duration is influenced by the number of elements.

Figure 2.46 shows the results of this convergence analysis for both beams, where the red dot indicates the point at which convergence is achieved for either program. Each beam is represented with two graphs - the graph to the right plots the same data as its neighbour, but the scale of the x-axis is significantly reduced. It is clear that Augustus-II is much more stable with respect to the number of elements - the program requires almost two orders of magnitude fewer elements to fully converge (~ 100 vs. ~ 5000 elements), and yields reasonable results with only 20 elements. Figure 2.46 shows the relationship between the number of elements and the runtime of the program. The HyPT element is clearly a more computationally efficient element at its convergence point - Augustus-II requires under 20 seconds to complete the analysis of both beam, while VecTor2 ranges from 15-30 minutes. Although more computationally demanding, VecTor2 is still a useful general program that can provide a level of detail not possible with the 2d-HyPT implementation.

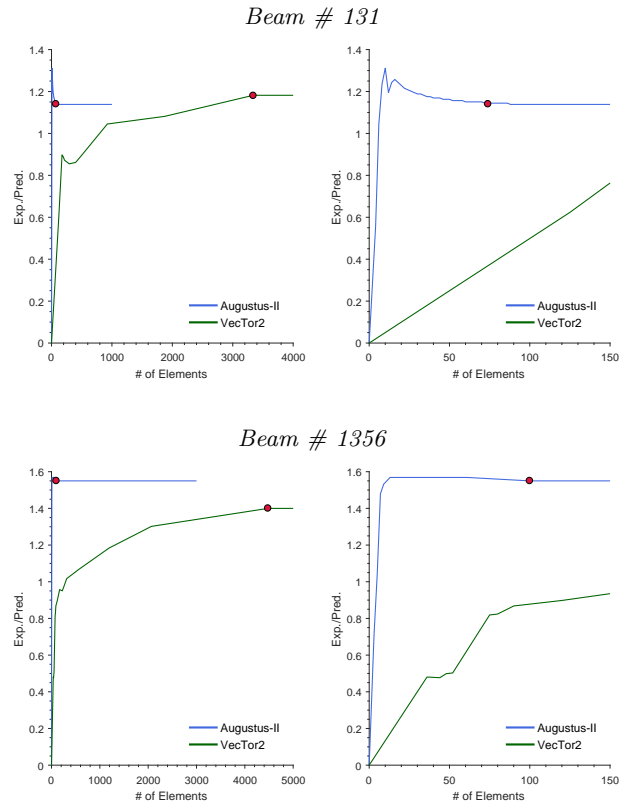


Figure 2.46: *Convergence Analysis (Right = Zoomed in Plot)*

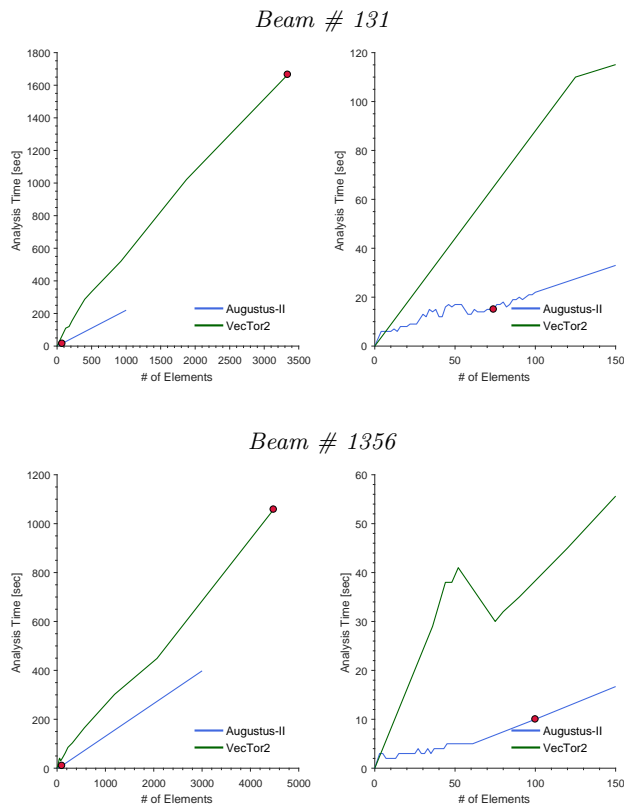


Figure 2.47: *Runtime Analysis (Right = Zoomed in Plot)*

Chapter 3

Description of Experimental Program

The following chapter will present the experimental component of this project, which consisted of constructing, instrumenting and conducting the world’s first large-scale pure torsion tests on reinforced concrete shell specimens. The tests were performed using the Shell Element Tester (SET) located in the Mark Huggins Structural Laboratory at the University of Toronto. The chapter is organized into sections pertaining to the specimen design (Table 3.1), material properties, experimental set-up, and instrumentation.

Table 3.1: Summary of Specimen Properties

Test	Loading	[Days] Age	[MPa] f'_c	[MPa] $\rho_x \cdot f_{y,x}$	[MPa] $\rho_y \cdot f_{y,y}$	[MPa] $\rho_z \cdot f_{y,z}$
ES1	Torsion	26	30.4	15.0	9.93	-
ES2	Torsion	77	37.6	15.0	9.93	1.52

3.1 Specimen Design and Construction

The two specimens (ES1 & ES2) were designed as an extension to a previous experimental program undertaken at the University of Toronto [34, 35]. This previous research consisted of a partnership with the Seoul National University [36], hence the reinforcement ratios and concrete strengths selected in the current study are nominally the same as those typically seen in Korean nuclear containment structures [37]. Although the percentages used for the current program are higher, the ρf_y values are comparable when considering the higher strength steel in the Korean shells.

The two specimens presented in this thesis had nominal dimensions of 1626 x 1626 mm square, with a thickness of 285 mm. Both specimens had identical orthogonal in-plane longitudinal (X-direction) and transverse (Y-direction) reinforcement arrangements, equivalent to 2.95% and 1.95% of their respective cross-sectional areas. Despite some variation in the concrete strengths, the only significant experimental difference between the two specimens was the additional out-of-plane (Z-direction) T-head reinforcement included in ES2, equivalent to a ratio of 0.32% of the cross-sectional area. Keeping all other parameters constant across the two specimens meant that the effect of the out-of-plane reinforcement could be clearly discerned. The reinforcement spacing, and the resulting percentages are summarized in Table 3.2.

Table 3.2: Summary of Specimen Reinforcement

Name	[mm] Dimensions	[mm] X-Bars	[mm] Y-Bars	[mm] Z-Bars	[%] ρ_x	[%] ρ_y	[%] ρ_x
ES1	1626x1626x285	20M @ 72	20M @ 108	-	2.95	1.95	-
ES2	1626x1626x285	20M @ 72	20M @ 108	#4	2.95	1.95	0.32

20M bars = 300 mm²

#4 bars = 129 mm²

3.1.1 Reinforcement Schematic

Each specimen was constructed and assembled as two separate but identical reinforcement cages that represented the inner and outer faces of a shell structure. Each cage consisted of a layer of orthogonal X and Y direction reinforcement, but oriented at 45° to the plane of the applied loading. The X direction was considered the principal reinforcement direction and was therefore closest to the surface of the shell on either side. Henceforth these faces will be referred to as the the South and North faces respectively to stay consistent with the naming convention resulting from the orientation of the test set-up. Figures 3.1 & 3.2 show the North faces of specimens ES1 and ES2 respectively, note the T-head bars in specimen ES2.

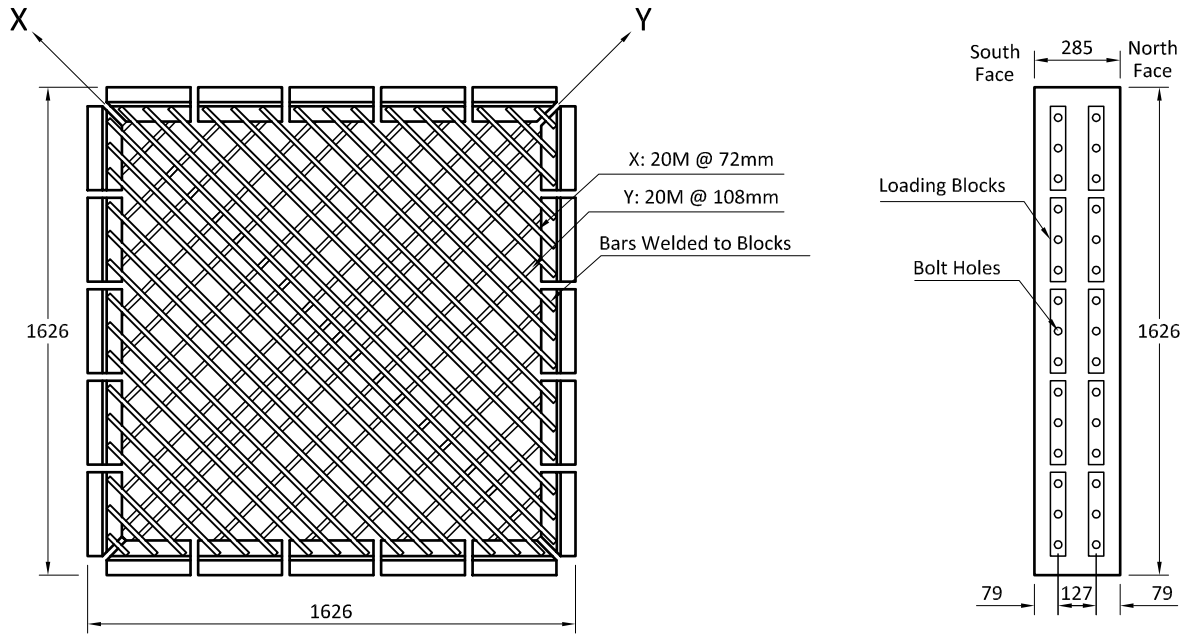


Figure 3.1: ES1 North Face Cage (South Face is Identical)

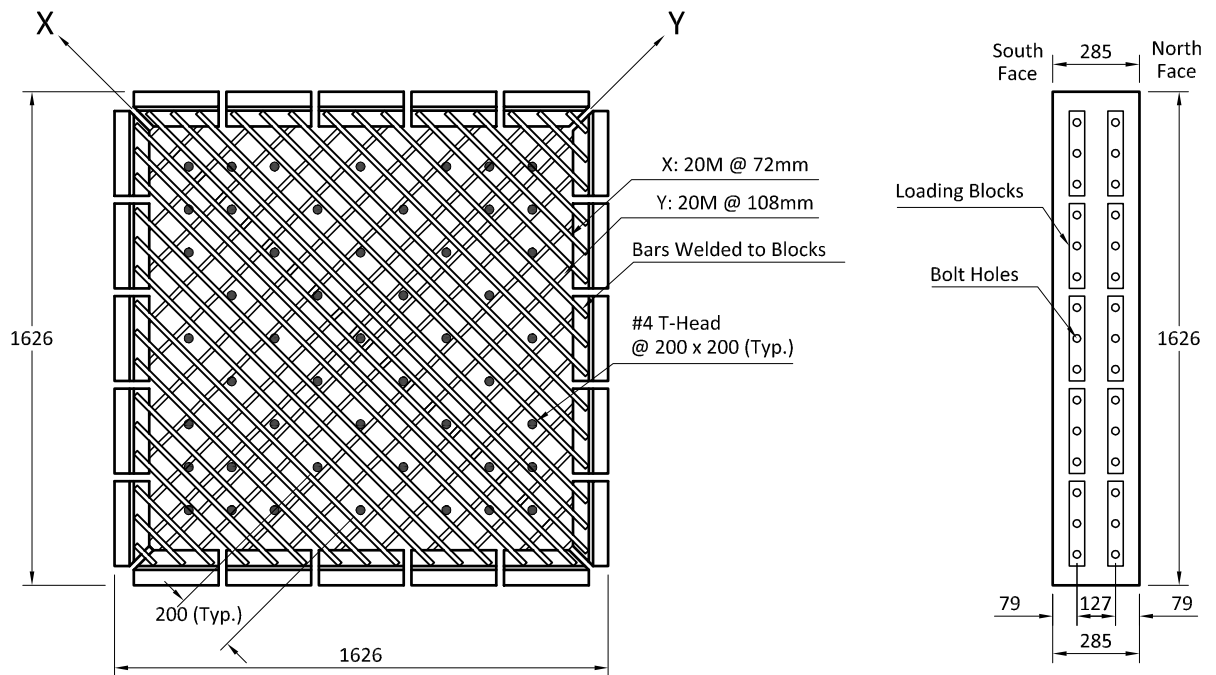


Figure 3.2: ES2 North Face Cage (South Face is Identical)

3.1.2 Specimen Construction

The longitudinal reinforcement bars were placed across the the face of the assembly jig and welded to the loading blocks at either end. The quality of the welds was of utmost importance in guaranteeing that the specimen could develop its full strength and not suffer an unwanted localized edge failure. Figure 3.3 shows a cage that has been fully welded and is in the process of being moved to the concrete casting forms. This cage represents half of the specimen, either the North or South face of the shell.



Figure 3.3: *Welded Reinforcement Cage*

Figure 3.4a shows an assembled specimen ready for casting, with the North and South face cages anchored to the casting forms. Figure 3.4b shows the same specimen after concrete casting, but before finishing of the surface. The hollow tubes sticking through the surface of the specimen are necessary for the out-of-plane instrumentation, which will be discussed further in Section 3.4.

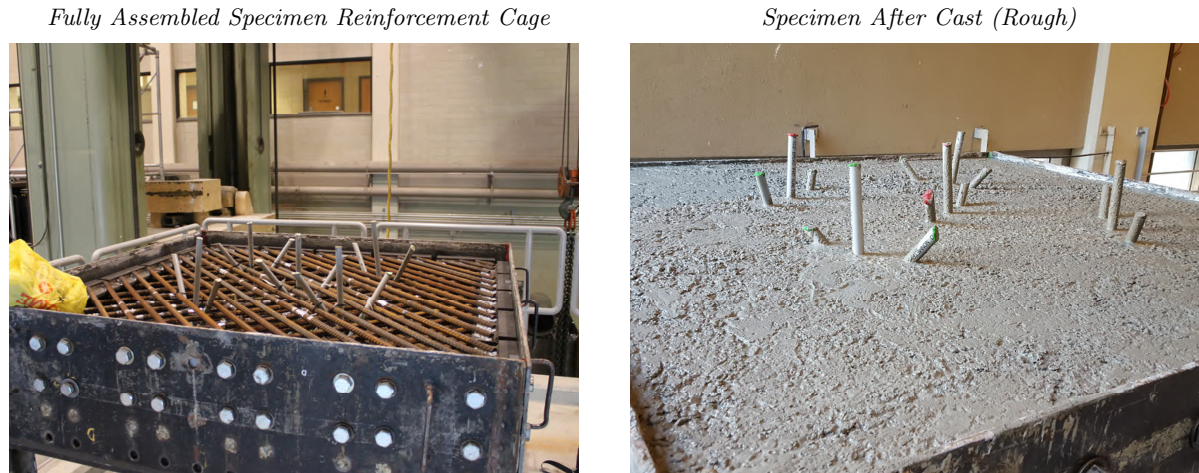


Figure 3.4: *Casting Reinforced Concrete Specimen*

Figure 3.5 shows a finished specimen with a painted surface awaiting the installation of all the in-plane and out-of-plane instrumentation. The thin coat of white paint makes identifying surface cracks during the test easier. The smaller holes are approximately 1 cm deep and are required for the in-plane instrumentation mounts, while the larger holes provide an uninterrupted path all the way through the specimen.

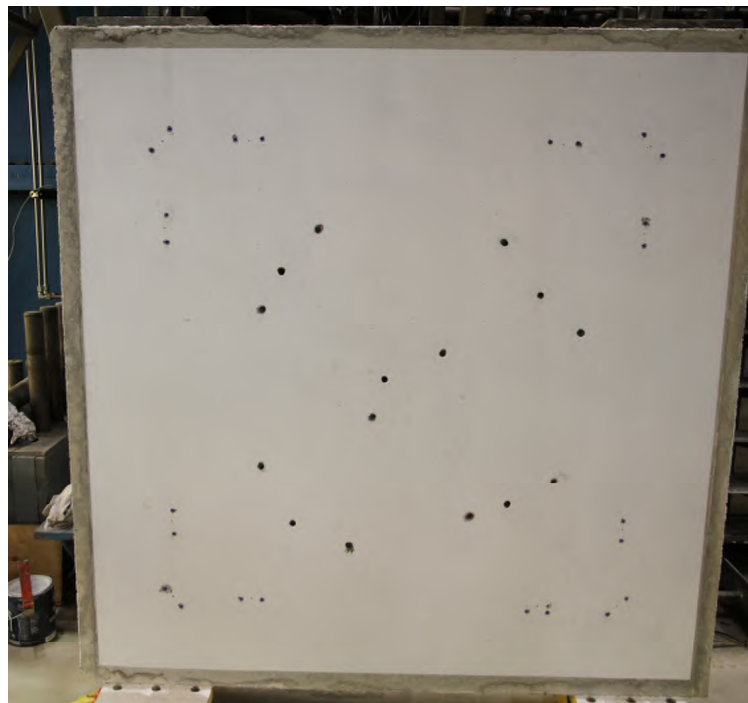


Figure 3.5: *Completed Shell Specimen*

3.2 Material Properties

The individual stress-strain responses of the steel and concrete components in reinforced concrete are necessary to properly model large-scale structural behaviour. Hence axial tests were performed on steel reinforcement bar coupons and concrete cylinders representative of the materials used to build the shell specimens.

3.2.1 Concrete Cylinder Tests

Plain concrete cylinders (6" x 12") were cast from the same concrete batch as the shell specimens. Both shells were cast on October 5th, 2016 - the results from the cylinder tests were used to determine the compressive strength gain curve (Figure 3.6). The points represent the average of three separate cylinder tests performed at 7, 21 & 28 days after the cast, and on the dates of the shell tests. Specimen ES1 was tested early, slightly before 28 days, since it was concluded that reasonable strength had already been achieved. The concrete compressive strength difference between the two specimens is reasonable for regular strength concrete, and will have to be accounted for when modelling the specimens. Concrete tensile strength was not a critical factor in the tests and was therefore not determined explicitly.

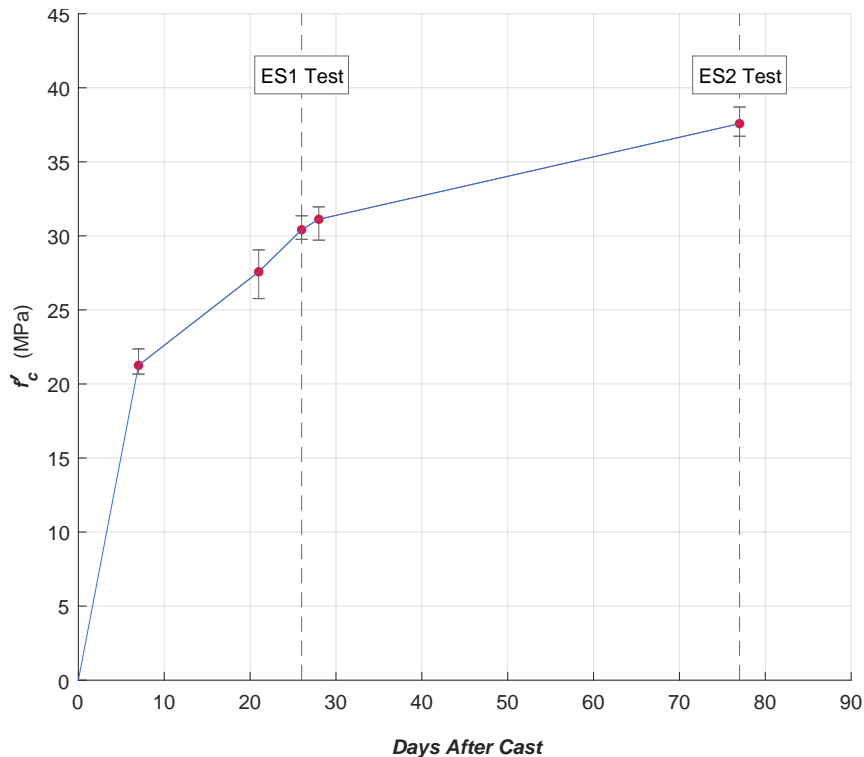


Figure 3.6: *Concrete Compressive Strength Gain*

Detailed compressive stress-strain curves were determined at 28 days (Figure 3.7) and on the dates of the actual shell tests (Figure 3.8). At each of these dates three separate cylinders were tested to account for the variability in concrete. Average peak stress and strain values on the test days are summarize in Table 3.3.

Table 3.3: Average Test Day Concrete Properties

Test	[MPa]	[$\times 10^{-3}$]
	f'_c	ϵ'_c
ES1	30.4	1.75
ES2	37.6	1.87

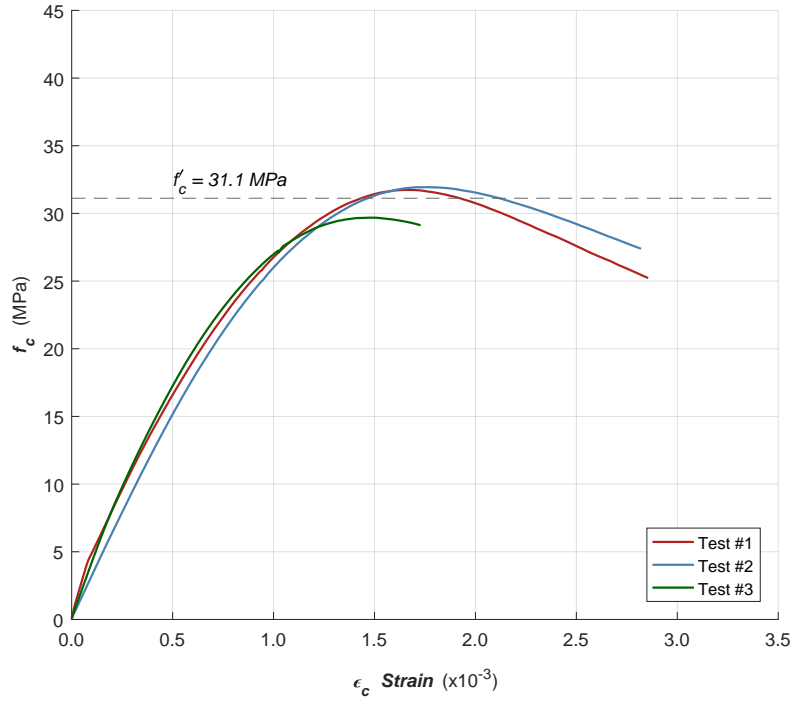


Figure 3.7: Cylinder Stress-Strain Curve at 28 Days

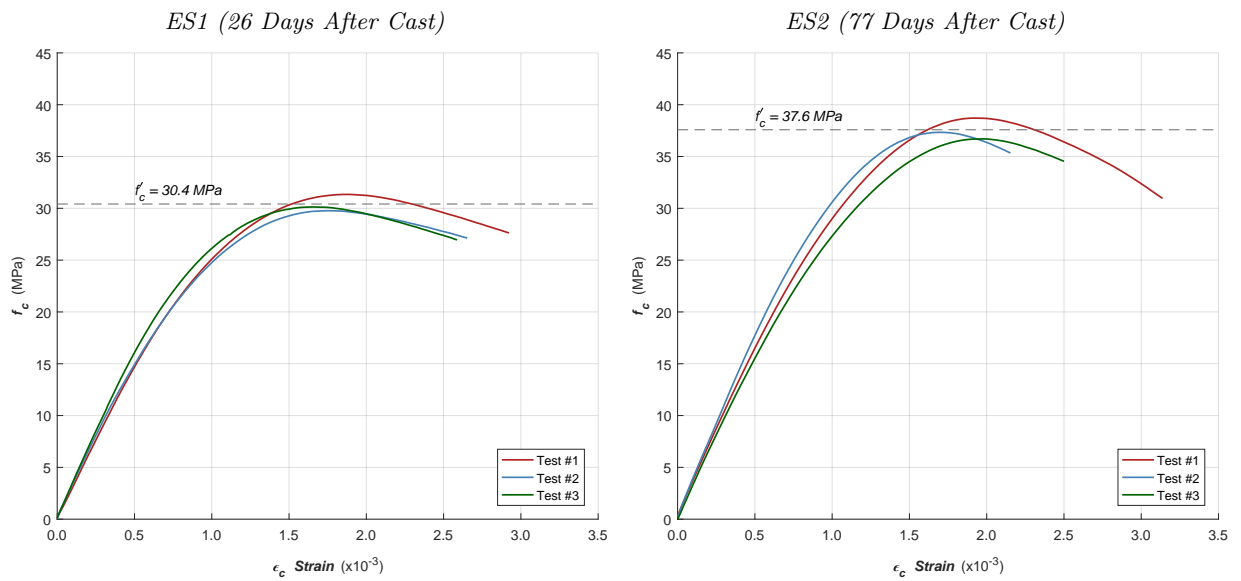


Figure 3.8: Cylinder Stress-Strain on Test Day

3.2.2 Steel Coupon Tests

Table 3.4: Average Reinforcement Steel Properties

Bar	[mm^2] Area	[MPa] f_y	[MPa] f_u	[$\times 10^{-3}$] ϵ_y	[$\times 10^{-3}$] ϵ_{sh}	[$\times 10^{-3}$] ϵ_u
20M	200	509	636	3.45	15.1	110
#4	129	474	657	2.23	11.5	133

In-Plane Steel

20M steel reinforcement bars from the same batch were used for all the in-plane steel (X & Y Direction) in both specimens. Three separate coupon tests were performed; the results are shown in Figure 3.9.

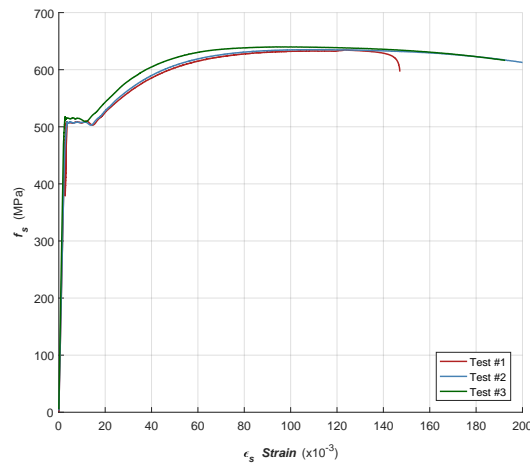


Figure 3.9: Steel (XY) Coupon Stress-Strain Curve

Out-of-Plane Steel

#4 steel T-headed bars were used as the out-of-plane shear reinforcement in specimen ES2. Six separate coupon tests were performed; the results are shown in Figure 3.10)

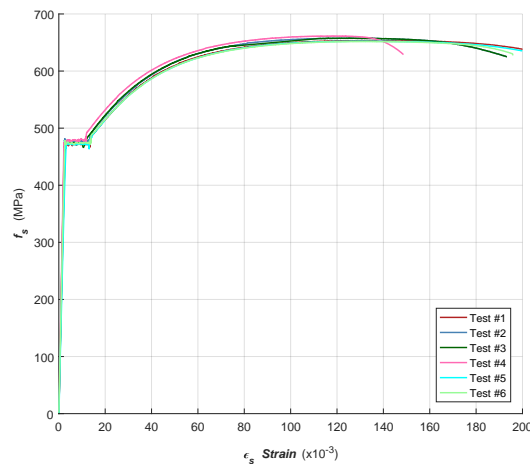


Figure 3.10: Steel (Z) Coupon Stress-Strain Curve

3.3 Experimental Set-up

The experiments were performed with the Shell Element Tester - a unique experimental set-up capable of applying any combination of the eight stress resultants potentially experienced by a shell structure. By varying the loading ratios and the orientation of the longitudinal reinforcement, different combinations of in-plane and out-of-plane shear stresses, axial stresses, and moments can be applied to the appropriate section. The Shell Element Tester consists of servo-controlled actuators operated with the MTS[®] FlexTest controller interfaced with a computer running the AeroPro[™] Data Acquisition System [38], which allows for a high level of control and precision throughout the test. The actuators are connected to the shell specimen through loading yokes bolted to blocks cast into the concrete. For a detailed technical description of the Shell Element Tester and the preparation and installation of a specimen see the work of Dr. Ruggiero [39], Figure 3.11 is adapted from this PhD Thesis.

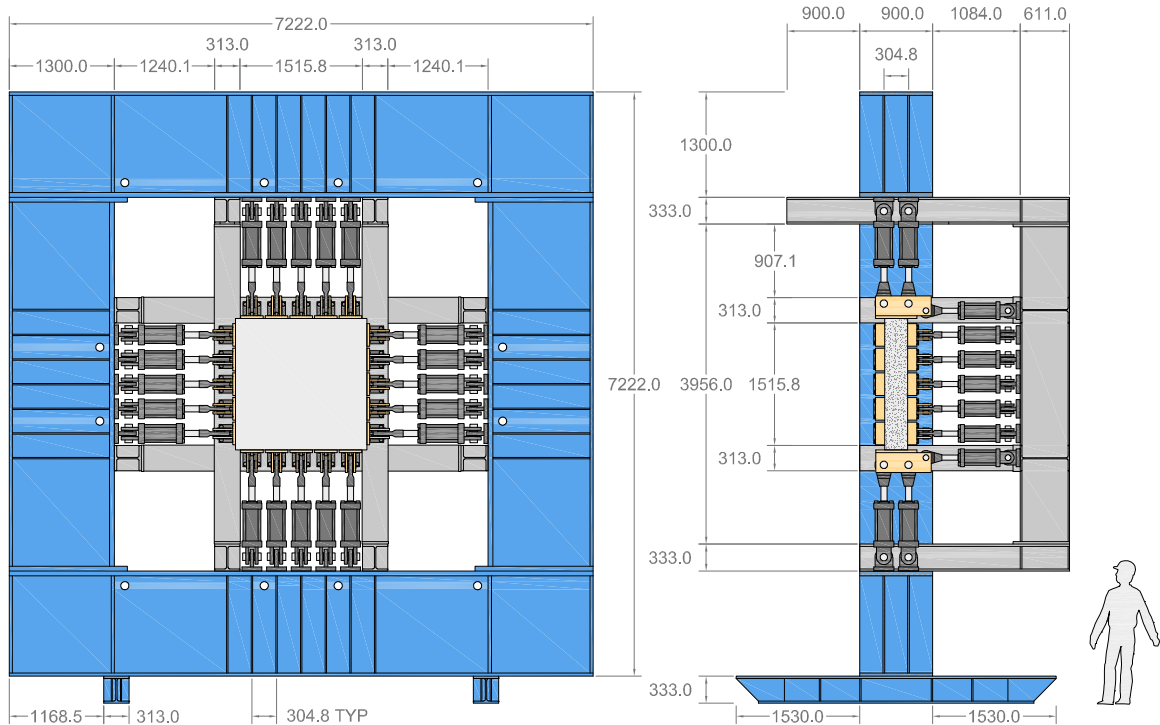


Figure 3.11: Shell Element Tester Schematic (Ruggiero [39])

3.3.1 Actuator Configuration

The Shell Element Tester consists of 60 servo-controlled hydraulic actuators, their properties are summarized in Table 3.5. The reported maximum values are based on achieving a system pressure of 4300 psi, which is considered to be the highest pressure that can be consistently maintained with the help of the laboratory's booster pump.

Table 3.5: Loading Actuator Summary

Location	Quantity	Type	[kN]	[kN]
			Max. Tens.	Max. Comp.
In-Plane	40	100-ton	+765	-940
Out-of-Plane	20	50-ton	+440	-530

The actuators are positioned around the four sides of the frame. Each side has 10 in-plane actuators (aligned in two banks of 5), along with 5 out-of-plane actuators. Figure 3.12 shows the actuator numbering used in the control system, and a 2D representation of their arrangement. For example, the bottom face has in-plane actuators numbered 1-10 (1-5 on the front, 6-10 on the back), and out-of-plane actuators numbered 11-15.

To stabilize the specimen and prevent rigid body motion during the test, six of the actuators were placed in displacement control and set to maintain zero displacement. This is analogous to a simply-supported beam, where three restraints are needed to achieve statical determinacy. Fixing fewer points would lead to instability, while fixing more would lead to a statically indeterminate structure. Actuators #21, #25 & #40 (red box) provided the three necessary in-plane restraints, while actuators #11, #15 & #28 (blue box) provided the necessary out-of-plane restraints. Actuator #8 (green box) is the control displacement channel, which is discussed further in Section 3.3.3.

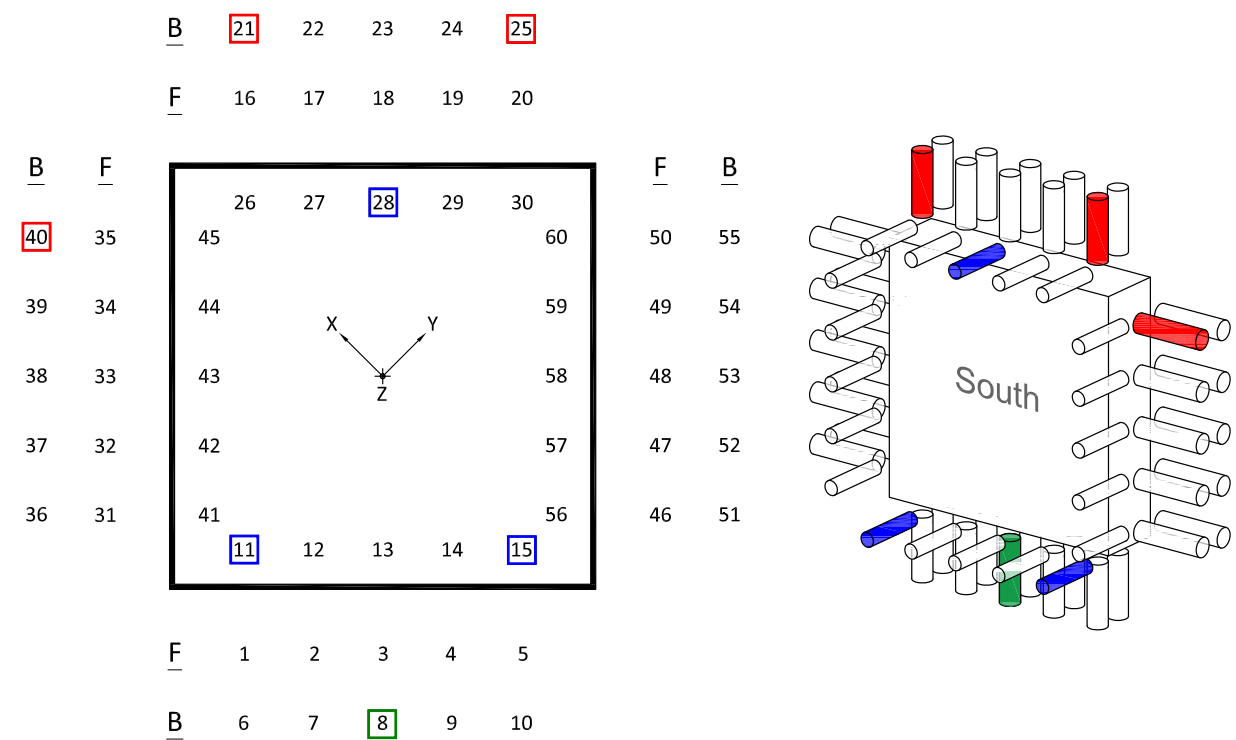


Figure 3.12: Actuator Placement and Numbering

3.3.2 Coordinate System

The specimen coordinate system (XY) is rotated 45° to the plane of the actuators (HV), where the XY -plane coincides with the location of the longitudinal reinforcement. The right-hand rule dictates that the $+Z$ direction is taken into the page when looking from the North, which is the case for the left image in the actuator placement figure (3.12) from the previous section. It is important to note that previous experimental programs have defined the shell coordinate system differently, so care must be taken when comparing results across sources.

The nature of pure torsion loading, and the placement of the instrumentation, requires one to refer to the North and South face as separate entities at times. In such cases it is important to keep a consistent coordinate system - Figure 3.13 depicts the same coordinate systems viewed from either a North or South frame of reference. Subsequent discussion in this thesis will be consistent with this notation.

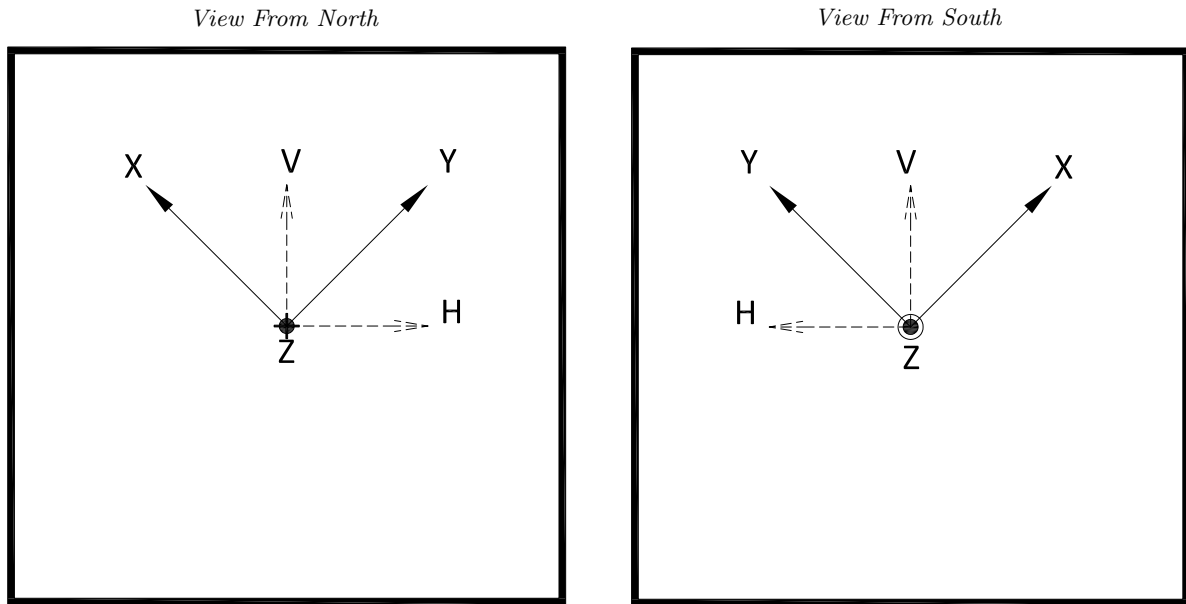


Figure 3.13: *Shell Element Coordinate System*

3.3.3 Loading Protocol

In both experiments only the 40 in-plane actuators were necessary to apply pure torsion to the shell specimen. The three out-of-plane rigid links were active to provide the necessary static restraint, but the remaining out-of-plane actuators were simply set to a constant ± 5 kN of force during the test to further stabilize the shell and prevent buckling. These experiments were effectively in-plane tests, so for clarity the out-of-plane actuators are not included in subsequent images detailing the loading protocol.

Both experiments were performed in a displacement control mode, which is a new development in the capabilities and usage of the Shell Element Tester. Tests are typically conducted in a force-controlled mode, which meant that the user simply controlled and incremented the forces in the actuators until the specimen failed. Although this simplified the execution of the test, it did not allow for any post-peak behaviour and could on occasion lead to sudden and dangerous specimen failures. A displacement-controlled test was much more complicated to implement and execute, but allowed for accurate post-peak behaviour and user controlled load-shedding once the test was completed. In this experimental program the master displacement was assigned to actuator #8; the displacement on this channel was increased as the test progressed, and the load that was developed to achieve the target displacement was used as the input for all other actuators.

To apply pure torsion in the XY-plane, moments of equal magnitude and opposite sign were applied along the H & V edge of the shell. In the Shell Element Tester, moments are applied by setting one bank of actuators into tension, while simultaneously setting the adjacent bank to compression. In these tests the magnitude of the compression and tension along one face was kept equal, resulting in a pure couple with no net axial force. Figure 3.14 shows the sign of the force in each of the in-plane actuators throughout the test, while 3.15 shows the same loading condition represented on both the North and South faces respectively.

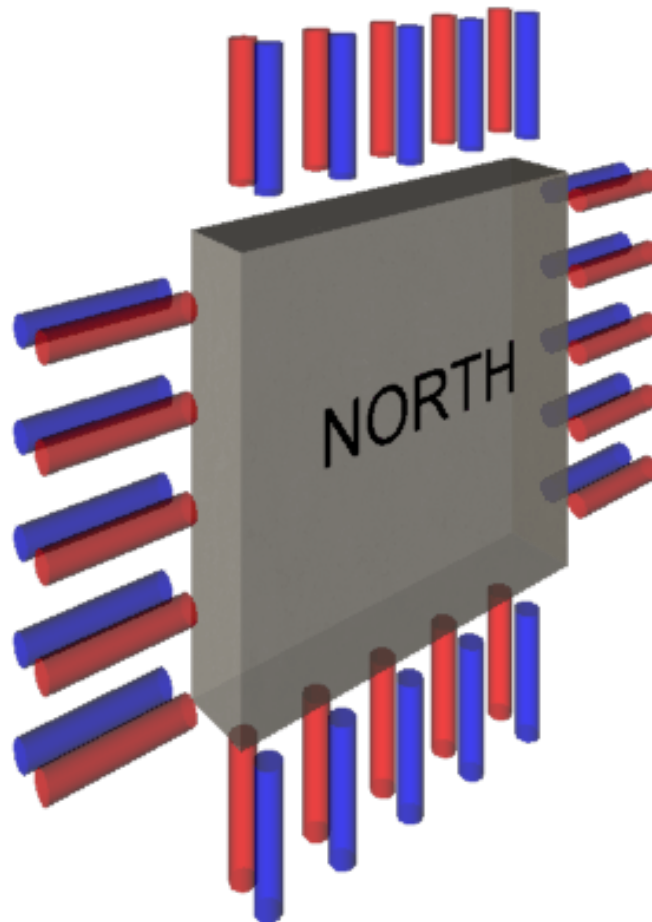


Figure 3.14: *In-Plane Actuator Forces During Test (Tension, Compression)*

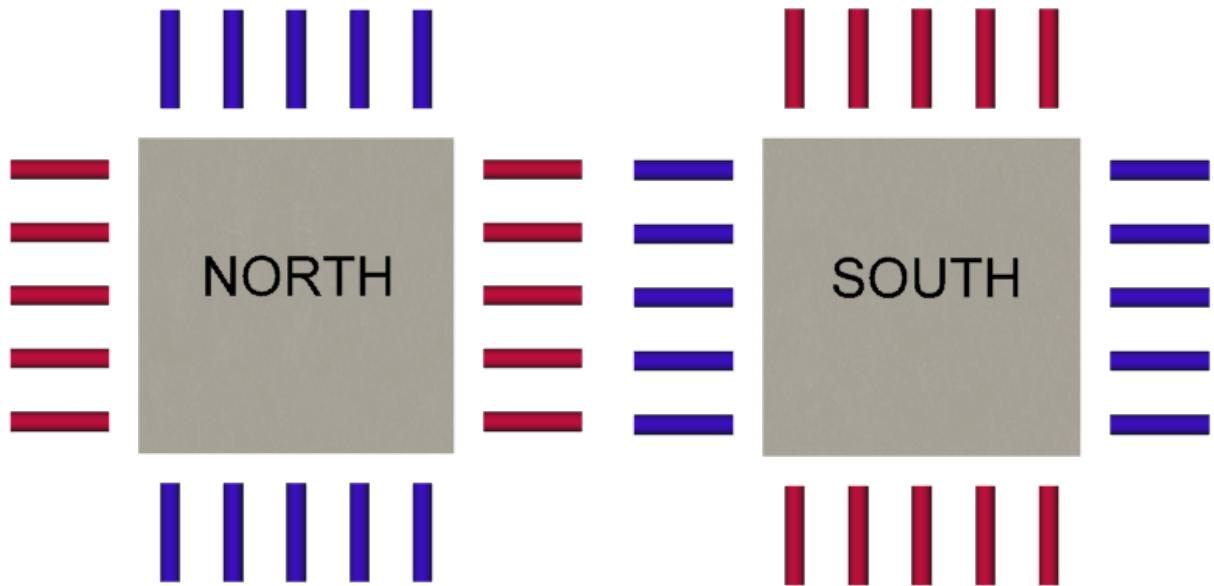


Figure 3.15: Actuator Forces on North/South Face (*Tension, Compression*)

The Shell Element Tester can only apply axial forces in the H & V directions. Yet the actual test region is defined by the orthogonal axis of the longitudinal reinforcement, which is rotated 45° to the HV-plane. The square element (XY-plane) inscribed inside the full shell specimen in Figure 3.16 represents the test region.

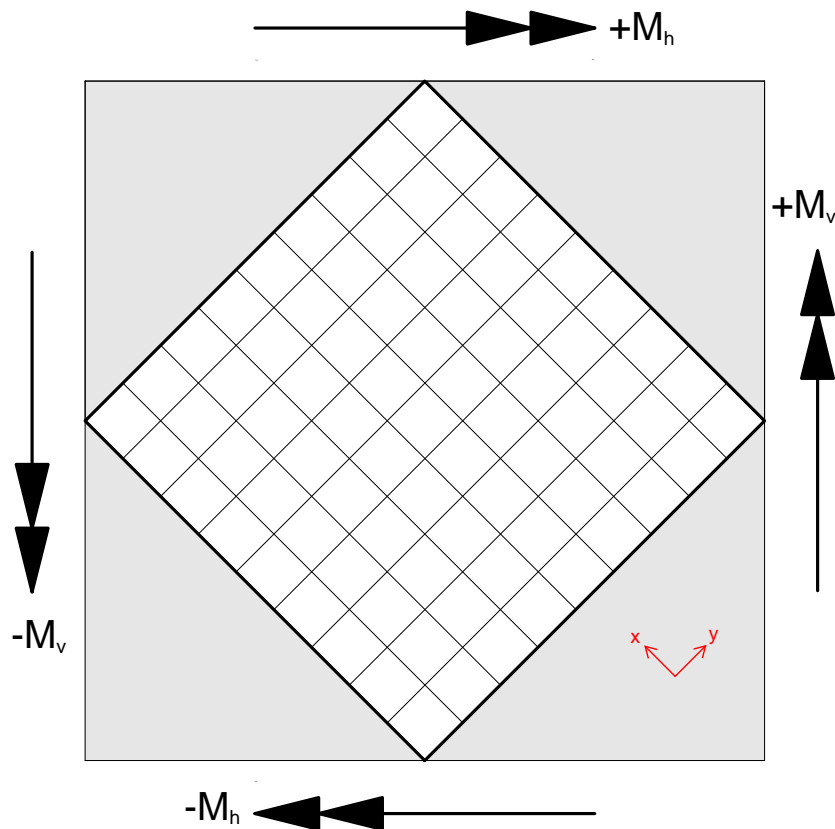


Figure 3.16: External Moments Applied to the Specimen (*Viewed from North*)

Resultants can be found by satisfying static equilibrium at the boundaries of the test region. This calculation is straightforward as the internal cut is at 45° , and the magnitudes of external moments on adjacent faces are equal (i.e. $|M_h| = |M_v|$). Figure 3.17 shows the free-body diagram of the resultant moment on the test region. The external moments clearly result in pure torsion on the test region (XY-plane), where the magnitudes of torsional moments on adjacent faces are equal (i.e. $|M_{xy}| = |M_{yx}|$).

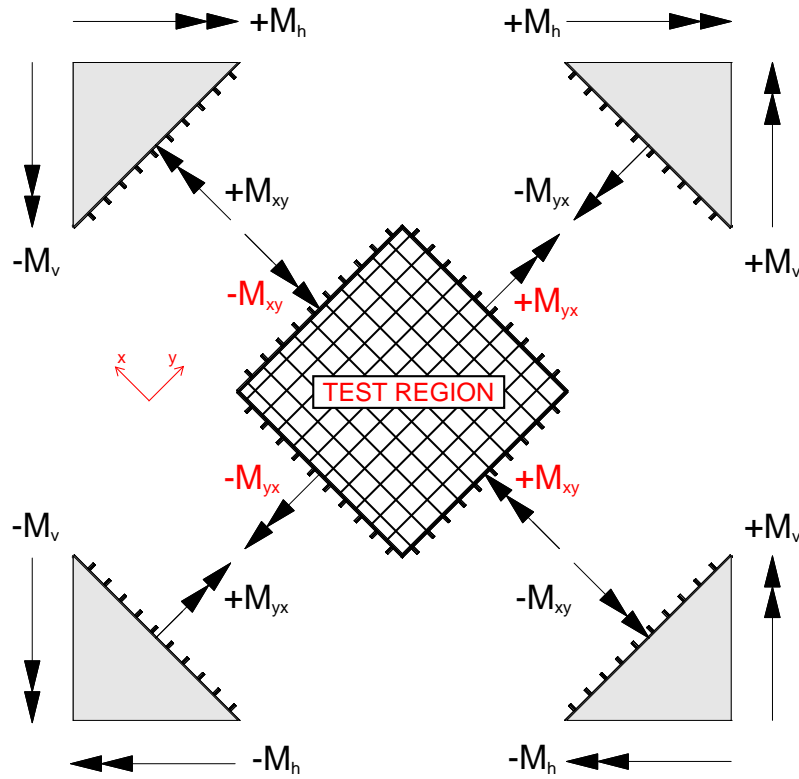


Figure 3.17: Pure Torsion Applied to the Test Region

Pure torsion can also be thought of as a couple resulting from pure in-plane shear forces on the North and South faces respectively. Figure 3.18 shows both faces of the shell as viewed from the North, the moment created by the shear forces is equivalent to the torsion on the test region (direction and magnitude).

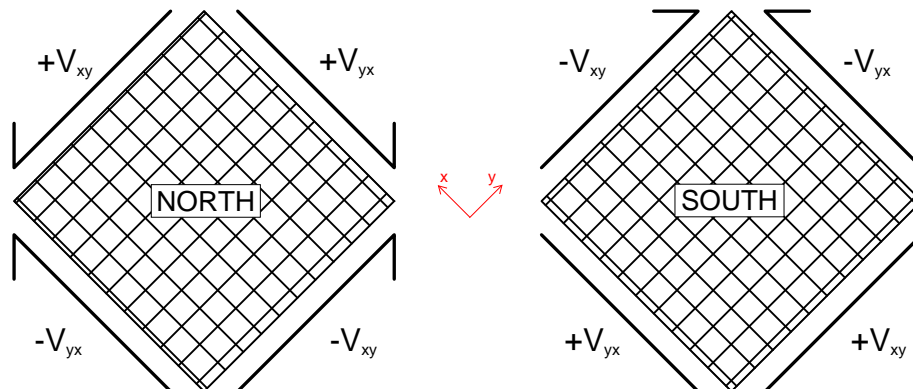


Figure 3.18: Torsion Represented as In-Plane Shear Forces (Viewed from North)

3.4 Instrumentation

The Shell Element Tester actuators come equipped with displacement and force sensors, but to improve the quality of data gathered additional surface and embedded measurement devices were included with the specimens. There were two main data streams for these external devices: the force and strain/displacement data routed through the AeroPro[™] Data Acquisition System (DAQ), and the three-dimensional surface coordinate data captured by the Nikon[®] (formerly Metris) metrology system. The following sections will outline the placement and orientation of the additional instrumentation used in both experiments; to establish data consistency across the tests both ES1 & ES2 were instrumented in the same manner.

3.4.1 Built-in Actuator Sensors

Each of the 60 actuators on the Shell Element Tester had its own built-in sensors capable of providing continuous data: a load cell to measure the force exerted, and an external string potentiometer to measure the displacement. The proper functioning of these sensors was of particular importance to the test as they provided information regarding the external loading, and experimental control and execution. For example, the string potentiometer for actuator #8 was used as the master displacement control channel for the whole test, while the six string potentiometers on the rigid link actuators had to be kept at zero displacement throughout the test to ensure stability. Accurate load cell readings from the in-plane actuators were also used to determine the magnitude of torsion being applied to the shell specimen during the test.

3.4.2 Linear Variable Differential Transformers (LVDTs)

To measure average in-plane strains, six LVDTs were mounted on both the North and South face of the specimen: two horizontal, two vertical, one in the X-direction, and one in the Y-direction. Figure 3.19 shows the placement of the LVDTs on the specimen, both faces are shown from the North (i.e. the South face is shown like an x-ray view through the specimen). The diagonal LVDTs on the South face are slightly shifted to avoid interfering with the three-dimensional coordinate measurement system. The naming convention used is as follows: 1st letter = face, 2nd letter = measurement direction, 3rd letter = relative locations

Only two independent strain measurements are necessary to find the magnitude of the shear strain across an element, but defining the whole Mohr's circle of strain requires a third measurement. In this experimental set-up the LVDTs provide four independent strain measurements, so a Mohr's circle of best fit using all four measurements is calculated instead. This method is discussed further in Section 4.2.

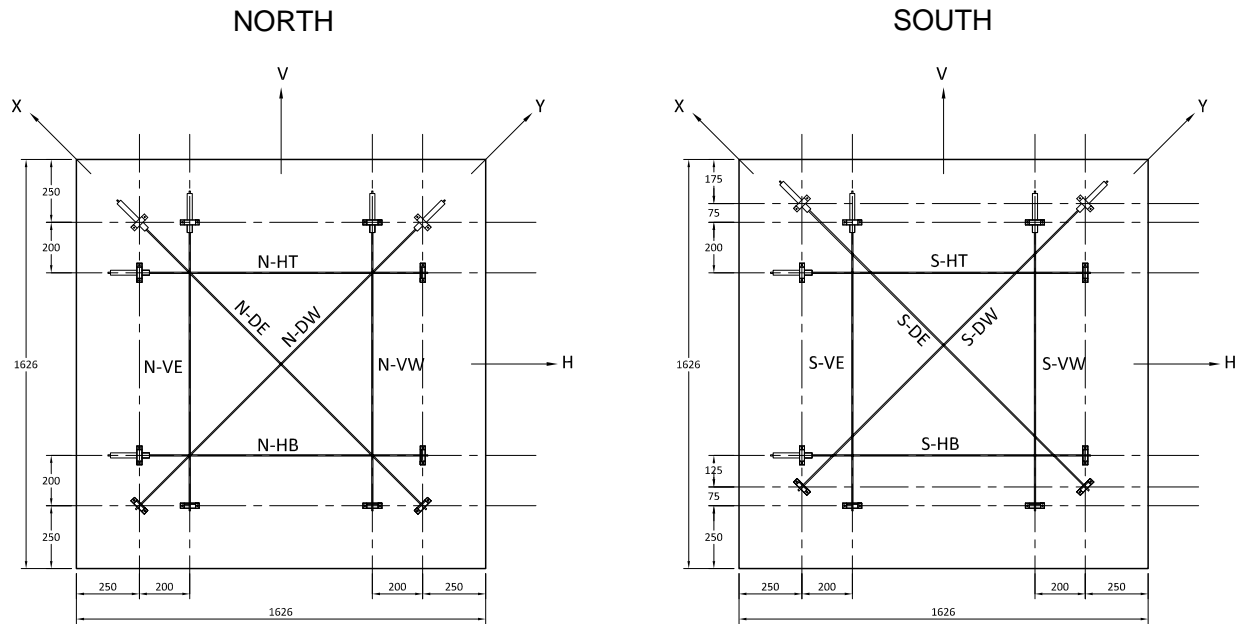


Figure 3.19: *In-Plane LVDT Locations (Viewed from North)*

3.4.3 Three-Dimensional Coordinate Measurement System

Surface displacements and in-plane strains on the South face were measured using a three-dimensional position tracking system, which consisted of a camera coupled with infrared light emitting diode (LED) targets. The positions of the LEDs were recorded throughout the test using the Metris software sampling the targets at 10 Hz, which was later synchronized with the data stream from the AeroProTM Data Acquisition System (DAQ).

In both tests, a 6 x 6 rotated square grid of LEDs (total of 36) was placed so as to subdivide the test region into 25 equal sized elements (200 mm x 200 mm). Figure 3.20 shows the placement and numbering of the LED targets and the resulting elements (red text) as seen from the South. The LED displacement data is useful since it allows both a qualitative look at the three-dimensional displaced shape of the shell, and detailed in-plane strain measurements over the test region. The LVDTs are providing the same type of in-plane data as the LEDs, but are doing so over the whole surface of the shell and cannot therefore represent localized behaviour. Meanwhile, each square LED element can act as its own independent four-strain measurement system - the best fit Mohr's circle of strain can be calculated for each of the 25 LED elements, allowing a look at the South face in-plane strain on a finer spatial scale.

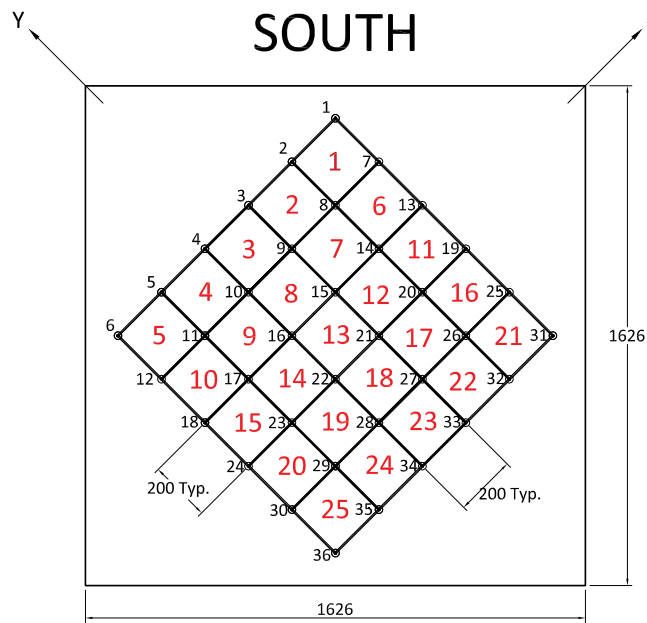


Figure 3.20: *In-Plane LED Locations (Viewed from South)*

3.4.4 Linear Potentiometers (LPs)

A total of 15 LPs were used to determine the out-of-plane strains over the full thickness of the shell. Hollow PVC pipes, which are visible during construction (Figure 3.4b & 3.27), were tied to the reinforcement cage and cast into the concrete at the specified locations. These embedded tubes provided a clear path through the shell, allowing the LPs to measure the relative strain between the North and South face.

The LPs were placed inside the test region, organized in sets of three along the orthogonal reinforcement directions. Three LP triplets (total of nine) were placed in the Y-direction, and two LP triplets (total of six) were placed in the X-Direction. In each set, one LP was placed directly through the thickness (Z-direction), while the remaining two were inclined at roughly $\pm 45^\circ$ to either the XZ or YZ planes as seen in Figure 3.21. Three independent strain readings at known directions provide enough information to define the complete Mohr's circle of strain over this area.

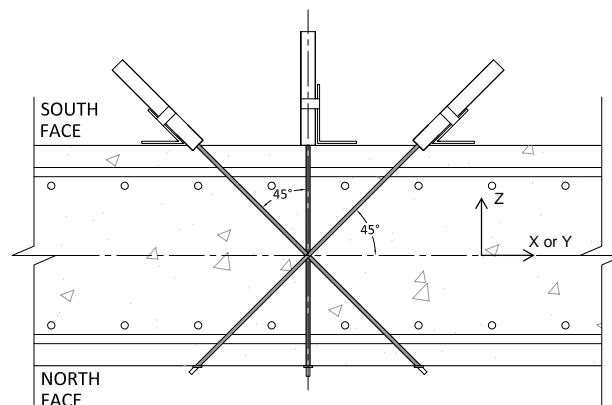
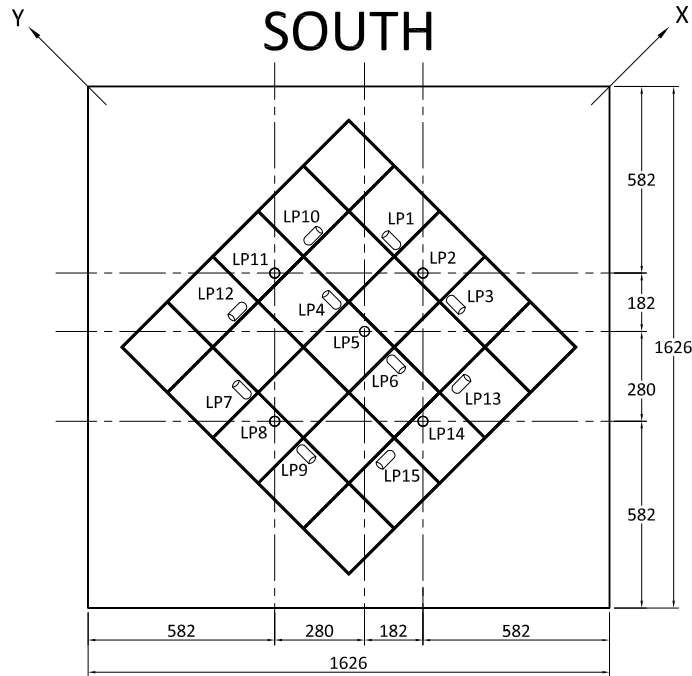


Figure 3.21: *LP Through-Thickness Placement*

Figure 3.22 is a schematic of the LP locations on the South face of the shell, and Table 3.6 summarizes information about each of the five LP triplets. The central Y-direction triplet is slightly shifted to avoid interfering with the three-dimensional coordinate measurement system.



Name	Plane	LP #'s
LP Y1	YZ	1,2,3
LP Y2	YZ	4,5,6
LP Y3	YZ	7,8,9
LP X1	XZ	10,11,12
LP X2	XZ	13,14,15

Figure 3.22 & Table 3.6: Out-of-Plane LP Locations (Viewed from South)

Figure 3.23 shows an example of what the LPs look like when installed on specimen ES1, the individual numbers have been added for clarity. When comparing the North and South face, note that the diagonal LPs change relative placement as they pass through the shell.

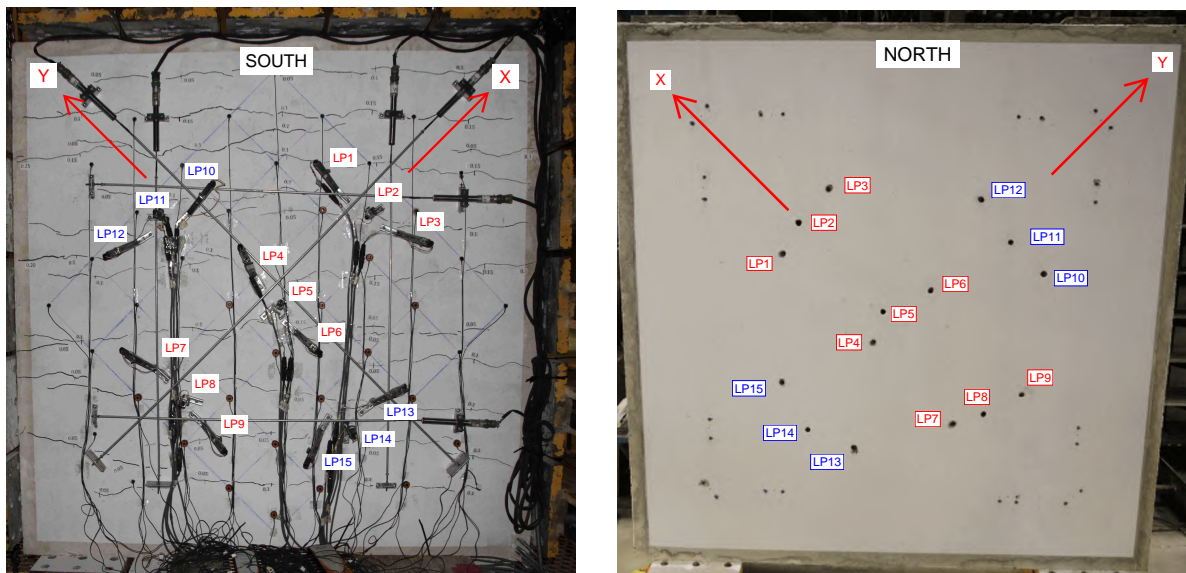


Figure 3.23: LP Placement on Specimen ES1

3.4.5 Embedded Concrete Strain Gauges (EGs)

A total of four EGs (PML with 60 mm gauge length) were used in each specimen to complement the out-of-plane measurements from the LPs. The EGs work on the same principal as the LP triplets, except in their case the three separate gauges are pre-arranged and fixed into a 45° rosette as shown in Figure 3.24.

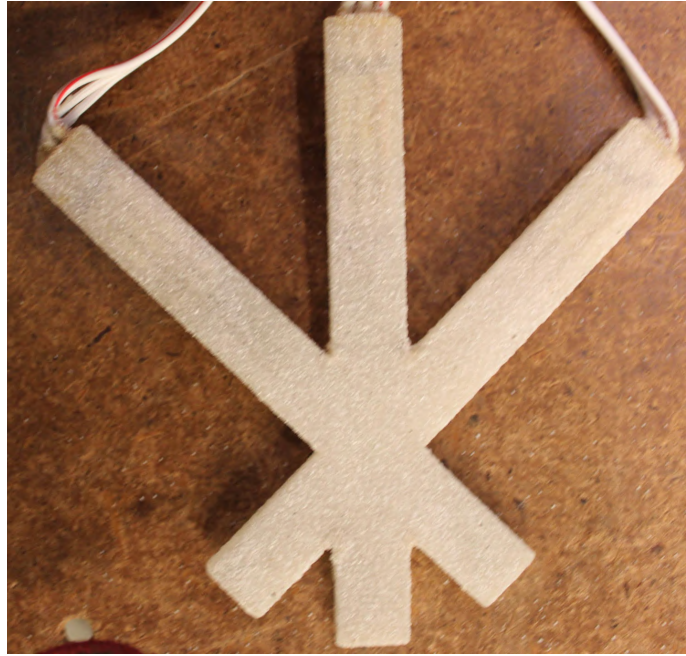


Figure 3.24: *Embedded Strain Gauge Rosette*

The main difference between the EGs and LPs, is that the EGs are fully encased in concrete and only define the Mohr's circle of strain at a localized internal point as show in Figure 3.25, while the LPs define the Mohr's circle of strain over the whole thickness of the shell. The likelihood of an internal local concrete crack occurring right across one of the individual gauges is high; such an occurrence would either cause the gauge to fail or skew the resulting Mohr's circle in an unrealistic way, both options effectively rendering the EG data useless. Hence relying on the EGs for more than simple verification is not recommended.

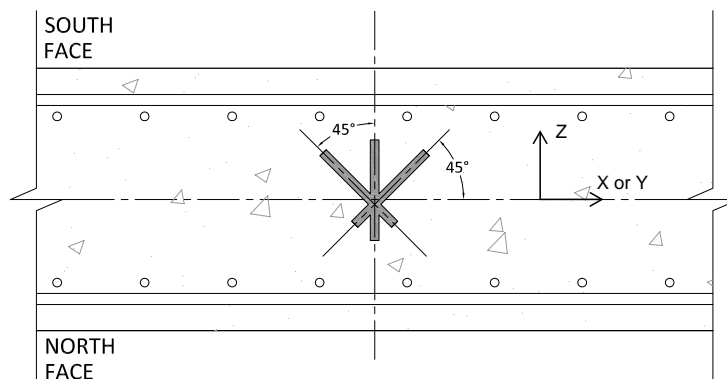


Figure 3.25: *EG Through-Thickness Placement*

Figure 3.26 is a schematic of the four EG locations inside the test region. Two of the EGs are oriented in the XZ plane, and the remaining two are oriented in the YZ plane. The naming convention simply indicates in which plane the EG is placed.

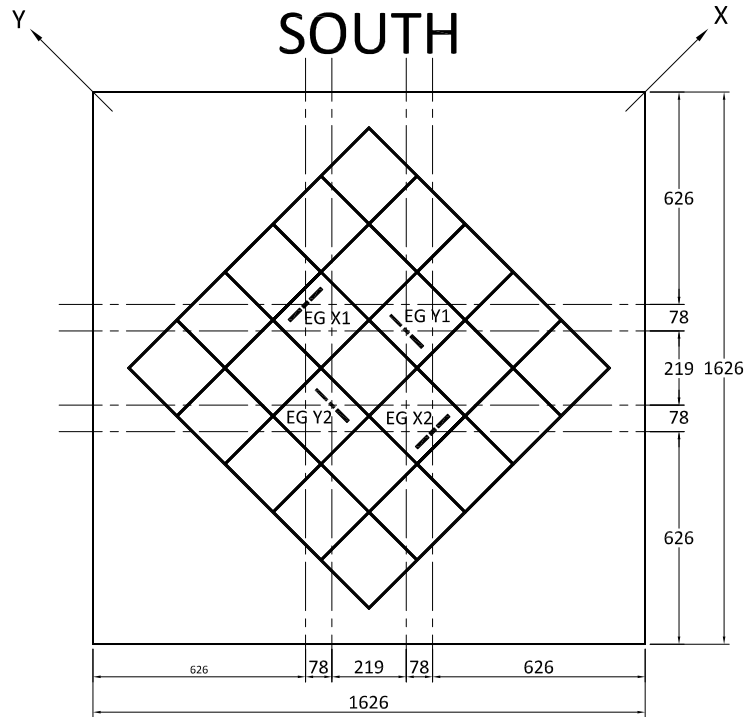


Figure 3.26: *Out-of-Plane EG Locations (Viewed from South)*

The EGs are placed as close as possible to the center of the shell between the North and South faces, and in the direction of the longitudinal reinforcement. Figure 3.27 shows a shell specimen cage before casting, with the EGs located just below the level of the top reinforcement. The hollow PVC ducts, which are necessary for the installation of the LPs, can be seen extending through the thickness of the shell.



Figure 3.27: *Out-of-Plane Instrumentation in Reinforcement Cage*

3.4.6 Reinforcement Strain Gauges (SGs)

To measure reinforcement strains during the test, each specimen had 20 foil SGs (FLA with 5 mm gauge length) placed on several longitudinal bars in the test region. These gauges were equally divided between the North and South cages: 6 in the Y-direction, and 4 in the X-direction per cage. Figure 3.28 is a schematic of the SG locations on the South reinforcement cage, and the North face cage is identically instrumented. The naming convention used is as follows: 1st letter = face, 2nd letter = direction, 3rd letter = relative location.

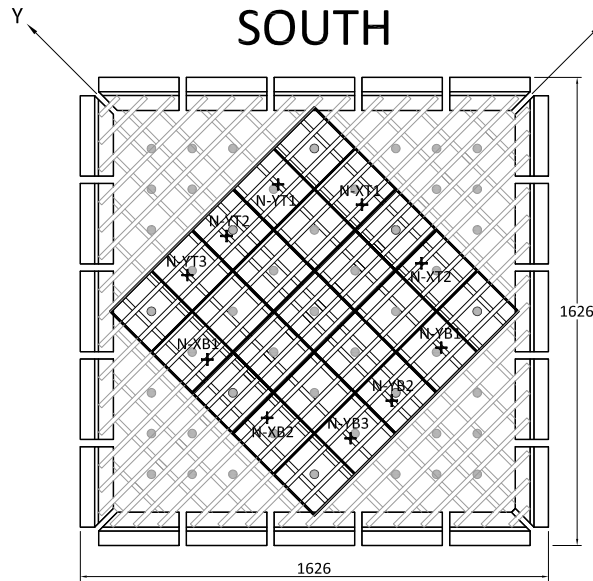


Figure 3.28: Longitudinal Bar SG Locations (Viewed from South)

Specimen ES2 had an additional 8 SGs, each placed in the center of an out-of-plane T-head reinforcement bar located in the test region. Figure 3.29 shows which T-head bars were instrumented.

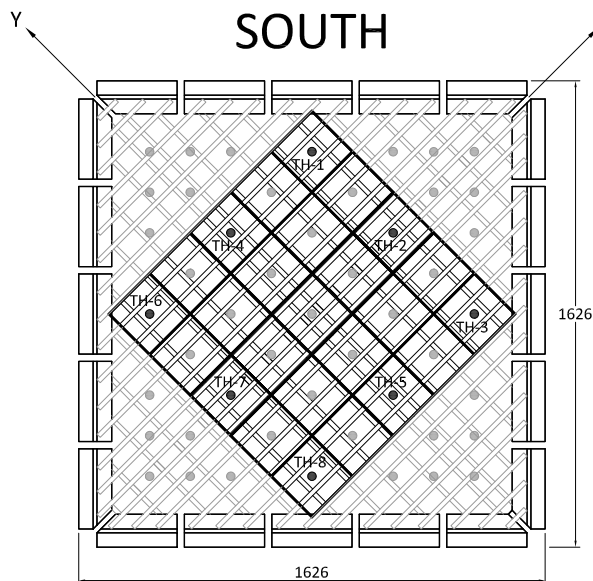


Figure 3.29: T-Head Bar SG Locations in ES2 (Viewed from South)

Chapter 4

Experimental Results

The following chapter will present the test data from all the instrumentation (Load Cell, LVDT, LED, LP, EG, and SG) placed on both torsion specimens. No discussion or comparison of the results is made, each type of instrumentation and its respective data are presented separately. A typical section starts with an explanation of how the readings from a certain type of instrumentation are processed, followed by a table summarizing the data, and concluding with plots of the processed data. Note that to plot the post-peak region of these tests the x-axis scale was often increased by an order of magnitude. Therefore, to maintain the readability of the plots across the whole test, the same data is always presented as a separate 'full' and 'pre-peak' plot.

For consistency, data gathered from the different instruments will be presented at the same points (load stages) in each test. These load stages correspond to applied external torsions shown in Table 4.1. All the reduced data from both experiments can be found in Appendix B.

Table 4.1: Applied Torsion at Load Stages

ES1		ES2	
$[\frac{kN \cdot m}{m}]$		$[\frac{kN \cdot m}{m}]$	
M_{xy}		M_{xy}	
LS 1	86.8	LS 1	64.8
LS 2	168.8	LS 2	110.5
Peak	187.2	LS 3	173.4
LS 3	182.9	LS 4	214.7
LS 4	170.4	Peak	250.5
LS 5	147.9	LS 5	219.6
LS 6	101.8	LS 6	138.9

4.1 Actuator Load Cell Measurements

Table 4.2 summarizes the actuator forces, and the resulting moments, applied on each face of the shell and recored by the built-in load cells during the two tests. The values presented in the force columns represent the sum of all five actuators in each bank on the edge and face indicated. The moments are found by multiplying the force couple by the lever arm distance between the actuator banks (304.8 mm) and dividing this by the nominal side dimension of the shell (1524 mm). Recall that the magnitude of the moments along the Horizontal (top and bottom) and Vertical (east and west) axes are intended to be equal, although due to 2nd order effects in the shell there are minor discrepancies between the magnitude of forces applied between certain North and South face actuators. Yet this error is negligible, and the applied torsional moment at each load stage is simply taken as the average of the Horizontal and Vertical moments.

Table 4.2: Applied Forces and Resulting Moments

	$[kN]$ <i>Top</i>		$[kN]$ <i>Bottom</i>		$[kN]$ <i>East</i>		$[kN]$ <i>West</i>		$[\frac{kN \cdot m}{m}]$ M_{xy}	
	<i>North</i>	<i>South</i>	<i>North</i>	<i>South</i>	<i>North</i>	<i>South</i>	<i>North</i>	<i>South</i>	$ M_h $	$ M_v $
<i>ES1</i>										
<i>LS1</i>	-416.3	447.7	-458.5	420.5	438.1	-397.4	438.1	-438.1	87.6	86.0
<i>LS2</i>	-829.2	844.5	-871.0	833.4	851.5	-783.2	851.3	-851.5	169.8	167.8
<i>Peak</i>	-921.9	932.6	-963.9	926.1	944.3	-871.3	944.3	-944.2	188.2	186.2
<i>LS3</i>	-900.2	911.8	-942.2	904.4	922.6	-850.9	922.6	-922.6	183.9	181.9
<i>LS4</i>	-837.6	851.0	-879.3	842.0	860.0	-790.2	859.8	-860.1	171.4	169.4
<i>LS5</i>	-725.0	740.5	-767.0	729.2	747.1	-683.6	747.0	-747.1	148.9	147.0
<i>LS6</i>	-492.8	512.9	-534.8	497.1	515.0	-467.3	514.9	-514.9	102.4	101.1
<i>ES2</i>										
<i>LS1</i>	-305.2	342.5	-347.3	309.4	326.8	-294.6	326.8	-326.8	65.6	64.1
<i>LS2</i>	-535.8	565.8	-577.9	539.9	557.5	-504.0	557.6	-557.5	111.6	109.4
<i>LS3</i>	-853.0	869.9	-895.0	857.1	874.9	-800.1	874.9	-875.1	174.7	172.2
<i>LS4</i>	-1060.0	1072.1	-1101.8	1064.3	1082.5	-997.0	1082.4	-1082.4	216.0	213.3
<i>Peak</i>	-1240.8	1243.6	-1282.8	1245.0	1263.1	-1167.2	1263.1	-1263.1	251.9	249.1
<i>LS5</i>	-1085.6	1091.5	-1127.7	1089.7	1107.8	-1019.3	1107.9	-1107.8	220.9	218.3
<i>LS6</i>	-681.1	698.5	-722.9	685.5	703.0	-629.9	702.8	-703.1	140.1	137.7

4.2 In-Plane LVDT Measurements

The LVDTs were used to measure the average surface strains in four directions (H,V,X,Y) as defined on both the North and South face (Figure 3.13). The individual linear strains were found by dividing the recorded displacements over their respective gauge lengths, which were measured as the distance between the LVDT anchor points. A degree of redundancy was provided as two LVDTs were placed in both the H and V directions - their readings were averaged to produce a single strain measurement in the given direction.

Although LVDTs are precise devices (noise level of $\pm 5\mu m$), they can only measure the strains between discrete points over a large surface area. Hence the measured strains are considered to be averaged over the whole specimen, which provides no information about local nonlinearity in the test region. This can pose a problem in experiments where a non-uniform in-plane strain field is expected (e.g. applied out-of-plane forces, double curvature tests). But since pure torsion in a shell can be reduced to equal and opposite pure in-plane shears on opposing faces, the strain field across the faces was expected to be relatively uniform - the strains should be similar regardless of what point in the test region one observed. Therefore, it was concluded that the average strain data gathered by the LVDTs could also serve as a reasonable approximation of what was occurring in the test region of the shell.

The twist strain (ϕ_{xy}) was calculated using data from both the North and South face sets of LVDTs; together with the applied torsional moment (M_{xy}) this established the important torque-twist relationship for each specimen. Assuming small angles, the twist strain (in units of rad/length) was calculated as the change in the in-plane shear strains (γ_{xy}) over the thickness of the shell. The surface shear strains were approximately equal in magnitude, but "+" on the North and "-" on the South face, which corresponded to vertical and horizontal cracks respectively. These shear strains were assumed to vary linearly through the thickness of the shell, with the twist strain represented as the angle of the resulting strain profile (Figure 4.1).

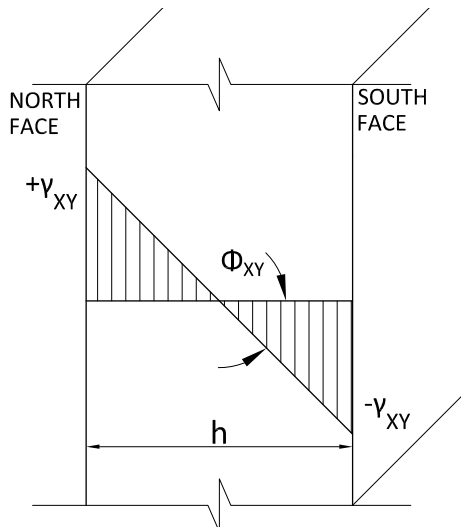


Figure 4.1: Calculating Experimental Twist Strain

It is not possible to explicitly measure shear strains in the reinforcement XY-plane, since shear deformations are an angular quantity and LVDTs can only measure linear quantities. Yet by determining two independent and orthogonal linear strains at 45° to the reinforcement (i.e. strains in the HV-plane) the magnitude of the XY-plane shear strain can be calculated as their difference. But with only two strains just the center of the Mohr's circle can be defined, not its exact size or orientation. Figure 4.2 shows how two drastically different but equally valid circles could be drawn from the same two measurements, where important information such as the principal angle and strains can not be determined.

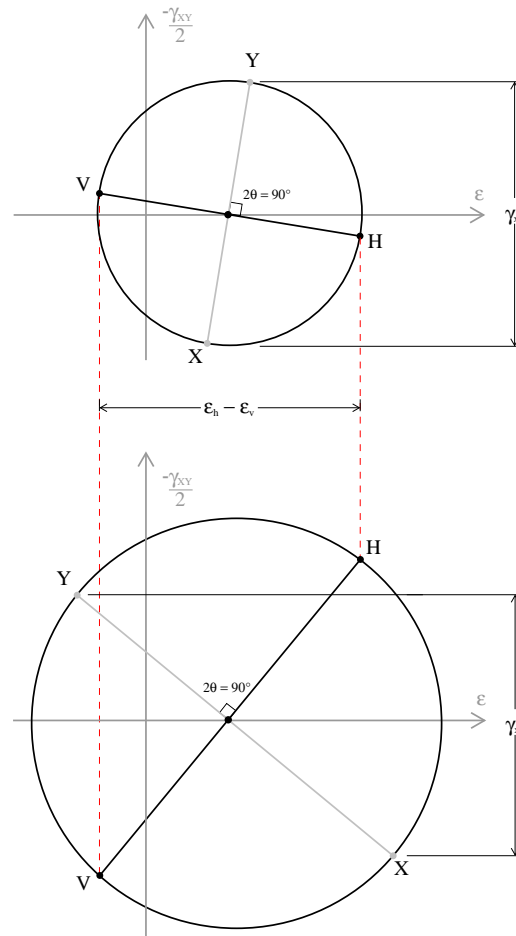


Figure 4.2: *Calculating Shear Strain from Two Linear Strains*

To fully define a Mohr's circle of strain (i.e. allowing one to calculate the full strain state in any two-dimensional plane) three independent axial strain measurements at known angles are necessary. This is achieved by using an additional LVDT measurement, oriented in either the X or Y direction in this case, to explicitly calculate the size and position of the Mohr's circle. This means that one of the directions in our four LVDT set-up is not necessary (the Mohr's circle is considered over-defined) and is typically discarded to reduce it to a three strain system that can be explicitly calculated (Figure 4.3a). But rather than waste useful data, the Mohr's circle calculations in this thesis use a procedure that has been developed [39] to determine a Mohr's circle of best fit using all four LVDTs while minimizing the overall error (Figure 4.3b).

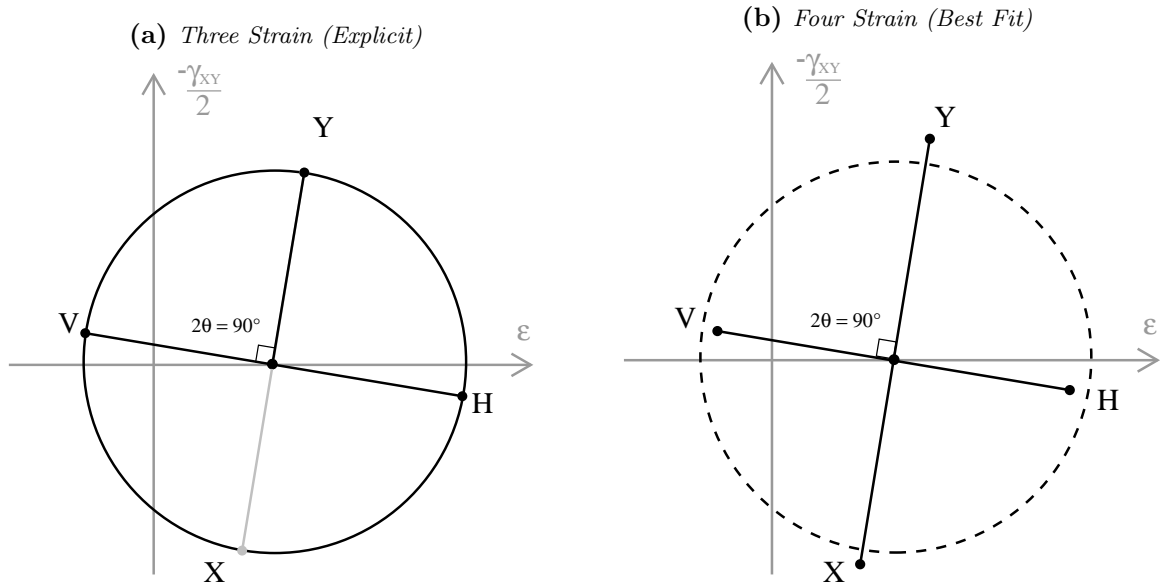


Figure 4.3: *Fully Defined Mohr's Circles*

Table 4.3 summarizes the calculated LVDT Mohr's circle data at the individual load stages for both tests. The North and South face sets are shown separately, but for consistency the perspective is always taken from the North face, which results in different signs for the shear strain. The same information is also presented in the subsequent graphs, which better show the actual progression of each test. Both faces are loaded with the same magnitude of pure in-plane shear as a result of the applied torsional moment, therefore similar behaviour is expected on either face. Both tests were run into the post-peak region, and while this was done in a controlled manner significant cover spalling and cracking makes these LVDT data less reliable. It is important to remember that the specimens are cast with the South side facing up. This results in more bleed water and hence a lower concrete modulus on the South face, which explains the higher strains measured.

Table 4.3: LVDT Data at Load Stages

	$\left[\frac{kN \cdot m}{m}\right]$	$\left[\frac{mrad}{m}\right]$	$[\times 10^{-3}]$		$[\times 10^{-3}]$		$[\times 10^{-3}]$		$[\circ]$		$[\times 10^{-3}]$		$[\times 10^{-3}]$	
	M_{xy}	ϕ_{xy}	γ_{xy}		ϵ_x		ϵ_y		θ_{xy}^*		ϵ_1		ϵ_2	
			North	South	North	South	North	South	North	South	North	South	North	South
ES1														
<i>LS1</i>	86.8	15.5	1.94	-2.47	0.22	0.42	0.17	0.48	-0.7	89.3	1.16	1.68	-0.77	-0.79
<i>LS2</i>	168.8	46.3	6.18	-7.03	0.73	0.97	1.42	1.21	3.2	89.0	4.18	4.60	-2.03	-2.43
<i>Peak</i>	187.2	58.7	7.91	-8.83	0.84	1.07	1.75	1.40	3.3	89.0	5.28	5.65	-2.68	-3.18
<i>LS3</i>	182.9	60.4	8.11	-9.10	0.80	1.09	1.78	1.43	3.4	88.9	5.38	5.82	-2.80	-3.29
<i>LS4</i>	170.4	80.8	10.99	-12.05	1.99	1.36	1.90	1.89	-0.3	88.7	7.44	7.65	-3.55	-4.40
<i>LS5</i>	147.9	96.6	13.56	-13.99	3.76	1.50	1.70	2.41	-4.3	-88.2	9.59	8.96	-4.12	-5.05
<i>LS6</i>	101.8	139.7	19.74	-20.10	6.74	0.45	3.16	8.48	-5.1	79.1	14.98	15.28	-5.09	-6.35
ES2														
<i>LS1</i>	64.8	8.2	0.99	-1.34	0.00	0.26	0.12	0.27	3.4	90.0	0.56	0.93	-0.44	-0.40
<i>LS2</i>	110.5	21.4	2.73	-3.38	0.23	0.68	0.59	0.70	3.7	89.8	1.78	2.38	-0.97	-1.00
<i>LS3</i>	173.4	39.0	5.14	-5.97	0.53	1.18	1.19	1.19	3.6	89.9	3.45	4.17	-1.74	-1.80
<i>LS4</i>	214.7	56.7	7.58	-8.58	0.79	1.56	1.63	1.69	3.1	89.6	5.02	5.91	-2.60	-2.66
<i>Peak</i>	250.5	89.4	12.07	-13.40	1.07	2.07	2.17	2.38	2.6	89.3	7.68	8.93	-4.45	-4.48
<i>LS5</i>	219.6	111.0	14.59	-17.02	1.17	2.18	2.39	2.60	2.4	89.3	9.10	-6.12	-5.54	-6.12
<i>LS6</i>	138.9	223.0	32.50	-31.10	1.21	2.05	2.76	6.53	1.4	85.9	18.24	20.00	-14.27	-11.43

* Measured from Horizontal Axis (CCW = +)

4.2.1 Specimen ES1

Torque-Twist Relationship

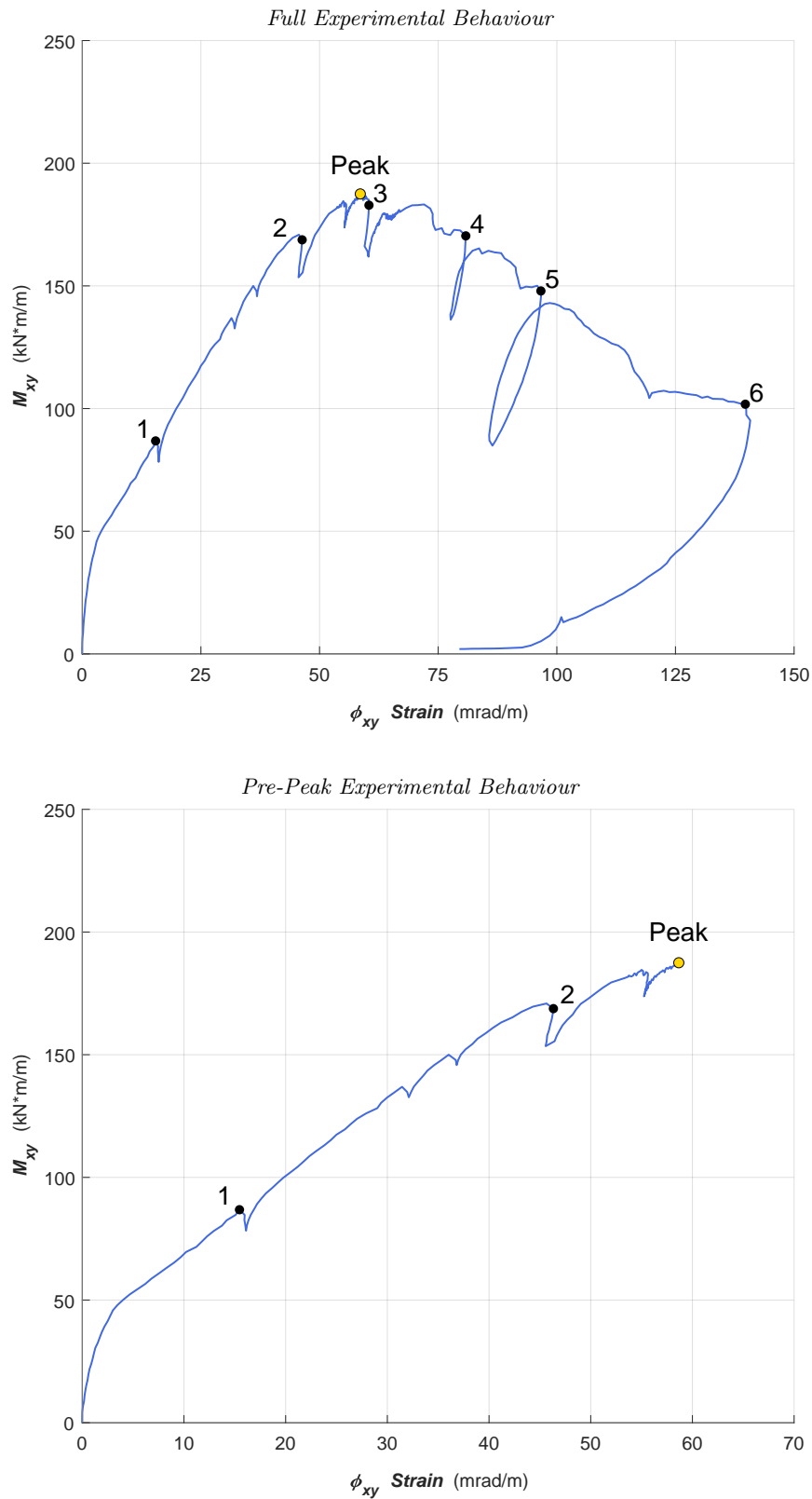


Figure 4.4: ES1 Applied Torsion vs. Twist Strain

In-Plane (XY) Strains

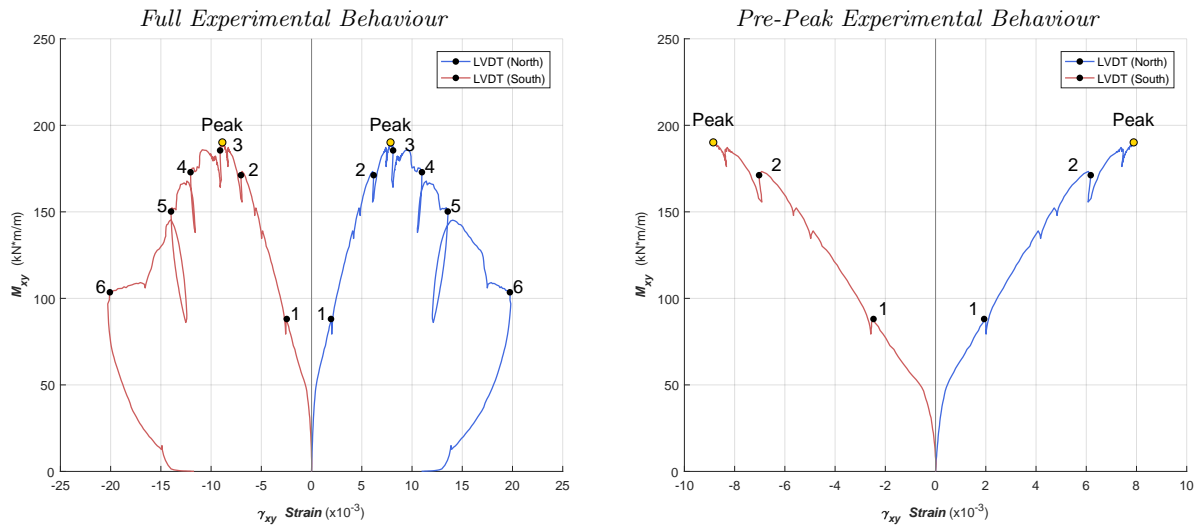


Figure 4.5: *ES1 Applied Torsion vs. In-Plane (XY) Shear Strain*

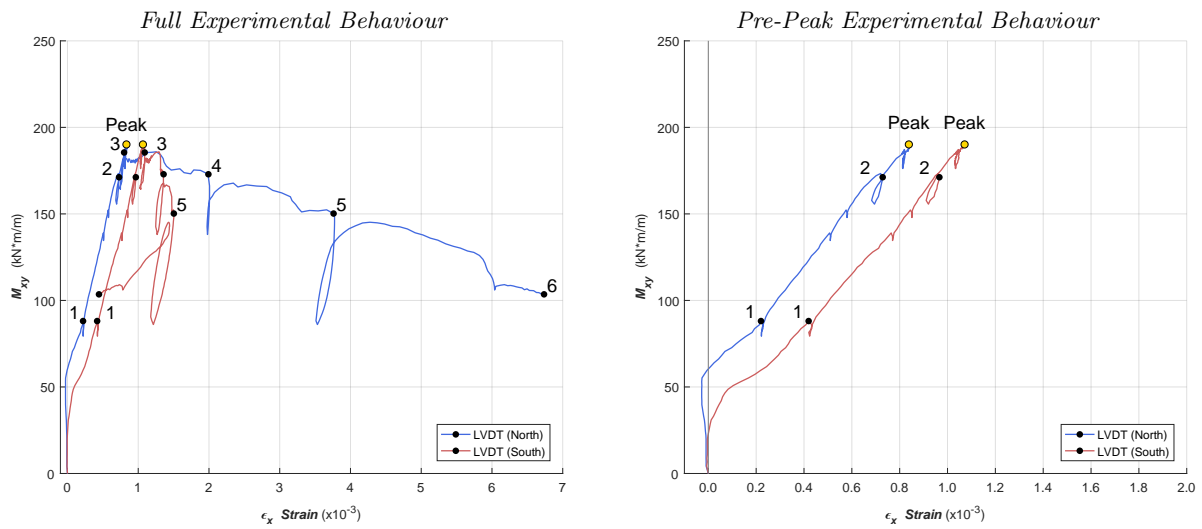


Figure 4.6: *ES1 Applied Torsion vs. X-Direction Strain*

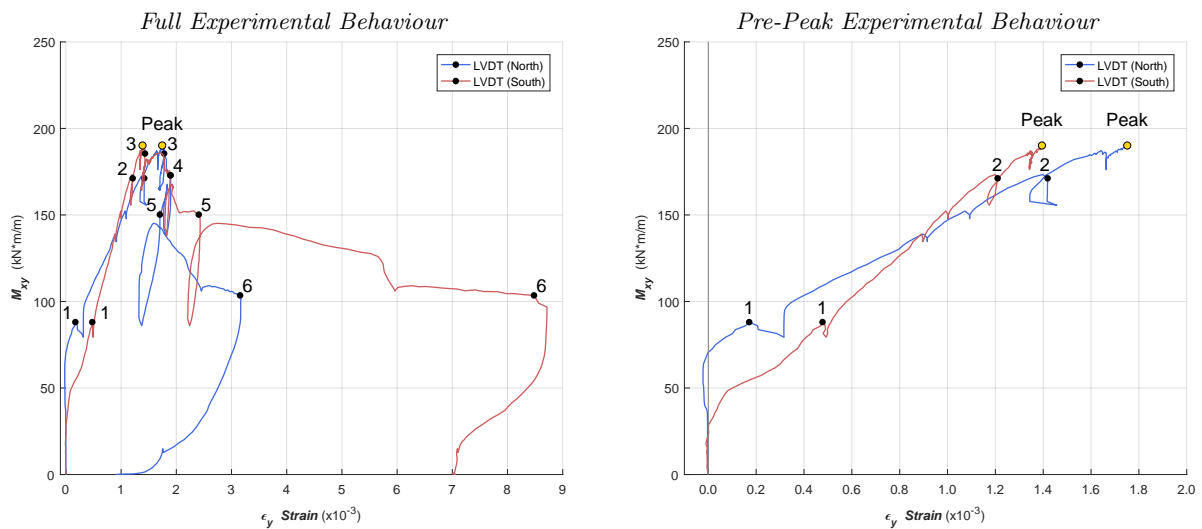


Figure 4.7: *ES1 Applied Torsion vs. Y-Direction Strain*

In-Plane (XY) Principal Strains

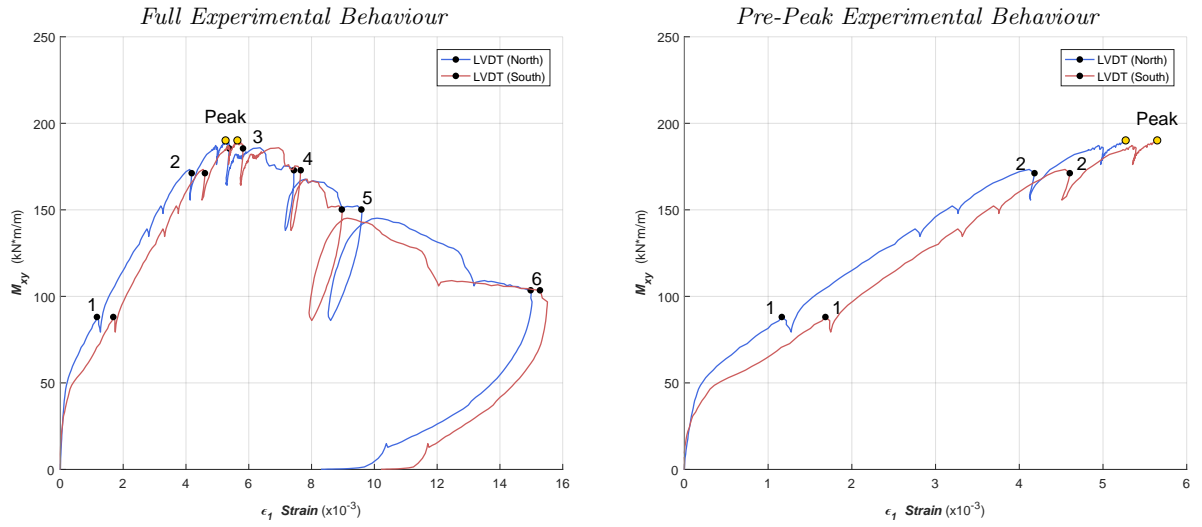


Figure 4.8: *ES1 Applied Torsion vs. Principal Tensile Strain*

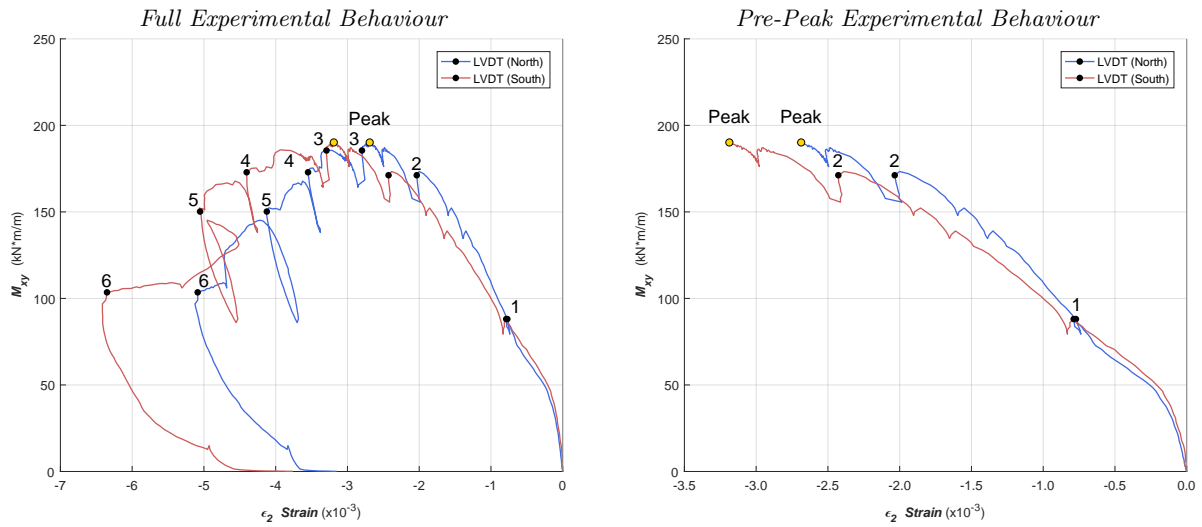


Figure 4.9: *ES1 Applied Torsion vs. Principal Compressive Strain*

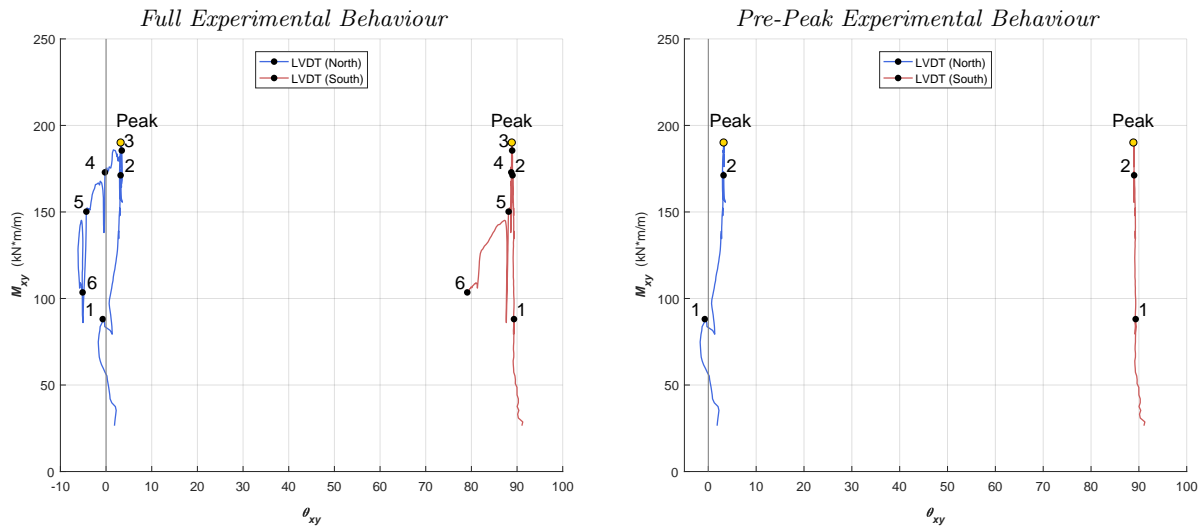


Figure 4.10: *ES1 Applied Torsion vs. Angle of Principal Strain (CCW+)*

4.2.2 Specimen ES2

Torque-Twist Relationship

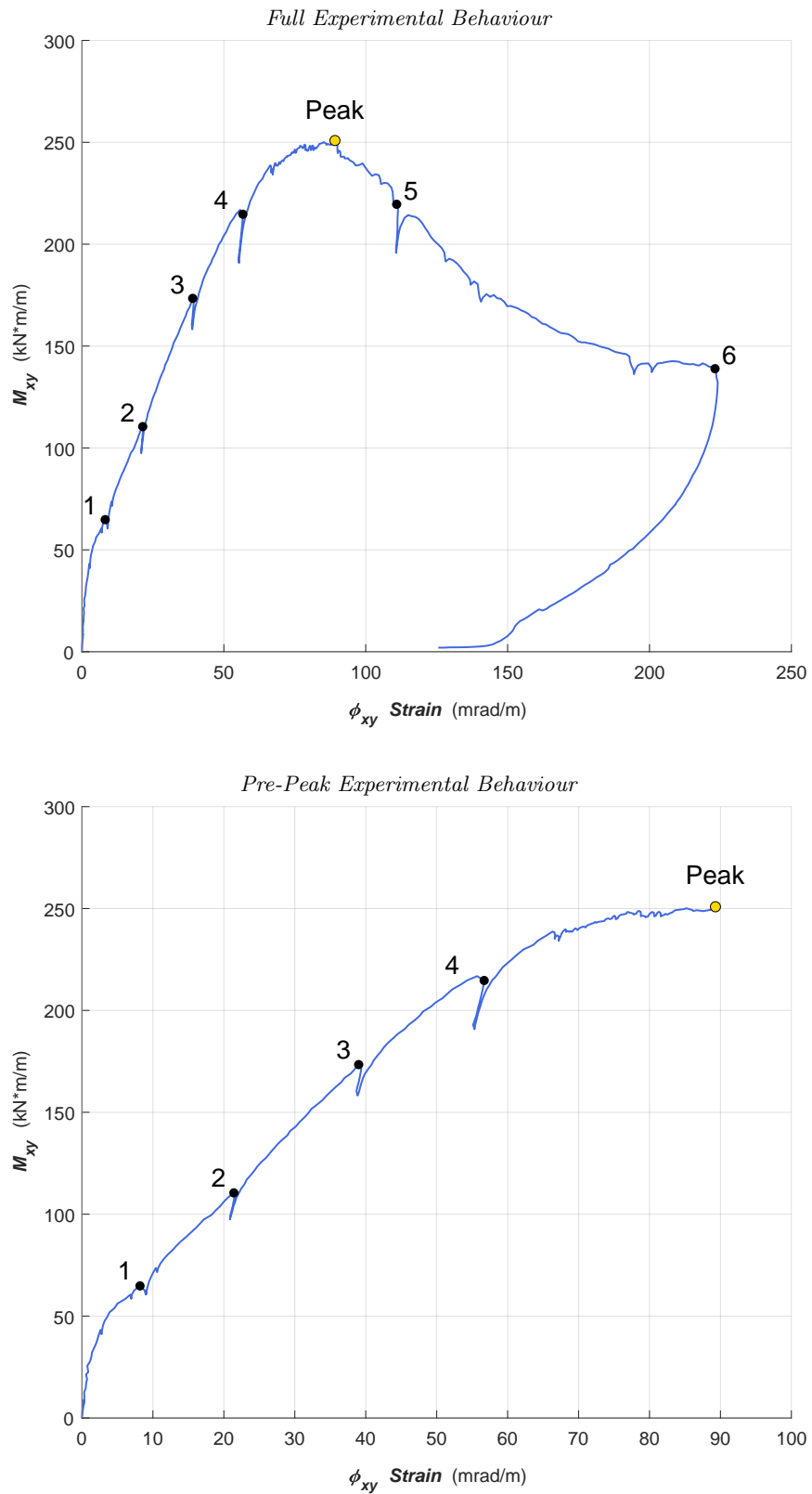


Figure 4.11: ES2 Applied Torsion vs. Twist Strain

In-Plane (XY) Strains

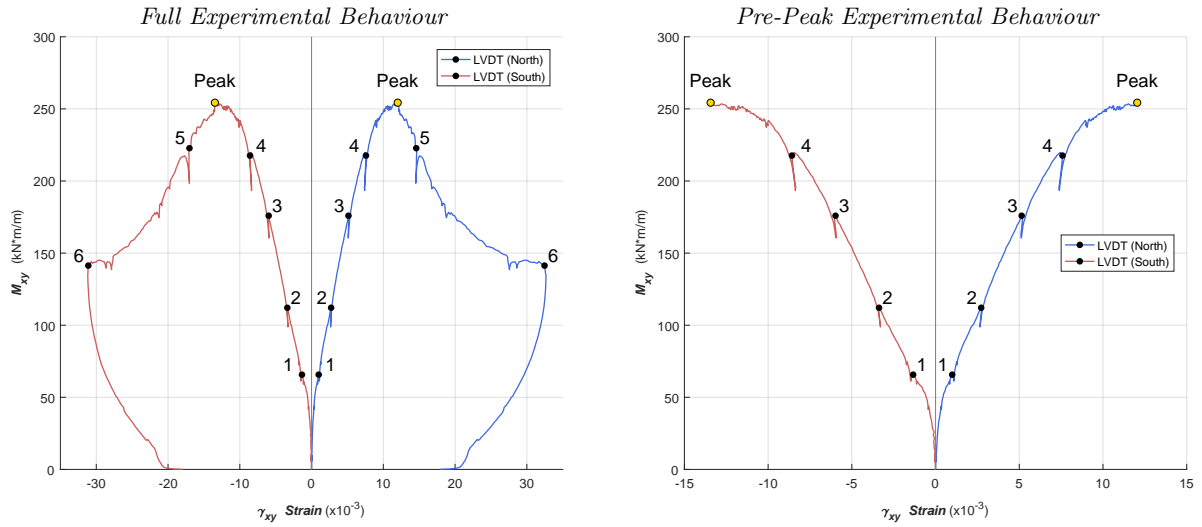


Figure 4.12: ES2 Applied Torsion vs. In-Plane (XY) Shear Strain

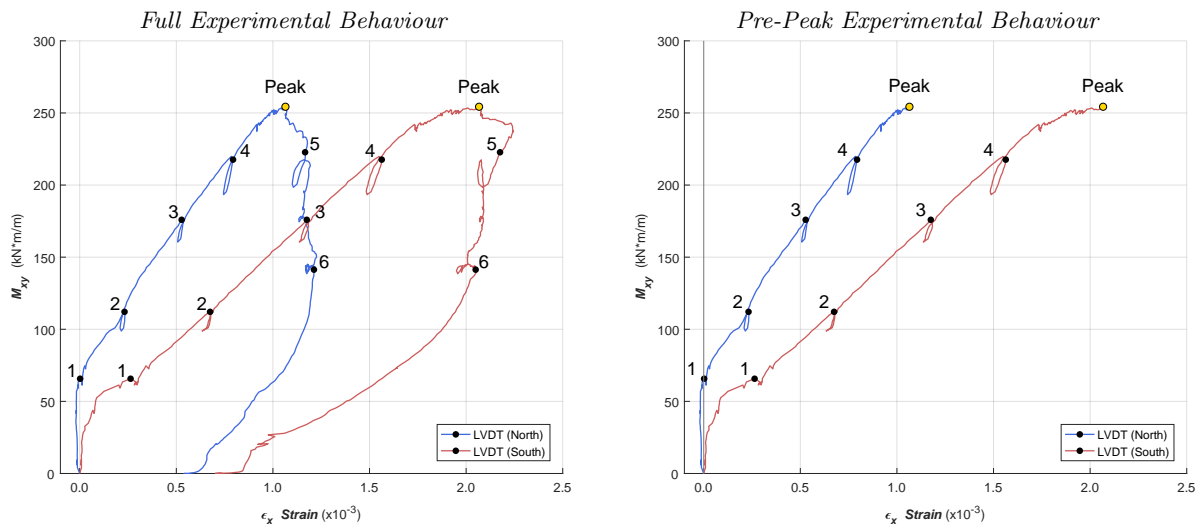


Figure 4.13: ES2 Applied Torsion vs. X-Direction Strain

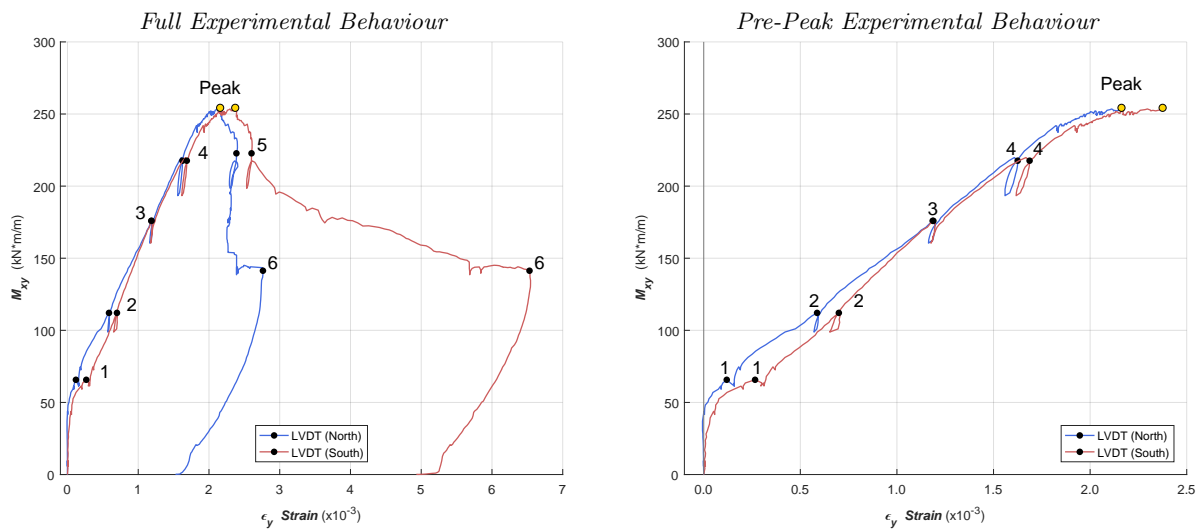


Figure 4.14: ES2 Applied Torsion vs. Y-Direction Strain

In-Plane (XY) Principal Strains

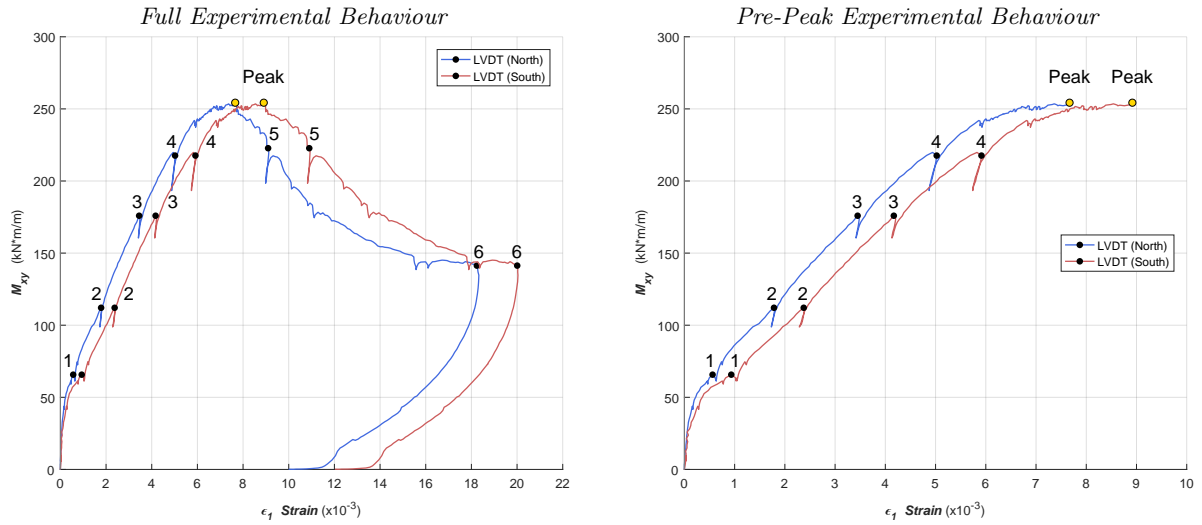


Figure 4.15: ES2 Applied Torsion vs. Principal Tensile Strain

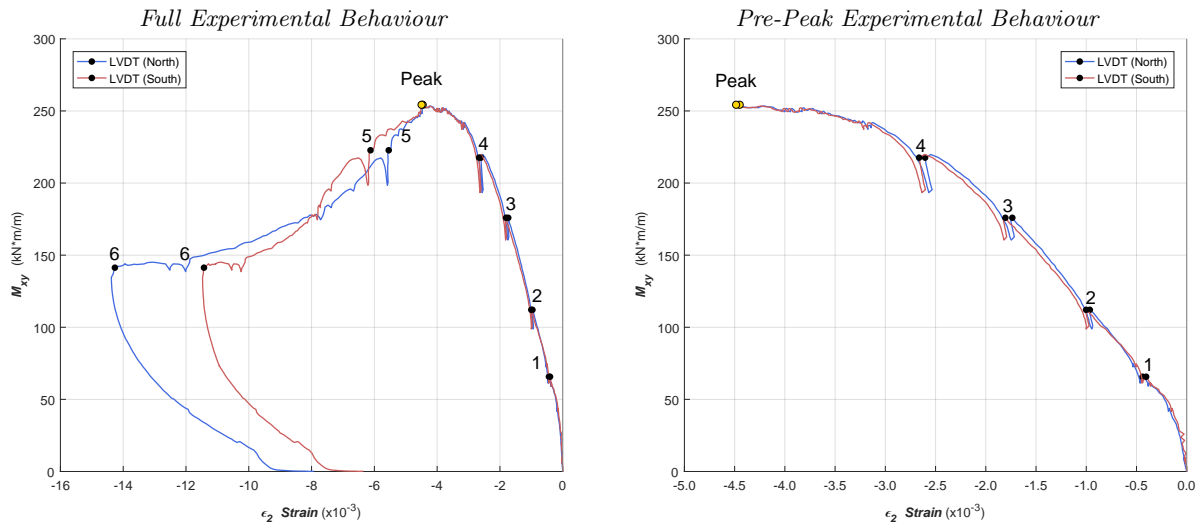


Figure 4.16: ES2 Applied Torsion vs. Principal Compressive Strain

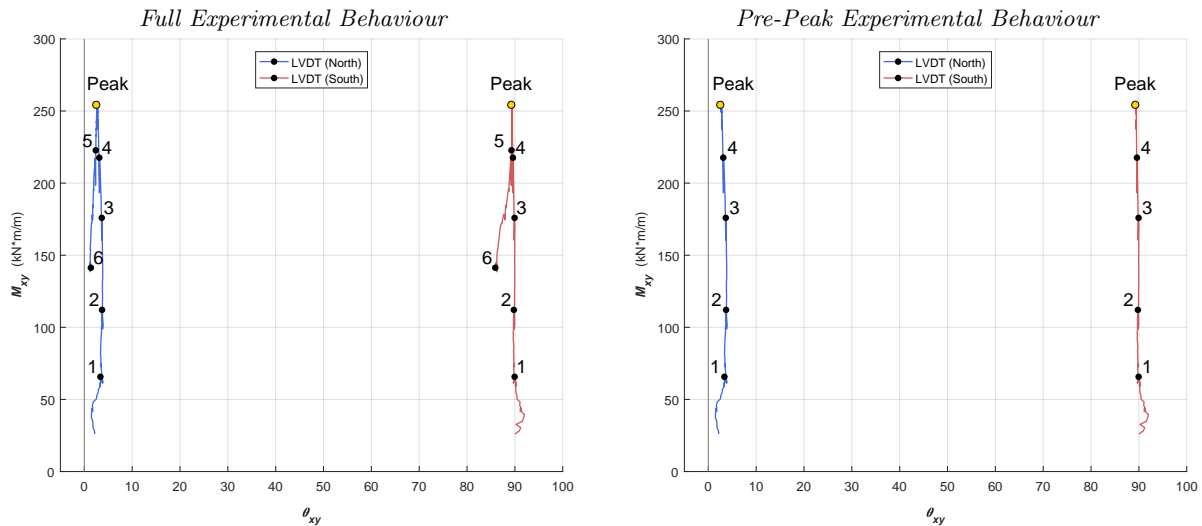


Figure 4.17: ES2 Applied Torsion vs. Angle of Principal Strain (CCW+)

4.3 In-Plane LED Measurements

The LED targets, arranged in a 6 x 6 grid on the South face, provided in-plane strain measurements throughout the tests. The test region was subdivided into 25 equal sized elements, where the deformations in each element were approximately uniform, and could therefore be represented by a Mohr's circle of strain. The same four-strain approach as described in the previous section was used for each of element, with the only difference being that the LED elements were already rotated to the plane of the reinforcement so there were two measurements averaged in both the X and Y directions. Figure 4.18 shows a sample element (#1) and the individual strain measurements used to define the Mohr's circle.

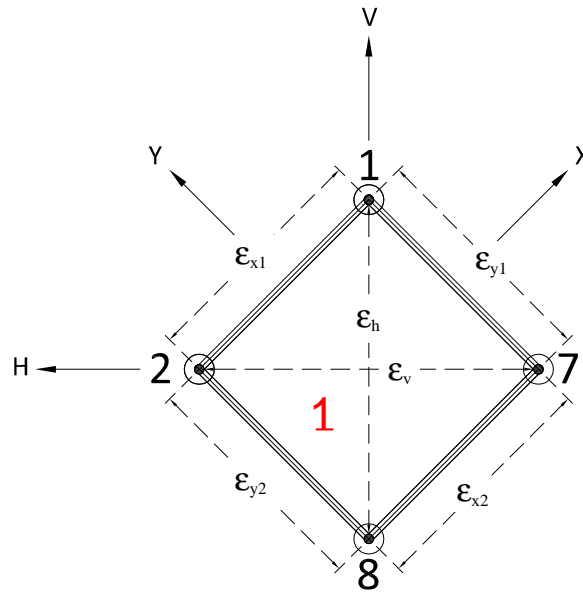


Figure 4.18: LED Element Strains (Viewed from South)

Table 4.4 summarizes the calculated LED Mohr's circle data at the individual load stages for both tests. Rather than list every single element individually, the average of all 25 elements is given, followed by the coefficients of variation for these data. In the post-peak region, localized regions of the shell begin to fail resulting in certain LED elements experiencing large non-uniform jumps in strain. This is reflected in the growing variation values, which imply that the LED average value is a less reliable measure in the post-peak region of the tests. For comparison, the LVDT data from the South face is also shown in this table; the LEDs and LVDTs are both measuring in-plane strains, and their similar measurements are validation for the data collected.

The full data range is also plotted in the subsequent figures, where the red line represents the average value of the individual LED elements shown in grey. A two-dimensional snapshot of the test region is also shown at the peak applied torsion value, showing the individual element readings. For the snapshots at each load stage see Appendix B.2

Table 4.4: LED Data at Load Stages

	$\left[\frac{kN \cdot m}{m}\right]$ M_{xy}	$\left[\frac{mrad}{m}\right]$ ϕ_{xy}	$[\times 10^{-3}]$ γ_{xy}			$[\times 10^{-3}]$ ϵ_x			$[\times 10^{-3}]$ ϵ_y			$[\circ]$ θ_{xy} ¹			$[\times 10^{-3}]$ ϵ_1			$[\times 10^{-3}]$ ϵ_2		
			Avg.	c.o.v.	LVDT ²	Avg.	c.o.v.	LVDT ²	Avg.	c.o.v.	LVDT ²	Avg.	c.o.v.	LVDT ²	Avg.	c.o.v.	LVDT ²	Avg.	c.o.v.	LVDT ²
ES1																				
LS1	86.8	15.5	-2.40	22.0%	-2.47	0.50	69.4%	0.42	0.52	64.7%	0.48	89.7	5.8%	89.3	1.72	28.7%	1.68	-0.71	27.1%	-0.79
LS2	168.8	46.3	-6.44	21.7%	-7.03	1.02	70.9%	0.97	1.12	80.6%	1.21	89.6	4.7%	89.0	4.32	30.4%	4.60	-2.18	20.3%	-2.43
Peak	187.2	58.7	-8.02	19.8%	-8.83	1.15	70.2%	1.07	1.25	83.5%	1.40	89.7	4.2%	89.0	5.24	27.9%	5.65	-2.84	21.1%	-3.18
LS3	182.9	60.4	-8.30	19.6%	-9.10	1.16	72.9%	1.09	1.31	80.6%	1.43	89.5	4.2%	88.9	5.42	27.5%	5.82	-2.94	21.5%	-3.29
LS4	170.4	80.8	-11.21	21.3%	-12.05	1.31	71.6%	1.36	1.63	85.4%	1.89	89.3	3.8%	88.7	7.11	27.3%	7.65	-4.17	25.0%	-4.40
LS5	147.9	96.6	-13.54	23.9%	-13.99	1.35	68.1%	1.50	2.01	95.0%	2.41	89.0	4.4%	-88.2	8.52	28.6%	8.96	-5.15	29.0%	-5.05
LS6	101.8	139.7	-22.27	45.0%	-20.10	-0.52	951.8%	0.45	2.14	241.3%	8.48	86.8	8.0%	79.1	12.35	27.7%	15.28	-10.73	80.1%	-6.35
ES2																				
LS1	64.8	8.2	-1.26	21.6%	-1.34	0.32	57.9%	0.26	0.28	57.9%	0.27	91.1	4.9%	90.0	0.94	28.6%	0.93	-0.34	14.5%	-0.40
LS2	110.5	21.4	-3.16	18.0%	-3.38	0.79	49.6%	0.68	0.68	44.9%	0.70	91.0	4.2%	89.8	2.33	23.6%	2.38	-0.87	10.6%	-1.00
LS3	173.4	39.0	-5.57	16.0%	-5.97	1.28	52.1%	1.18	1.10	47.0%	1.19	90.9	4.2%	89.9	4.00	22.2%	4.17	-1.63	10.0%	-1.80
LS4	214.7	56.7	-7.95	15.0%	-8.58	1.68	56.0%	1.56	1.46	46.0%	1.69	90.8	4.4%	89.6	5.58	20.6%	5.91	-2.44	14.7%	-2.66
Peak	250.5	89.4	-12.35	17.3%	-13.4	2.09	82.7%	2.07	2.03	41.0%	2.38	90.2	5.9%	89.3	8.31	20.3%	8.93	-4.19	24.6%	-4.48
LS5	219.6	111.0	-16.47	22.7%	-17.02	1.88	107.0%	2.18	1.89	93.2%	2.60	90.4	3.9%	89.3	10.17	19.8%	-6.12	-6.40	45.3%	-6.12
LS6	138.9	223.0	-32.47	49.2%	-31.10	0.65	1755.0%	2.05	3.16	174.3%	6.53	89.4	10.0%	85.9	18.91	29.3%	20.00	-15.10	95.0%	-11.43

¹ Measured from Horizontal Axis (CCW = +)² South Face

4.3.1 Specimen ES1

In-Plane Shear Strain

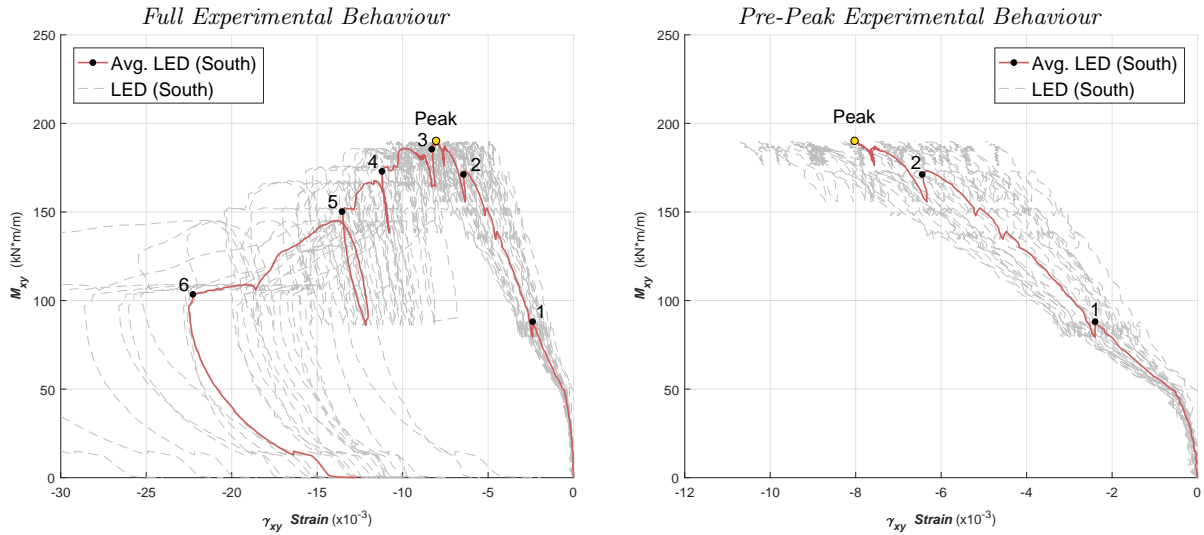


Figure 4.19: ES1 Applied Torsion vs. In-Plane (XY) Shear Strain

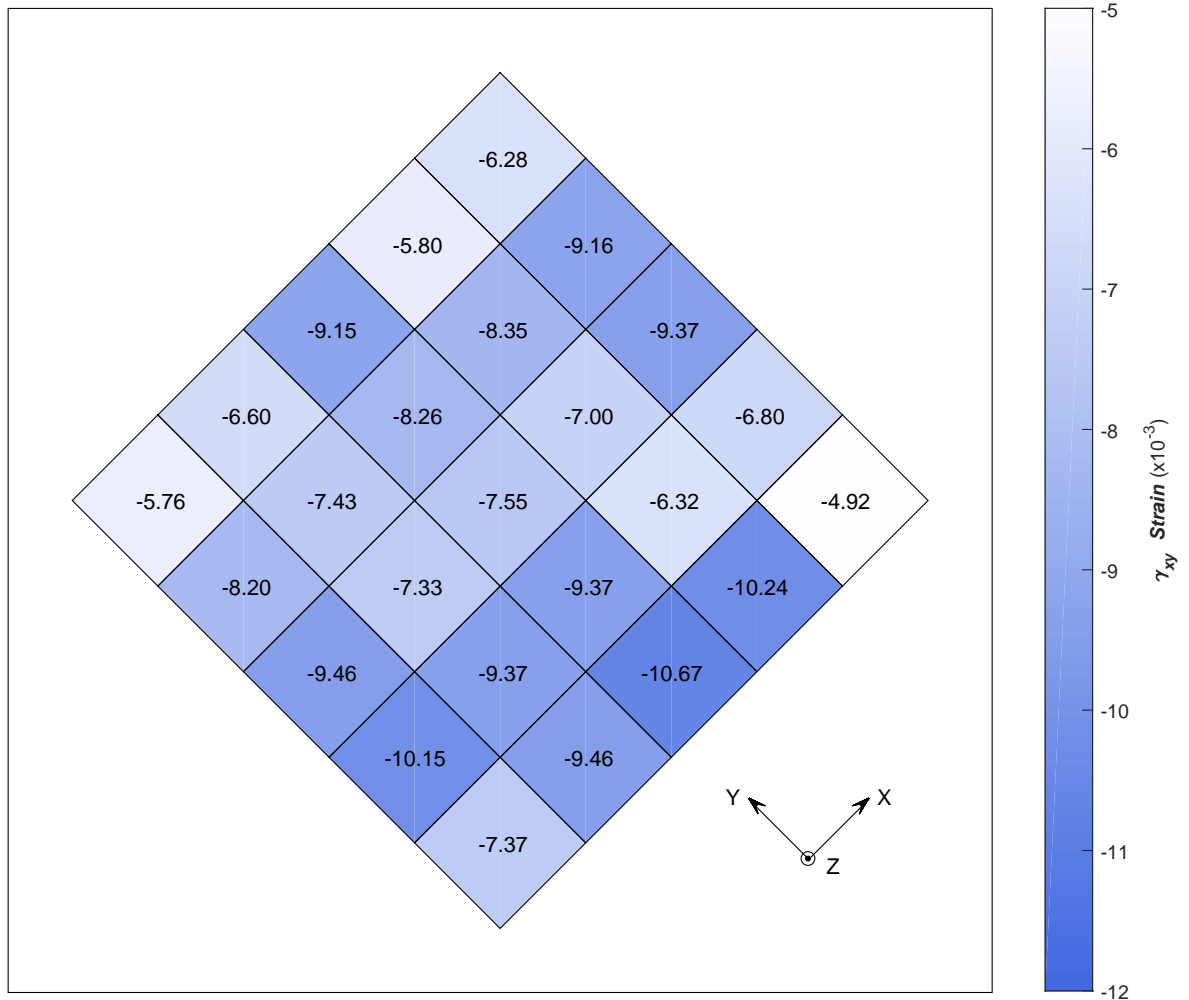


Figure 4.20: ES1 In-Plane (XY) Shear Strain at 'Peak' Torsion

X-Direction Strain

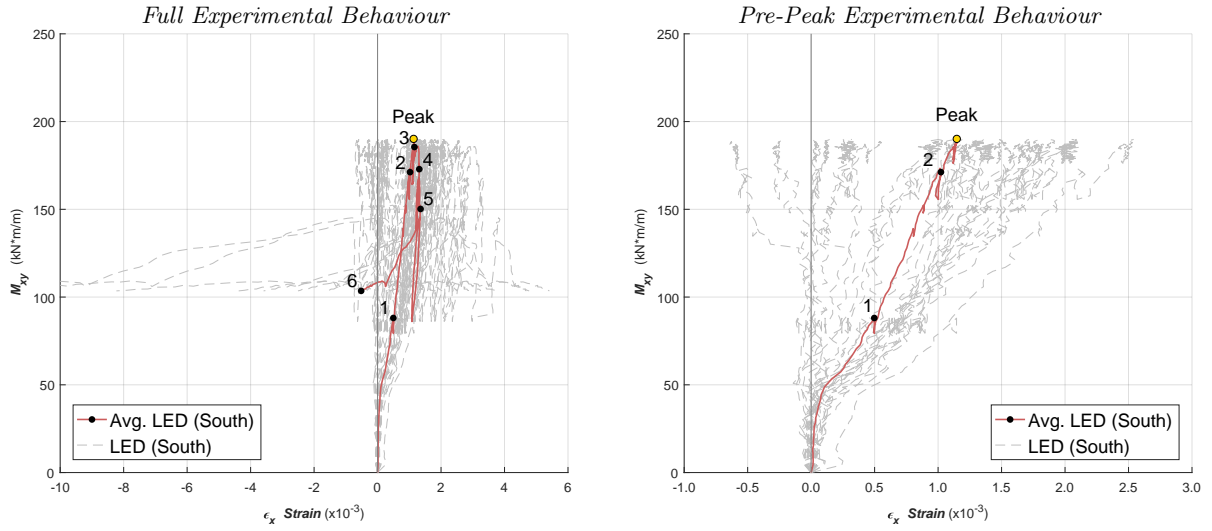


Figure 4.21: *ES1 Applied Torsion vs. X-Direction Strain*

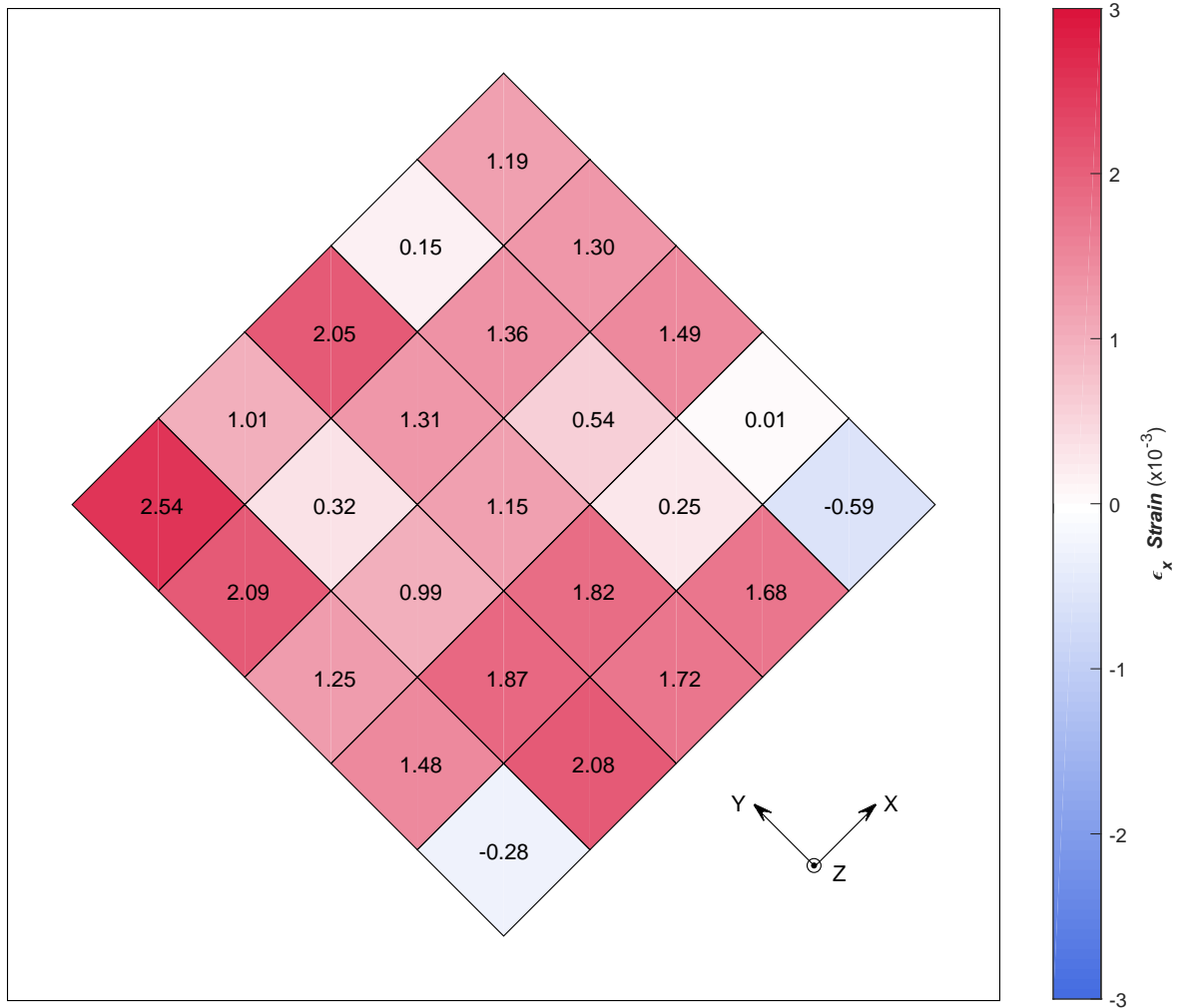


Figure 4.22: *ES1 X-Direction Strain at 'Peak' Torsion*

Y-Direction Strain

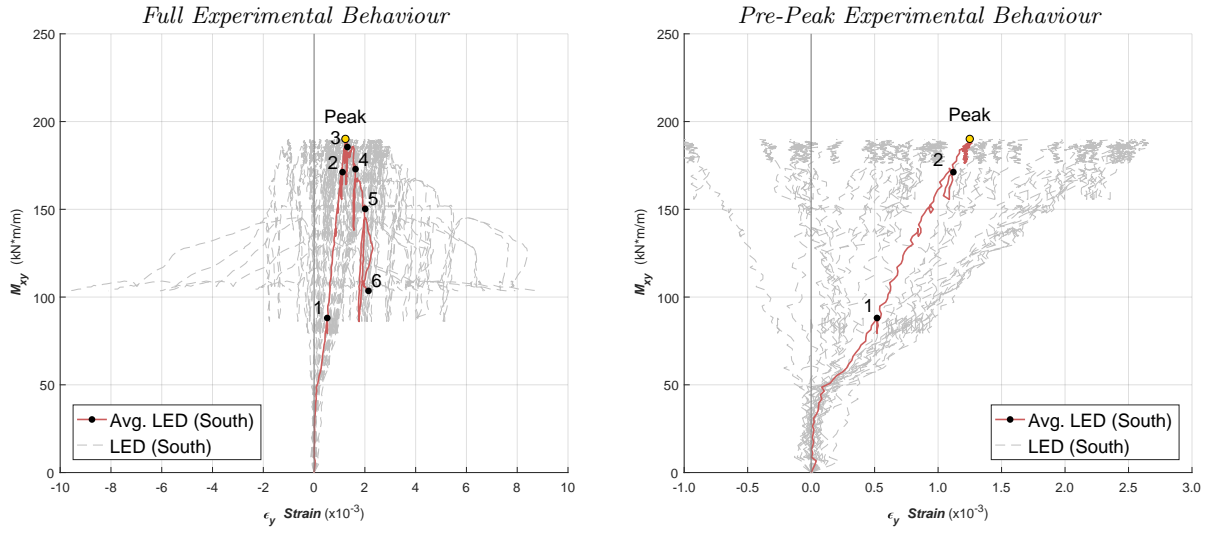


Figure 4.23: ES1 Applied Torsion vs. Y-Direction Strain

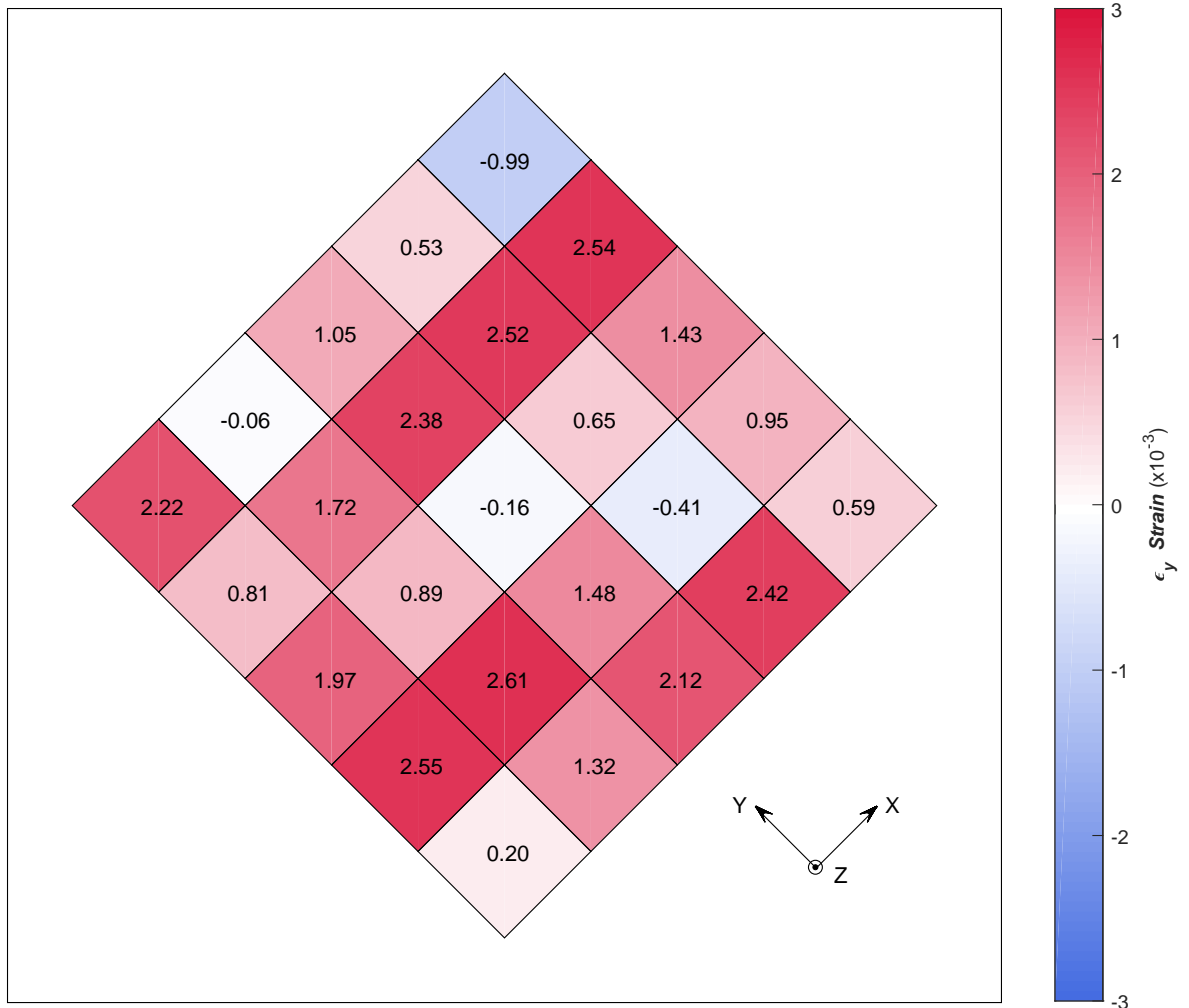


Figure 4.24: ES1 Y-Direction Strain at 'Peak' Torsion

Principal Tensile Strain

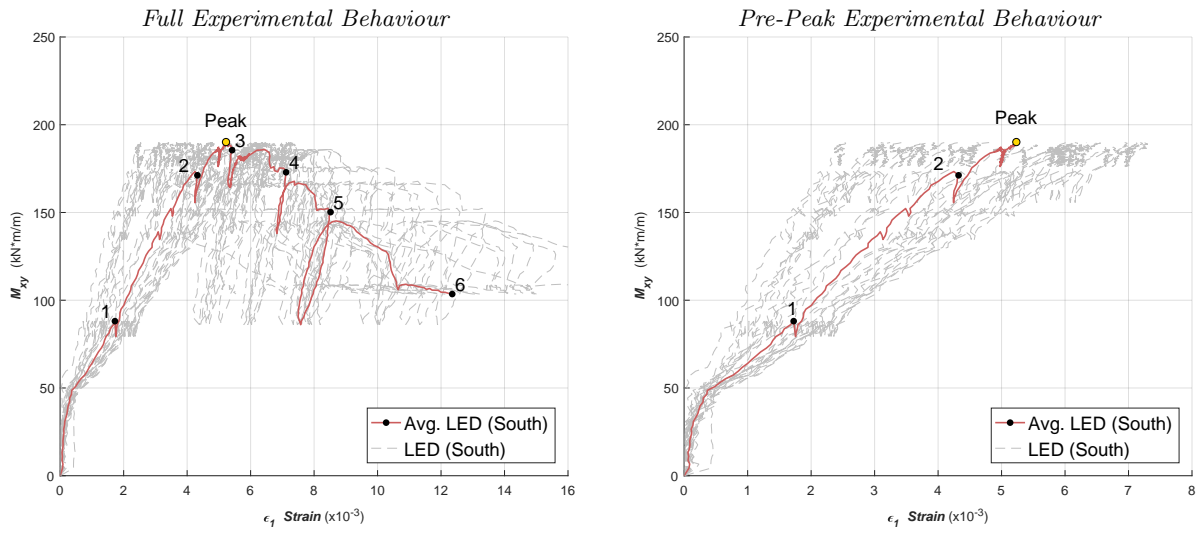


Figure 4.25: ES1 Applied Torsion vs. Principal Tensile Strain

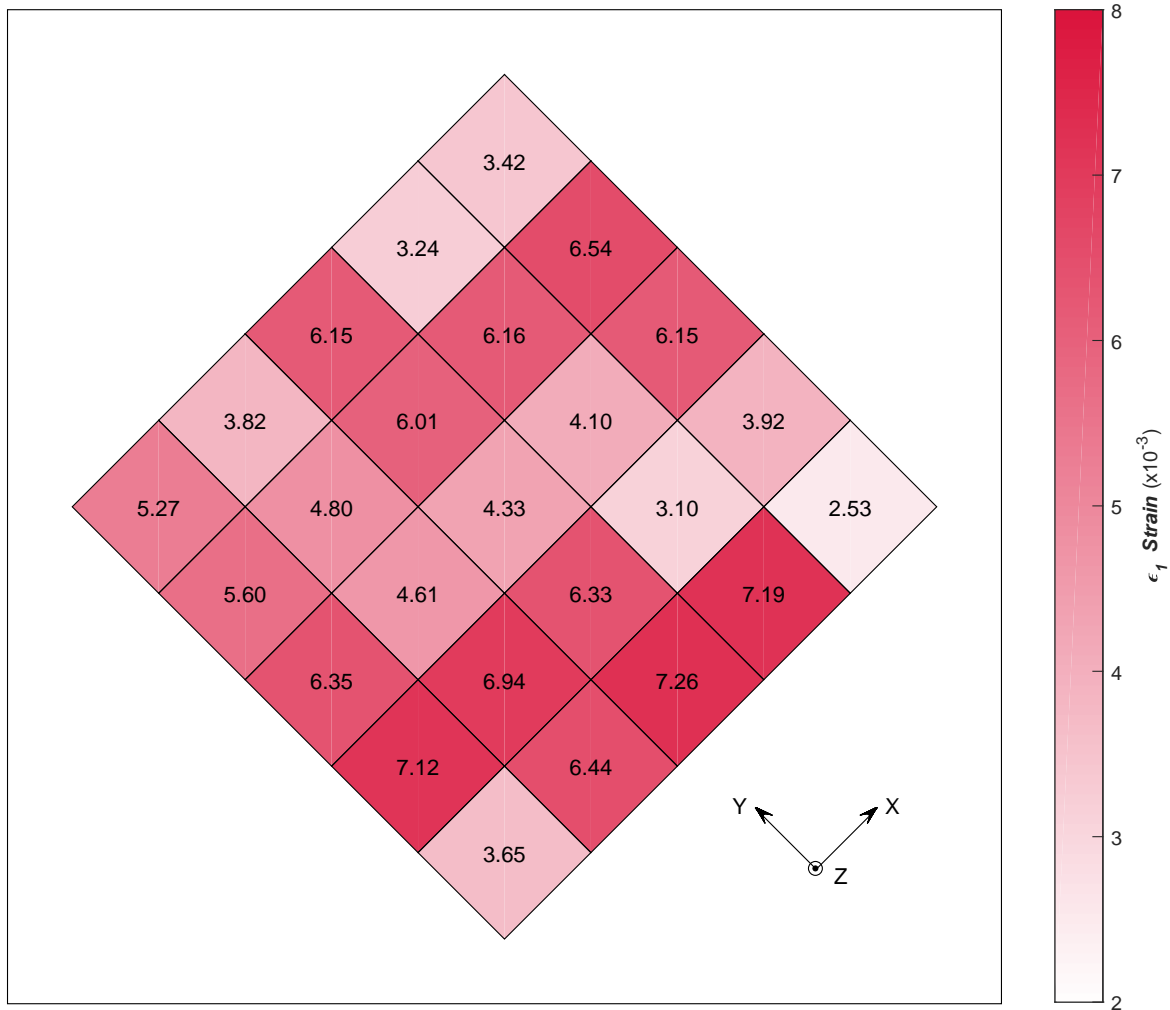


Figure 4.26: ES1 Principal Tensile Strain at 'Peak' Torsion

Principal Compressive Strain

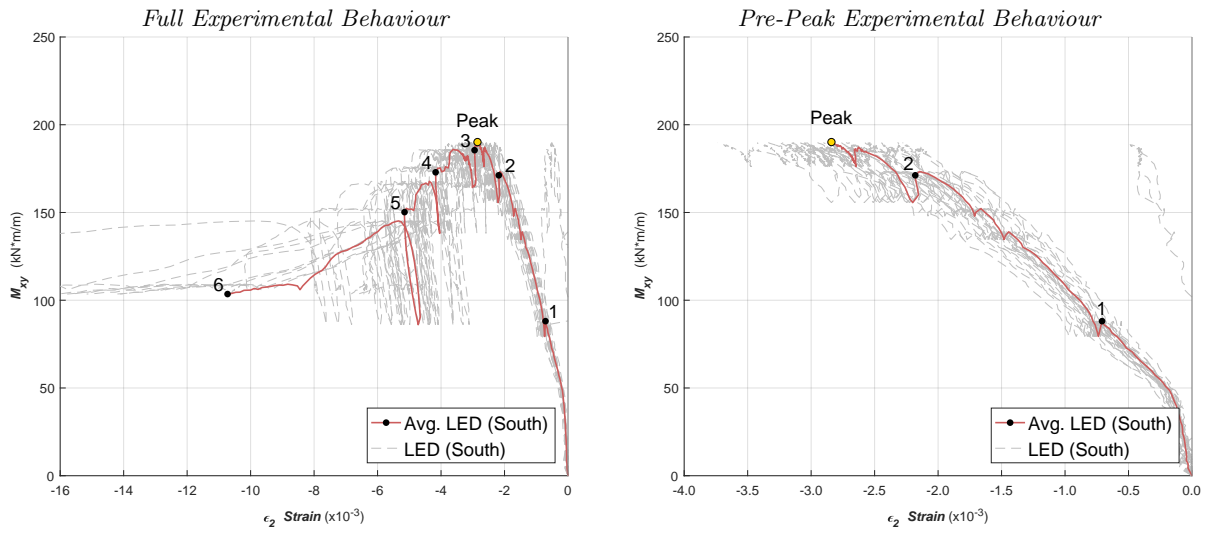


Figure 4.27: ES1 Applied Torsion vs. Principal Compressive Strain

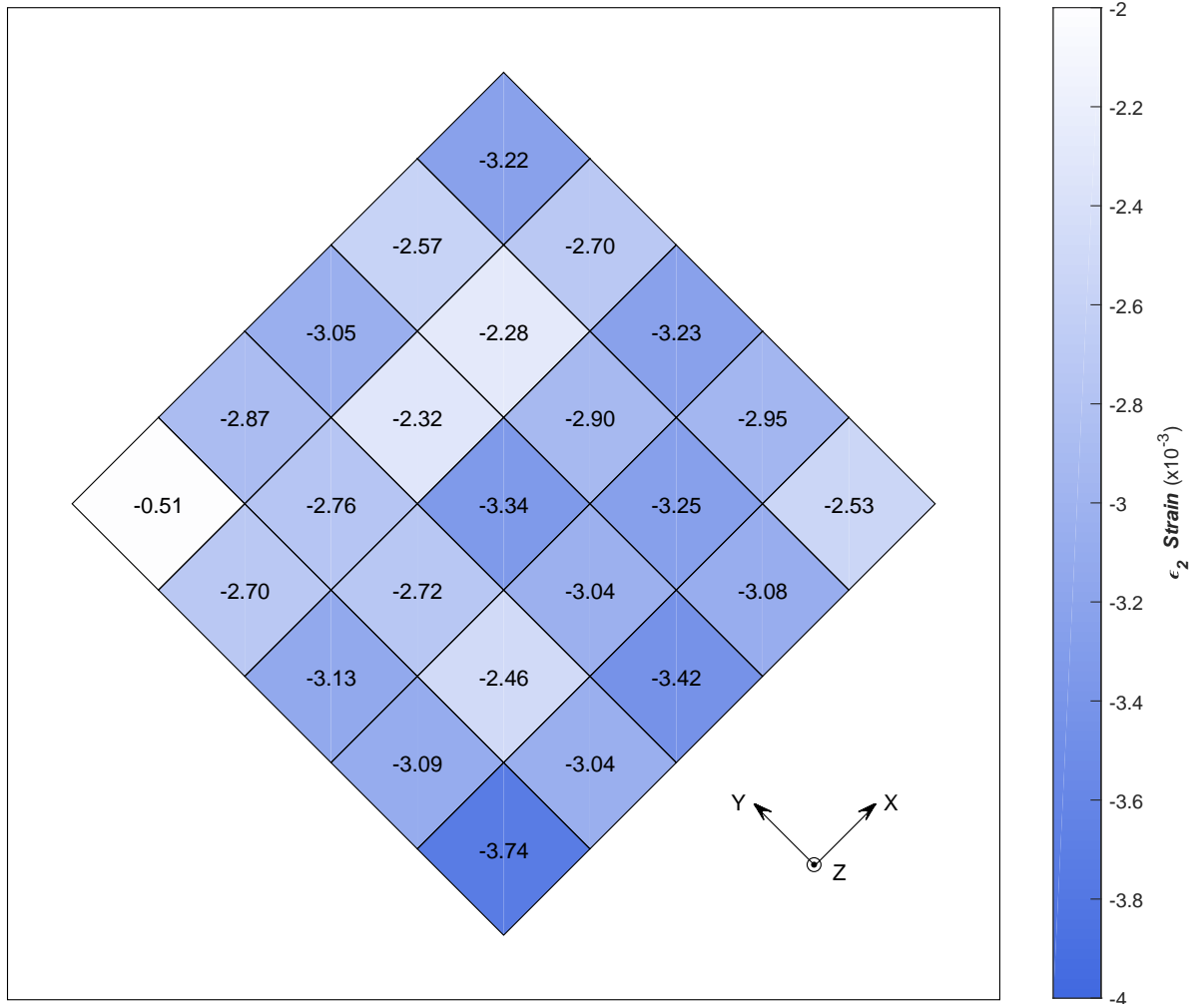


Figure 4.28: ES1 Principal Compressive Strain at 'Peak' Torsion

Angle of Principal Strain

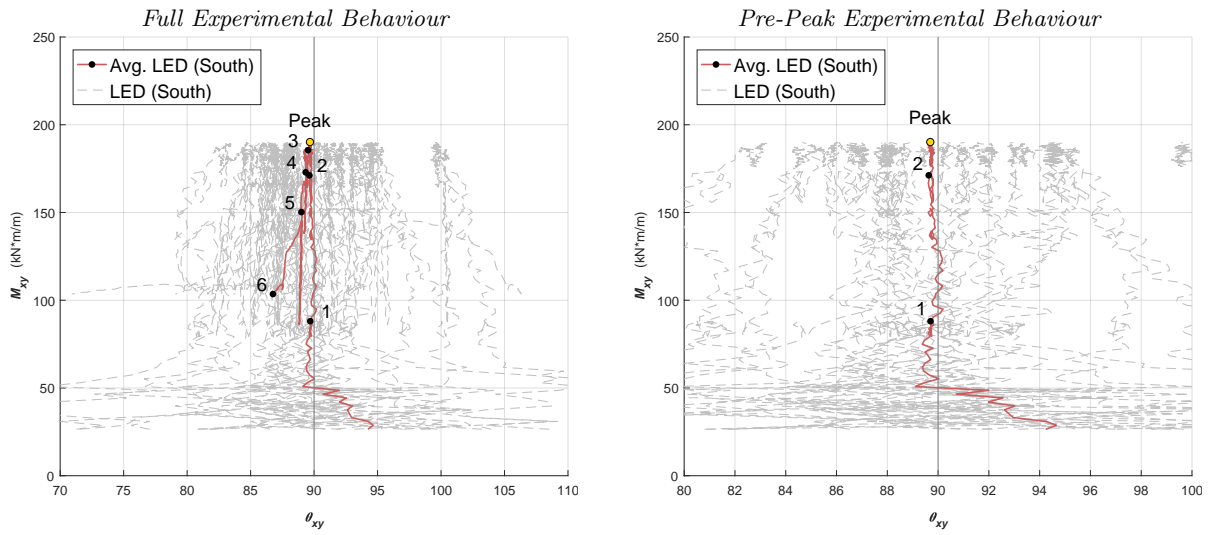


Figure 4.29: ES1 Applied Torsion vs. Angle of Principal Strain (CCW+)

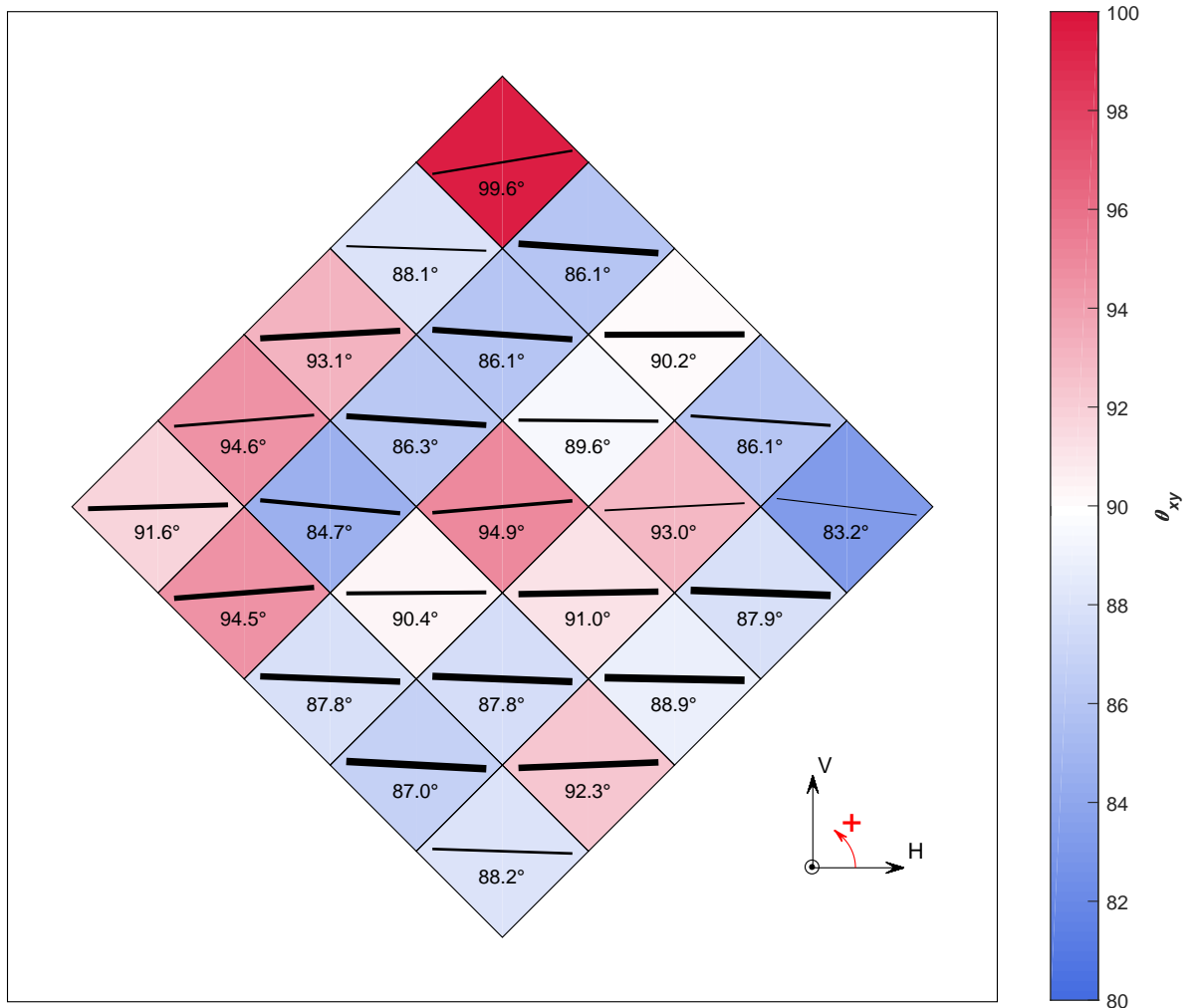


Figure 4.30: ES1 Angle of Principal Strain (CCW+) at 'Peak' Torsion

4.3.2 Specimen ES2

In-Plane Shear Strain

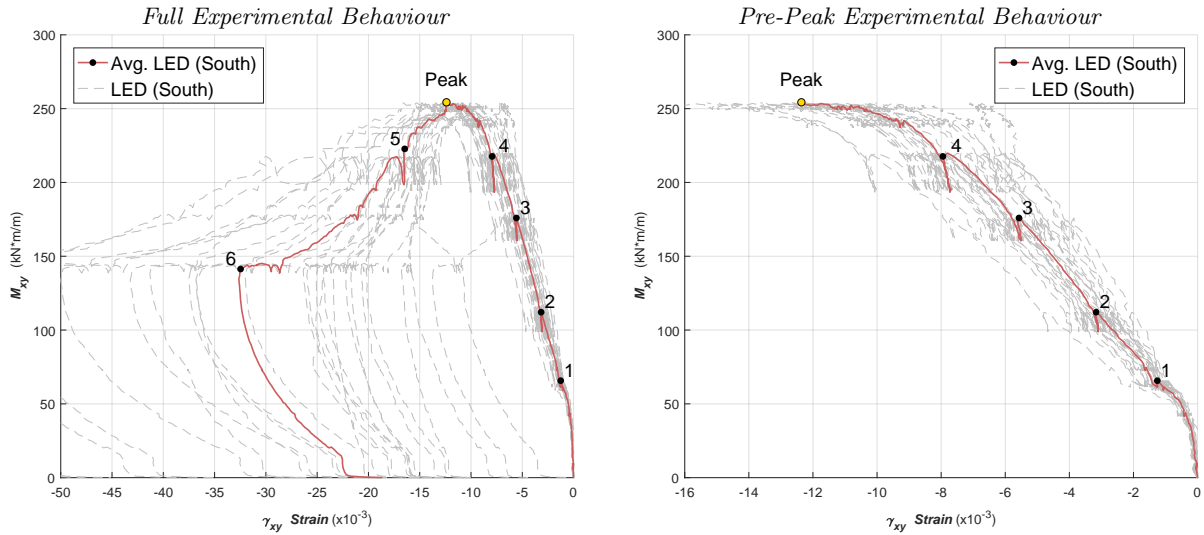


Figure 4.31: ES2 Applied Torsion vs. In-Plane (XY) Shear Strain

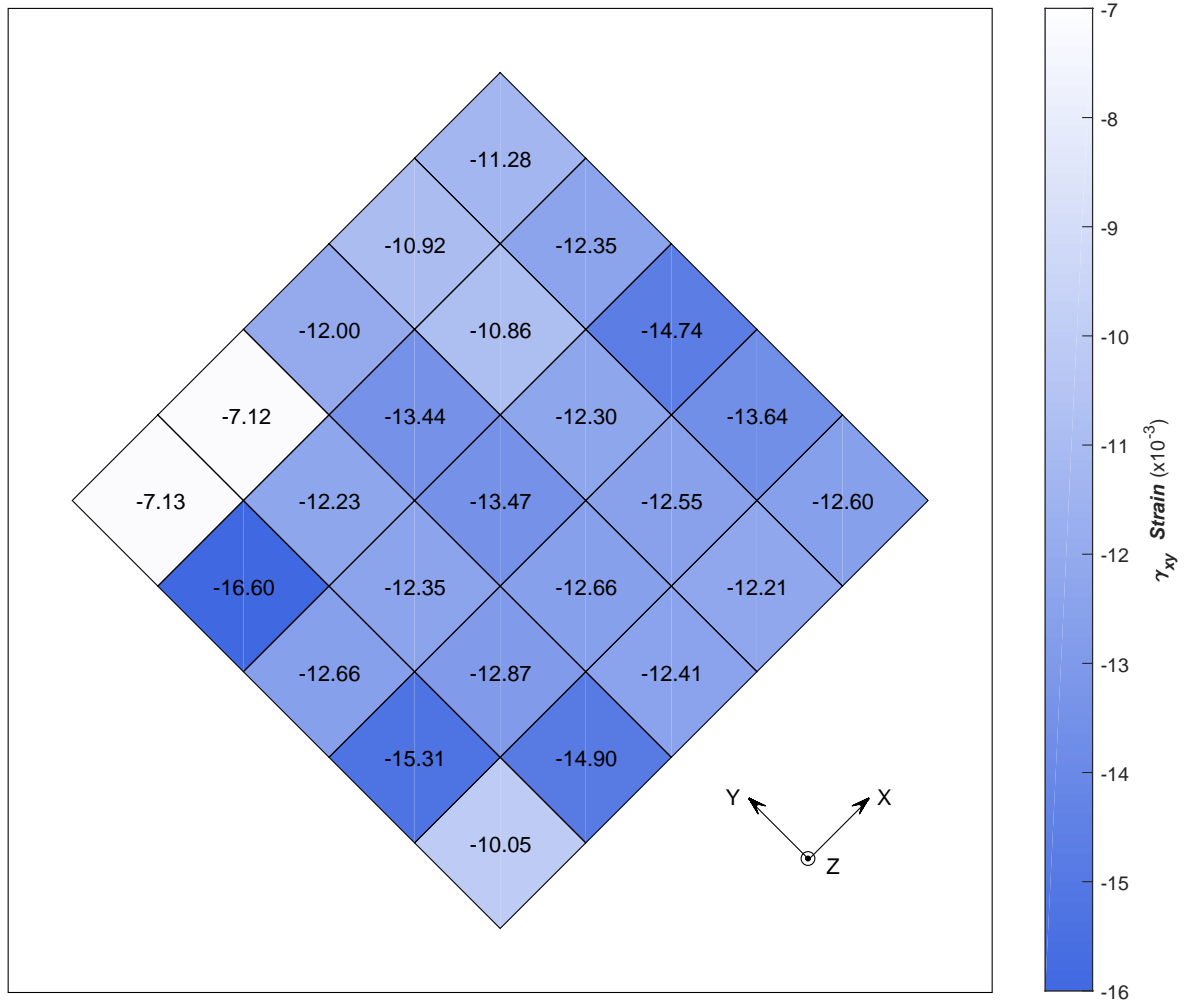


Figure 4.32: ES2 In-Plane (XY) Shear Strain at 'Peak' Torsion

X-Direction Strain

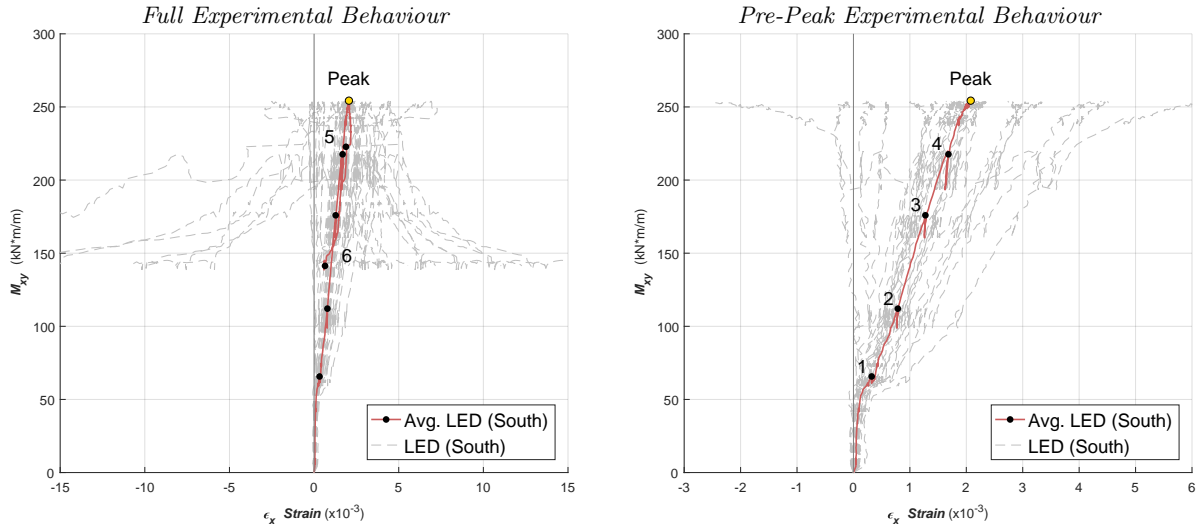


Figure 4.33: ES2 Applied Torsion vs. X-Direction Strain

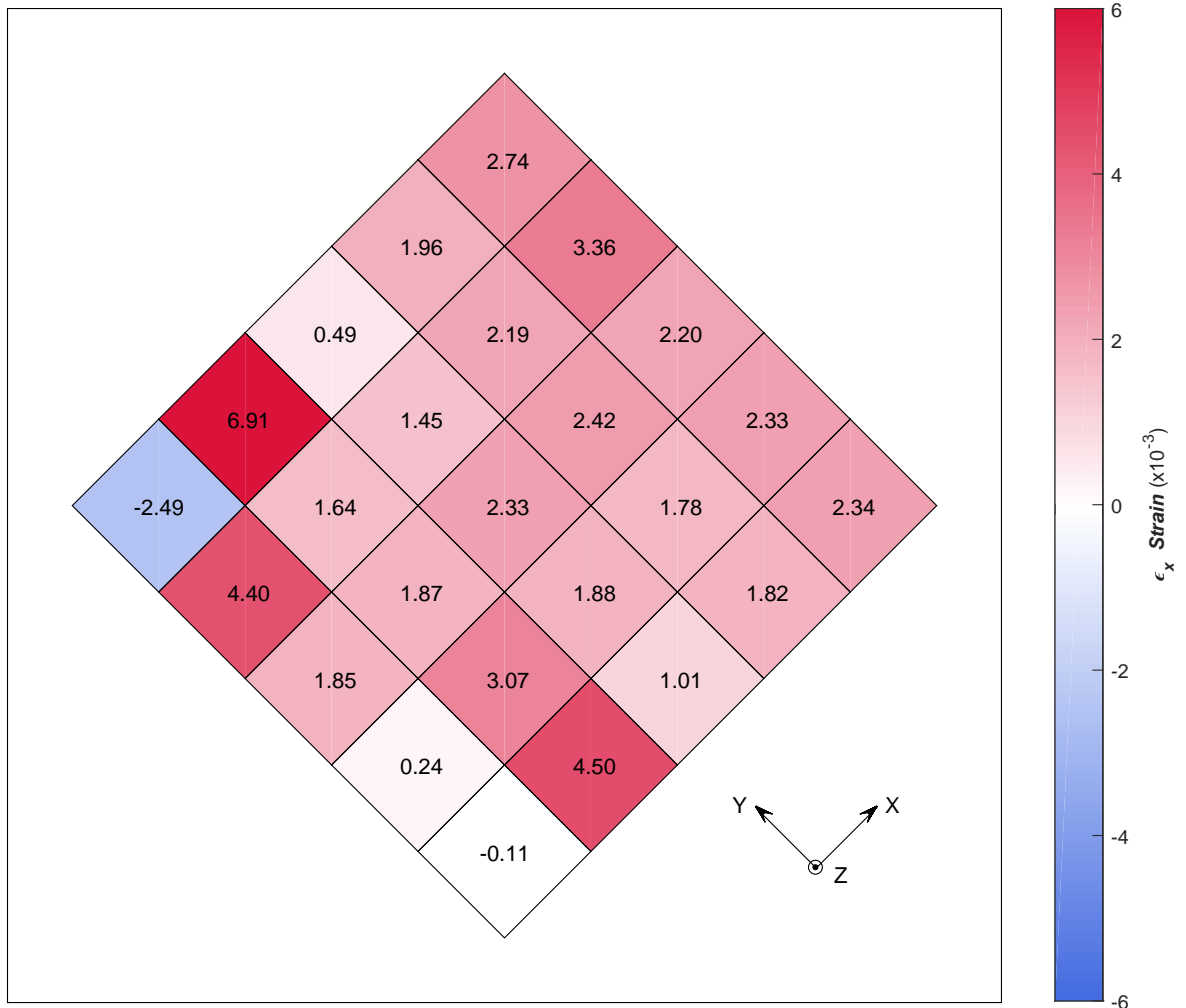


Figure 4.34: ES2 X-Direction Strain at 'Peak' Torsion

Y-Direction Strain

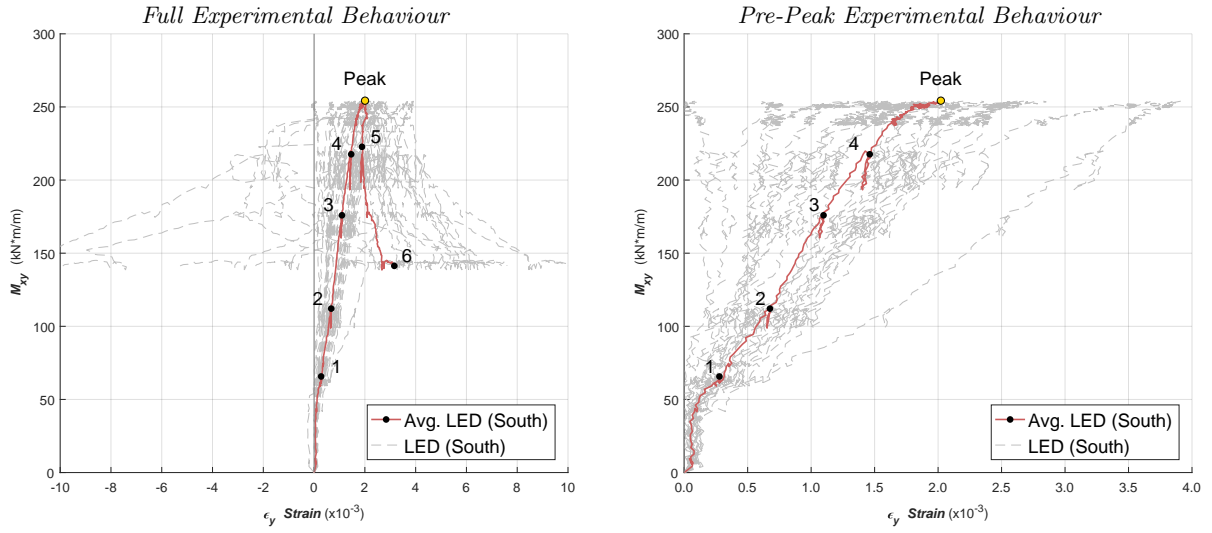


Figure 4.35: ES2 Applied Torsion vs. Y-Direction Strain

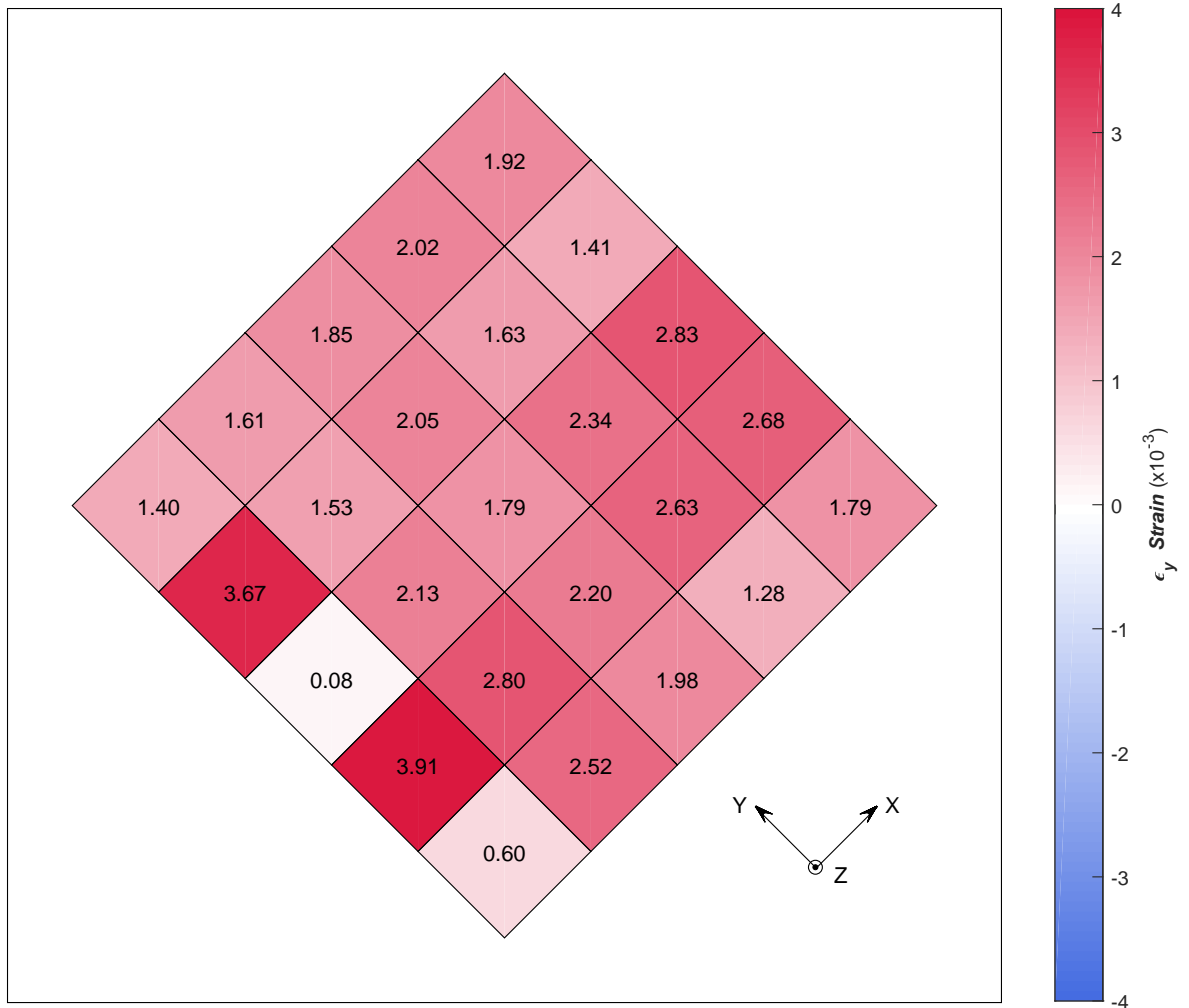


Figure 4.36: ES2 Y-Direction Strain at 'Peak' Torsion

Principal Tensile Strain

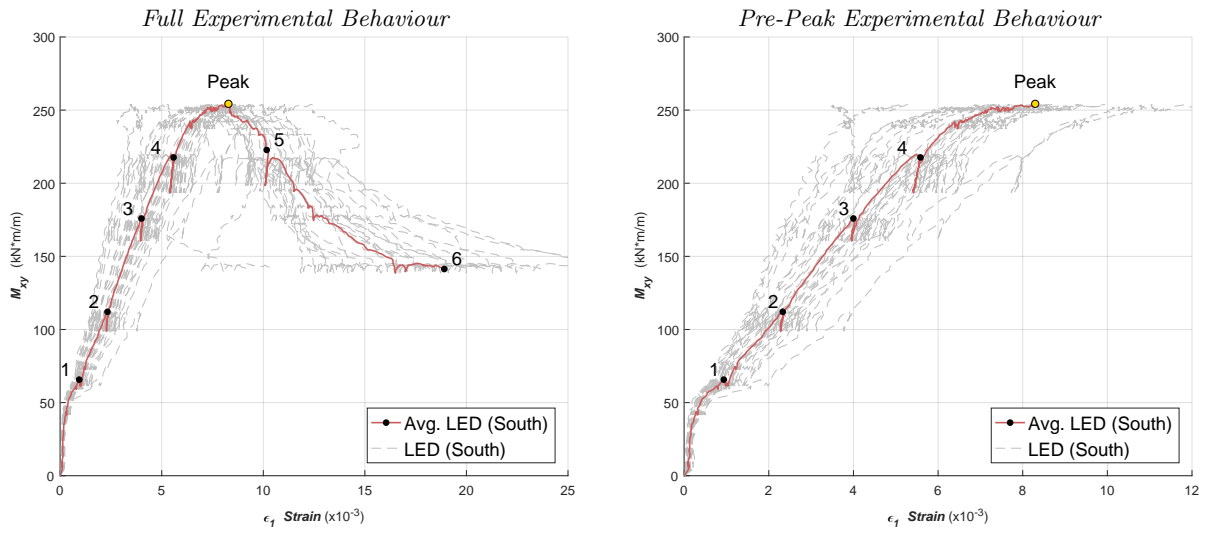


Figure 4.37: ES2 Applied Torsion vs. Principal Tensile Strain

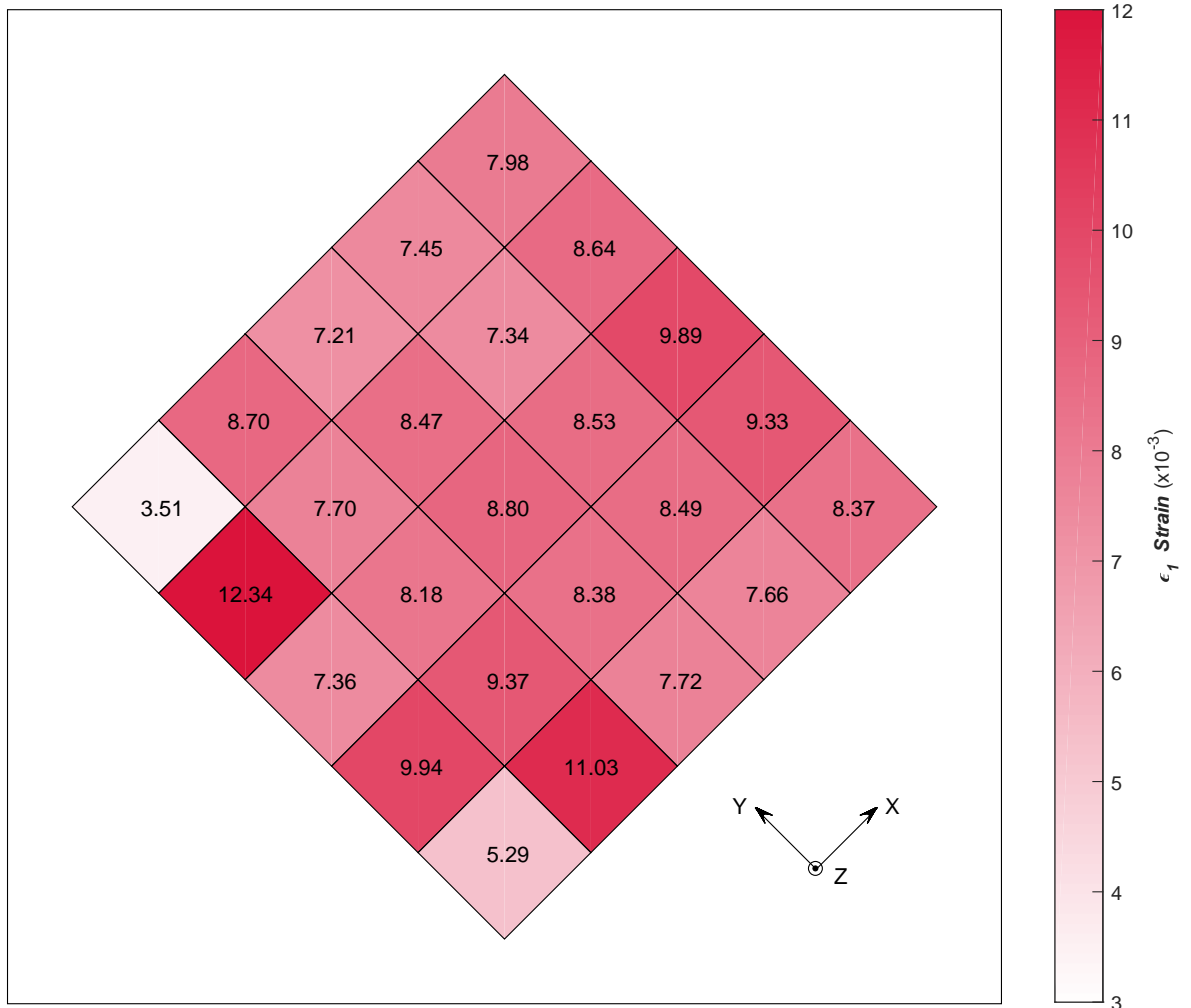


Figure 4.38: ES2 Principal Tensile Strain at 'Peak' Torsion

Principal Compressive Strain

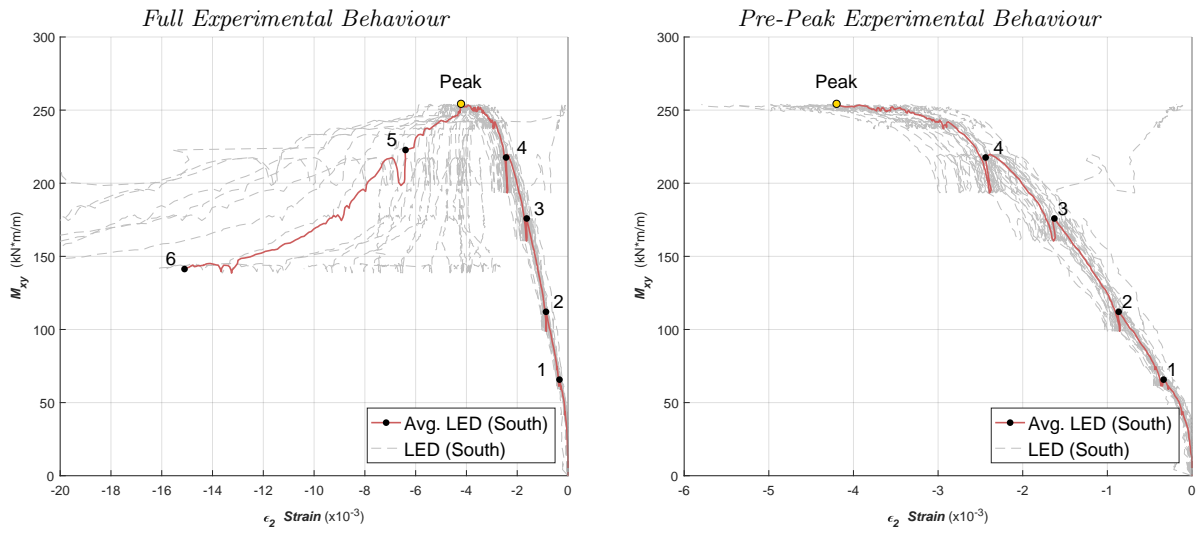


Figure 4.39: ES2 Applied Torsion vs. Compressive Tensile Strain

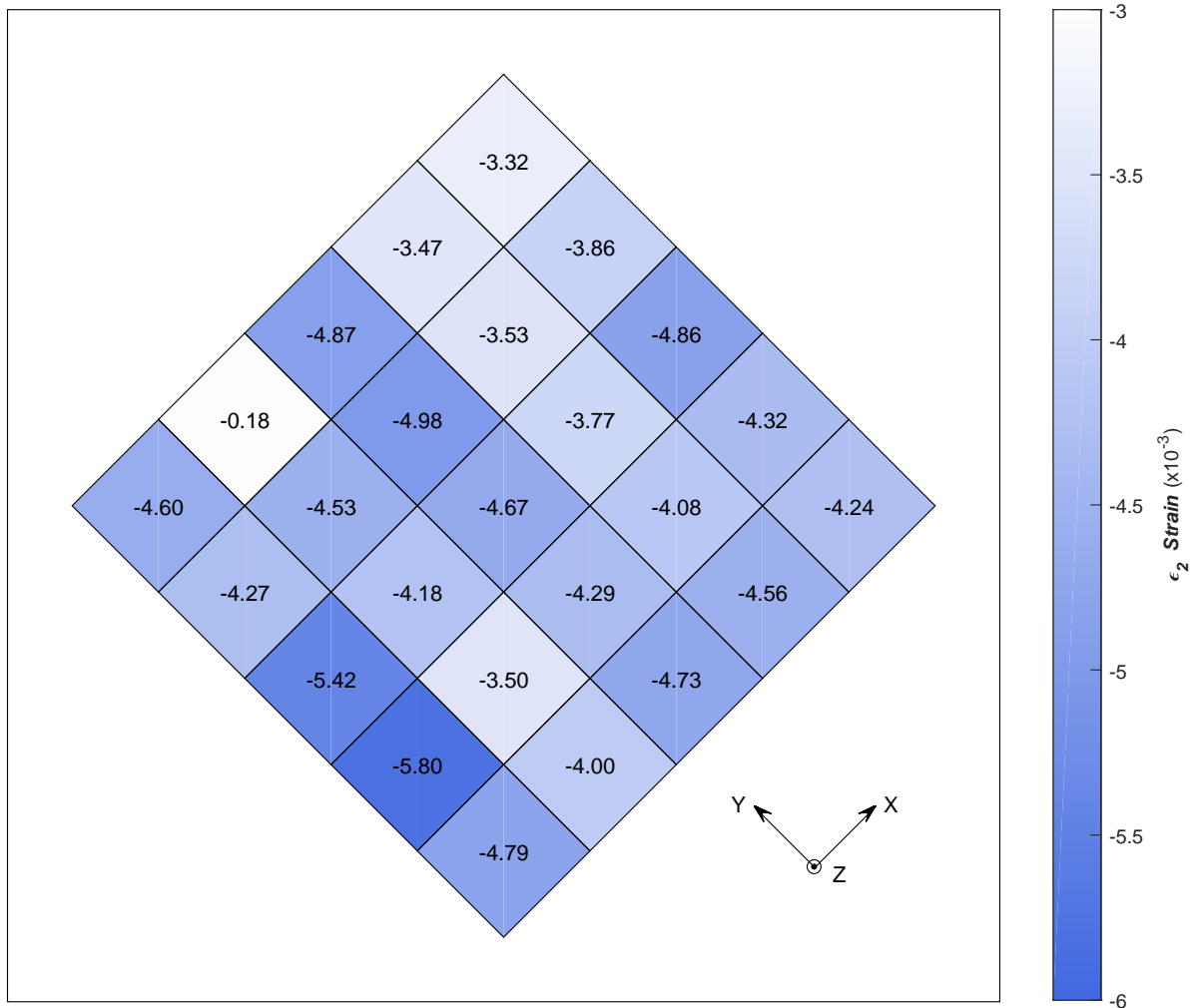


Figure 4.40: ES2 Principal Compressive Strain at 'Peak' Torsion

Angle of Principal Strain

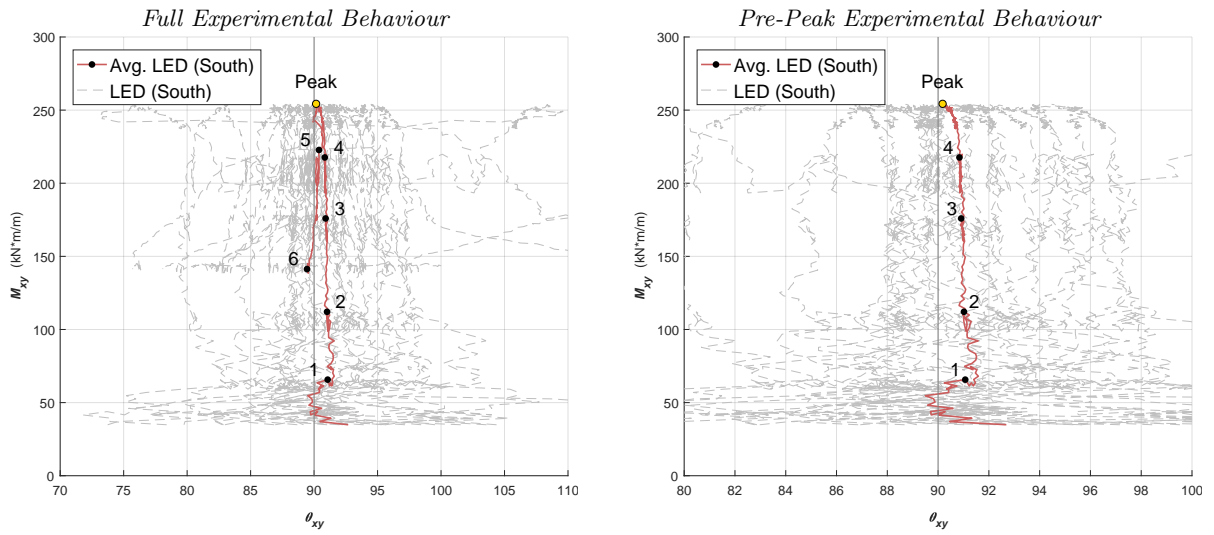


Figure 4.41: ES2 Applied Torsion vs. Angle of Principal Strain (CCW+)

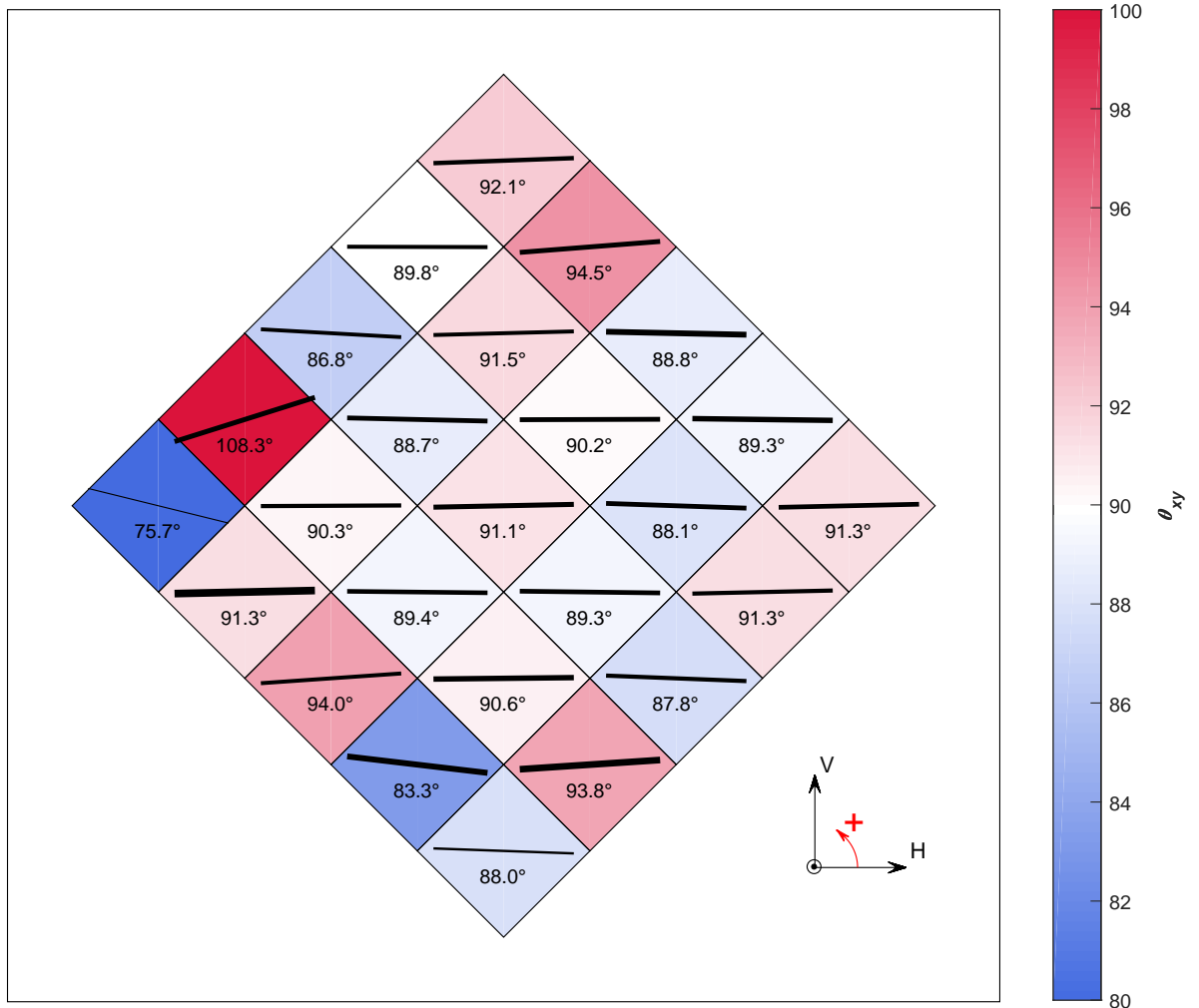


Figure 4.42: ES2 Angle of Principal Strain (CCW+) at 'Peak' Torsion

4.4 Out-of-Plane LP & EG Measurements

The LPs and EGs were used to measure the strain state through the thickness of the shell during the test. When analyzing the out-of-plane behaviour, it was considered important to distinguish between the strains in the XZ and YZ planes, defined by the direction of the X and Y reinforcement respectively (Figure 4.43). Therefore, in Tables 4.5 & 4.6 and the subsequent plots, the experimental strain information for the XZ and YZ planes is presented separately.

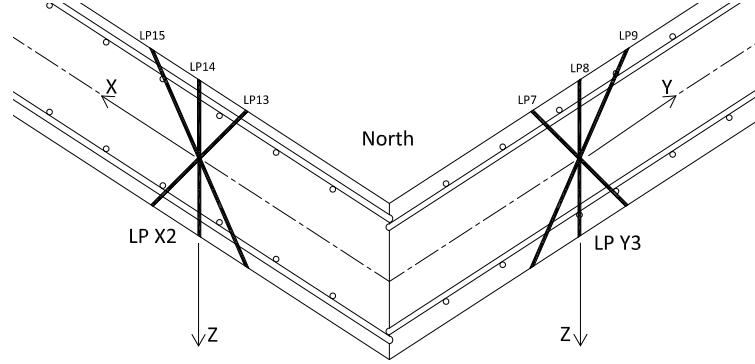
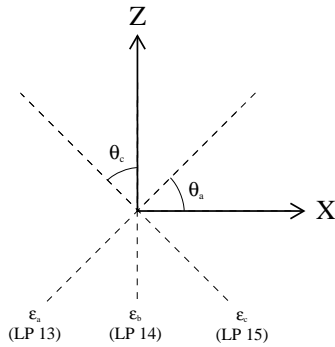


Figure 4.43: Example of LP arrangement in XZ and YZ Planes

Three independent strain measurements were taken at each location and the out-of-plane Mohr's circle of strain was then calculated explicitly. For the EGs, the angles between the individual gauges was fixed at 45° , while for the LP triplets these angles could vary by $\pm 5^\circ$ as the hollow tubes through the concrete shifted during casting. Equation 4.1 presents an explicit solution for the strain in the X-direction and shear strain in the XZ-plane given three strains at known angles in the same plane (same approach for YZ-plane). For simplicity, the central measurement is assumed to coincide perfectly with the Z-direction.



$$\epsilon_x = \left[A - B \cdot \frac{\tan(\theta_a - 90)}{\tan \theta_c} \right] \cdot \frac{\tan \theta_c}{\tan \theta_c - \tan(\theta_a - 90)}$$

$$\gamma_{xz} = B \cdot \tan(\theta_a - 90) - \epsilon_x \cdot \tan(\theta_a - 90) \quad (4.1)$$

$$\text{where: } A = \frac{\epsilon_c - \epsilon_b \cdot \cos^2 \theta_c}{\sin^2 \theta_c}, \quad B = \frac{\epsilon_a - \epsilon_b \cdot \sin^2 \theta_a}{\cos^2 \theta_a}$$

It is important to reiterate that the LPs measured the average strains through the thickness, as the relative displacement between the North and South faces. They provided accurate information about the shell on a macro scale, but were not reliable in the post-peak region of the test as the surface concrete began to spall. Meanwhile, the EGs measured strains through the thickness of the shell at discrete points, but the general out-of-plane behaviour should not be characterized on the basis of this localized information alone. In addition, the XZ-plane EGs for ES1 were damaged, and only the Z-direction strain readings were salvageable.

Table 4.5: LP & EG Data in XZ-Plane at Load Stages

	$\left[\frac{kN \cdot m}{m}\right]$ M_{xy}	$\left[\frac{mrad}{m}\right]$ ϕ_{xy}	$[\times 10^{-3}]$ γ_{xz}				$[\times 10^{-3}]$ ϵ_x				$[\times 10^{-3}]$ ϵ_z			
			LPX1	LPX2	EGX1	EGX2	LPX1	LPX2	EGX1	EGX2	LPX1	LPX2	EGX1	EGX2
			ES1											
<i>LS1</i>	86.8	15.5	-63	-74	-	-	105	383	-	-	78	-51	-63	8
<i>LS2</i>	168.8	46.3	274	-563	-	-	-203	2180	-	-	527	-353	-30	159
<i>Peak</i>	187.2	58.7	557	-571	-	-	-199	2640	-	-	754	-255	13	209
<i>LS3</i>	182.9	60.4	572	-661	-	-	-267	2810	-	-	826	-212	41	219
<i>LS4</i>	170.4	80.8	819	-7130	-	-	-508	11760	-	-	1434	2370	389	797
<i>LS5</i>	147.9	96.6	1620	-12010	-	-	72	5040	-	-	2740	16810	1326	1250
<i>LS6</i>	101.8	139.7	12030	-2080	-	-	9120	-904	-	-	13880	53000	1450	2617
ES2														
<i>LS1</i>	64.8	8.2	-65	-37	-31	119	-21	-45	146	-118	57	7	-17	-11
<i>LS2</i>	110.5	21.4	-149	-66	-110	207	-43	113	596	252	138	45	-30	3
<i>LS3</i>	173.4	39.0	-234	215	-191	35	-54	506	843	675	276	87	-73	31
<i>LS4</i>	214.7	56.7	-560	354	-268	-92	464	666	905	912	435	336	-18	144
<i>Peak</i>	250.5	89.4	-736	798	119	-559	606	1324	813	1276	1544	1259	176	370
<i>LS5</i>	219.6	111.0	-1664	1378	989	-660	-2320	2040	642	1124	5360	2430	703	503
<i>LS6</i>	138.9	223.0	-21400	10680	195	907	11940	14660	-273	845	20200	10220	3350	3100
	$\left[\frac{kN \cdot m}{m}\right]$ M_{xy}	$\left[\frac{mrad}{m}\right]$ ϕ_{xy}	$[\circ]$ θ_{xz}				$[\times 10^{-3}]$ ϵ_1				$[\times 10^{-3}]$ ϵ_2			
			LPX1	LPX2	EGX1	EGX2	LPX1	LPX2	EGX1	EGX2	LPX1	LPX2	EGX1	EGX2
ES1														
<i>LS1</i>	86.8	15.5	-33.7	-4.8	-	-	125	387	-	-	57	-54	-	-
<i>LS2</i>	168.8	46.3	-100.3	-6.4	-	-	552	2210	-	-	-228	-353	-	-
<i>Peak</i>	187.2	58.7	-105.1	-5.6	-	-	830	2670	-	-	-275	-283	-	-
<i>LS3</i>	182.9	60.4	-103.8	-6.2	-	-	896	2840	-	-	-337	-247	-	-
<i>LS4</i>	170.4	80.8	-101.4	-18.6	-	-	1517	12960	-	-	-591	1170	-	-
<i>LS5</i>	147.9	96.6	-105.6	-67.2	-	-	1970	19330	-	-	-154	2519	-	-
<i>LS6</i>	101.8	139.7	-124.2	-88.9	-	-	17970	53000	-	-	5030	-924	-	-
ES2														
<i>LS1</i>	64.8	8.2	-70.1	-72.3	-5.4	66.1	68	13	147	16	-33	-51	-19	-145
<i>LS2</i>	110.5	21.4	-70.2	-22.2	-5.0	19.9	165	127	601	289	-69	32	-34	-34
<i>LS3</i>	173.4	39.0	-72.3	13.6	-5.9	1.6	313	532	853	675	-91	61	-82	30
<i>LS4</i>	214.7	56.7	-43.5	23.5	-8.1	-3.4	730	743	924	915	169	259	-37	141
<i>Peak</i>	250.5	89.4	-70.9	42.7	5.3	-15.8	1671	1692	818	1356	479	891	170	291
<i>LS5</i>	219.6	111.0	-83.9	53.0	46.8	-23.4	5450	2950	1168	1267	-2400	1521	177	361
<i>LS6</i>	138.9	223.0	-55.6	33.7	88.5	-100.9	27600	18220	3350	3190	4590	6660	-275	757

Table 4.6: LP & EG Data in YZ-Plane at Load Stages

	$\left[\frac{kN \cdot m}{m}\right]$ M_{xy}	$\left[\frac{mrad}{m}\right]$ ϕ_{xy}	$[\times 10^{-3}]$ γ_{yz}					$[\times 10^{-3}]$ ϵ_y					$[\times 10^{-3}]$ ϵ_z					
			LPY1	LPY2	LPY3	EGY1	EGY2	LPY1	LPY2	LPY3	EGY1	EGY2	LPY1	LPY2	LPY3	EGY1	EGY2	
			ES1															
LS1	86.8	15.5	-145	-243	100	63	112	470	347	208	374	149	18	-18	83	29	-3	
LS2	168.8	46.3	-258	-192	359	-19	297	886	861	1036	659	583	469	47	304	109	187	
Peak	187.2	58.7	-268	-93	438	-66	349	830	1210	1350	775	686	705	195	453	116	220	
LS3	182.9	60.4	-278	-112	452	-78	362	857	1216	1340	800	699	745	238	496	114	225	
LS4	170.4	80.8	-3590	129	1119	-6	370	7260	1876	2850	851	815	2620	1162	1141	77	200	
LS5	147.9	96.6	-10370	-294	8570	209	74	17510	2200	13690	859	911	3920	3250	2650	397	252	
LS6	101.8	139.7	-13960	-12430	11190	232	-247	77100	3000	24900	680	1354	25600	19120	15470	1557	1295	
ES2																		
LS1	64.8	8.2	-227	-151	-40	-36	-98	-282	231	98	38	279	64	-11	-18	-87	32	
LS2	110.5	21.4	-364	-277	-34	-79	-153	190	489	142	240	1141	249	0	28	-28	106	
LS3	173.4	39.0	-722	-226	132	84	-322	444	1045	486	888	1924	495	4	88	164	152	
LS4	214.7	56.7	-1113	-334	-132	273	-417	363	1033	1242	1230	2420	893	230	145	229	237	
Peak	250.5	89.4	-2157	-426	-1822	396	-819	-4110	1023	5810	1580	2790	4590	1247	1258	414	416	
LS5	219.6	111.0	-4670	-210	-1495	551	-1505	-3430	234	8350	1593	2700	7210	3340	6570	659	737	
LS6	138.9	223.0	-12060	3820	1645	140	-2880	-28200	3960	20900	693	2530	36900	11480	25700	2230	2180	

	$\left[\frac{kN \cdot m}{m}\right]$ M_{xy}	$\left[\frac{mrad}{m}\right]$ ϕ_{xy}	$[^\circ]$ θ_{yz}					$[\times 10^{-3}]$ ϵ_1					$[\times 10^{-3}]$ ϵ_2					
			LPY1	LPY2	LPY3	EGY1	EGY2	LPY1	LPY2	LPY3	EGY1	EGY2	LPY1	LPY2	LPY3	EGY1	EGY2	
			ES1															
LS1	86.8	15.5	8.9	16.9	-19.3	-5.2	-18.3	481	384	225	377	167	7	-55	66	26	-21	
LS2	168.8	46.3	15.9	6.6	-13.1	1.0	-18.4	923	872	1078	659	633	432	36	263	109	138	
Peak	187.2	58.7	32.6	2.6	-13.0	2.9	-18.4	915	1212	1401	777	744	620	193	402	115	162	
LS3	182.9	60.4	34.1	3.3	-14.1	3.2	-18.7	951	1219	1397	802	760	652	235	440	112	164	
LS4	170.4	80.8	18.8	-5.2	-16.7	0.2	-15.5	7870	1876	3010	851	866	2000	1157	974	77	148	
LS5	147.9	96.6	18.7	-97.8	-18.9	-12.2	-3.2	19260	3270	15160	882	913	2170	2180	1177	375	250	
LS6	101.8	139.7	7.6	-108.8	-24.9	-82.6	38.2	78000	21200	27500	1572	1451	24700	884	12870	665	1198	
ES2																		
LS1	64.8	8.2	73.4	16.0	9.5	8.1	10.9	98	253	101	41	288	-316	-32	-21	-89	23	
LS2	110.5	21.4	49.6	14.8	8.3	8.2	4.2	404	526	145	246	1147	35	-36	26	-34	100	
LS3	173.4	39.0	47.0	6.1	-9.2	-3.3	5.2	831	1057	497	891	1939	107	-9	78	162	137	
LS4	214.7	56.7	57.8	11.3	3.4	-7.6	5.4	1244	1066	1246	1248	2430	12	196	141	211	217	
Peak	250.5	89.4	83.0	58.9	10.9	-9.4	9.5	4720	1376	5980	1613	2850	-4240	894	1082	382	347	
LS5	219.6	111.0	78.2	88.1	20.1	-15.3	18.7	7700	3350	8620	1668	2950	-3920	230	6300	584	481	
LS6	138.9	223.0	84.8	103.5	99.4	-87.4	41.5	37500	11940	25900	2230	3810	-28700	3510	20800	690	906	

4.4.1 Specimen ES1

Out-of-Plane (XZ) Strains

Note: No Embedment Gauge data available for specimen ES1 in XZ-plane

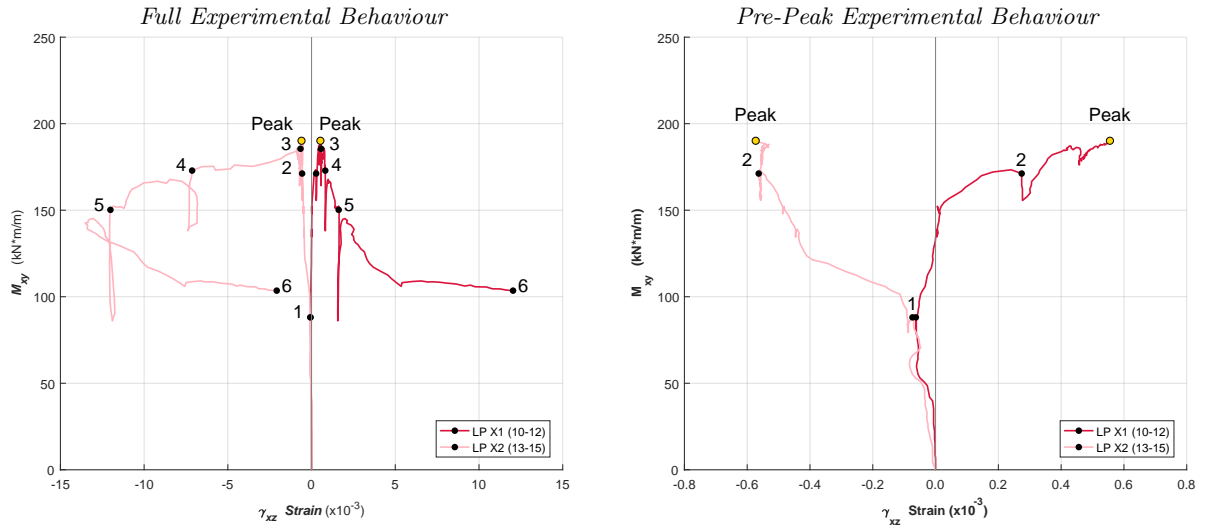


Figure 4.44: ES1 Applied Torsion vs. Out-of-Plane (XZ) Shear Strain

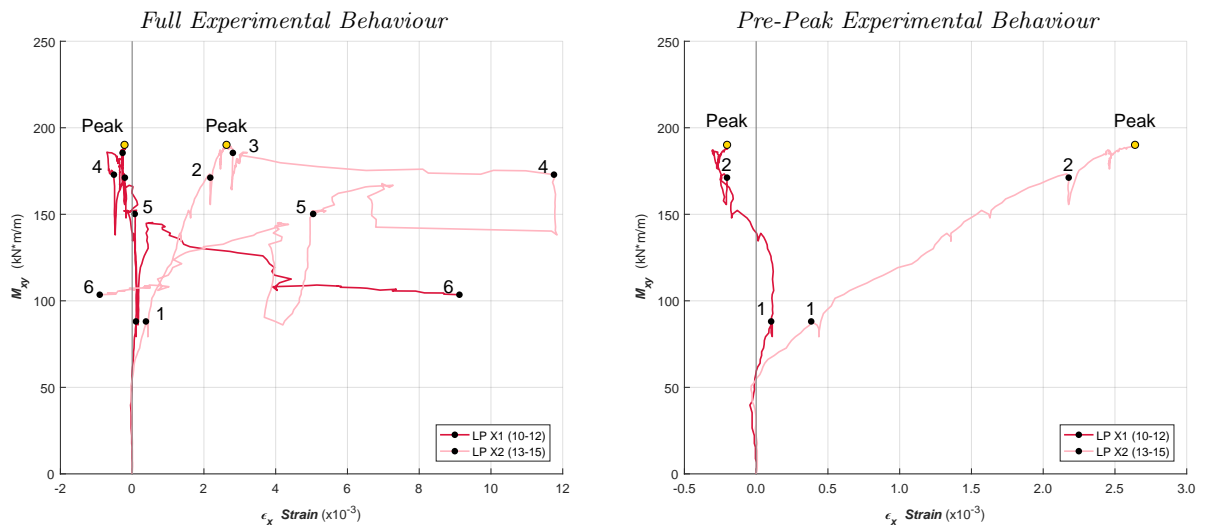


Figure 4.45: ES1 Applied Torsion vs. X-Direction Strain

Out-of-Plane (XZ) Principal Strains

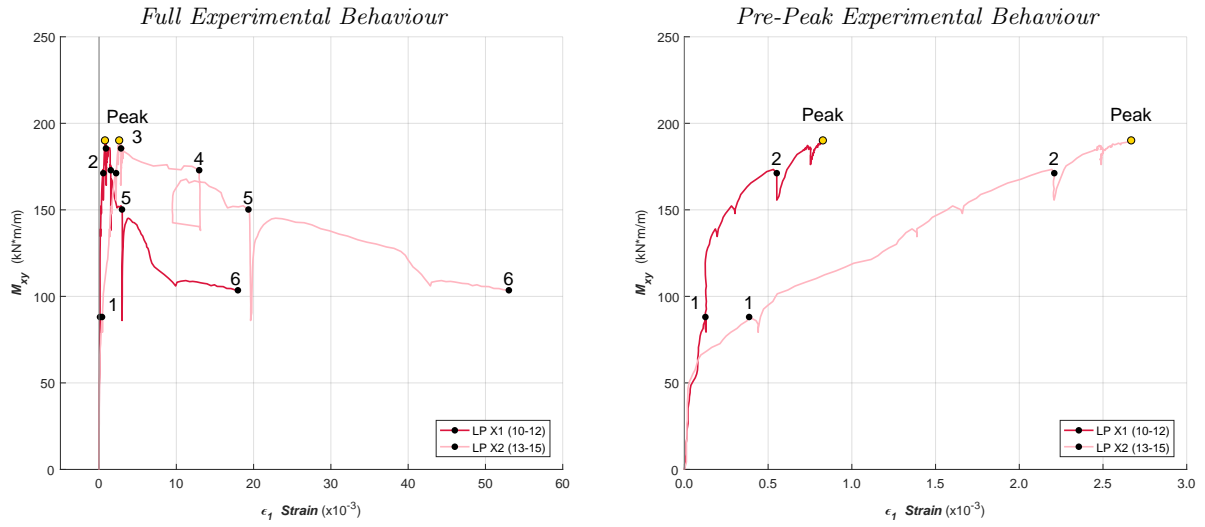


Figure 4.46: ES1 Applied Torsion vs. Principal Tensile Strain

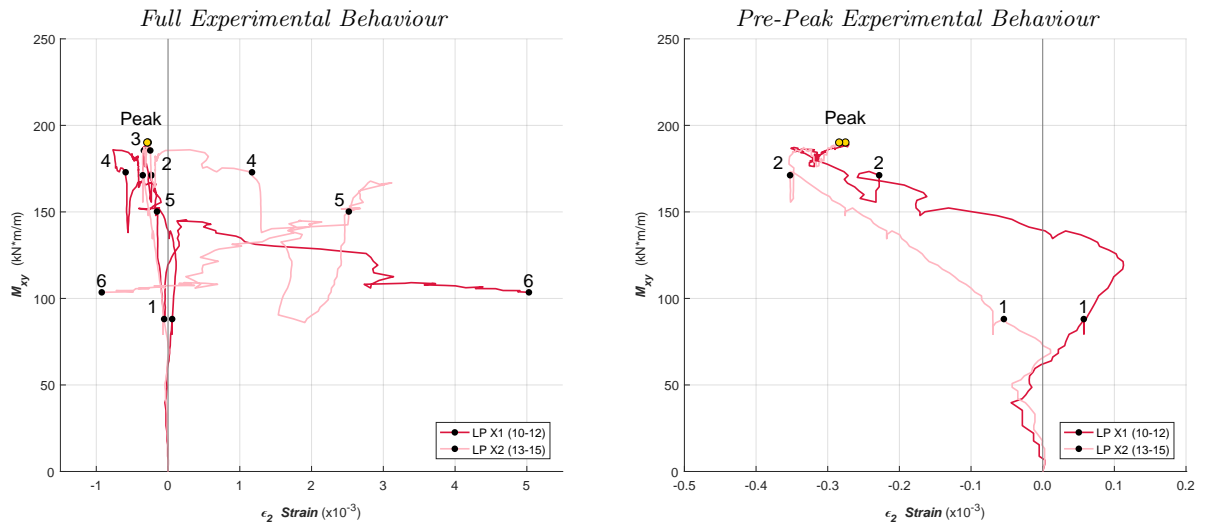


Figure 4.47: ES1 Applied Torsion vs. Principal Compressive Strain

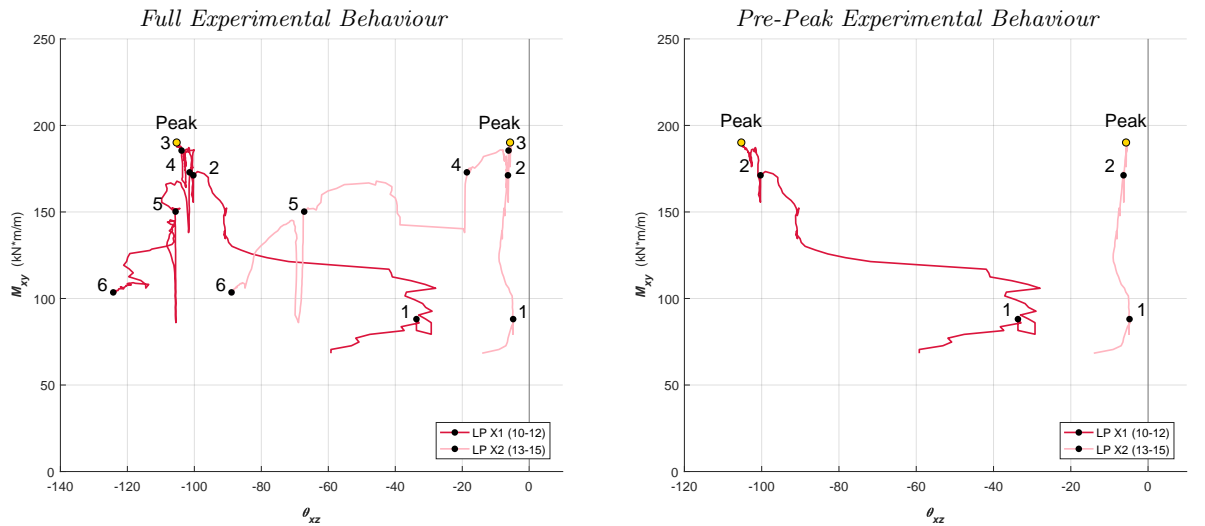


Figure 4.48: ES1 Applied Torsion vs. Principal Angle

Out-of-Plane (YZ) Strains

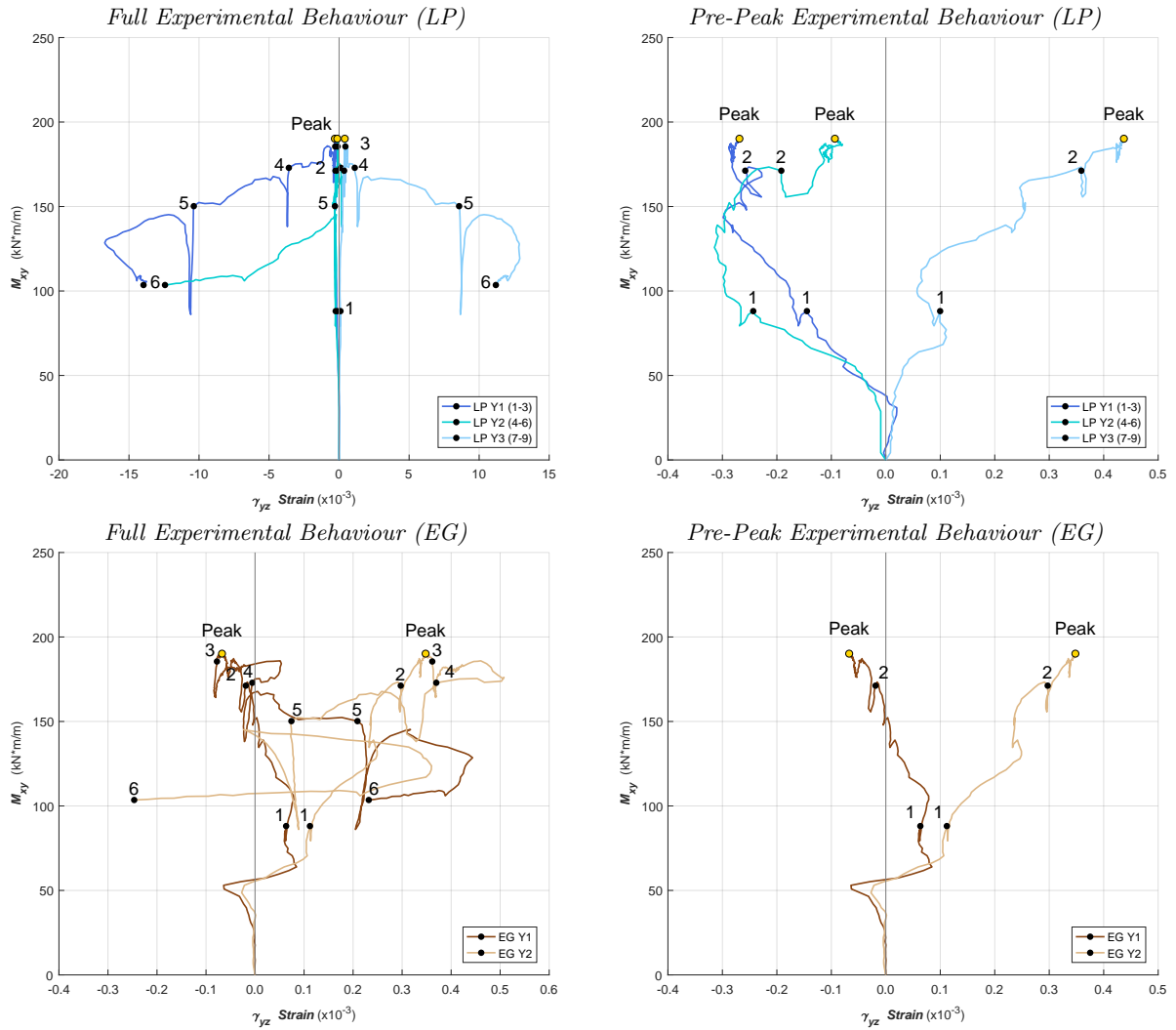


Figure 4.49: ES1 Applied Torsion vs. Out-of-Plane (YZ) Shear Strain

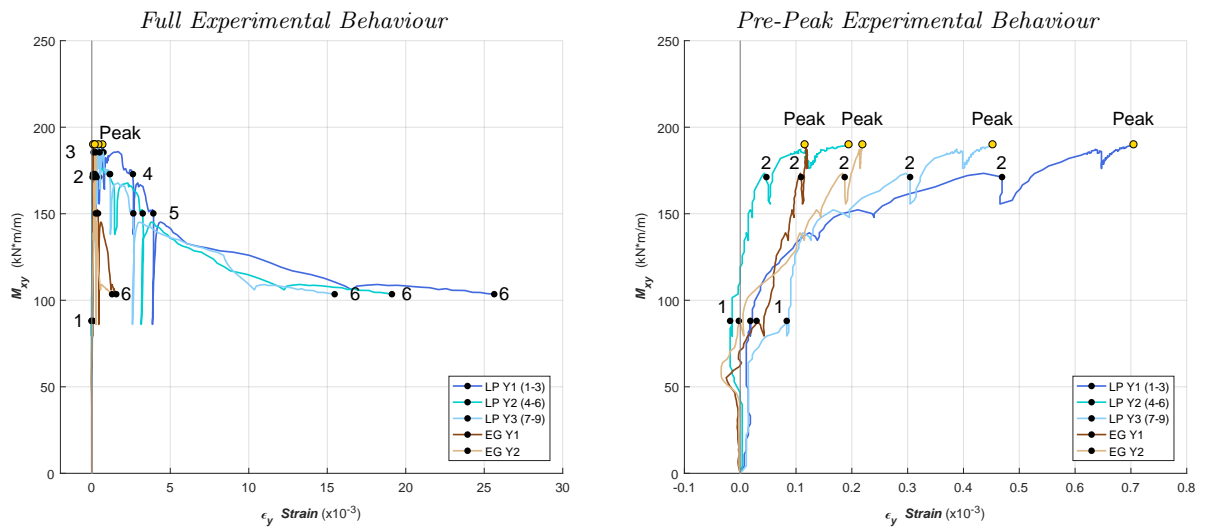


Figure 4.50: ES1 Applied Torsion vs. Y-Direction Strain

Out-of-Plane (YZ) Principal Strains

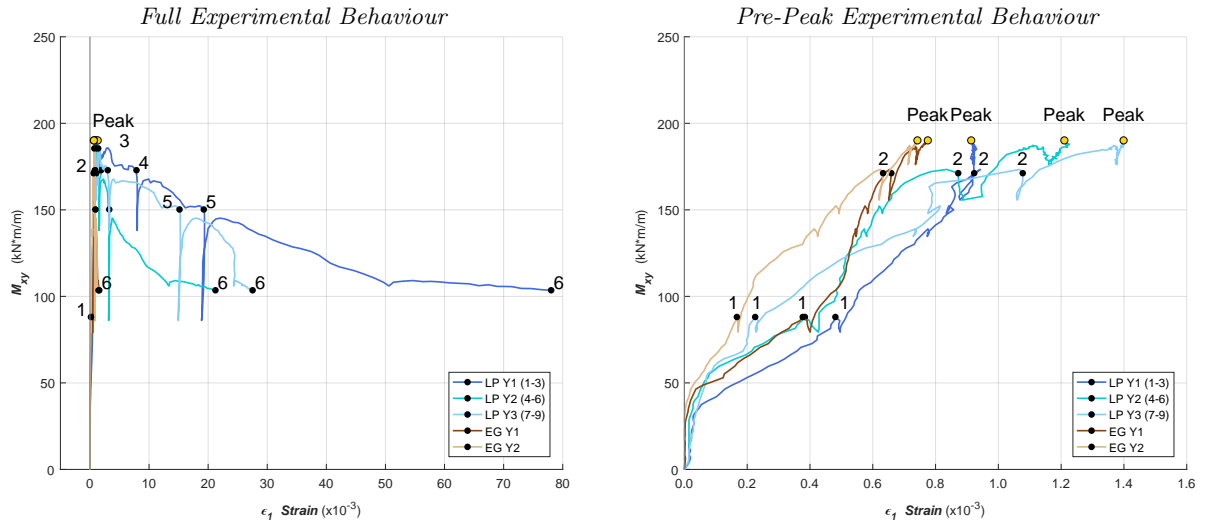


Figure 4.51: ES1 Applied Torsion vs. Principal Tensile Strain

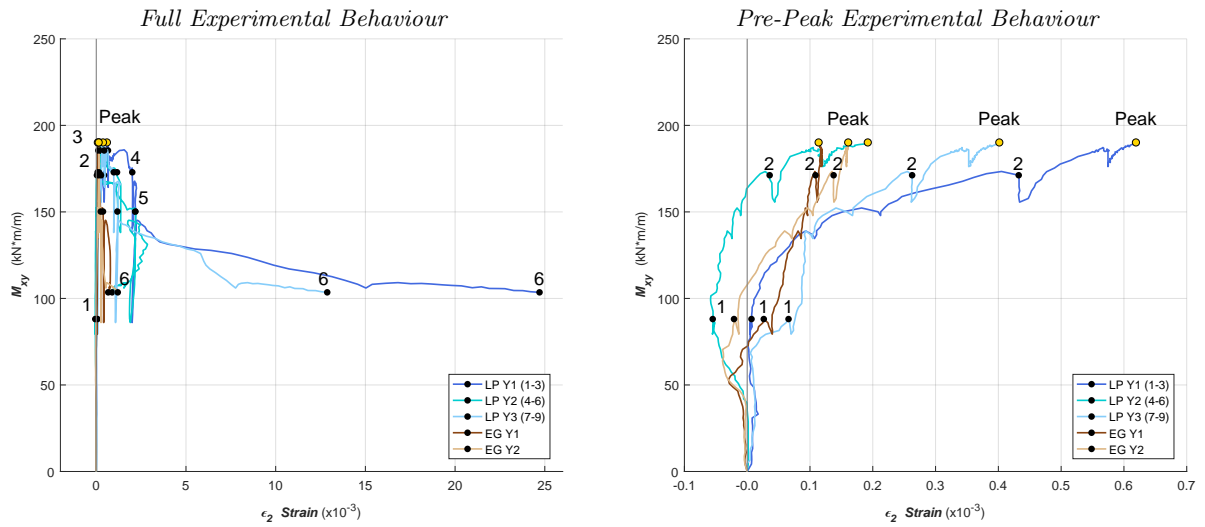


Figure 4.52: ES1 Applied Torsion vs. Principal Compressive Strain

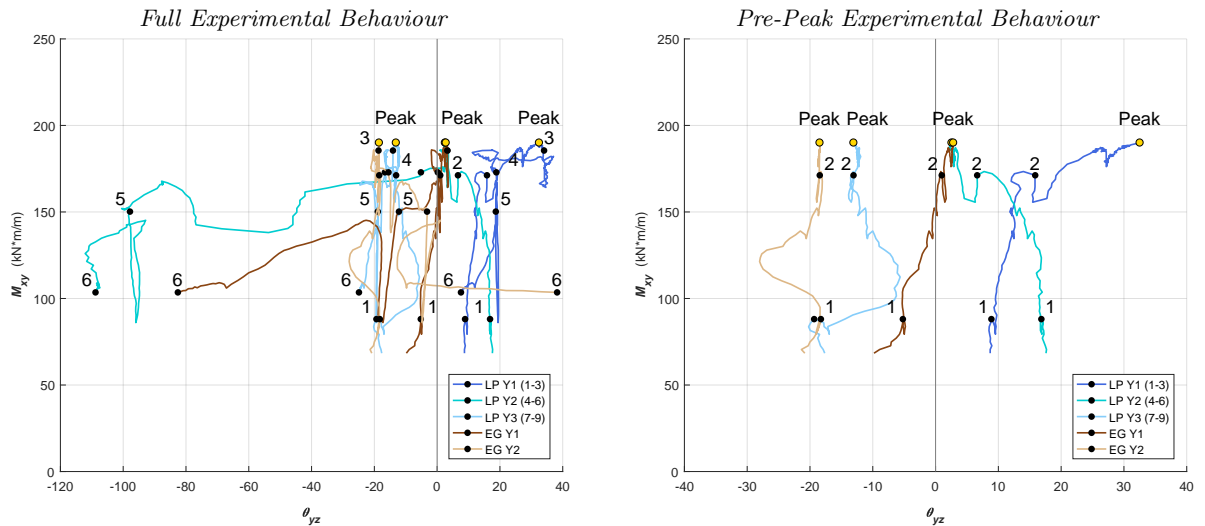


Figure 4.53: ES1 Applied Torsion vs. Principal Angle

Out-of-Plane (YZ & XZ) Z-Direction Strains

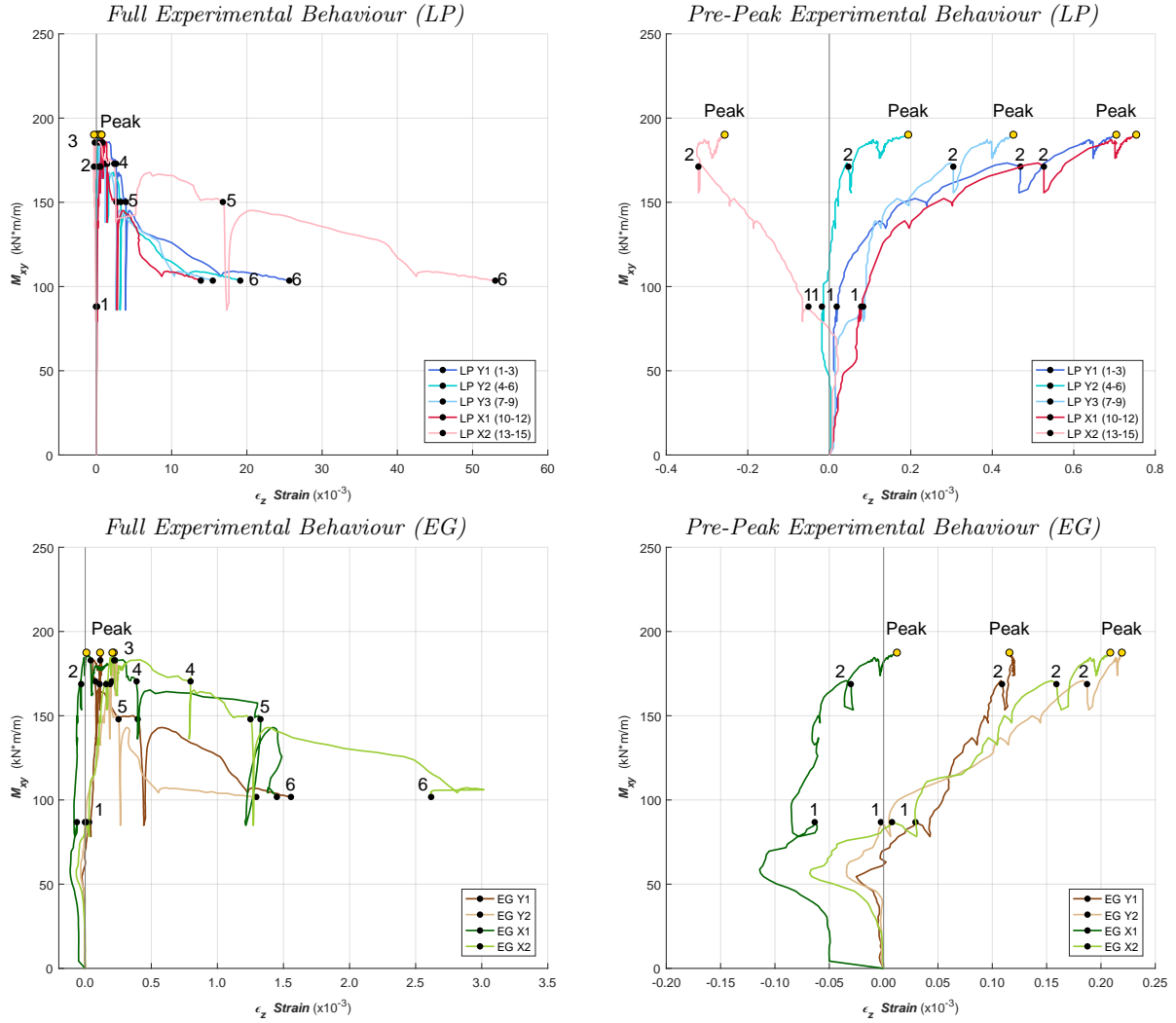


Figure 4.54: ES1 Applied Torsion vs. Through the Thickness (Z) Strain

4.4.2 Specimen ES2

Out-of-Plane (XZ) Strains

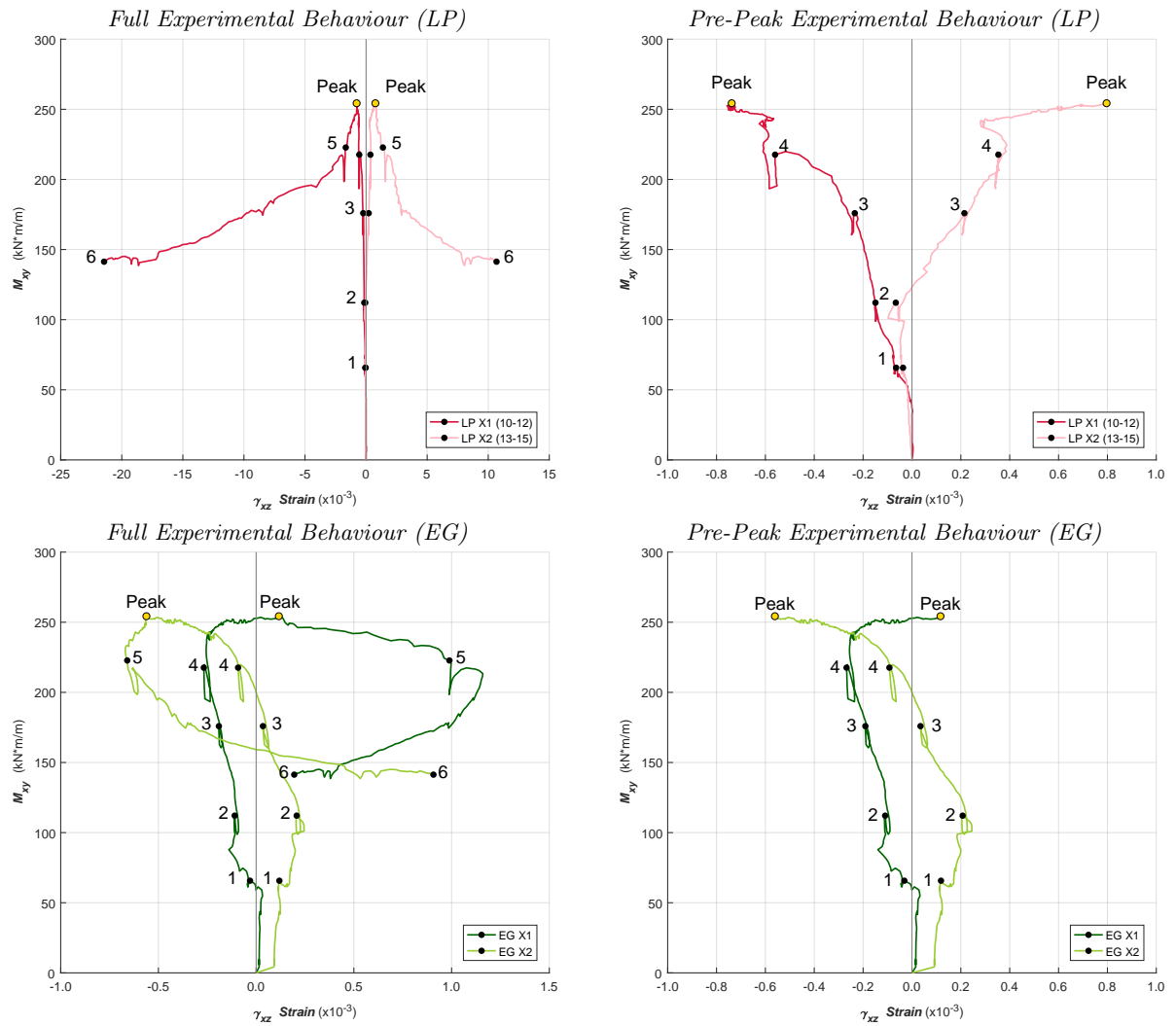


Figure 4.55: ES2 Applied Torsion vs. Out-of-Plane (XZ) Shear Strain

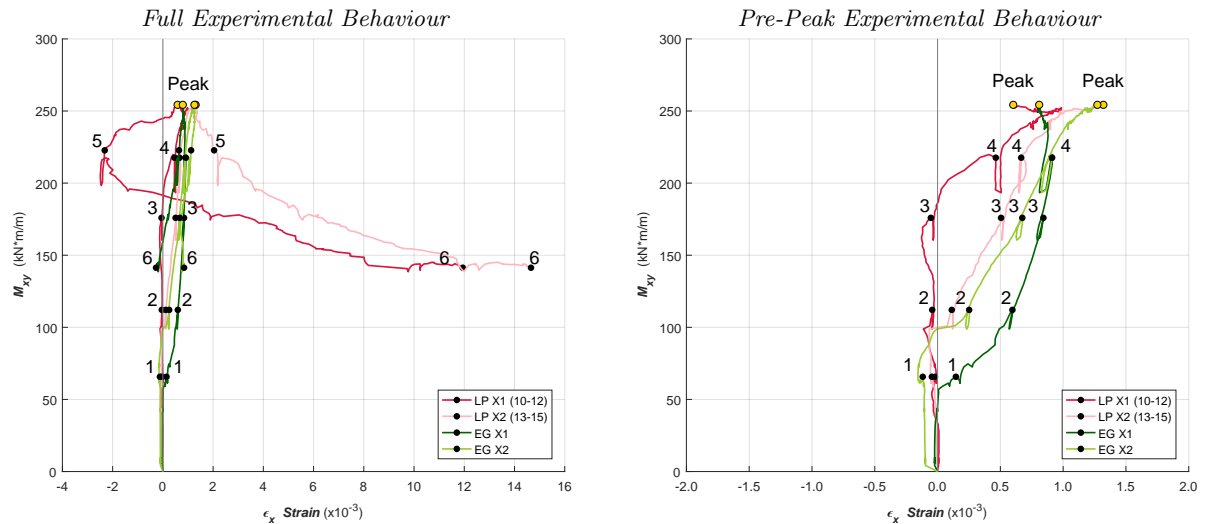


Figure 4.56: ES2 Applied Torsion vs. X-Direction Strain

Out-of-Plane (XZ) Principal Strains

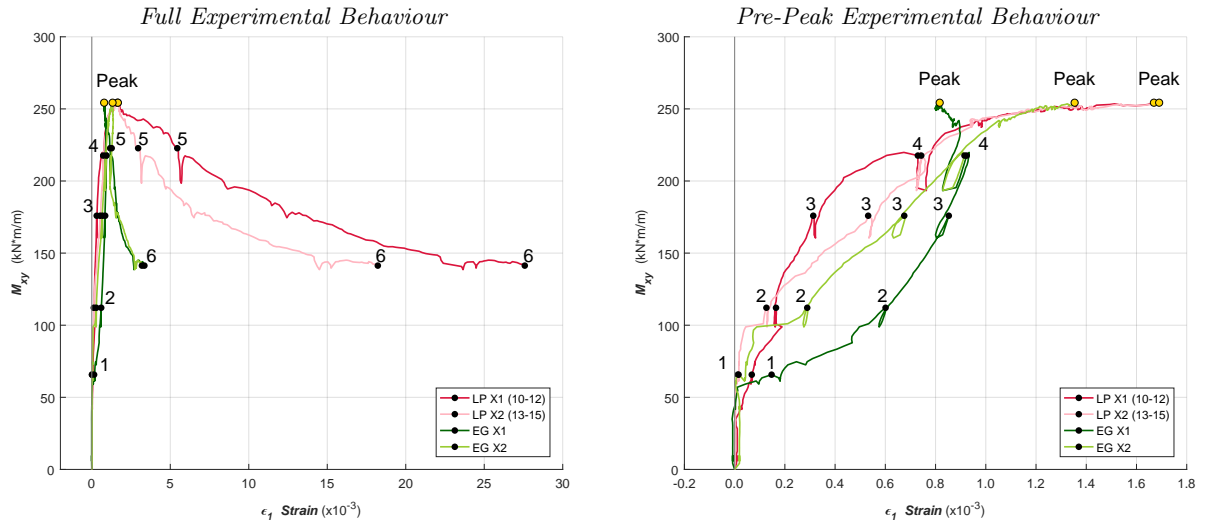


Figure 4.57: ES2 Applied Torsion vs. Principal Tensile Strain

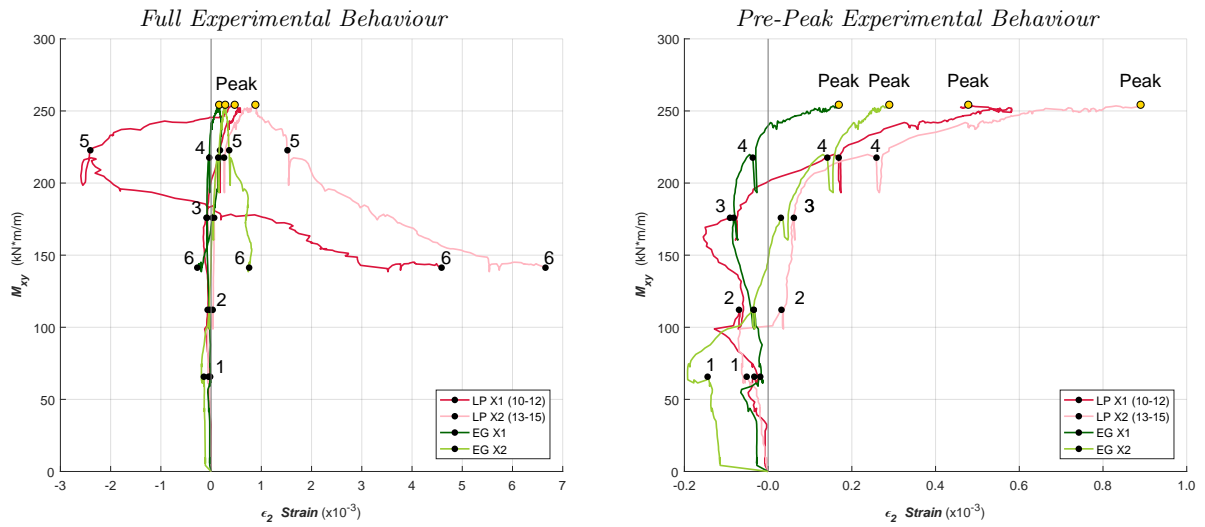


Figure 4.58: ES2 Applied Torsion vs. Principal Compressive Strain

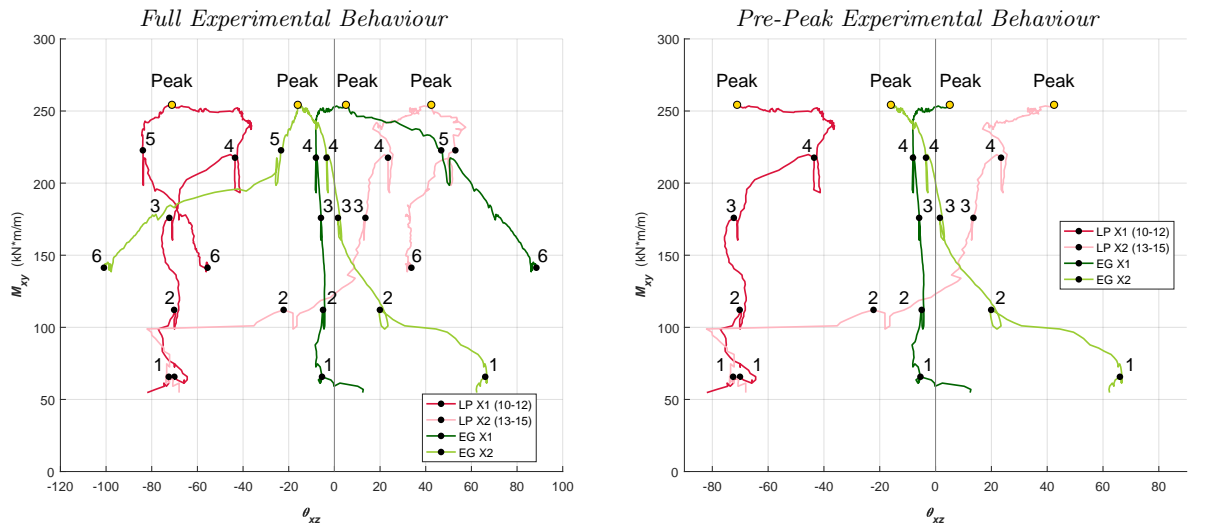


Figure 4.59: ES2 Applied Torsion vs. Principal Angle

Out-of-Plane (YZ) Strains

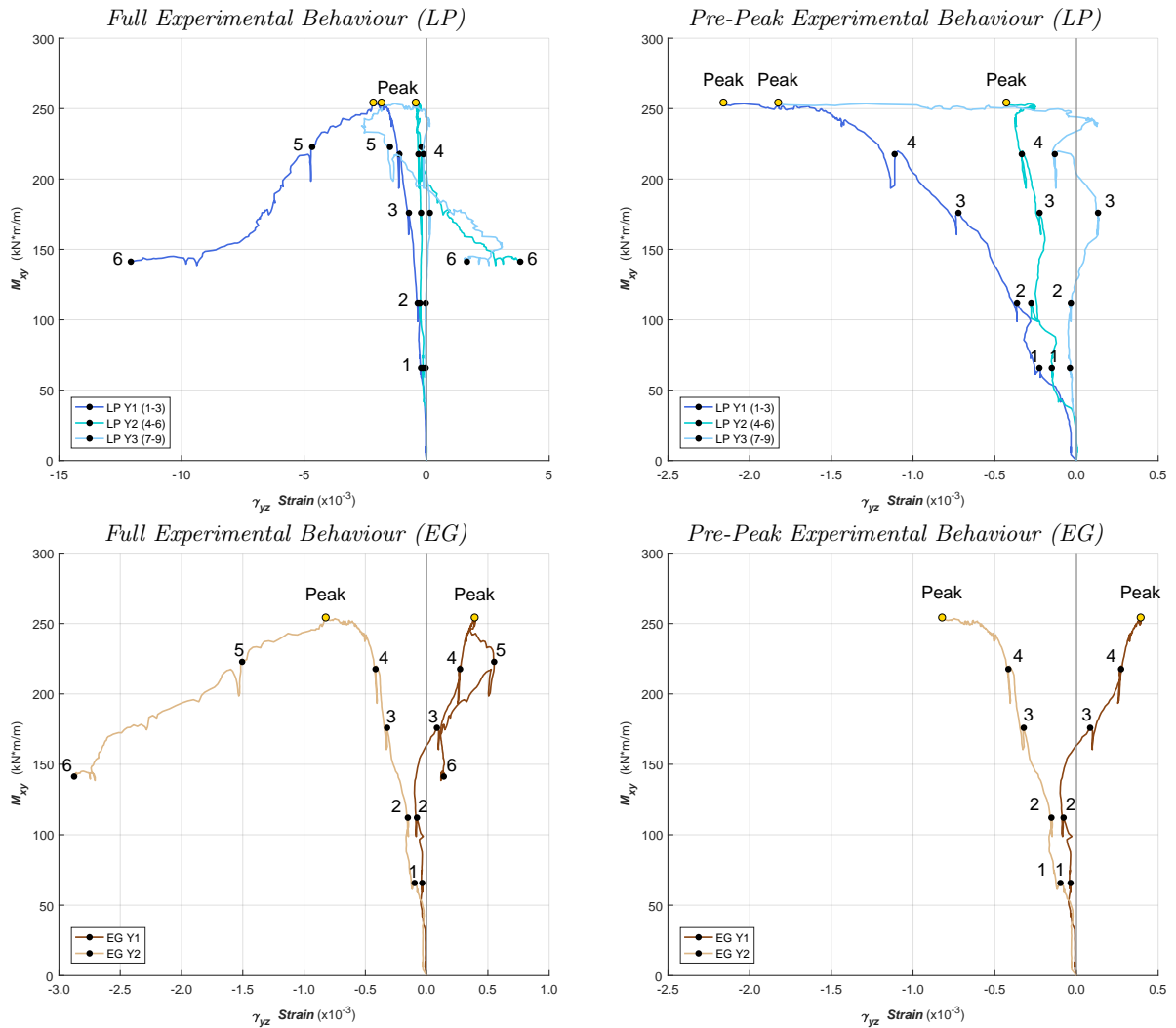


Figure 4.60: ES2 Applied Torsion vs. Out-of-Plane (YZ) Shear Strain

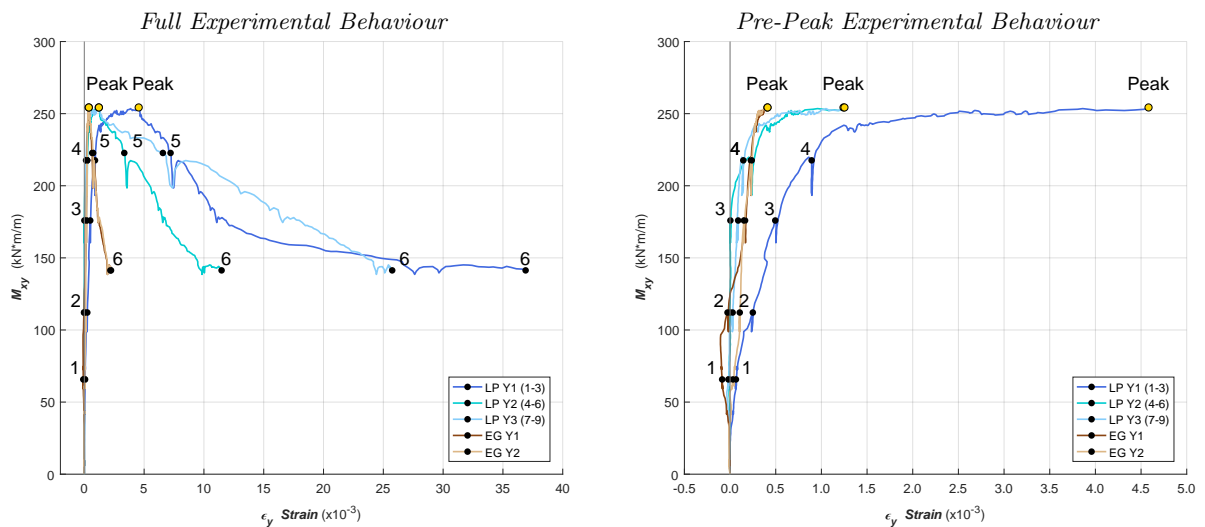


Figure 4.61: ES2 Applied Torsion vs. Y-Direction Strain

Out-of-Plane (YZ) Principal Strains

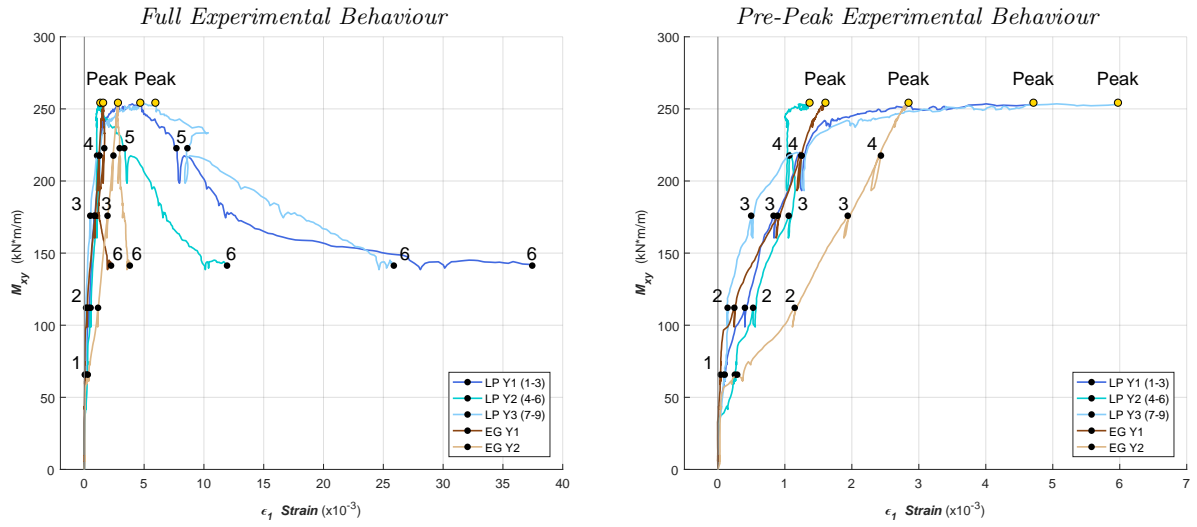


Figure 4.62: ES2 Applied Torsion vs. Principal Tensile Strain

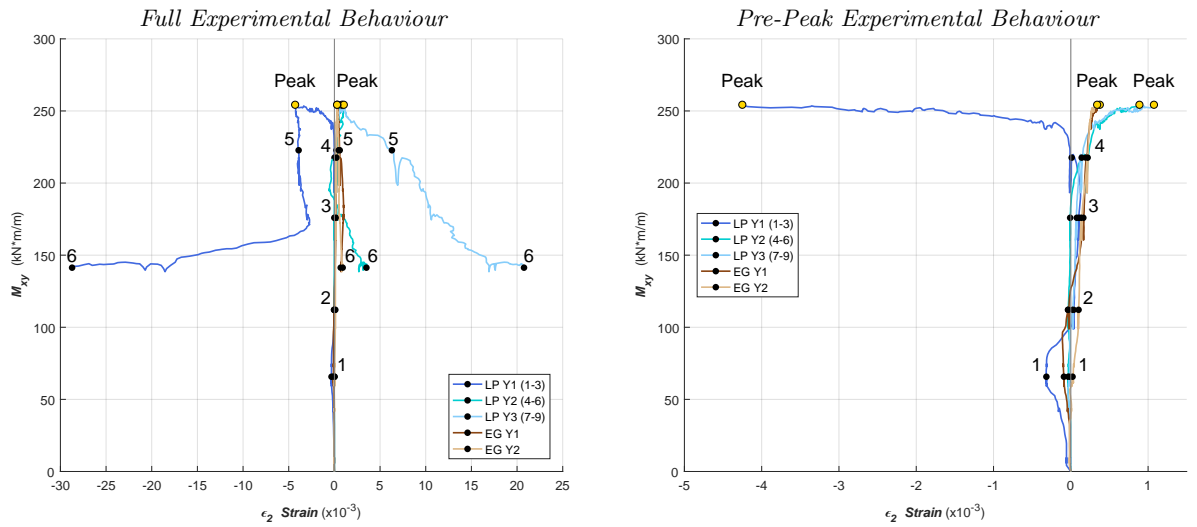


Figure 4.63: ES2 Applied Torsion vs. Principal Compressive Strain

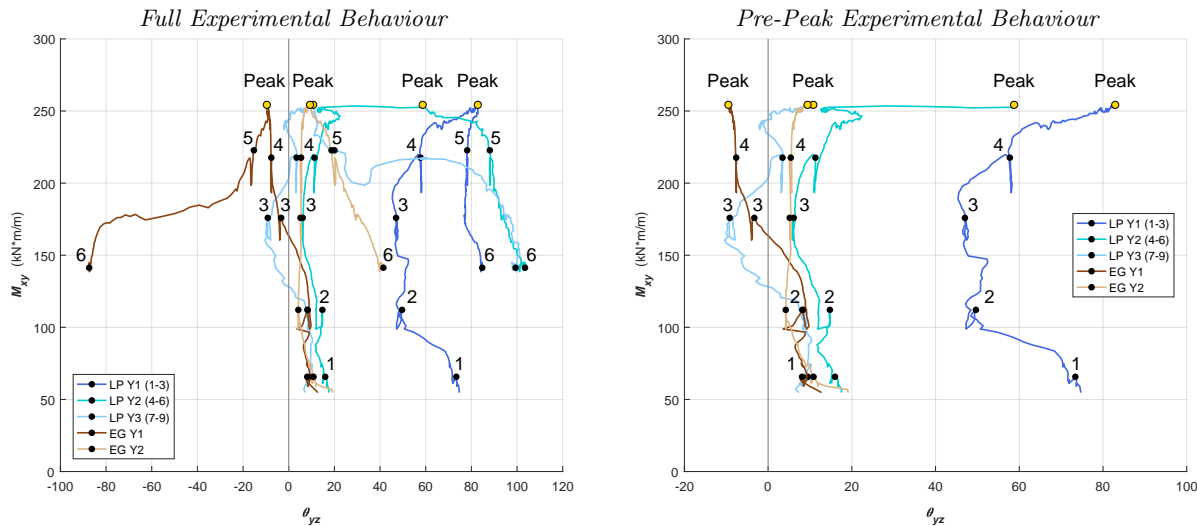


Figure 4.64: ES2 Applied Torsion vs. Principal Angle

Out-of-Plane (YZ & XZ) Z-Direction Strains

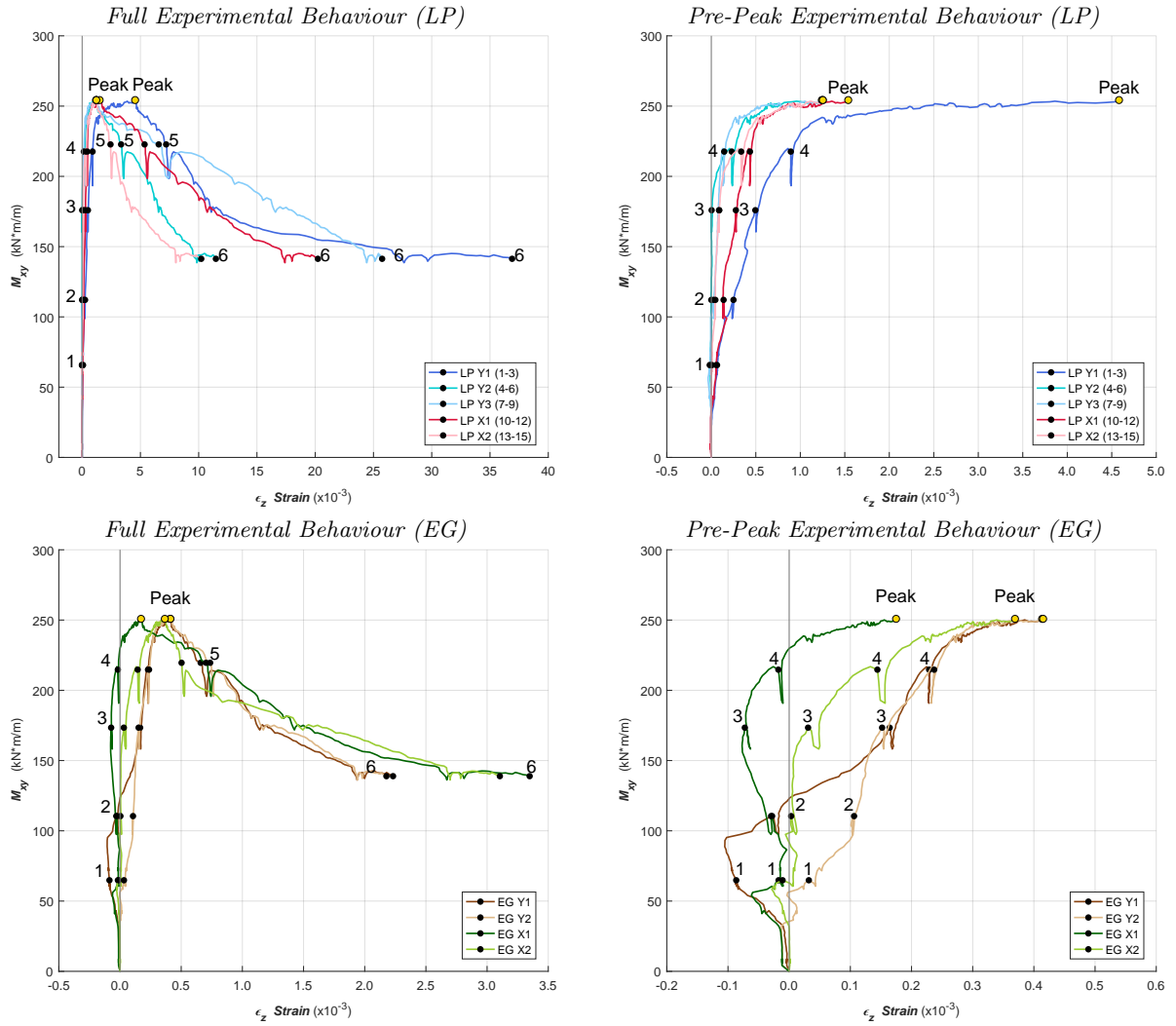


Figure 4.65: ES2 Applied Torsion vs. Through the Thickness (Z) Strain

4.5 Reinforcement SG Measurements

The gauges mounted on the steel reinforcement provided axial strain data for the duration of the tests. No additional calculations were required, the averaged data for each reinforcement direction and specimen face are simply presented in Table 4.7 and in the subsequent figures. Several gauges failed before LS 6 in specimen ES1, hence the omission of this row. Also, there were no T-heads used in ES1, hence the lack of data in the $\epsilon_{s,z}$ column.

Table 4.7: SG Data at Load Stages

	$[\frac{kN \cdot m}{m}]$	$[\frac{rad}{km}]$	$[\times 10^{-3}]$		$[\times 10^{-3}]$		$[\times 10^{-3}]$
	M_{xy}	ϕ_{xy}	$\epsilon_{s,x}$		$\epsilon_{s,y}$		$\epsilon_{s,z}$
			<i>North</i>	<i>South</i>	<i>North</i>	<i>South</i>	
ES1							
<i>LS1</i>	86.8	15.5	0.272	0.432	0.435	0.451	-
<i>LS2</i>	168.8	46.3	0.939	1.036	1.189	1.153	-
<i>Peak</i>	187.2	58.7	1.101	1.205	1.348	1.394	-
<i>LS3</i>	182.9	60.4	1.120	1.223	1.346	1.422	-
<i>LS4</i>	170.4	80.8	1.222	1.435	1.364	1.630	-
<i>LS5</i>	147.9	96.6	1.369	1.521	1.250	1.660	-
<i>LS6</i>	101.8	139.7	-	-	-	-	-
ES2							
<i>LS1</i>	64.8	8.2	0.166	0.186	0.170	0.234	0.000
<i>LS2</i>	110.5	21.4	0.442	0.572	0.571	0.657	0.046
<i>LS3</i>	173.4	39.0	0.768	1.055	1.081	1.131	0.102
<i>LS4</i>	214.7	56.7	1.058	1.459	1.484	1.517	0.157
<i>Peak</i>	250.5	89.4	1.481	1.905	1.976	1.974	0.315
<i>LS5</i>	219.6	111.0	1.554	1.961	2.020	2.040	0.572
<i>LS6</i>	138.9	223.0	1.824	1.827	2.000	1.927	1.421

4.5.1 Specimen ES1

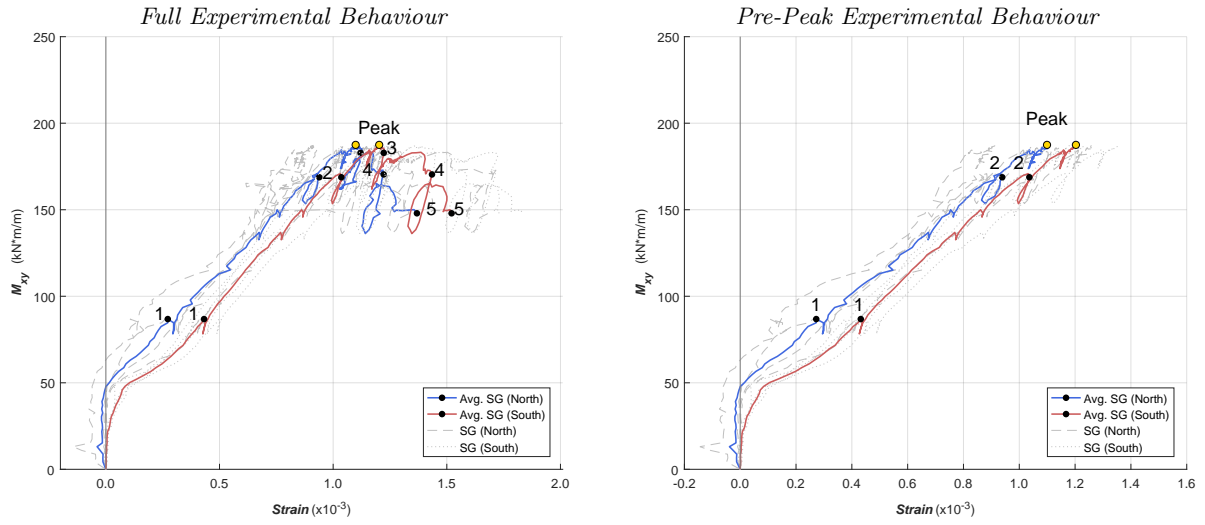


Figure 4.66: ES1 Applied Torsion vs. X-Reinforcement Strain

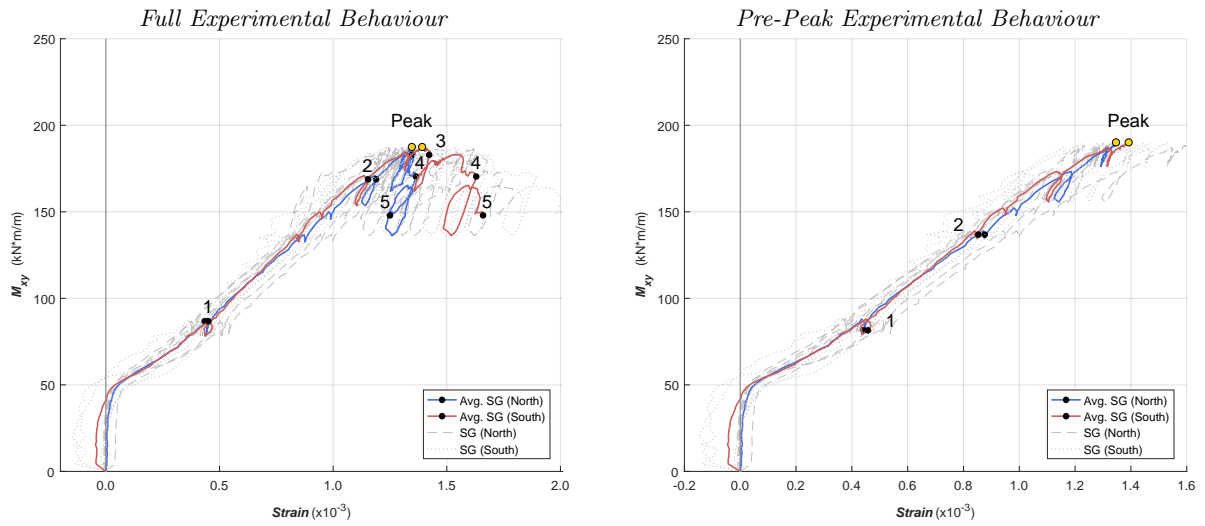


Figure 4.67: ES1 Applied Torsion vs. Y-Reinforcement Strain

4.5.2 Specimen ES2

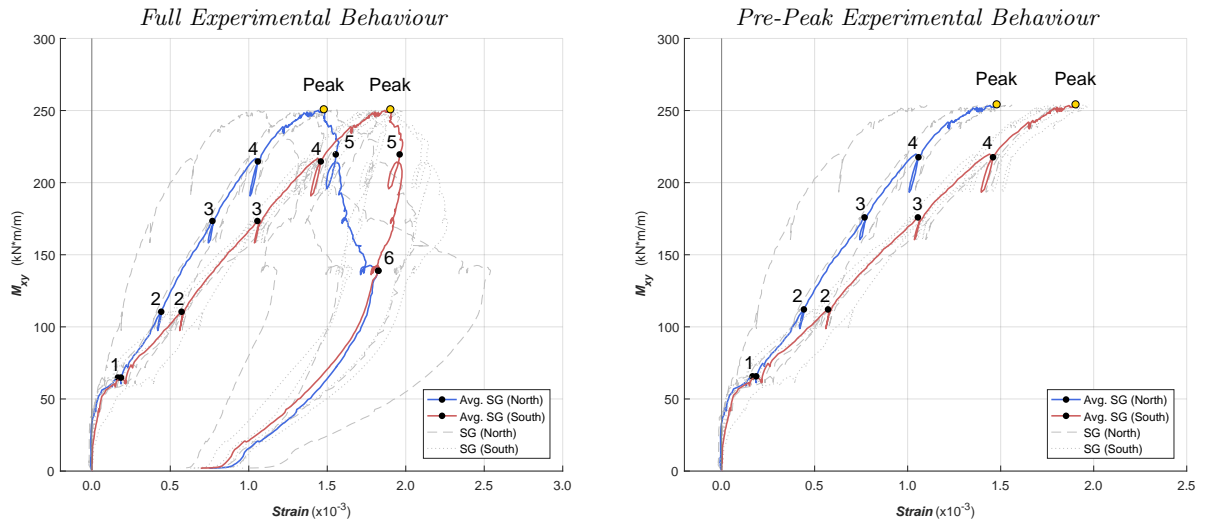


Figure 4.68: ES2 Applied Torsion vs. X-Reinforcement Strain

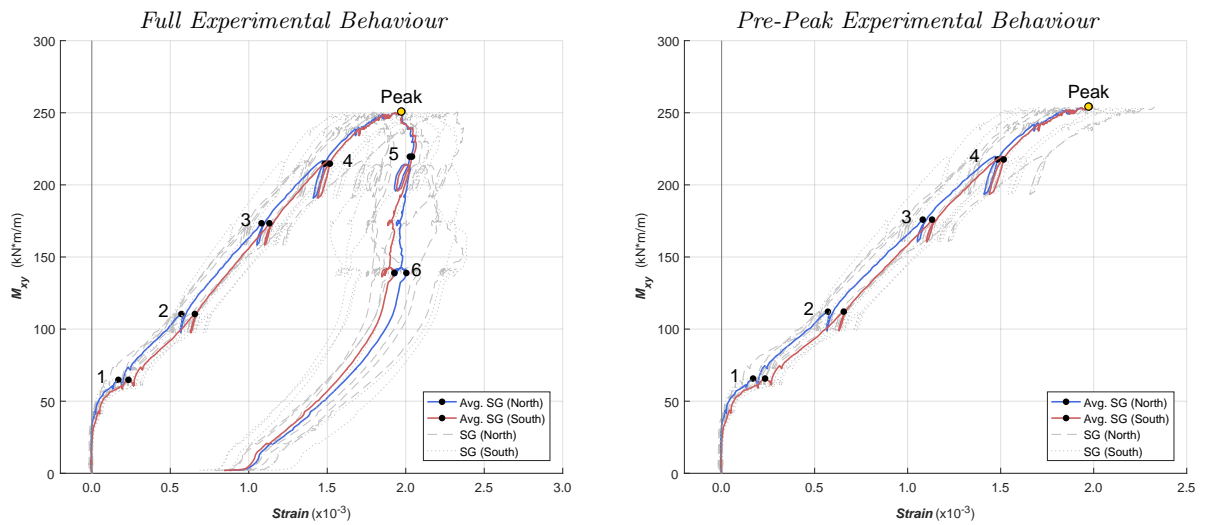


Figure 4.69: ES2 Applied Torsion vs. Y-Reinforcement Strain

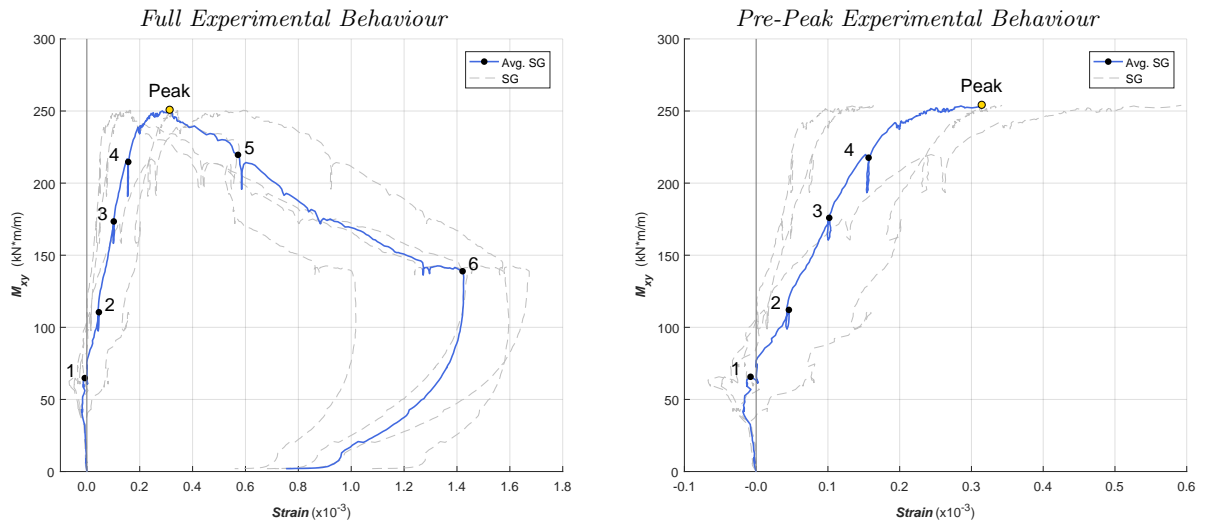


Figure 4.70: ES2 Applied Torsion vs. Z-Reinforcement Strain

Chapter 5

Discussion of Experimental Results and Observations

The following chapter will present a discussion on the qualitative observations made during both tests, followed by numerical comparisons and further analysis of certain important variables that were introduced in the previous chapter.

The first part of the chapter describes the progression of the experiments, with reference to photographs taken at the load stages for both tests. This is followed by a discussion on the physical deformation of the specimens as represented by the LED element grid position data, along with photos of the specimens post-failure. The purpose is to visually show the deformation patterns associated with applied torsion while introducing cover-spalling as the ultimate failure mechanism in both specimens.

The discussion of the numerical results in the second part of the chapter is based on the comparison of the important in-plane and out-of-plane variables for both specimens. This is used to determine what effect adding T-head reinforcement had on the peak strength and post-peak behaviour, and to justify the conclusion that cover-spalling resulted in the failure of both specimens. To simplify the comparison and discussion, averages are taken of the individual instrument readings that were shown in the previous chapter. In addition to presenting the first comprehensive analysis of pure torsion on reinforced concrete shells, this section will also be used to introduce and validate certain assumptions that were made in the derivation of the 3d-HyPT element presented in the following chapter.

5.1 Experimental Progression

The progress through the ES1 and ES2 experiments is detailed in Sections 5.1.1 & 5.1.2 through images taken of the North face of the specimens during the load stages. For reference, the torque-twist data is presented again to show what stage in the tests these images correspond to. Both the North and South faces are also shown at failure once the specimen was unloaded and the instrumentation was removed - the different crack directions visible (vertical and horizontal) are expected for a torsion test where equal and opposite in-plane shear stresses are applied on the North and South faces.

Table 5.1 summarizes the relevant information from the North face load stage photos: the number of vertical cracks, the characteristic crack width range, the maximum crack width, and additional observations. The crack width range and maximum values are in units of 'mm', and are based on the cracks measured in the test region. The cracks around the edges of the specimen are typically larger and spaced further apart due to the additional stiffness provided by the loading yokes; they are omitted from this summary as not being representative of the structural test region.

Table 5.1 is not intended as precise data since the crack measurements are based on visual inspection and are hence prone to human error. Yet this summary of the surface cracks is enough to illustrate the different behaviour in the pre-peak and post-peak phases of the tests. In the pre-peak load stages the number and size of the cracks steadily increases with the applied torsion, while in the post-peak region the surface cracking is virtually unchanged as the applied torsion drops. This is evidence of surface spalling occurring in the specimen at the peak load. As the surface concrete begins to separate from the specimen core it is essentially free to bulge outwards as the specimen progressively weakens and sheds the applied load.

Table 5.1: North Face Crack Width Summary at Load Stages

	$\left[\frac{kN \cdot m}{M_{xy}^p} \right]$	<i>Type</i>	<i>Cracks</i>			<i>Observations</i>
			#	<i>Width</i>	<i>Max.</i>	
ES1						
LS1	86.8	Pre-peak	11	0.05 - 0.10	0.15	-
LS2	168.8	Pre-peak	16	0.10 - 0.15	0.35	-
LS3*	182.9	Pre-peak	18	0.15 - 0.20	0.40	-
LS4	170.4	Post-peak	18	0.15 - 0.20	0.40	Crushing at top edge
LS5	147.9	Post-peak	19	-	-	Crack slipping and flaking
LS6	101.8	Post-peak	19	-	-	Visible spalling
ES2						
LS1	64.8	Pre-peak	6	0.05 - 0.10	0.10	-
LS2	110.5	Pre-peak	11	0.10 - 0.15	0.20	-
LS3	173.4	Pre-peak	15	0.10 - 0.20	0.35	-
LS4	214.7	Pre-peak	16	0.15 - 0.25	0.55	-
LS5	219.6	Post-peak	16	0.15 - 0.25	0.55	Surface flaking
LS6	138.9	Post-peak	16	-	-	Significant cover spalling

* Slightly past the peak value, but considered in pre-peak group

5.1.1 Specimen ES1 Load Stage Photographs

Figure 5.1 presents the torque-twist relationship for specimen ES1, which corresponds to the images shown in Figures 5.2 and 5.3 at failure and at the load stages respectively.

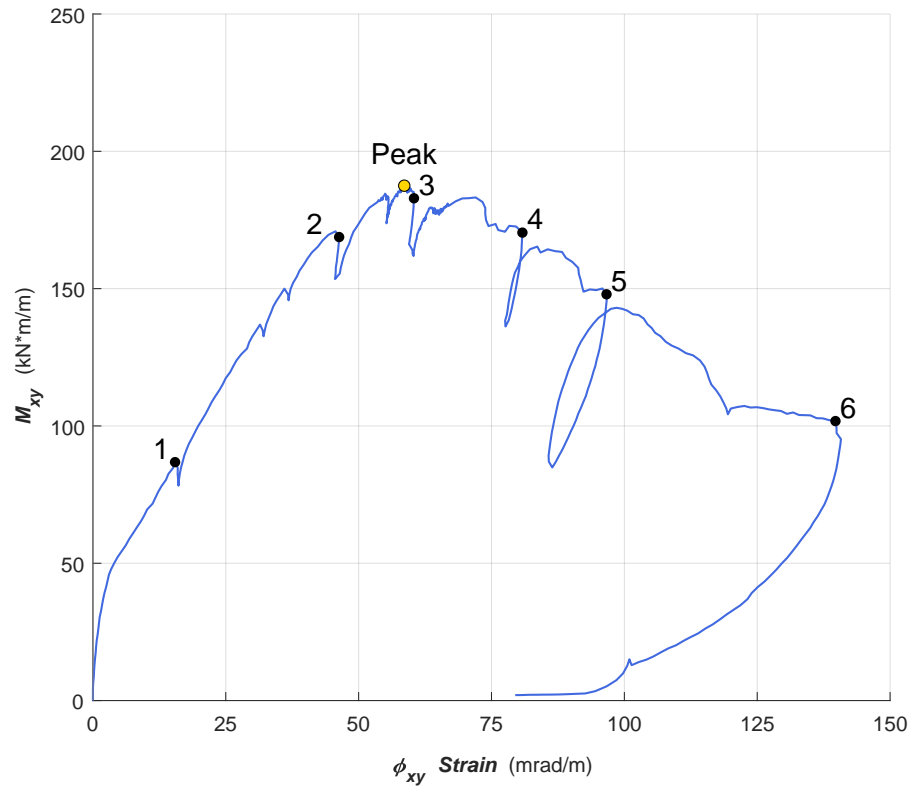


Figure 5.1: ES1 Applied Torsion-Twist at Load Stages

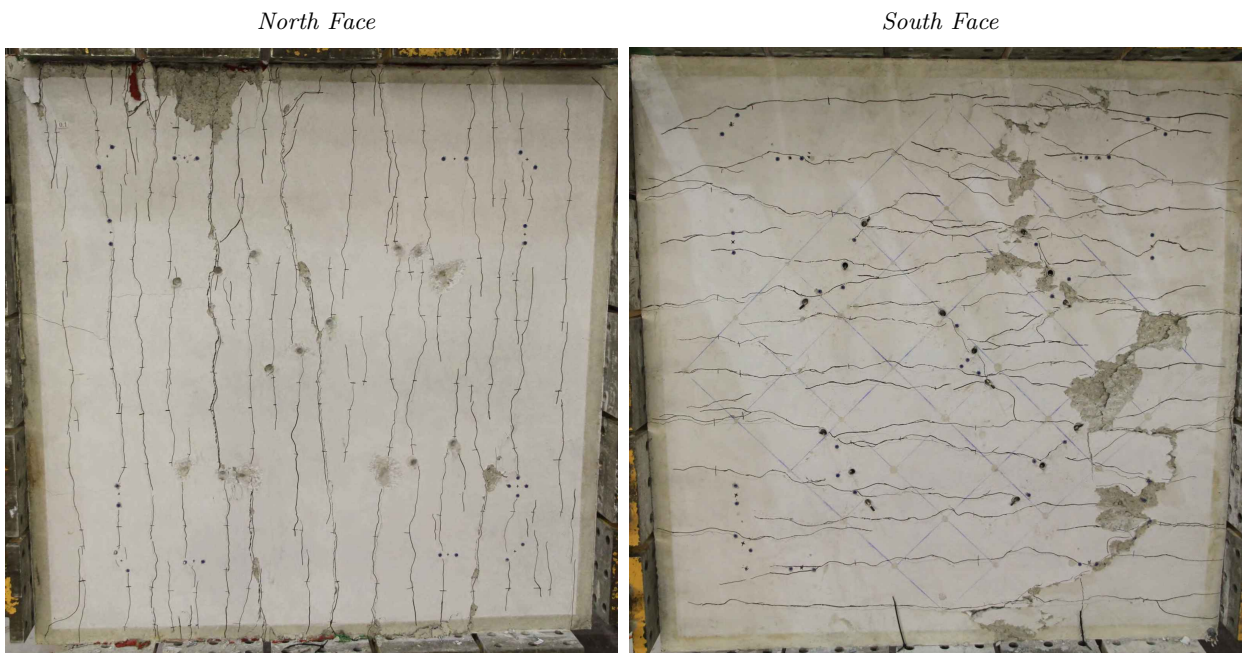
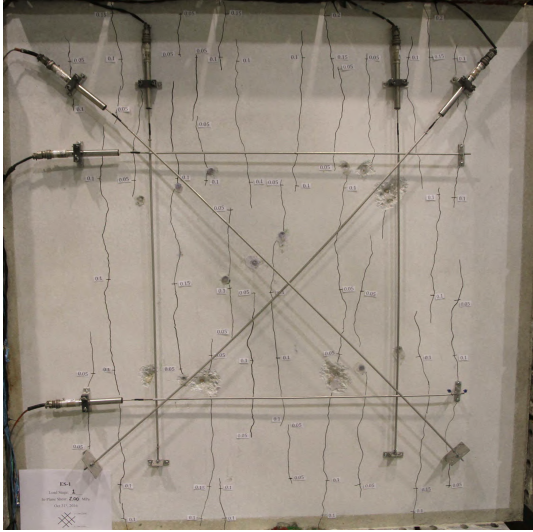
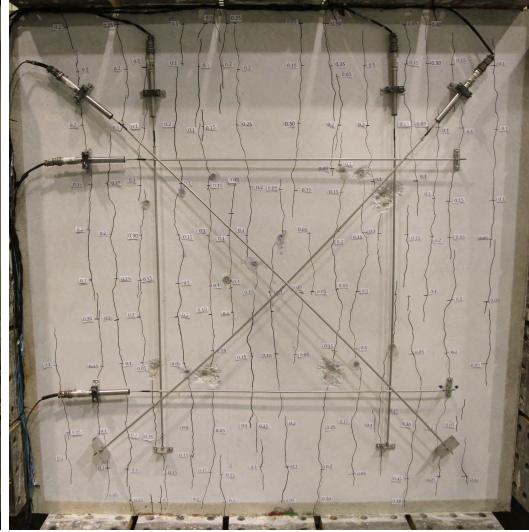


Figure 5.2: ES1 at Failure (Black Lines = Cracks)

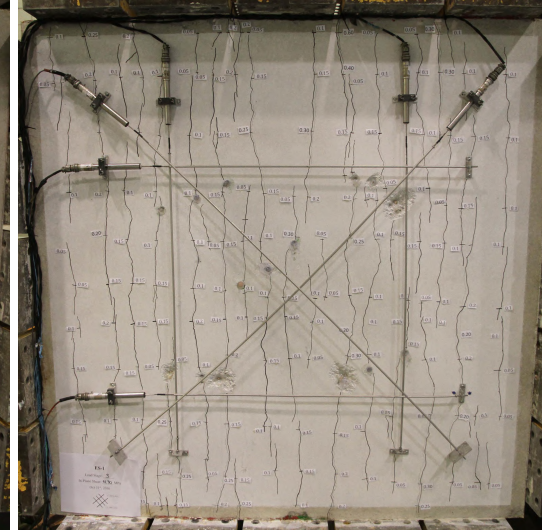
$$LS-1: M_{xy} = 86.8 \frac{kN \cdot m}{m}$$



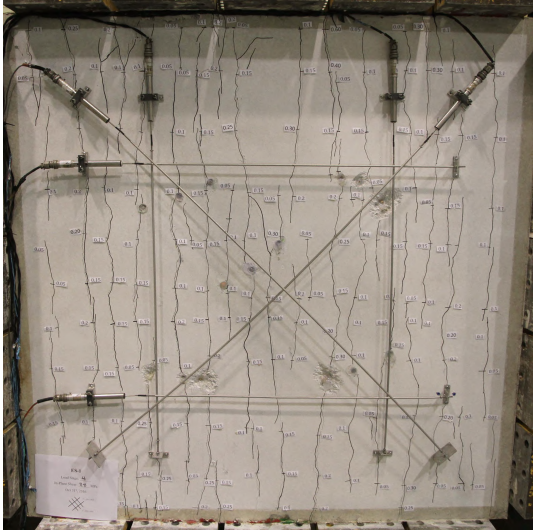
$$LS-2: M_{xy} = 168.8 \frac{kN \cdot m}{m}$$



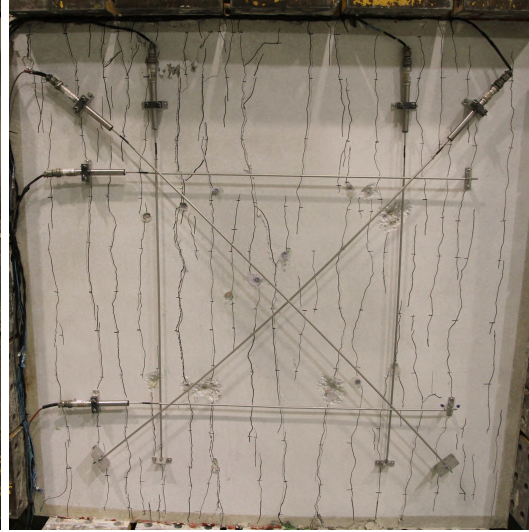
$$LS-3: M_{xy} = 187.2 \frac{kN \cdot m}{m}$$



$$LS-4: M_{xy} = 170.4 \frac{kN \cdot m}{m}$$



$$LS-5: M_{xy} = 147.9 \frac{kN \cdot m}{m}$$



$$LS-6: M_{xy} = 101.8 \frac{kN \cdot m}{m}$$

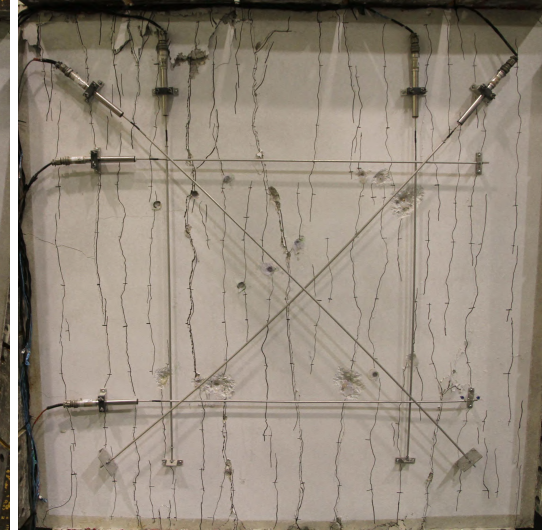


Figure 5.3: ES1 Load Stage Photographs (North Face)

5.1.2 Specimen ES2 Load Stage Photographs

Figure 5.4 presents the torque-twist relationship for specimen ES2, which corresponds to the images shown in Figures 5.5 and 5.6 at failure and at the load stages respectively.

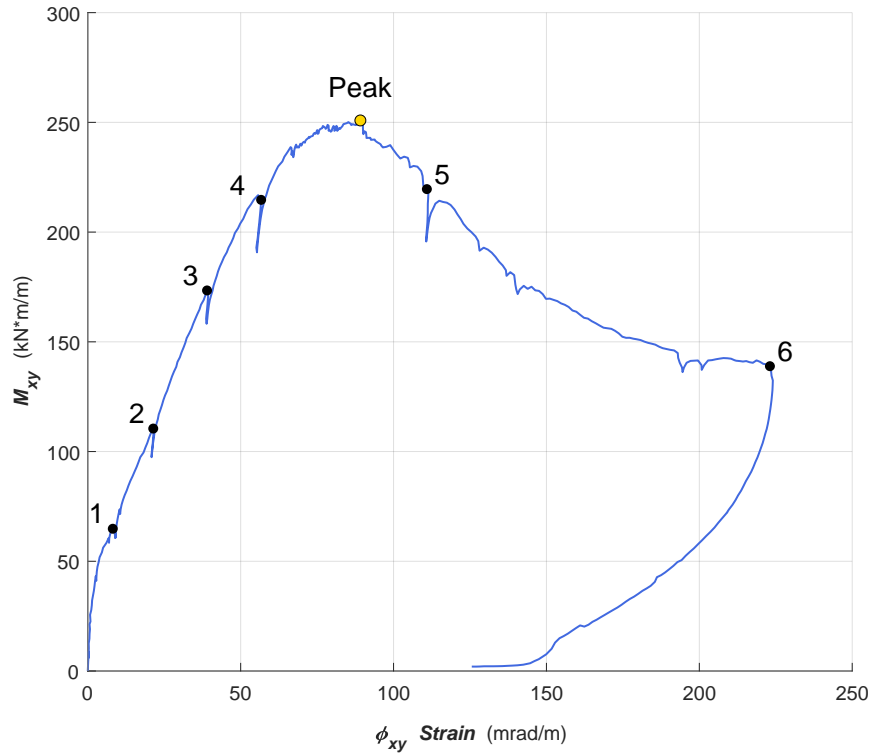


Figure 5.4: ES2 Applied Torsion-Twist at Load Stages



Figure 5.5: ES2 at Failure (Black Lines = Cracks)

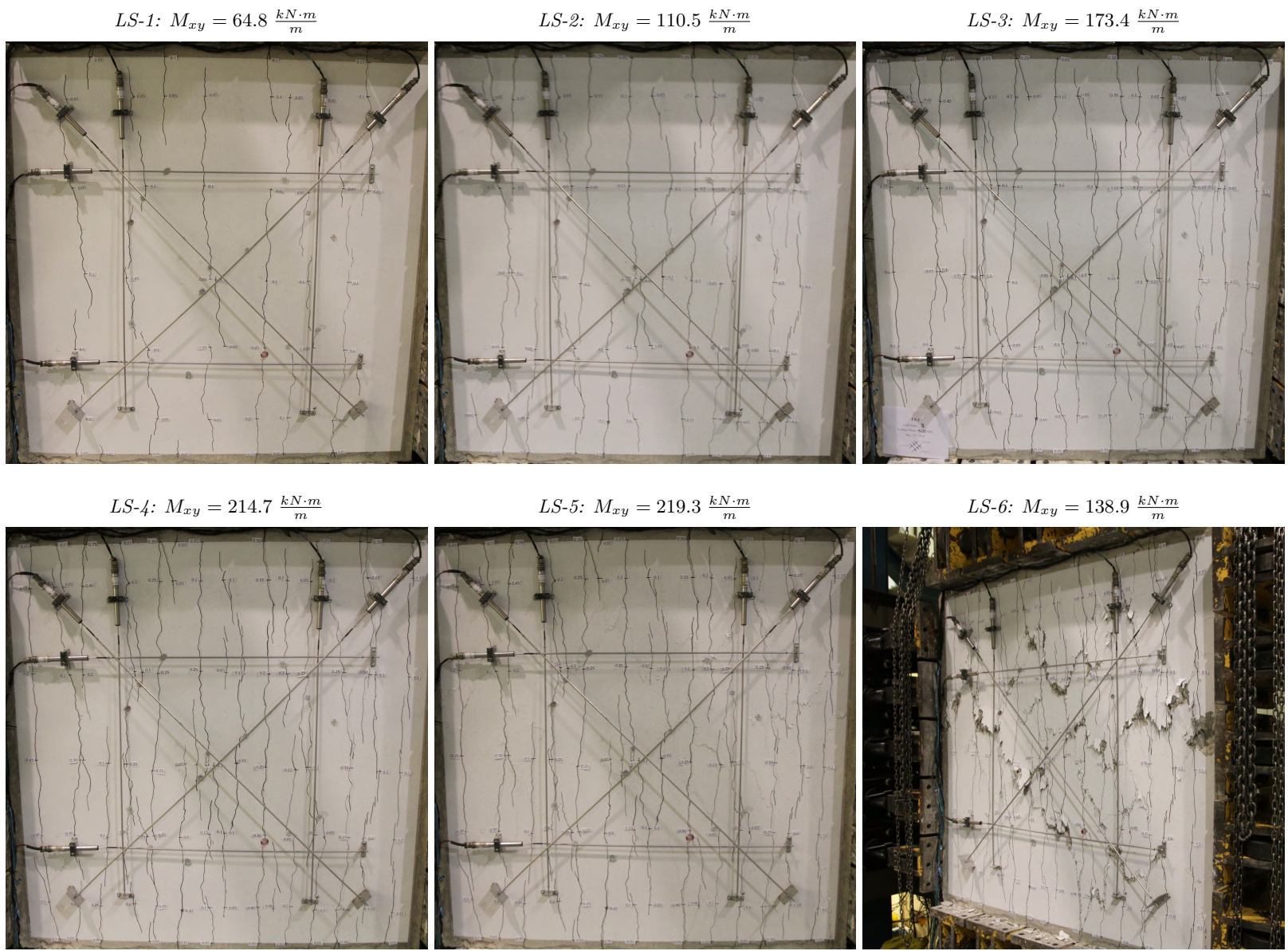


Figure 5.6: ES2 Load Stage Photographs (North Face)

5.2 Specimen Deformation and Damage

Looking more closely at the deformations and the type of damage sustained is helpful in understanding the behaviour of the specimens. Using the position data from the LED target system provides further evidence of significant cover spalling between the peak and final load stages, while the photographs of the cored locations shows separation between the core and surface concrete.

5.2.1 Surface Deformation Pattern

The surface displacement of both specimens can be mapped with a high level of precision with the LED targets that are placed on the South face. While this data is intended for the calculation of the in-plane strain state of the specimen, it can also be used to show the deformed shape of the specimen (Figure 5.7 and Figure 5.8). The initial position of the LEDs is represented by the grey plane, while the new position at either the 'Peak' or 'Final' load stage is shown in red; the corresponding point on the torque-twist plot is also shown for reference. The relative displacements between load stages and the deformed shape of the LED plane will be referred to in the following discussion.

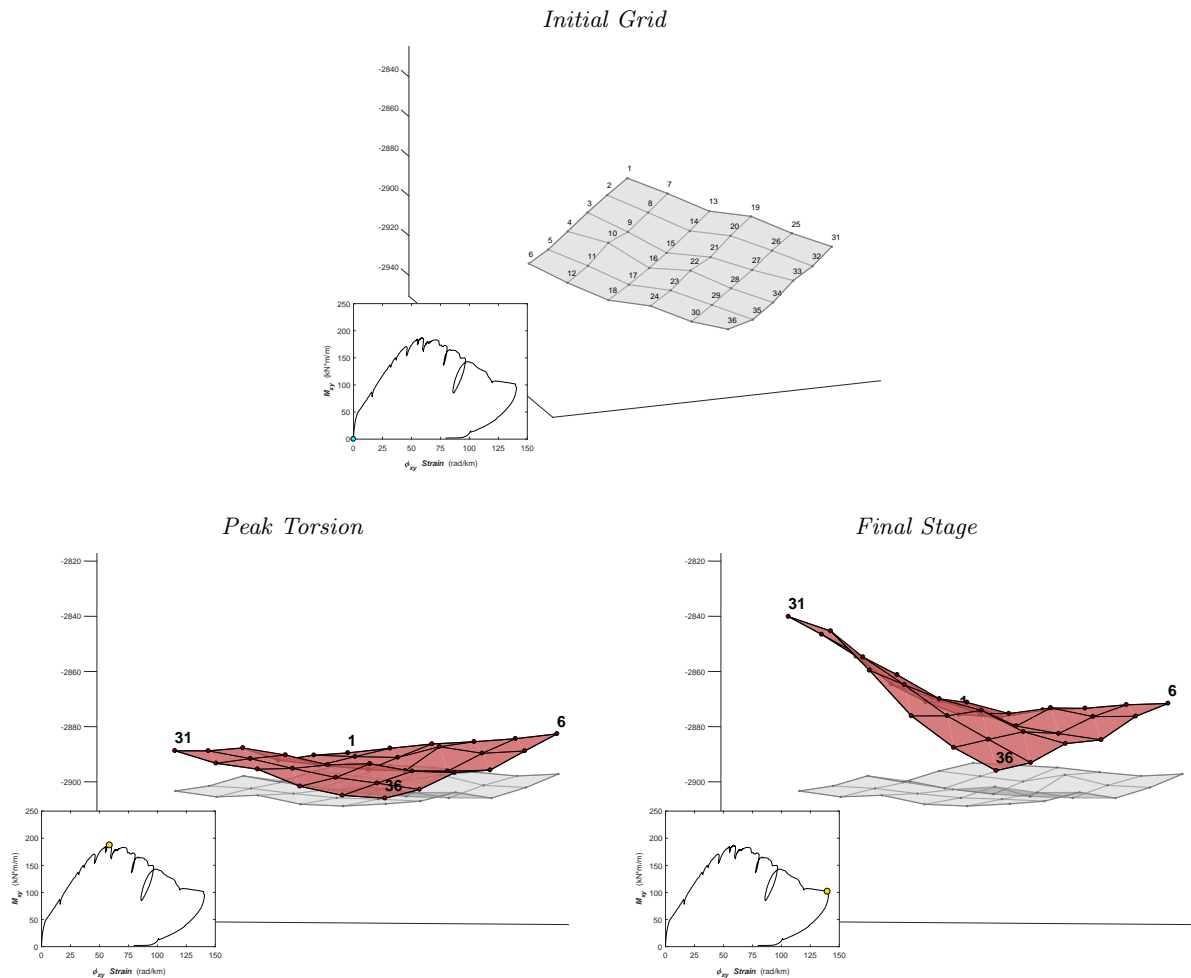


Figure 5.7: *ES1 Surface Deformations Measured by LED Targets*

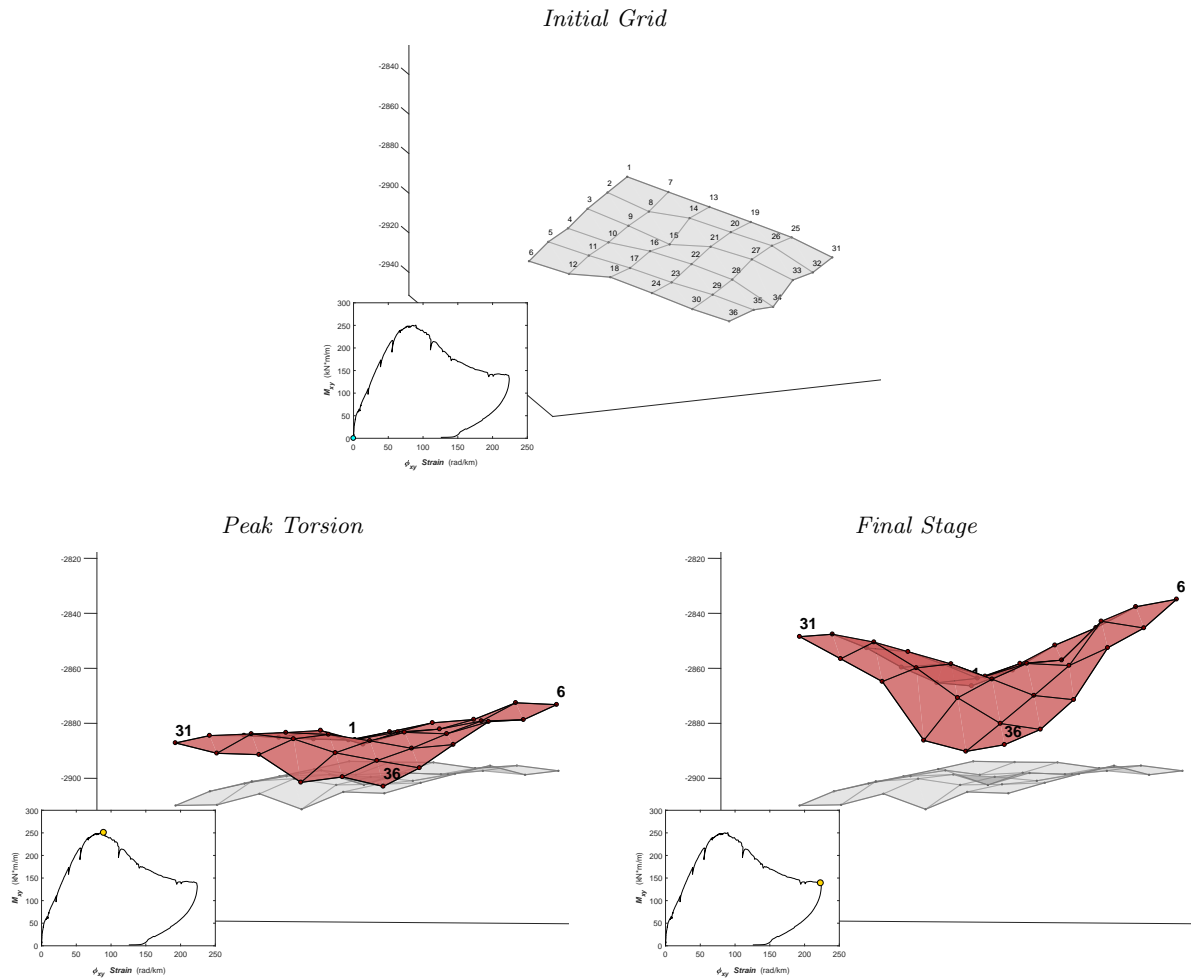


Figure 5.8: *ES2 Surface Deformations Measured by LED Targets*

The four corner LEDs in the deformed plane have been annotated according to the convention presented in Section 3.4.3, where LED #1 corresponds to the top of the test region. For any readers skeptical of the load application procedure used in the Shell Element Tester to create torsion, the deformations visible at both load stages are characteristic of applied torsion in a shell and serve as evidence for the successful execution of the test. The adjacent corners move in opposite direction relative to each other (i.e. 1 & 36 down, 6 & 31 up), forming a saddle point in the middle of the specimen. At the scale shown, this shape is beginning to form at the peak and is clearly visible at the final load stage. Another important observation from these surface deformation plots is the rate at which the cover bulges out. Between the start of the test and the peak, the surface moves proportionally much less than between the peak and the final load stage, which is evidence of cover spalling beginning at the peak and accelerating in the post-peak region. This conclusion can be inferred more easily in a frame-by-frame look at the surface deformations, which is better suited to presentation as a video rather than snapshots.

5.2.2 Spalling of Cover Concrete

Further evidence of cover spalling was documented as the specimen was removed from the testing set-up. Figure 5.9 shows the vertical cracks visible at the edge of the specimens where the front layer has separated almost completely from the core concrete. The loading yokes partially obscure the cracks and are only kept in the image because they are holding the concrete in place.

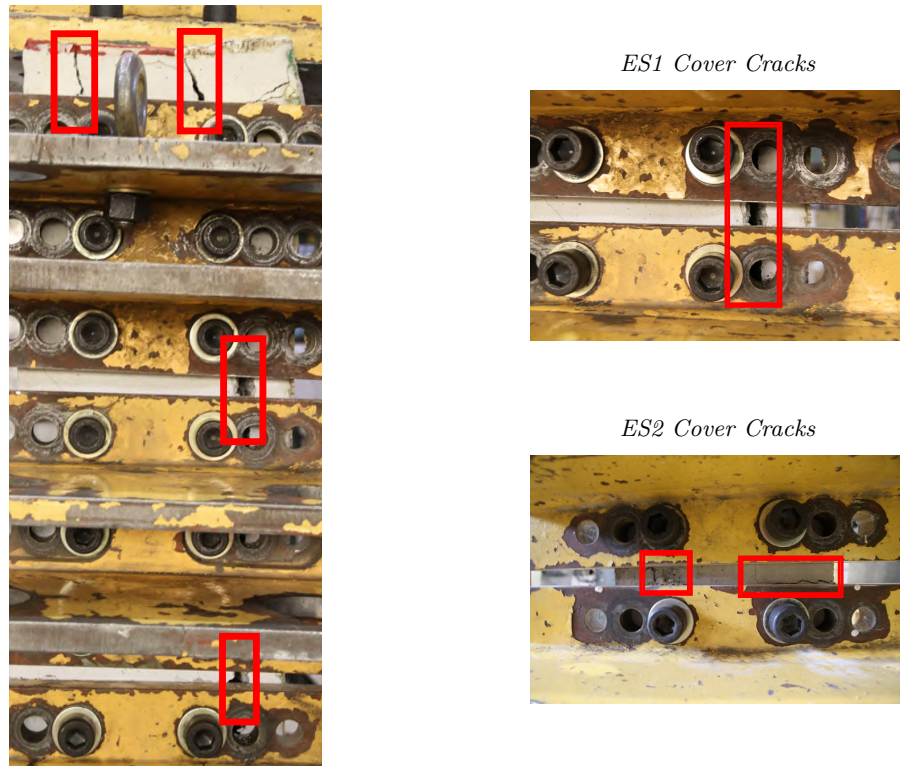


Figure 5.9: *Visible Cover Spalling at Specimen Edge*

Figure 5.10 shows the middle of the test region, where cores were extracted after completion of the experiment to better observe the interior damage. The surface concrete, at the elevation of the top layer of reinforcement, is clearly separated from the rest of the specimen. Four of these probes were made throughout the test region in both specimens, with the same observation at each location.



Figure 5.10: *Visible Cover Spalling at Cored Locations*

5.2.3 Additional Observations

The specimen was relatively intact at the conclusion of the experiment, which is an added benefit of using a displacement-controlled loading protocol. This presented a rare opportunity to observe certain characteristic mechanisms in reinforced concrete that are typically lost when a specimen fails in a load-controlled test. For example, Figure 5.11 clearly shows the post-peak slipping of the main surface crack on the North face of specimen ES1 - the horizontal black lines are marked crossing the crack at its initial formation, and the final offset indicates a relative displacement of either side.

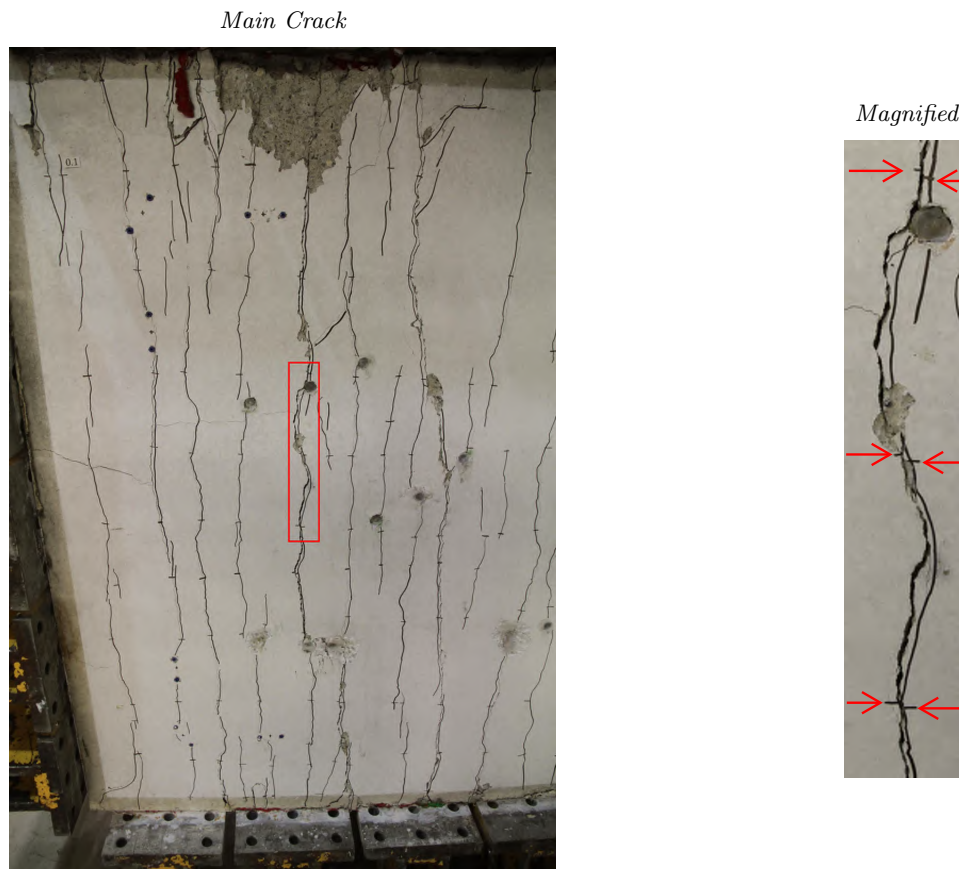


Figure 5.11: *Crack Slip in Failed ES1 Specimen (North Face)*

Figure 5.12 shows the bottom edge of the shell where the residual curvature at the end of the test is visible - the central portion covers more of the loading yoke holes than the outer edges.



Figure 5.12: *Bulging Cover and Residual Curvature in Failed ES1 Specimen (North Face)*

5.3 In-Plane Experimental Data Comparison

The following section will present a closer look at the in-plane experimental data, consisting of the LED targets, surface LVDTs, X & Y reinforcement strain gauges. The results will be compared across both specimens and different types of instrumentation, to clearly explain the differences and similarities in the experimental behaviour. For the sake of clarity, only the peak torsion points for each specimen are explicitly shown on the following plots, data on the specific load stages can be found in the previous chapter.

5.3.1 Torque-Twist

Figure 5.13 presents the high-level behaviour of both specimens in the form of the applied torsion in relation to the twist strain. The two specimens initially exhibit the same cracked stiffness, which was expected since their concrete strengths and longitudinal reinforcement ratios were the same. Although specimen ES1 begins to soften towards its peak torsion point, deviating from the linear stiffness. The addition of T-head reinforcement has a significant impact on both the strength and ductility of specimen ES2, an improvement over ES1 of 33.8% and 52.2% respectively. While experimental variability and the difference in concrete strength could possibly accounts for some of the variation, the magnitude of the difference implies that there is an inherent benefit when including T-heads. The post-peak stiffness is similar as in this region as cover spalling continues to develop in both specimens.

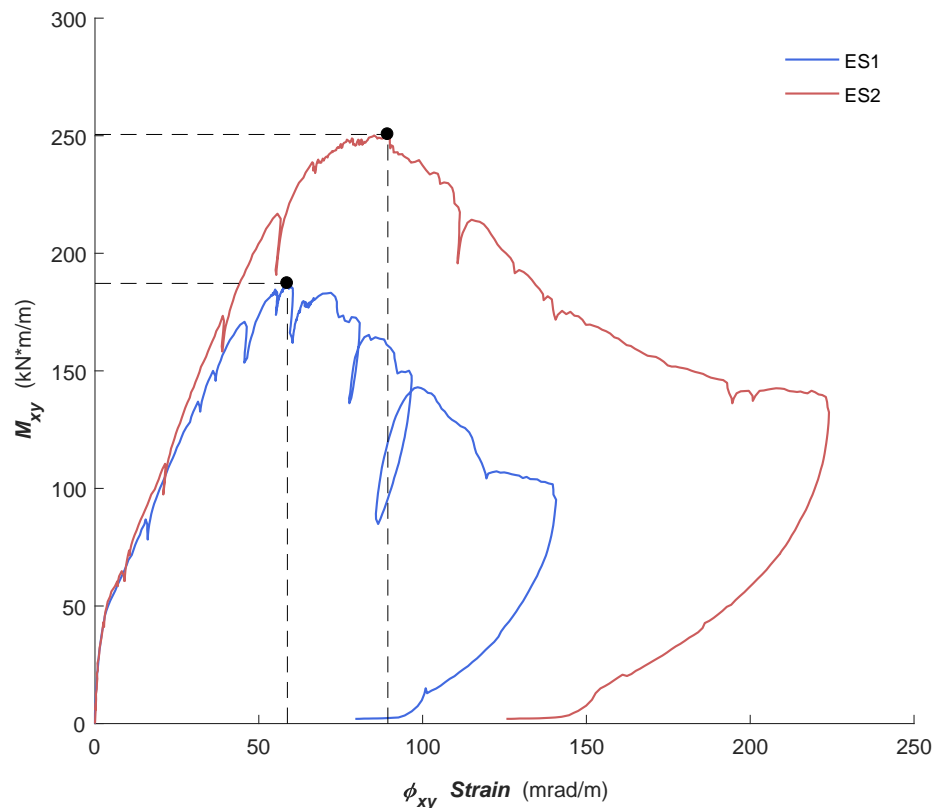


Figure 5.13: *Applied Torsion-Twist Comparison*

5.3.2 In-Plane Shear Strain

Figure 5.14 presents the in-plane shear strain as a function of the applied torsion for both specimens. The average of the 25 LED elements are plotted against the South face LVDT results only - the excellent agreement across these two measurement systems is validation for using either method. The results begin to diverge in the post-peak region as certain individual LED elements experience a greater degree of cracking and spalling than others, yet even this difference is minimal. Recall that the twist strain is calculated from the change in the in-plane shear strains across the thickness of the specimen, hence the similarity to the shape of the curve in the previous figure.

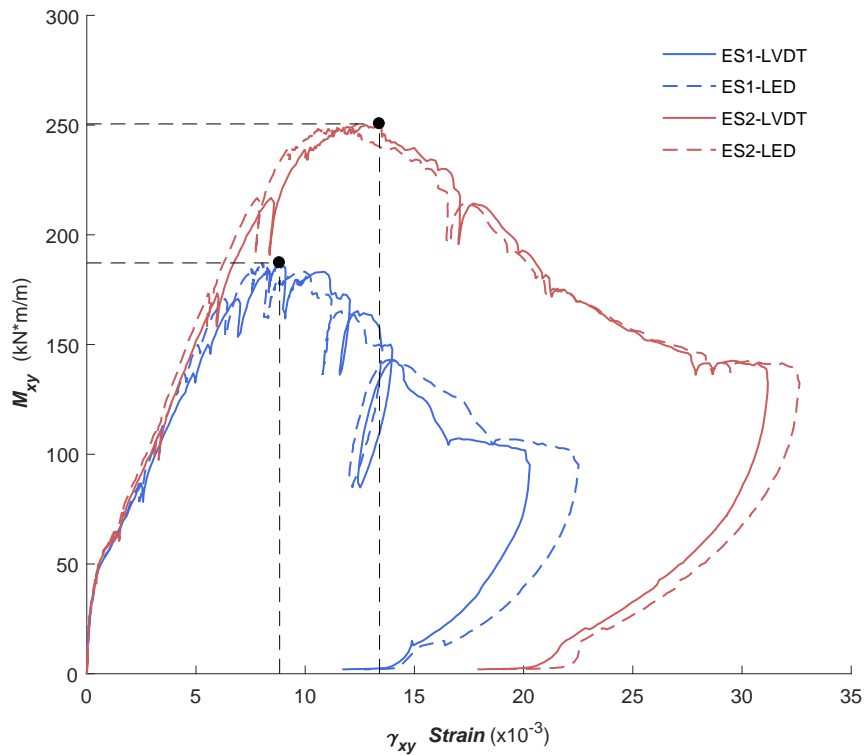


Figure 5.14: *In-Plane Shear Strain Comparison (South Face LVDTs and LEDs)*

5.3.3 Principal Tensile & Compressive Strain

The principal tensile and compressive strains in ES1 and ES2, based on the averaged LVDT data, are seen in Figure 5.15 to follow a similar trend - the same initial behaviour, followed by a deviation from the cracked linear response prior to the peak. ES2 exceeds the strains seen at the peak torsion in ES1 by 52.2% and 51.7%, for the compressive and tensile strains at respectively. Such large principal strains would typically imply either crushing of the concrete or yielding of the reinforcement, neither of which was happening based on the physical observations and data. A possible explanation for such values is the separation and subsequent deformation of the surface concrete - the curvatures achieved by such a delaminated surface would affect the readings of surface mounted instrumentation and explain such high principal strains.

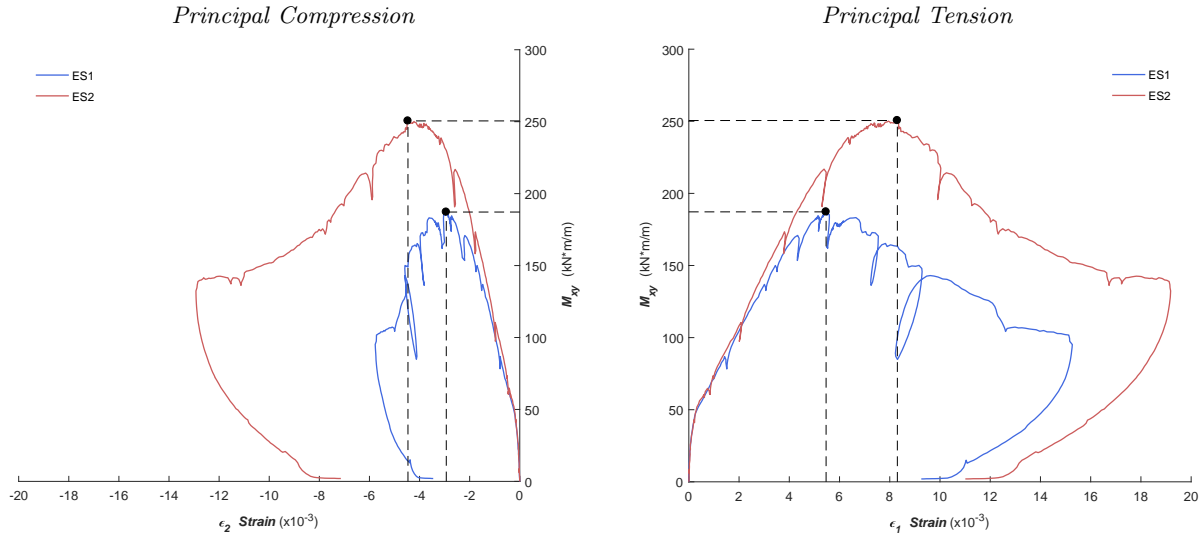


Figure 5.15: *In-Plane Principal Strain Comparison*

To further investigate these experimental results, a simplified model of ES1 was made in the program Membrane-2000, which is able to calculate the nonlinear response of a two-dimensional reinforced concrete membrane element. The North or South half of the specimen can each be roughly approximated as membranes subjected to in-plane shear stresses, the resultants of which together create a torsion in the shell. It is important to note that the nature of this program leads to several limitations in the context of recreating the real experimental conditions: no out-of-plane effects are considered, and the shear stresses are uniform over the thickness. Nonetheless, this analysis is still helpful in validating the in-plane test results.

Figure 5.16 shows a schematic of the membrane model, and the results at the peak applied shear. When compared to the experimental results for ES1 at the peak torsion there is some agreement: 7.57×10^{-3} vs. 8.37×10^{-3} for the in-plane shear strain, 6.14×10^{-3} vs. 5.47×10^{-3} for the principal tensile strain, and -1.44×10^{-3} vs. -2.93×10^{-3} for the principal compressive strain. This comparison is far from perfect, but does show that the experimental results fall within a range that can be reasonably captured by existing models. Yet these results are significantly worse when used to represent ES2 - the simplified membrane analogy is harder to justify in this case since as there are out-of-plane effects that should not be ignored.

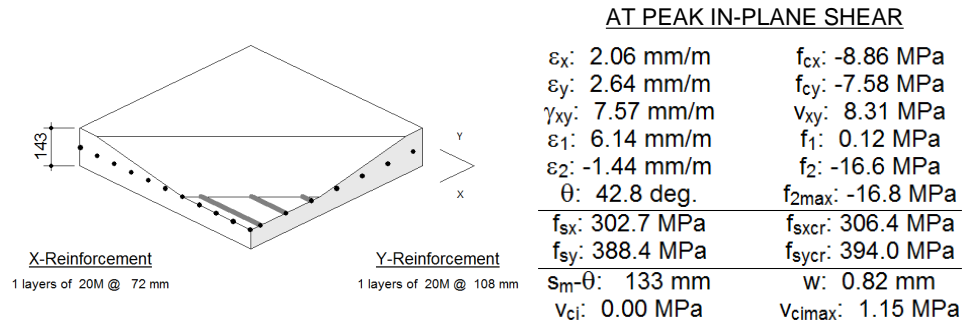


Figure 5.16: *Membrane Representation of ES1 and Results at Peak Shear Stress*

5.3.4 Strain Gauges

Figure 5.17 shows the experimental strain in the X & Y direction in-plane reinforcement as a function of the applied torsion, where the strain is an average of all gauges in both the North and South face cages. The South cage gauges typically experienced higher strains than their counterparts on the North, which is expected as the specimen was cast with the South face upwards, resulting in weaker concrete due to bleed water. The Y-direction strains are expected to be higher than the X-direction since this direction was more weakly reinforced (1.95% vs. 2.95%).

There was one fundamental conclusion drawn from these results - yielding of the reinforcement was not a factor in the failure of the specimens. Based on the material tests presented in Chapter 3, the yield strain of the 20M reinforcement bars was 3.45×10^{-3} , which is significantly higher than the average values measured in the bars at the peak torsion. On an individual basis, the highest reinforcement strain recorded at the peak torsion is approximately 2.40×10^{-3} , which is still significantly below the yielding strain.

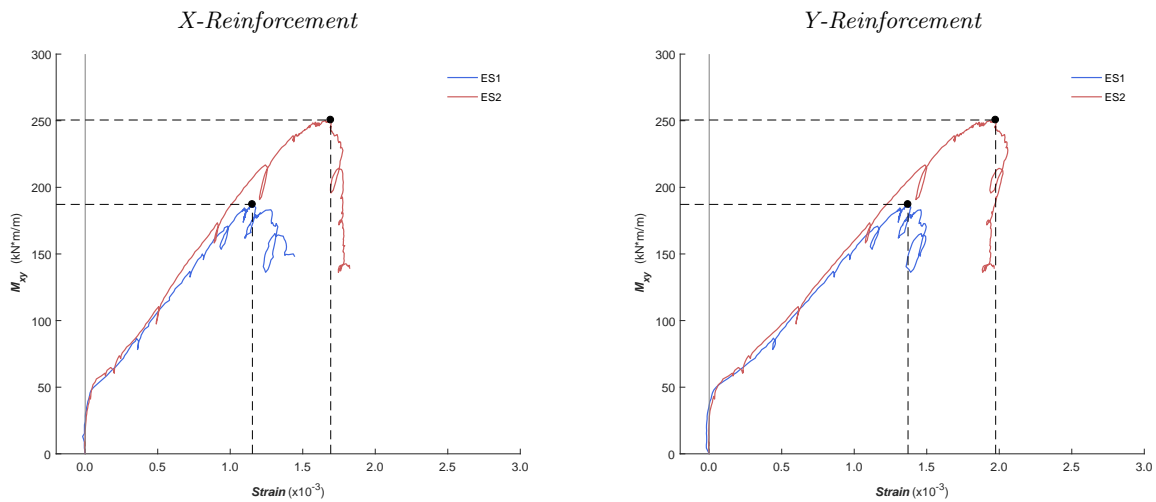


Figure 5.17: In-Plane Reinforcement Strain Comparison

The results from the membrane analysis also support this conclusion, as Figure 5.18 shows that the reinforcement stresses in the X & Y direction in-plane reinforcement are only 76% (2.62×10^{-3}) and 59% (2.04×10^{-3}) of their respective yield points. These values are much higher than what was observed in the experiments, but can be taken as an upper-bound estimate since they are based on a uniformly applied shear stress.

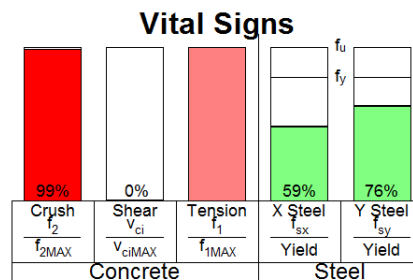


Figure 5.18: Membrane Vital Signs for ES1 at Peak Shear Stress

5.4 Out-of-Plane Experimental Data Comparison

The following section will present a closer look at the out-of-plane experimental data, consisting of the LPs and EGs in both the XZ and YZ planes, and the T-head reinforcement strain gauges. For the sake of clarity, only the peak torsion points for each specimen are explicitly indicated on the following plots. The full post-peak data is not shown since it is highly erratic, and beyond showing that failure has occurred and that the specimen cover has begun to spall is no longer useful in representing the behaviour of the specimens.

5.4.1 Out-of-Plane Shear Strain

Figure 5.19 presents the out-of-plane shear strain data as a function of the applied torsion for both specimens, where absolute values are taken of the shear strains and averaged across the type of instrumentation. The behaviour between the XZ and YZ planes was found to be similar, therefore there is no distinction between these planes in this comparison. Note that the two EGs in the YZ plane in ES1 were damaged during the casting of the specimen, which meant that no shear strain data could be calculated for these strain rosettes. Since LP-Y2 was located at the center of the specimen (in the saddle point), while all the other LPs were offset around the edges of the test region, it has been omitted from the average values for consistency.

The data from the EGs and LPs is shown separately since including them in the same average would be forcing a false equivalency. While they both measure the deformations in the XZ and YZ planes, they do so at different scales: the EGs measure the strains at a point in the core of the specimen, while the LPs measure the strains across the whole width of the specimen. For example, as the cover concrete begins to spall the LPs will record a deformation that will not be captured by the EGs located in the core of the specimen. This difference is clearly manifested in the data when comparing the the pre-peak and post-peak regions. The ratio of the LP/EG strain at the point where flattening of the curves begins (indicating that failure is imminent) occurs at 2.19 and 1.62 for ES1 and ES2 respectively. Looking one load stage into the post-peak region these ratios have increased to 3.07 and 2.18 for ES1 and ES2 respectively.

These data show that there are significant deformations in the out-of-plane direction in both specimens, which was a hypothesis this experimental program was designed to investigate. The flattening of the shear strain curves, indicating the cracking and relative separation of the North and South face of the shells, clearly precedes the peak loads in both experiments. As the out-of-plane shear strain in the core increases (see EGs), ES1 as a whole weakens and the peak load is reached as the cover begins to spall shortly after. Meanwhile, ES2 exhibits similar behaviour up to the point where ES1 fails, but has a stiffer response beyond this. The specimen is clearly softening beyond this point (see EGs), but does so in a much more gradual manner resulting in a higher peak torsion. An explanation for this is that the out-of-plane T-head reinforcement provides additional resistance to the core of the specimen, giving the specimen as a whole more capacity in resisting the out-of-plane deformations and delaying the core failure and subsequent cover spalling.

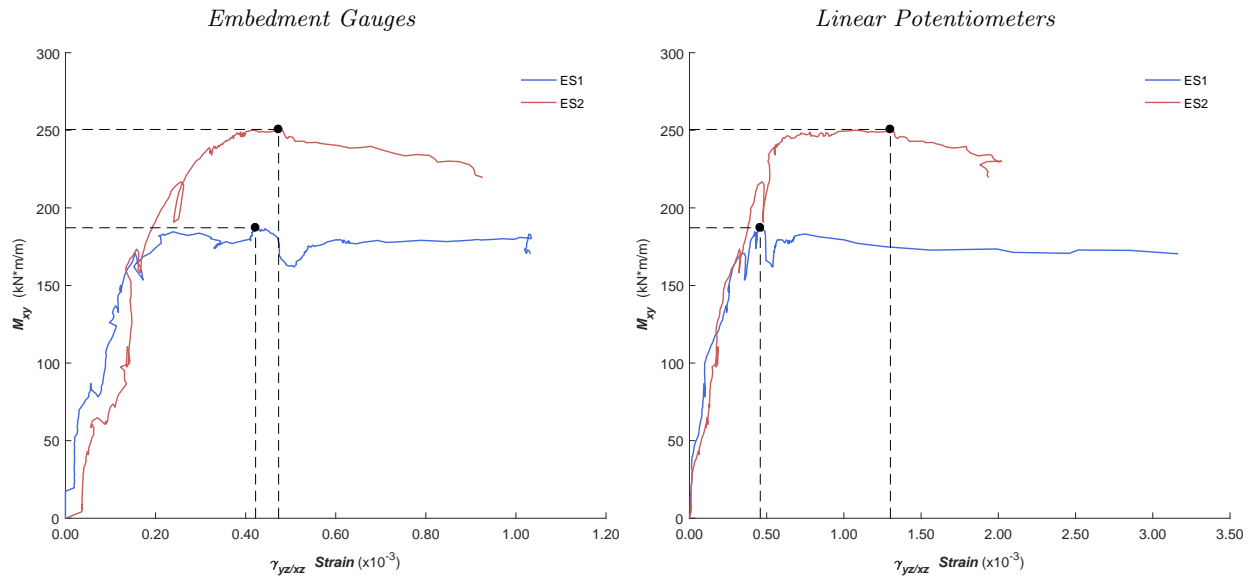


Figure 5.19: Out-of-Plane Shear Strain Comparison

5.4.2 Through the Thickness Strain (Z-dir)

The relative deformation of the North and South face, or the expansion of the specimen, is represented by the strain in the Z-direction shown in Figure 5.20. These averaged values are based on all the out-of-plane instrumentation, even the EGs in the YZ plane for ES1 were useful as the Z-direction gauge was functional. As the cover begins to spall the strains increase rapidly, which continues into the post-peak region as seen by the data one load stage into this region (plotted in Figure 5.20). The relative difference in the magnitude of the EGs and LPs also indicates that bulging of the surface is where the subsequent deformations were concentrated.

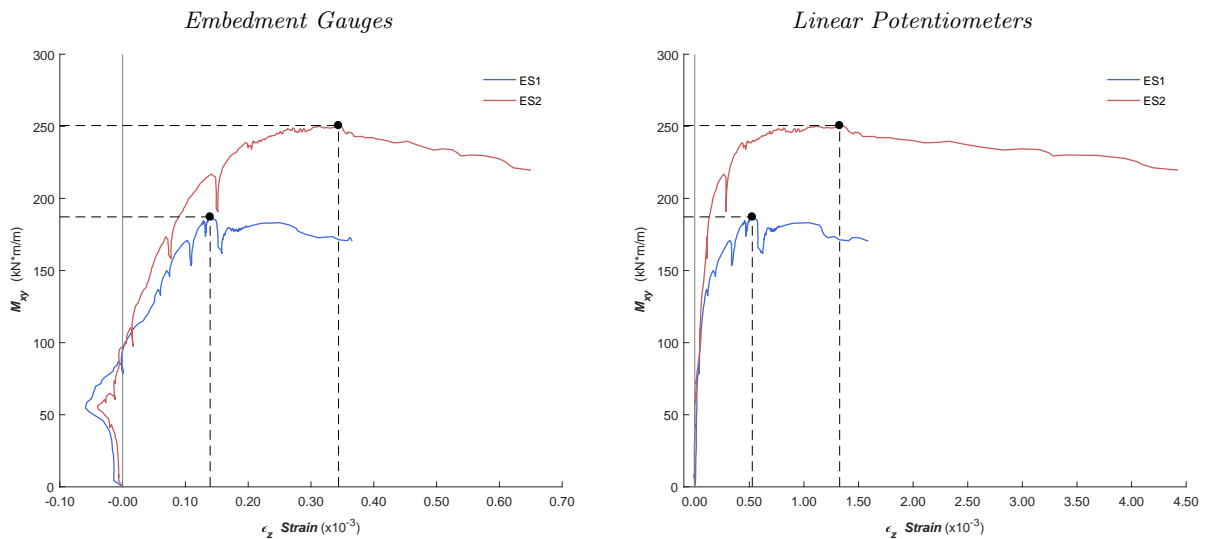


Figure 5.20: Out-of-Plane Concrete Expansion Comparison

A critical piece of information gathered from the testing of ES2 were the strains measured in the out-of-plane T-head reinforcement. While only 4 out of the 8 strain gauges were functional during the experiment, they were enough to show that these reinforcement bars played an active part in improving the capacity of the specimen. The strains at the peak are similar to the those measured in the concrete by the EGs, indicating that the strains in the core of the specimen were consistently measured. Unlike the in-plane reinforcement in the X & Y directions, the reinforcement in the Z-direction continues to develop strain in the post-peak region of the test. This suggests that the post-peak deformations in the specimen are concentrated in the relative separation of the North and South faces of the specimen.

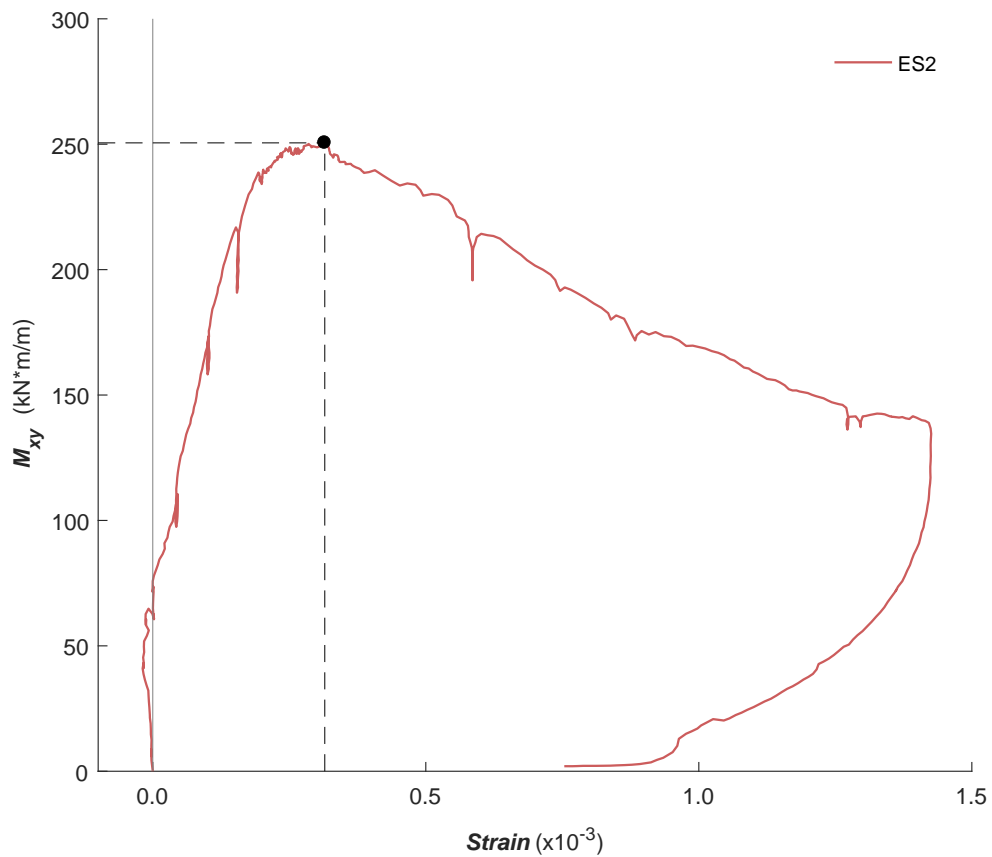


Figure 5.21: *Out-of-Plane T-Head Reinforcement Strain*

Chapter 6

A Finite Element for the Analysis of Reinforced Concrete Shells: Derivation and Verification

The following chapter will present the numerical derivation and verification of a finite element for the non-linear structural analysis of reinforced concrete shells subject to all eight sectional resultants. This element, referred to as the three-dimensional Hybrid Panel-Truss (3d-HyPT) element, builds heavily upon the two-dimensional derivation presented in Chapter 2. Therefore, the current chapter is not intended to be a standalone document - wherever possible references to the work presented in previous chapters will be made to avoid repetition.

This chapter begins by discussing how the information from the two pure torsion tests have influenced the 3d-HyPT derivation; the main conclusion being that out-of-plane deformations must be explicitly dealt with in the element. Next, a schematic description of the element is given, followed by the mathematical derivation of the various components of the stiffness matrix. Lastly, the finite element computer program that was written to implement the element is explained, and the numerical results produced by this program are evaluated against the experimental results.

6.1 Preliminary Modelling Considerations

At the outset of this thesis there was ambiguity regarding the out-of-plane deformations that would result from applying pure torsion. Therefore, the results from the experimental program were necessary to answer this question before commencing the derivation of the 3d-HyPT element.

With respect to the experiments, one preliminary hypothesis was that since no out-of-plane forces were directly applied to create torsion there would not be any out-of-plane deformations, and hence the T-head reinforcement would have no impact on the strength of the specimen. The other possibility was that since the North and South faces were being pulled in opposite directions relative to each other there would be resultant out-of-plane strains, and hence the addition of steel through the thickness of the specimen would result in better performance.

6.1.1 Shell-2000 Prediction

The program Shell-2000 [40], developed by Professor Bentz at the University of Toronto, was used to test the first hypothesis. In this program, a shell is constructed by stacking a series of in-plane membranes through the thickness, where the overall stress resultants are taken as an aggregate of these membranes. Therefore, when representing torsion as a linearly varying in-plane strain through the thickness, this formulation results in all the out-of-plane stresses being zero (plane stress). Figure 6.1 shows a schematic of the two models made in the program, the only difference between them is the addition of transverse T-head reinforcement and higher concrete strength in ES2.

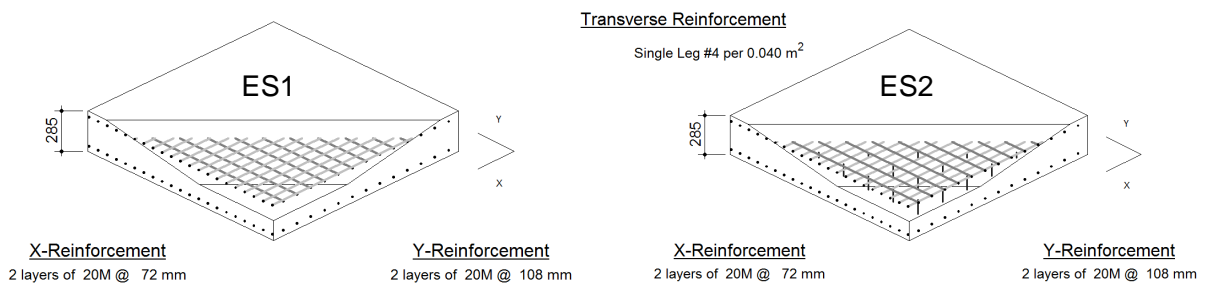


Figure 6.1: *Shell-2000 Models of Experimental Specimens*

As expected, in both models the in-plane shear strain (γ_{xy}) follows a linear distribution through the thickness, but the out-of-plane shear stresses (σ_{xz} & σ_{yz}) are zero. This meant that the T-head reinforcement in ES2 was not engaged. Therefore, the program predicted similar torque-twist behaviour for both specimens where the difference is thought to result from the higher concrete strength in ES2. The in-plane shear strain distribution through the thickness at peak torsion, along with the torque-twist behaviour for specimen ES1 are shown in Figure 6.2.

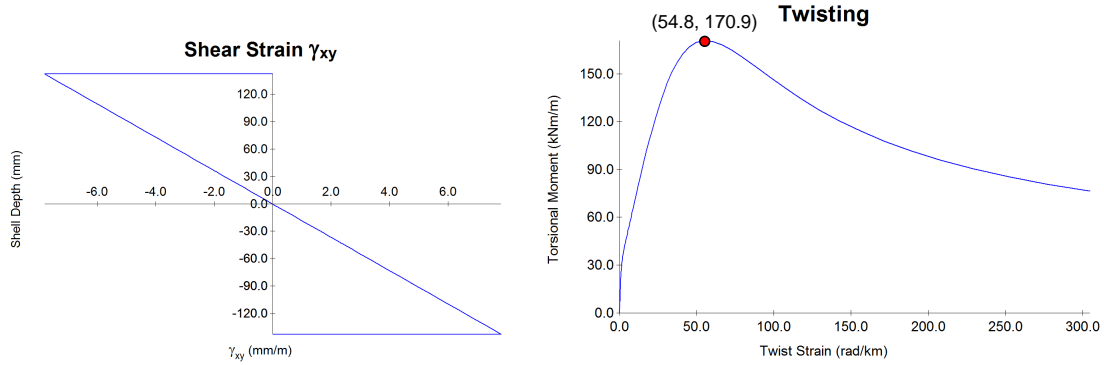


Figure 6.2: *Shell-2000 In-Plane Shear Strain and Torque-Twist Behaviour*

6.1.2 Lessons Learned

From the previous chapter's discussion, it is evident that the out-of-plane shear strain is not negligible and that the addition of T-head reinforcement played a role in improving the strength and ductility of ES2. Figure 6.3 shows the experimental torque-twist behaviour plotted against the Shell-2000 predictions, where the predicted peak is at $170.9 \frac{kN \cdot m}{m}$ and $54.8 \frac{mrad}{m}$ for ES1, $193 \frac{kN \cdot m}{m}$ and $60.2 \frac{mrad}{m}$ for ES2. When compared to the experimental results, the Exp./Pred. ratios for the peak are 1.10 and 1.07 for the torsion and twist in ES1, while the peak ratios are 1.30 and 1.49 for ES2. The conclusion is that the behaviour of specimens subjected to pure torsion without any out-of-plane strengthening is well-predicted by Shell-2000, which is not the case when out-of-plane reinforcement is added.

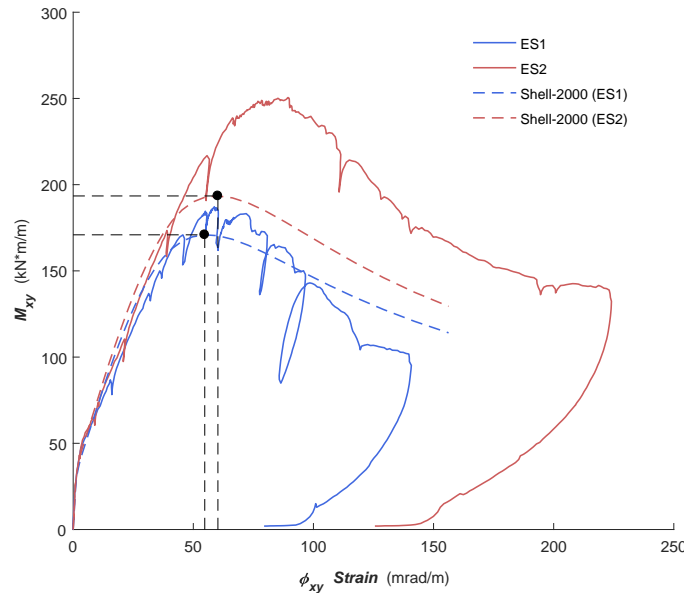


Figure 6.3: *Shell-2000 Torque-Twist Compared to Experimental Results*

Based on this comparison, the takeaway for the 3d-HyPT element is that it must explicitly account for out-of-plane deformations. Making the assumption that they are negligible, as was done in Shell-2000, has the potential to under-estimate the capacity of shells with transverse reinforcement in certain loading scenarios.

6.2 Description of 3d-HyPT Element

The three-dimensional Hybrid Panel-Truss (3d-HyPT) element has a total of eight nodes and 24 Degrees of Freedom (DOFs). Unlike most standard shell finite elements there are no explicit rotational DOFs, the formulation is therefore greatly simplified by only having three orthogonal translational DOFs (oriented in the cartesian plane) per node as shown in Figure 6.4. For consistency with the two-dimensional element derivation and the experimental data, the notation for the 3d-HyPT element has been kept as follows: the X-direction represents the main longitudinal direction, the Y-direction represents the secondary longitudinal direction, and the Z-direction is through the thickness of the member. Recall that in the two-dimensional case the Y-direction was simply a constant based on the cross-sectional width of the member, in three dimensions this direction is a variable based on the extent of the shell plane.

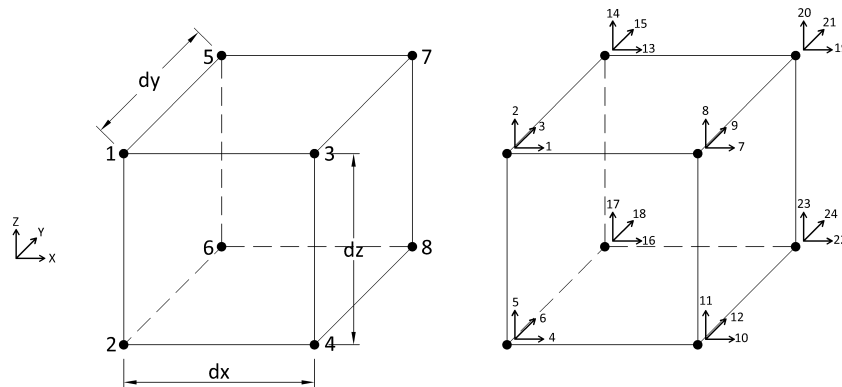


Figure 6.4: *3d-HyPT Element Numbering Convention: Nodes (Left) & DOFs (Right)*

Just like the two-dimensional version, the efficiency of this element comes from the combination of the flexure/axial truss and shear panel subcomponents that together are able to represent the internal action in reinforced concrete. Figure 6.5 is a schematic representation of the element showing the relative placement of these subcomponents.

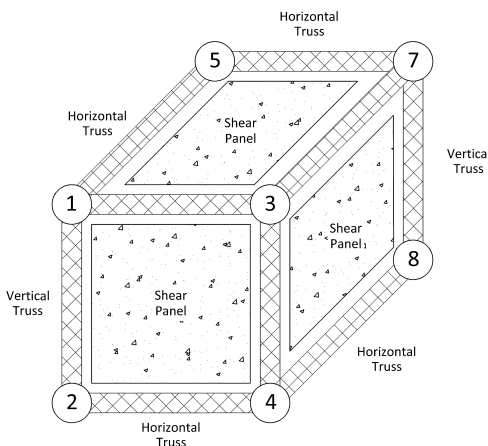


Figure 6.5: *Visualization of 3d-HyPT Element Subcomponents*

6.2.1 Two-Dimensional Visualization

The 3d-HyPT element can be thought of as a box where each of the six sides is represented by a separate 2d-HyPT element. Using this formulation has the benefit of improving the overall computation time since a complex 3d-element can be expressed as the aggregate of much simpler elements. The derivation is also a direct extension of the Panel and Truss concepts explained in Chapter 2, which have been adapted to account for three-dimensional effects as will be discussed in Section 6.3. Each face represents half the thickness of the element in the plane in which it lies (XZ, YZ or XY). So while a 2d-HyPT element can be thought of as just one face in the XZ-plane, the 3d-HyPT would split the element into a front and back face (XZ1 & XZ2) half the thickness of the original element, doing the same for the YZ and XY-planes. Figure 6.6 shows the six two-dimensional faces and their respective DOFs.

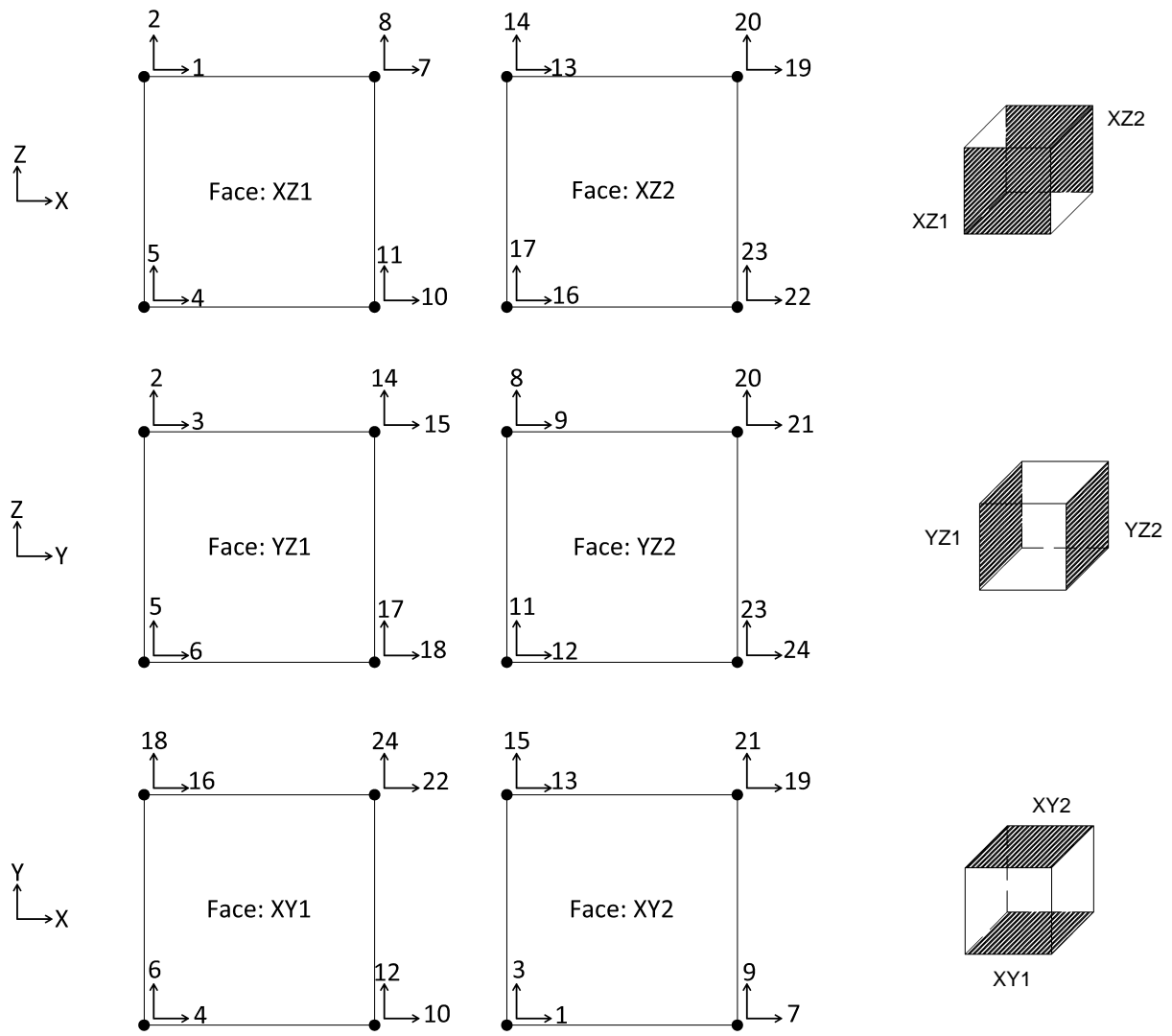


Figure 6.6: Six Faces Representing the 3d-HyPT Element

6.2.2 Full Member Representation

The 3d-HyPT element is similar to its two-dimensional counterpart in that the full height of a cross-section is represented by only one element. While the element has been derived with the intention of analyzing shells, its generalized form is also applicable to the analysis of beams. Figure 6.7 shows the same beam that was used as a schematic example of the 2d-HyPT application (Chapter 2, Figure 2.2) modelled with nine 3d-HyPT elements instead.

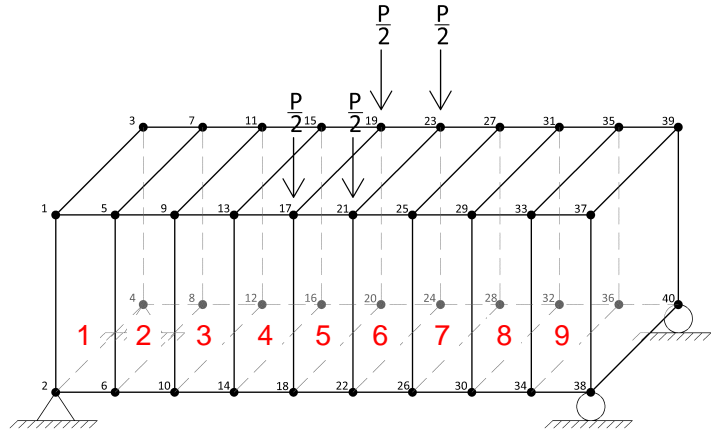


Figure 6.7: *Simply Supported Beam Modelled with 3d-HyPT Elements Placed in Series*

The structural analysis problem depicted in Figure 6.7 is effectively a two-dimensional problem since the loading is applied symmetrically to a rectangular beam. Therefore, modelling it with 3d-HyPT elements is unnecessarily complex, the analysis would take longer due to the large number of nodes but the final result would be the same as if one had used 2d-HyPT elements. Yet the three-dimensional application allows for the analysis of much more complex loading situations that cannot be captured in a 2d model. For example, Figure 6.8 shows the same beam subjected to a series of unbalanced loads acting in several different planes resulting in complex biaxial and twisting behaviour.

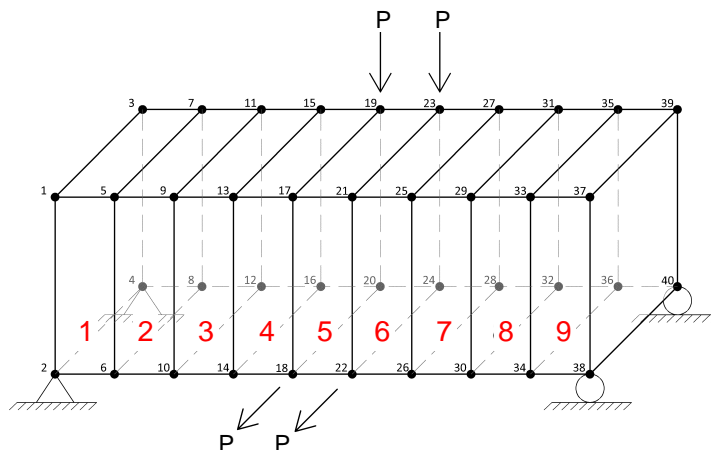


Figure 6.8: *Simply Supported Beam with Complex Loading*

Figure 6.9 shows how the 3d-HyPT element can be used to model a simply-supported flat slab with an off-center concentrated load at one end. The slab is represented with a 6x5 grid of elements where the supports and loads are specified at nodal locations.

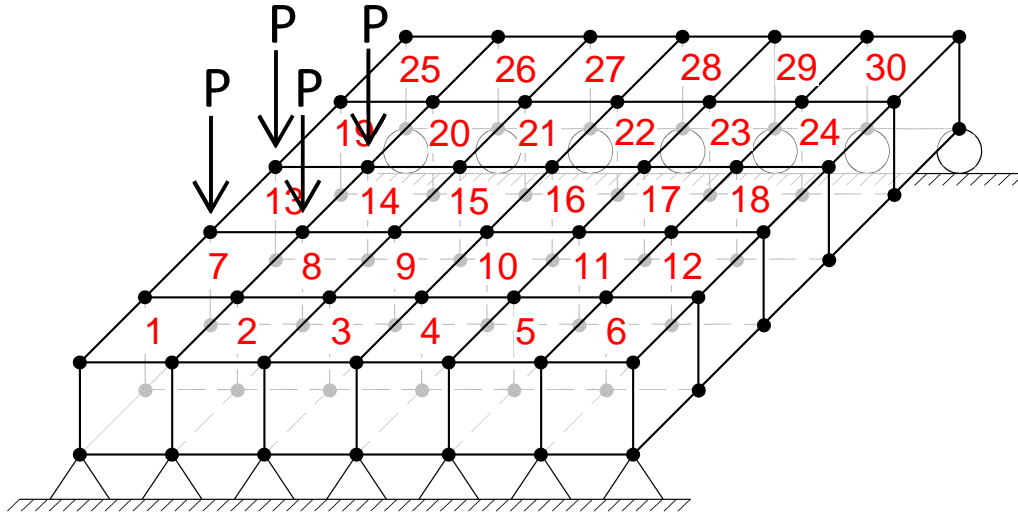


Figure 6.9: *Simply Supported Slab Modelled with 3d-HyPT Elements Placed in a Grid*

In general, the element can be used to model a wide range of three-dimensional structures with complex boundary conditions. For example, Figure 6.10 shows a schematic of a cantilevered member with off-center loading, a fixed condition is achieved by using pins at the top and bottom of the element.

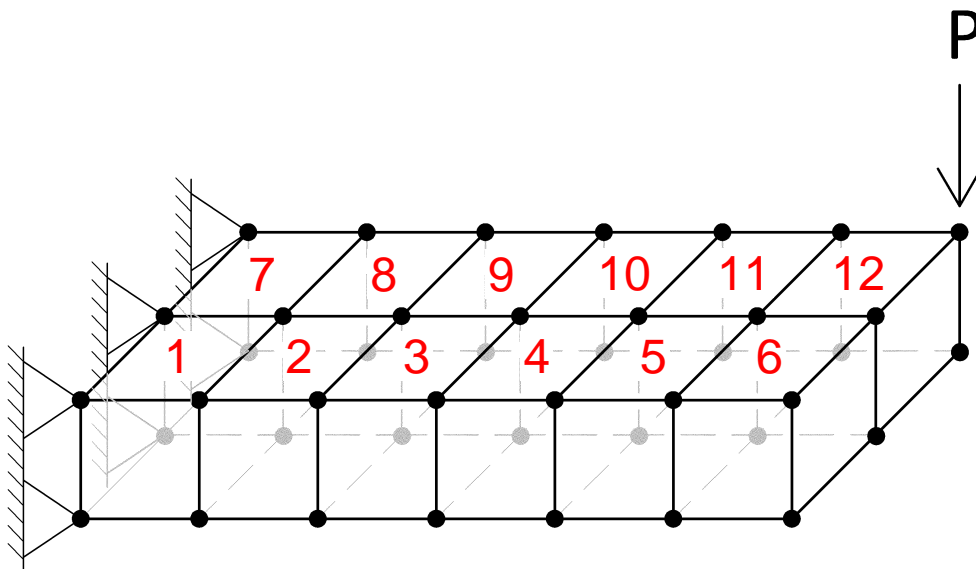


Figure 6.10: *Cantilevered Slab Modelled with 3d-HyPT Elements*

6.3 Derivation of Stiffness Matrix

The 3d-HyPT element is based on similar principles used to derive the two-dimensional element - the deformation patterns and rationale behind the different subcomponents is the same. The truss bars, which can only carry axial forces, link two adjacent nodes together, while panels provide shear stiffness and link the four nodes of a face together. But while the overall element appears to be taking a 2d-HyPT element and repeating it for each face of the cube, the derivation of the stiffness matrix is more complex as parallel faces must be linked to account for 3d effects. In the following section, only the additional modifications that are necessary will be explicitly discussed. For the basic justification and explanation of a truss or a panel stiffness matrix refer to the derivations presented in Chapter 2.

6.3.1 Horizontal Truss Stiffness Terms

In two dimensions there was only one moment resultant (about the y -axis), so just the relative displacement of the top and bottom horizontal trusses were needed to represent this deformation. It gets more complex in three dimensions, and with the 3d-HyPT element an added challenge was accounting for the relative displacement of the parallel faces. It is not certain that the front and back faces will deform in the same manner and the effects of any asymmetry must be explicitly captured in the stiffness matrix. Figure 6.11 illustrates such a case in the XZ -plane, where due to some asymmetric loading scenario the front face is experiencing positive flexure while the back face is experiencing negative flexure and tension.

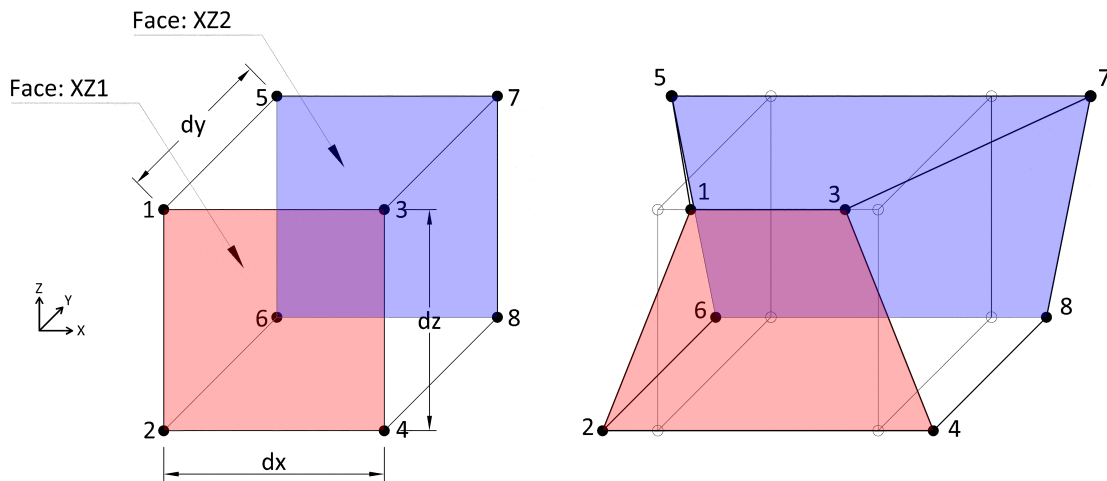


Figure 6.11: *Relative Deformations of Trusses in XZ-Plane Faces*

A simple way to formulate the stiffness matrix for such a case would be to completely decouple the action of the two parallel faces, allowing each to deform without influencing its neighbour. While this would allow a direct application of the 2d-HyPT truss terms already derived, it is too great a simplification of the internal connectivity in reinforced concrete members.

A more realistic approximation is shown in Figure 6.12, where the strains across whole element are based on a set of linear interpolations between the parallel faces. For clarity, only the "right" side of the element (nodes 3,4,7,8) is shown, note that the "left" face of the element (nodes 1,2,5,6) is experiencing the same strain profile. This differs from the two-dimensional case where the cross-section was only divided across the height into equal slices - in three dimensions the cross-section is divided into a grid, where each sub-element (or fiber) has its own strain value and corresponding force based on the material secant stiffness (Steps #1 & #2 in Section 2.2.4). The number of divisions across the height and width of the cross-section is optional, a finer mesh would result in a more accurate strain profile but would also increase the computation time.

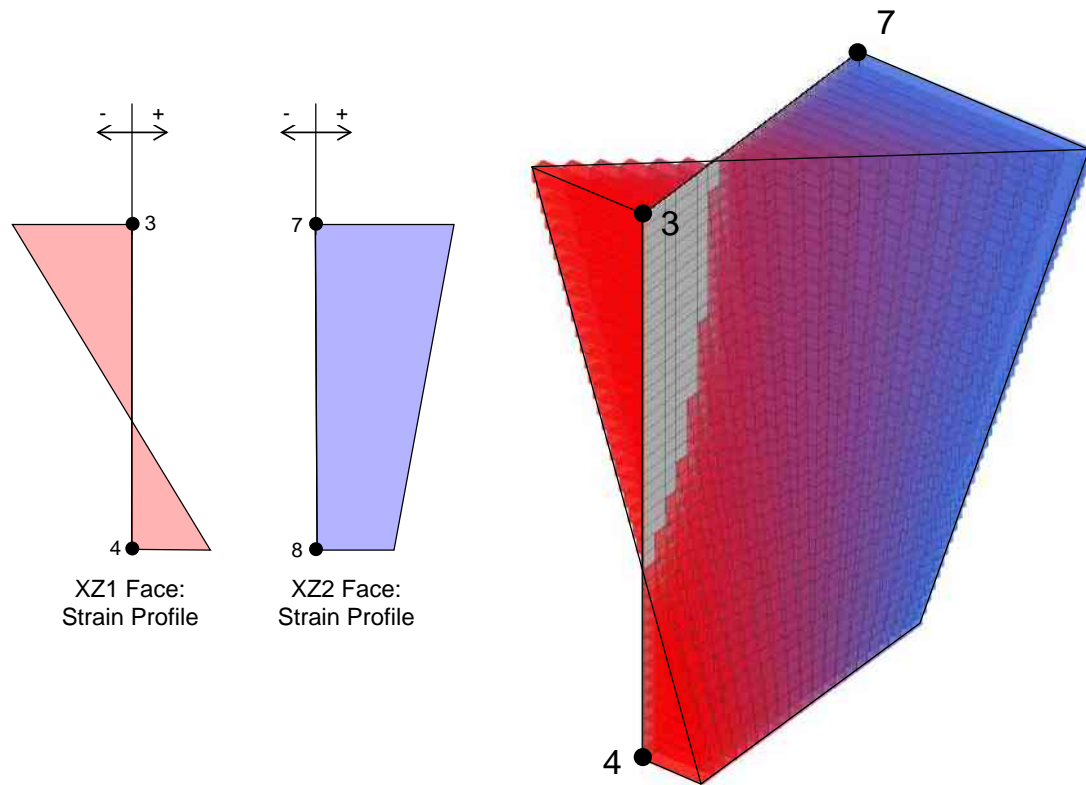


Figure 6.12: *Interpolated Strains Between Parallel Faces*

Just like in the 2d-HyPT derivation, a displacement applied to one of the nodes would have an effect on all the adjacent nodes, hence the need for off-diagonal terms in the stiffness matrix. While there was only one unique off-diagonal term in two dimensions ($K_{TB} = K_{BT}$), in three dimensions there are three adjacent nodes and therefore three unique off-diagonal terms that must be calculated. To derive the diagonal and off-diagonal stiffness terms associated with the current strain state the procedures outlined in Steps #3 through #6 in Section 2.2.4 are to be followed. The important thing to remember is that summations must be made over the height and width of the section, and transforming a section force to an equivalent nodal force requires solving moment equilibrium across two axes.

To solve for all the truss bar stiffness terms the stiffness method must be formulated four separate times, applying a unit displacement at the DOF of interest and keeping all others at zero while calculating the forces that develop at the nodes. As before, the incremented strain is assumed to distribute through the cross-section in a linear manner in both directions - a strain increment at each of the four X-Direction horizontal DOFs results in the distributions shown in Figure 6.13.

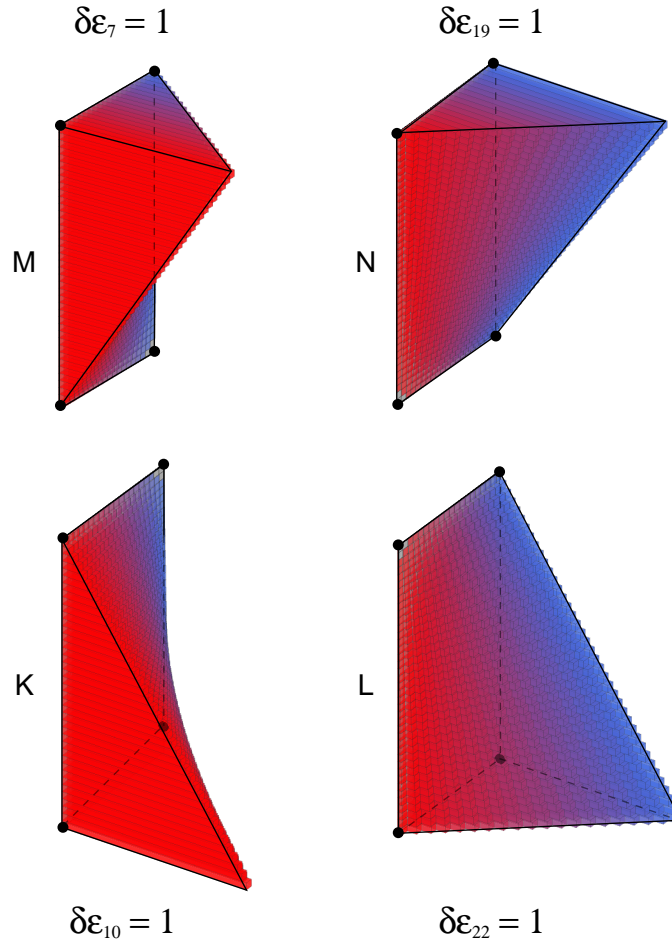


Figure 6.13: Unit Increments at Right Side of Element

The horizontal truss stiffness terms being solved for are shown in the reduced Equation 6.1, where each row corresponds to one of the increment cases. For example, the four terms in the 1st row are solved by looking at the $\delta\epsilon_7 = 1$ case. Note that the stiffness matrix is symmetric (i.e. $K_{7,10} = K_{10,7}$, $K_{7,19} = K_{19,7}$, etc.) and is mirrored on the left side of the element (i.e. $K_{7,7} = K_{1,1}$, $K_{7,10} = K_{1,4}$, etc.).

$$\begin{bmatrix} K_{7,7} & K_{7,10} & K_{7,19} & K_{7,22} \\ K_{10,7} & K_{10,10} & K_{10,19} & K_{10,22} \\ K_{19,7} & K_{19,10} & K_{19,19} & K_{19,22} \\ K_{22,7} & K_{22,10} & K_{22,19} & K_{22,22} \end{bmatrix} \begin{Bmatrix} \Delta_7 \\ \Delta_{10} \\ \Delta_{19} \\ \Delta_{22} \end{Bmatrix} = \begin{Bmatrix} F_7 \\ F_{10} \\ F_{19} \\ F_{22} \end{Bmatrix} \tag{6.1}$$

Looking at just the 1st row in more detail, the stiffness terms are expressed in Equation 6.2.

$$\begin{aligned}
 K_{7,7} &= \frac{dF_7}{d\varepsilon_7 \cdot d_x} = M_{TL} \\
 K_{7,10} &= \frac{dF_{10}}{d\varepsilon_7 \cdot d_x} = M_{BL} \\
 K_{7,19} &= \frac{dF_{19}}{d\varepsilon_7 \cdot d_x} = M_{TR} \\
 K_{7,22} &= \frac{dF_{22}}{d\varepsilon_7 \cdot d_x} = M_{BR}
 \end{aligned}
 \tag{6.2}$$

The incremental nodal forces are found by transforming the cross-sectional forces to their respective nodes. This is best illustrated through a diagram, Figure 6.14 shows how the four different nodal forces are found through moment equilibrium. For example, the two top forces (δF_7 and δF_{19}) are found by first transforming the cross-section forces to the top by equating them to the resultant moment about the bottom, and then equating them to either the left or right moment resultant. For more information regarding these calculations see the two dimensional approach outlined in Step # 5 in Section 2.2.4.

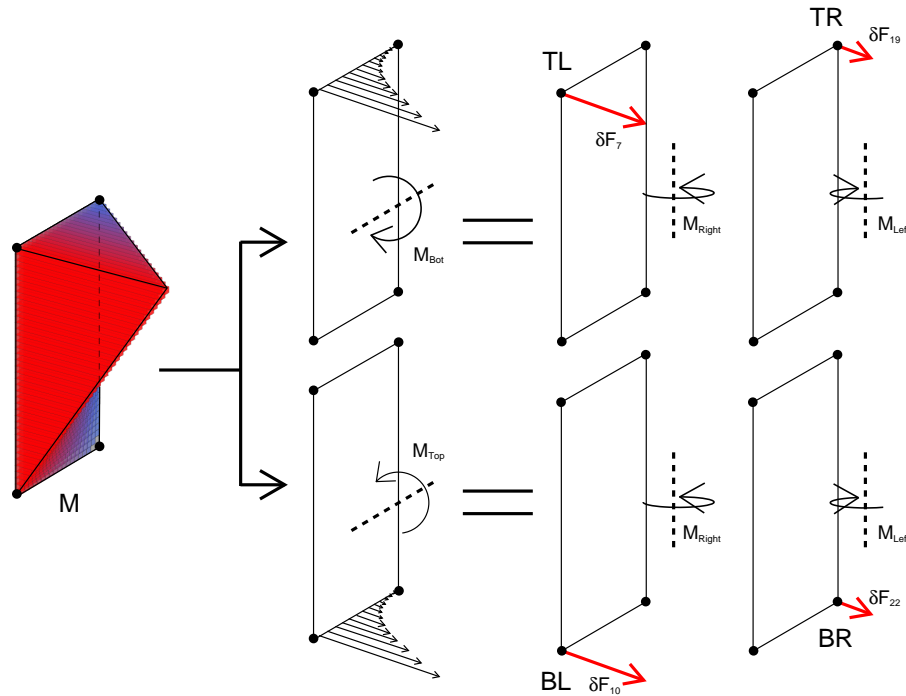


Figure 6.14: *Equivalent Nodal Forces Based on Strain Increment at DOF #7*

Repeat the process outlined in Figure 6.14 for the remaining incremented strain profiles for the XZ-plane. Equation 6.3 shows the complete horizontal truss stiffness matrix, where the capital letter refers to the type of increment, and the subscript refers to where the forces are resolved to when calculating the term. Equivalent off-diagonal terms are highlighted with the same colour, while the different diagonal terms are left clear for clarity. This whole process is then repeated for the YZ-plane.

6.3.2 Vertical Truss Stiffness Terms

The vertical trusses link the faces in the XY-plane, and provide stiffness through the thickness of the element in the Z-direction by connecting the following nodes: 1-2, 3-4, 5-6, and 7-8.

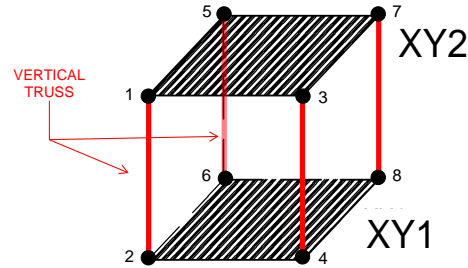


Figure 6.15: *Vertical Trusses in the 3d-HyPT Element*

When deriving the two-dimensional element clamping stresses were considered negligible, and therefore the stiffness of the vertical trusses was taken as a constant based on the uncracked stiffness and gross area of concrete. An added benefit of this decision was that the large stiffness in the vertical trusses helped improve the numerical stability of the finite element solution. Yet this simplification is unrealistic in a three-dimensional case - the experiments proved that the out-of-plane cracking and expansion in the Z-direction were significant under torsional loading, which should be explicitly reflected in the derivation of the vertical truss stiffness terms. The relationship between the internal Z-direction strain (measured by the EGs) is plotted against the experimental twist strain in Figure 6.16. This curve could perhaps be generalized by relating the Z-direction strain to some material property, such as the Poisson's ratio, although based on the data from the two shell experiments there was no clear trend.

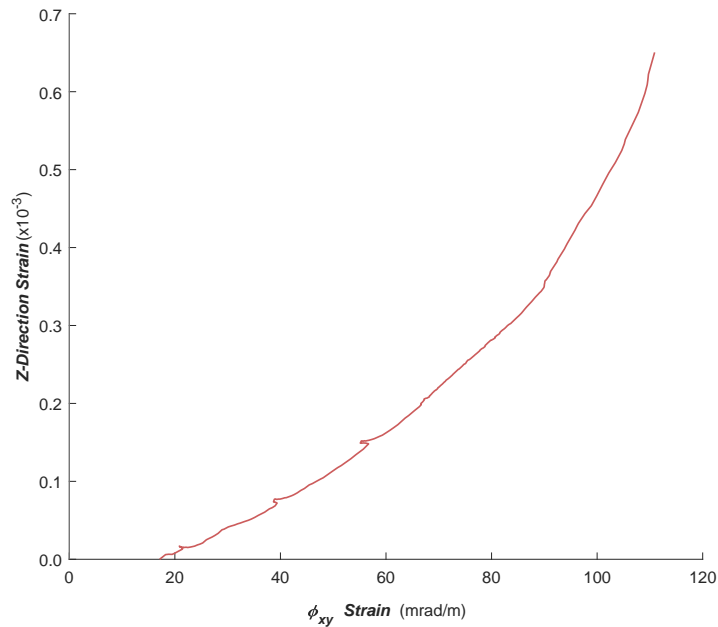


Figure 6.16: *Axial Strain in Vertical Direction Based on Twist Strain*

Based on the relative in-plane shear strain between the XY1 and XY2 faces (twist strain), the corresponding axial strain from Figure 6.16 is imposed on the vertical trusses. The stiffness is then calculated by the same procedure that was used for the the horizontal trusses - incrementing strains at the four nodes, and summing resultant forces. Without this modification to the stiffness of the vertical trusses, the 3d-HyPT element would over-predict the failure load since cover spalling and out-of-plane cracking would not be allowed to occur. Figure 6.17 shows the strain distribution through the element along with the physical representation of one vertical truss volume. The symmetrical distribution of strains, along with the fact that the cross-section is uniform, means that the vertical trusses are the same; only one set of calculations is necessary to calculate all the vertical truss stiffness terms.

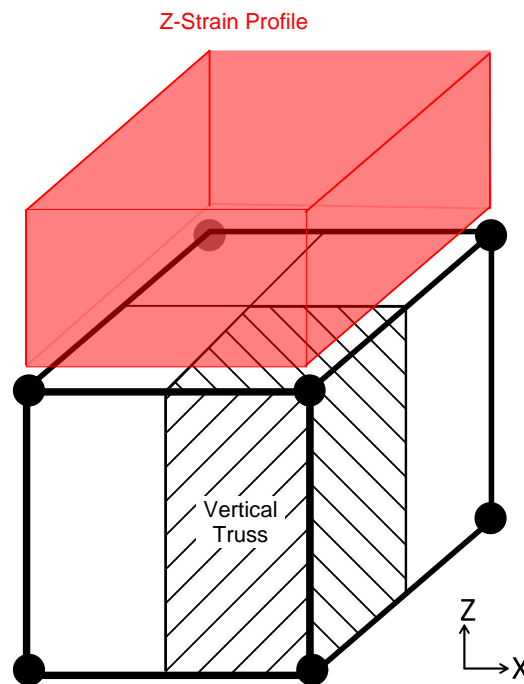


Figure 6.17: *Z-Direction Strain Applied to Vertical Trusses*

6.3.3 Shear Panel Stiffness Terms

The stiffness matrix for a shear panel representing one face of the 3d-HyPT element is based on the two dimensional geometric formulation derived in Section 2.3.4 - the shear modulus of the panel is determined from an MCFT analysis based on the nodal displacements in the plane of interest. The shear modulus and the cross-sectional geometry are then used to express the individual stiffness terms (8x8 matrix). When calculating these terms note that in the 3d-HyPT element there are two parallel panels per plane (front and back), therefore the total area represented by each is halved. Looking at the XZ-plane, the constant terms in the stiffness matrix for the front and back panel (XZ1 & XZ2) are shown in Equation 6.4.

$$C_1 = \frac{\bar{G}_1 \cdot d_y d_v}{8d_z} \quad (6.4)$$

$$C_2 = \frac{\bar{G}_2 \cdot d_y d_v}{8d_z}$$

Yet the deformations and forces developed in each panel must be linked through the stiffness matrix, otherwise the implication is that when one face of the element deforms in shear the adjacent parallel face experiences no force. From the relationship between load and stiffness (i.e. load path) comes the idea that the 'relative stiffness' and 'degree of connectivity' of two parallel faces are inversely related properties. Connectivity defines to what degree an imposed action on one face is experienced by the other face, and is represented by the off-diagonal (cross-stiffness) terms in the stiffness matrix. It is proposed that these terms be calculated by taking the average stiffness of the two faces as a starting point, and multiplying this value by two modification factor based on the relative difference between the panel shear stiffnesses and deformations (Equation 6.5).

$$C_x = F_1 \cdot F_2 \cdot \frac{C_1 + C_2}{2} \quad (6.5)$$

The first modification factor is calculated from Equation 6.6, but cannot be negative since this would imply negative stiffness (a negative value is rounded to 0). If the two panel stiffnesses are the same then perfect connectivity is assumed, which means that an applied displacement on one face would result in an even distribution of shear forces between both the faces. When a difference between the two stiffnesses exists the connectivity is no longer perfect, with the intuitive result that the stiffer face attracts proportionally more shear force when a displacement is applied to it. As the ratio between the stiffnesses approaches zero the connectivity does as well, which from a physical perspective means that the parallel faces begin to act more independently as one of them suffers more damage.

$$F_1 = 1 - 2 \cdot \frac{|\bar{G}_1 - \bar{G}_2|}{\bar{G}_1 + \bar{G}_2} \quad \text{where: } 0 \leq F_1 \quad (6.6)$$

The cross-stiffness terms exist only if the the two parallel faces are experiencing different deformations, measured as the difference in the calculated shear strain between them. If the shear strains are the same, the calculation of the shear forces on the element should collapse back to a two-dimensional case where no cross-stiffness terms are necessary since the whole element can be represented by just one panel. The second factor is calculated from Equation 6.7, depending on the direction of deformation the shear strains will be either positive or negative.

$$F_2 = 1 - \frac{\gamma_1 + \gamma_2}{2 \cdot |\gamma_{max}|} \quad \text{where: } F_2 \leq 1 \quad (6.7)$$

The reasoning behind this second factor is justified by comparing the resulting forces from a two-dimensional case with those from a three-dimensional case where the parallel panels deform the same. Equation 6.8 shows the stiffness formulation for a two-dimensional panel, where the total force on the element is equal to the stiffness matrix times the shear deformations on the panel.

$$\left\{ F_T \right\} = \left\{ F_1 \right\} = 2 \cdot \left[P_1 \right] \left\{ u_1 \right\} \quad \text{where: } P_1 = \text{The stiffness of half the element} \quad (6.8)$$

Meanwhile, Equation 6.9 shows the stiffness formulation for a three dimensional element in the same plane. The stiffness matrix is made up of sub-matrices, which are 8x8 in size, and represent the front and back panels respectively.

$$\begin{bmatrix} \left\{ F_1 \right\} \\ \left\{ F_2 \right\} \end{bmatrix} = \begin{bmatrix} \left[P_1 \right] \left[P_x \right] \\ \left[P_x \right] \left[P_2 \right] \end{bmatrix} \begin{bmatrix} \left\{ u_1 \right\} \\ \left\{ u_2 \right\} \end{bmatrix} \quad \text{where: } P_x = \text{The cross-stiffness terms} \quad (6.9)$$

Expanding Equation 6.9 and summing the forces in the element results in Equation 6.10.

$$\left\{ F_T \right\} = \left\{ F_1 \right\} + \left\{ F_2 \right\} = \left(\left[P_1 \right] \left\{ u_1 \right\} + \left[P_x \right] \left\{ u_2 \right\} \right) + \left(\left[P_x \right] \left\{ u_1 \right\} + \left[P_2 \right] \left\{ u_2 \right\} \right) \quad (6.10)$$

Now assume that we have a case where the front and back panel have the same stiffness ($P_1 = P_2$) and both faces experience the same nodal displacement ($u_1 = u_2$). The summation is simplified to Equation 6.11.

$$\left\{ F_T \right\} = \left\{ F_1 \right\} = 2 \cdot \left(\left[P_1 \right] \left\{ u_1 \right\} + \left[P_x \right] \left\{ u_2 \right\} \right) \quad (6.11)$$

The two and three-dimensional formulations should give the exact same result in this case (i.e. Equation 6.8 = Equation 6.11) but the cross-stiffness terms are leading to an unrealistic amplification of the forces in the element. The conclusion is that the closer the two panels are to deforming in unison, the closer the element is to resembling a two-dimensional problem and hence the value of the cross-stiffness terms must be reduced - the second modification factor looks at the magnitude of the average shear strain in proportion to the largest strain and adjusts the cross-stiffness terms accordingly.

Figures 6.18 and 6.19 show the calculated stiffness matrices for the XZ-plane panels under two different scenarios. The values of stiffness and displacement are arbitrarily set to illustrate a case where the two panels have different stiffnesses but are experiencing either equal and unequal shear strains. The blue and green terms represent the XZ1 and XZ2 panels respectively, where the lighter colours are the cross-stiffness terms. The dimensions of the element are as follows: $d_x = 200, d_y = 300, d_z = 600$. While the shear stiffnesses of the panels are set to: $\bar{G}_1 = 8000, \bar{G}_2 = 5000$. Note that to complete the 3d-HyPT element stiffness matrix this whole process must be repeated for the YZ-plane and XY-plane shear panels.

DOF	1	2	3	4	5	6	7	8	9	10	11	12	13	14	15	16	17	18	19	20	21	22	23	24	U	F	
1	100,000	-300,000	0	-100,000	-300,000	0	-100,000	300,000	0	-100,000	300,000	0	0	0	0	0	0	0	0	0	0	0	0	0	1	100,000	
2	-300,000	900,000	0	300,000	900,000	0	-300,000	-900,000	0	300,000	-900,000	0	0	0	0	0	0	0	0	0	0	0	0	0	0	0	-300,000
3	0	0	0	0	0	0	0	0	0	0	0	0	0	0	0	0	0	0	0	0	0	0	0	0	0	0	0
4	-100,000	300,000	0	100,000	300,000	0	100,000	-300,000	0	100,000	-300,000	0	0	0	0	0	0	0	0	0	0	0	0	0	0	0	-100,000
5	-300,000	900,000	0	300,000	900,000	0	-300,000	-900,000	0	300,000	-900,000	0	0	0	0	0	0	0	0	0	0	0	0	0	0	0	-300,000
6	0	0	0	0	0	0	0	0	0	0	0	0	0	0	0	0	0	0	0	0	0	0	0	0	0	0	0
7	100,000	-300,000	0	-100,000	-300,000	0	-100,000	300,000	0	-100,000	300,000	0	0	0	0	0	0	0	0	0	0	0	0	0	0	0	100,000
8	300,000	-900,000	0	-300,000	-900,000	0	300,000	900,000	0	-300,000	-900,000	0	0	0	0	0	0	0	0	0	0	0	0	0	0	0	300,000
9	0	0	0	0	0	0	0	0	0	0	0	0	0	0	0	0	0	0	0	0	0	0	0	0	0	0	0
10	-100,000	300,000	0	100,000	300,000	0	100,000	-300,000	0	100,000	-300,000	0	0	0	0	0	0	0	0	0	0	0	0	0	0	0	-100,000
11	300,000	-900,000	0	-300,000	-900,000	0	-300,000	900,000	0	-300,000	900,000	0	0	0	0	0	0	0	0	0	0	0	0	0	0	0	300,000
12	0	0	0	0	0	0	0	0	0	0	0	0	0	0	0	0	0	0	0	0	0	0	0	0	0	0	0
13	0	0	0	0	0	0	0	0	0	0	0	0	62,500	-187,500	0	-62,500	-187,500	0	-62,500	187,500	0	-62,500	187,500	0	0	62,500	
14	0	0	0	0	0	0	0	0	0	0	0	0	-187,500	562,500	0	187,500	562,500	0	-187,500	-562,500	0	187,500	-562,500	0	0	-187,500	
15	0	0	0	0	0	0	0	0	0	0	0	0	0	0	0	0	0	0	0	0	0	0	0	0	0	0	
16	0	0	0	0	0	0	0	0	0	0	0	0	-62,500	187,500	0	62,500	187,500	0	62,500	-187,500	0	62,500	-187,500	0	0	-62,500	
17	0	0	0	0	0	0	0	0	0	0	0	0	-187,500	562,500	0	187,500	562,500	0	-187,500	-562,500	0	187,500	-562,500	0	0	-187,500	
18	0	0	0	0	0	0	0	0	0	0	0	0	0	0	0	0	0	0	0	0	0	0	0	0	0	0	
19	0	0	0	0	0	0	0	0	0	0	0	0	-62,500	187,500	0	62,500	187,500	0	62,500	-187,500	0	62,500	-187,500	0	0	-62,500	
20	0	0	0	0	0	0	0	0	0	0	0	0	187,500	-562,500	0	-187,500	-562,500	0	-187,500	562,500	0	-187,500	562,500	0	0	187,500	
21	0	0	0	0	0	0	0	0	0	0	0	0	0	0	0	0	0	0	0	0	0	0	0	0	0	0	
22	0	0	0	0	0	0	0	0	0	0	0	0	0	0	0	0	0	0	0	0	0	0	0	0	0	0	
23	0	0	0	0	0	0	0	0	0	0	0	0	187,500	-562,500	0	-187,500	-562,500	0	187,500	562,500	0	-187,500	562,500	0	0	187,500	
24	0	0	0	0	0	0	0	0	0	0	0	0	0	0	0	0	0	0	0	0	0	0	0	0	0	0	

Figure 6.18: *XZ-Plane Panel Stiffness Matrix (Equal In-Plane Shear Strains)*

DOF	1	2	3	4	5	6	7	8	9	10	11	12	13	14	15	16	17	18	19	20	21	22	23	24	U	F
1	100,000	-300,000	0	-100,000	-300,000	0	-100,000	300,000	0	-100,000	300,000	0	21,875	-80,769	0	-21,875	-80,769	0	-21,875	80,769	0	-21,875	80,769	0	1	100,000
2	-300,000	900,000	0	300,000	900,000	0	-300,000	-900,000	0	300,000	-900,000	0	-80,769	242,308	0	80,769	242,308	0	-80,769	-242,308	0	80,769	-242,308	0	0	-300,000
3	0	0	0	0	0	0	0	0	0	0	0	0	0	0	0	0	0	0	0	0	0	0	0	0	0	0
4	-100,000	300,000	0	100,000	300,000	0	100,000	-300,000	0	100,000	-300,000	0	-21,875	80,769	0	21,875	80,769	0	21,875	-80,769	0	21,875	-80,769	0	0	-100,000
5	-300,000	900,000	0	300,000	900,000	0	-300,000	-900,000	0	300,000	-900,000	0	-80,769	242,308	0	80,769	242,308	0	-80,769	-242,308	0	80,769	-242,308	0	0	-300,000
6	0	0	0	0	0	0	0	0	0	0	0	0	0	0	0	0	0	0	0	0	0	0	0	0	0	0
7	100,000	-300,000	0	-100,000	-300,000	0	-100,000	300,000	0	-100,000	300,000	0	21,875	-80,769	0	-21,875	-80,769	0	-21,875	80,769	0	-21,875	80,769	0	0	100,000
8	300,000	-900,000	0	-300,000	-900,000	0	300,000	900,000	0	-300,000	-900,000	0	80,769	-242,308	0	-80,769	242,308	0	80,769	-242,308	0	-80,769	242,308	0	0	300,000
9	0	0	0	0	0	0	0	0	0	0	0	0	0	0	0	0	0	0	0	0	0	0	0	0	0	0
10	-100,000	300,000	0	100,000	300,000	0	100,000	-300,000	0	100,000	-300,000	0	-21,875	80,769	0	21,875	80,769	0	21,875	-80,769	0	21,875	-80,769	0	0	-100,000
11	300,000	-900,000	0	-300,000	-900,000	0	-300,000	900,000	0	-300,000	900,000	0	80,769	-242,308	0	-80,769	242,308	0	80,769	-242,308	0	-80,769	242,308	0	0	300,000
12	0	0	0	0	0	0	0	0	0	0	0	0	0	0	0	0	0	0	0	0	0	0	0	0	0	0
13	21,875	-80,769	0	-21,875	-80,769	0	-21,875	80,769	0	-21,875	80,769	0	62,500	-187,500	0	-62,500	-187,500	0	-62,500	187,500	0	-62,500	187,500	0	0	21,875
14	-80,769	242,308	0	80,769	242,308	0	-80,769	-242,308	0	80,769	-242,308	0	-187,500	562,500	0	187,500	-562,500	0	-187,500	562,500	0	187,500	-562,500	0	0	-80,769
15	0	0	0	0	0	0	0	0	0	0	0	0	0	0	0	0	0	0	0	0	0	0	0	0	0	0
16	-21,875	80,769	0	21,875	80,769	0	21,875	-80,769	0	21,875	-80,769	0	-62,500	187,500	0	62,500	-187,500	0	62,500	-187,500	0	62,500	-187,500	0	0	-21,875
17	-80,769	242,308	0	80,769	242,308	0	-80,769	-242,308	0	80,769	-242,308	0	-187,500	562,500	0	187,500	-562,500	0	-187,500	562,500	0	187,500	-562,500	0	0	-80,769
18	0	0	0	0	0	0	0	0	0	0	0	0	0	0	0	0	0	0	0	0	0	0	0	0	0	0
19	21,875	-80,769	0	-21,875	-80,769	0	-21,875	80,769	0	-21,875	80,769	0	-62,500	187,500	0	62,500	-187,500	0	62,500	-187,500	0	62,500	-187,500	0	0	21,875
20	80,769	-242,308	0	-80,769	-242,308	0	80,769	242,308	0	-80,769	242,308	0	187,500	-562,500	0	-187,500	562,500	0	187,500	-562,500	0	-187,500	562,500	0	0	80,769
21	0	0	0	0	0	0	0	0	0	0	0	0	0	0	0	0	0	0	0	0	0	0	0	0	0	0
22	-21,875	80,769	0	21,875	80,769	0	21,875	-80,769	0	21,875	-80,769	0	-26,923	80,769	0	26,923	-80,769	0	26,923	-80,769	0	26,923	-80,769	0	0	-21,875
23	80,769	-242,308	0	-80,769	-242,308	0	80,769	242,308	0	-80,769	242,308	0	187,500	-562,500	0	-187,500	562,500	0	187,500	-562,500	0	-187,500	562,500	0	0	80,769
24	0	0	0	0	0	0	0	0	0	0	0	0	0	0	0	0	0	0	0	0	0	0	0	0	0	0

Figure 6.19: *XZ-Plane Panel Stiffness Matrix (Unequal In-Plane Shear Strains)*

6.4 Explanation of Analysis Program

Both the 2d and 3d-HyPT elements derived in the previous sections are implemented in a program written in MATLAB. The following section will outline the high-level organization and operation of this program, with a focus on the input/output and analysis structure. For the sake of brevity, a detailed presentation of the code is omitted from this thesis.

6.4.1 MATLAB Main File

The program is executed through a main MATLAB file that is included for reference in Appendix D. To improve the organization of the analysis program, functions and variables are organized into separate classes that each serve a specific purpose. The names of these classes and their descriptions are as follows:

- **IO.m** = Input and output class. Serves as the master class where all program default variables and user defined variables are specified. Creates the preliminary "Global Summary" and "Section Summary" text files, and creates and updates the "Load Stage Iteration" and "Load Stage Summary" output text files.
- **R_Global.m** = Global structure definition class. Reads and saves the data specified in the "Global Input" structure text file. Holds all the node, restraint, load, and element data. Produces the undeformed structure plot so that the definitions in the text file can be verified.
- **R_Section.m** = HyPT element cross-section class. Reads the "Section Input" text files that are specified in the "Global Input" text file and assigns the properties to the appropriate element - more than one type of section can be used in a problem. Holds all the section geometry and reinforcement bar layout information. Calculates the reinforcement ratios and regions of tension stiffening. Displays a two-dimensional and three-dimensional representation of a single element so that the section definitions in the text file can be verified.
- **R_Material.m** = HyPT element material class. Reads the material information specified in the "Section Input" text files. Calculates the tension and compression curves for concrete and steel, which are referenced when finding the secant stiffnesses during the analysis.
- **Solver.m** = Stiffness method solver class. Initializes and populates the loading and displacement vectors based on the load stage and previous iteration results. Initializes the global stiffness matrix, and sums the element level stiffness matrices calculated for each element at each iteration. Checks the global convergence criteria and increments the load stage number if convergence has been reached. Plots the displaced shape and crack locations for chosen load stages.

- `Truss.m` = Truss bars stiffness class. Calculates the horizontal and vertical truss stiffness terms for each element and the face being analyzed. Determines the additional cross-stiffness terms if the problem is a three-dimensional analysis.
- `Panel.m` = Shear panel stiffness class. Calculates the secant shear stiffness based on an MCFT formulation. Iterates on the MCFT panel formulation until convergence has been reached. Determines the cross-stiffness terms if the problem is a three-dimensional analysis.
- `Crack.m` = Element cracking stiffness class. Records the location, type and size of cracks in each element. Calculates the shear-flexure cracked interaction stiffness terms for elements that are cracked and outside the disturbed region.

6.4.2 Input Files and Structure Generation

The first part of the program deals with specifying the analysis task and reading in all the relevant information that is necessary to create the finite element model. This section corresponds to Step #1 & #2 in the main program code structure shown in Appendix D. The operational structure is represented by the flowchart in Figure 6.20, where the user initiates the process by specifying the name of the "Global Input" text file.

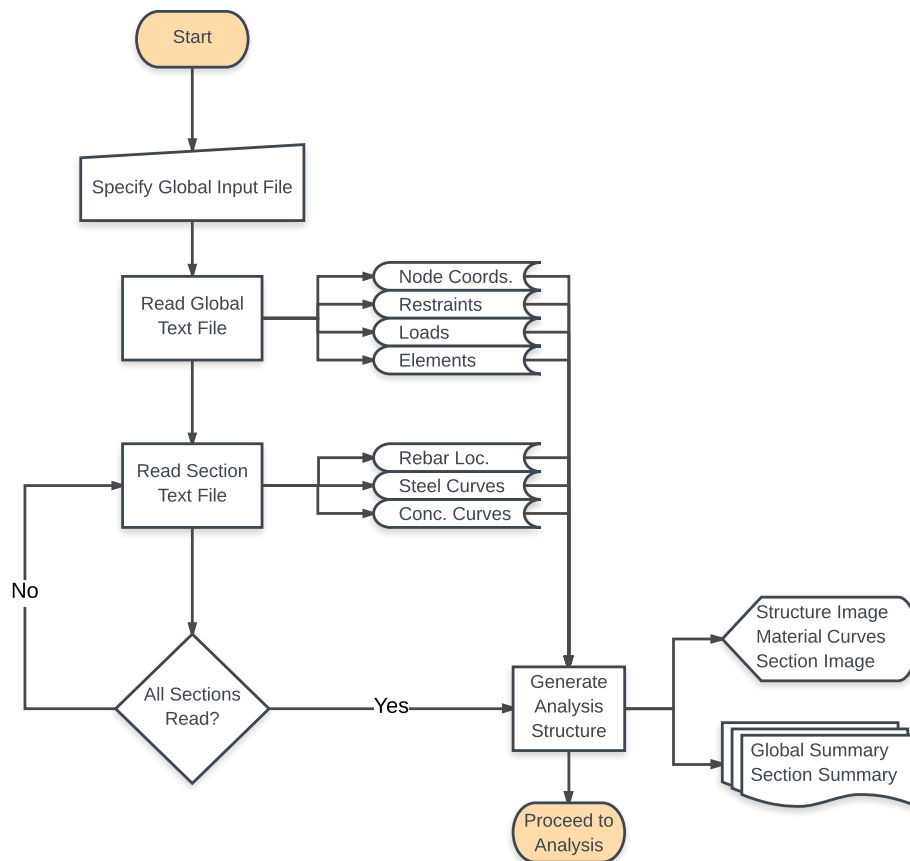


Figure 6.20: Preliminary Program Operational Flowchart

There is no preprocessor for the program, so all the problem specific information required for the computer analysis must be passed to the program through text files. A sample "Global Input" text file, for the creation of a fully fixed generic slab with a point load at the center, is shown in Figure 6.21. This text file also specifies the name(s) of the "Section Input" text files that are necessary to define the physical and material properties of the HyPT elements.

```

////////////////////////////////////
// Name:      Edvard Bruun
// Project:   Generic Slab Demo
// Created:   March 25th, 2016
// Updated:   July 1st, 2017
//
//
////////////////////////////////////

// Global file must be in same directory as the program

// FORMAT: Type = '2D' or '3D' (If 2D then ignore Y-data)
//          Number of Name Entries Must Match # of Sections Precisely
//          Enter the exact text file name to read
// NOTES : No Empty Lines in this list
//          Section names must be one word
//          For Multiple Sections, Add Additional Name Rows
-INPUT FILE-
Type      = 3D
Sections  = 2
Name      = section_shell.txt
Name      = section_shell2.txt
-INPUT FILE END-

// FORMAT: [X_Start (mm), Y_Start (mm), Z_Start (mm)] / [#_nodes, d_node_#, d_x, d_y, d_z] / [#_lines, d_node_#, d_x, d_y, d_z] /
// NOTES : White space is not important so long as information lies between ' / '
//          Start a line with '/' if you want it to not be read
//          If '2D' Problem then the Y-data will be ignored
-NODE LIST-
//
0 0    0 / 9 9 300 0 0 / 9 1 0 -300 0 /
0 0 -300 / 9 9 300 0 0 / 9 1 0 -300 0 /
//
-NODE LIST END-

// FORMAT: [node #] / [X_restrain (0 | 1 | 2), Y_restrain (0 | 1 | 2), Z_restrain (0 | 1 | 2)] / [ #_Restrains d_node_#]
// NOTES : 0 = Unrestrained
//          1 = Fully Restrained
//          2 = Conditionally Restrained
-RESTRAINT LIST-
//
1 / 1 1 1 / 9 1 /
82 / 1 1 1 / 9 1 /
73 / 1 1 1 / 9 1 /
154 / 1 1 1 / 9 1 /
//
10 / 1 1 1 / 7 9 /
73 / 1 1 1 / 7 9 /
//
18 / 1 1 1 / 7 9 /
99 / 1 1 1 / 7 9 /
//
-RESTRAINT LIST END-

// FORMAT: [node #] / [X_Load, Y_Load, Z_Load] / [#_Loads, d_node_#, d_Fx, d_Fy, d_Fz ] / [Constant Toggle] / #_steps d_Fx d_Fy d_Fz /
// NOTES : 1 = Constant - ON
//          0 = Constant - OFF
//          Loads on Repeating Nodes are Cumulative
-LOAD LIST-
//
41 / 0 0 -200000 / 2 81 0 0 0 / 0 / 10 0 0 -50000 /
//
-LOAD LIST END-

// FORMAT: [N_1, N_2, N_3, N_4] [N_5, N_6, N_7, N_8] / [Section File Name] / [ #_Elements, d_node_#] / [#_lines d_node_#] /
// NOTES : Front (XZ-Face) defined first - Left nodes first followed by right nodes
//          Back (YZ-Face) defined next - Left nodes first followed by right nodes (ONLY IF 3D)
//          Last Entry Section is only for 3D (not possible to do lines of elements in 2D)
-BEAM LIST-
//
2 83 11 92 1 82 10 91 / section_shell.txt / 8 9 / 8 1 /
//
-BEAM LIST END-

```

Figure 6.21: Sample Global Input File for Fixed Slab Model

The "Global Input" file indicates that the structure is composed of two distinct types of sections. A sample "Section Input" file, for a 300 mm cubed section with shear reinforcement, is shown in Figure 6.22. All the material properties for this particular section are also defined in this file, and will be assigned to the HyPT elements that make up the structure. Creating this text file is analogous to creating a section in Response-2000 when performing an Augustus-II analysis.

```

////////////////////////////////////
// Name:      Edvard Bruun
// Project:   Generic Shells (Stirrups)
// Created:   June 8th, 2016
// Updated:   July 1st, 2017
//
// Do Not Include Empty Rows Between Titles
// Do Not Change Title Names
//
////////////////////////////////////

// Unknown = 0 (Use Default Value)
-MATERIAL-
Concrete Comp. Str. [MPa] = 35
Concrete Tens. Str. [MPa] = 0
Poisson Ratio      = 0.15
Aggregate Size     [mm] = 10
X-Steel Yield      [MPa] = 420
X-Steel Ultimate   [MPa] = 515
X-Steel Modulus    [MPa] = 200000
Y-Steel Yield      [MPa] = 400
Y-Steel Ultimate   [MPa] = 515
Y-Steel Modulus    [MPa] = 200000
Z-Steel Yield      [MPa] = 300
Z-Steel Ultimate   [MPa] = 500
Z-Steel Modulus    [MPa] = 200000

// All Units in 'mm'
// 2D Problem: X = Element Length, Y = Section Width, Z = Section Height
// 3D Problem: X = Length in X-Dir, Y = Length in Y-Dir, Z = Out-of-Plane Thickness
-GEOMETRY-
X-width           = 300
Y-width           = 300
Z-width           = 300
Clear Cover       = 40
Filename          = section_shell.txt

// 1 Row:  bot_layers = 1 / rebar_size = 25 / num_bars = 7 / d = 572 /
// 1+ Row: bot_layers = 3 / rebar_size = 25 20 15 / num_bars = 7 3 3 / d = 572 500 400 /
// No Rebar: bot_layers = 0 /
// Use '/' Between Inputs, Whitespace on Both Sides

// 'd' is Measured From Top of Section (i.e. Towards Negative Z-dir)
-X-REINFORCEMENT-
xy-inclination = 0
xz-inclination = 0
bot_layers = 1 / rebar_size = 15 / num_bars = 2 / d = 250 /
top_layers = 1 / rebar_size = 15 / num_bars = 2 / d = 50 /

// 'd' is Measured From Top of Section (i.e. Towards Negative Z-dir)
-Y-REINFORCEMENT-
yx-inclination = 90
yz-inclination = 0
bot_layers = 1 / rebar_size = 10 / num_bars = 2 / d = 250 /
top_layers = 1 / rebar_size = 10 / num_bars = 2 / d = 50 /

// 'd' is Measured From Left of Section (i.e. Towards Positive X-dir)
-Z-REINFORCEMENT-
zx-inclination = 90
zy-inclination = 90
bot_layers = 1 / rebar_size = 10 / num_bars = 2 / d = 250 /
top_layers = 1 / rebar_size = 10 / num_bars = 2 / d = 50 /

```

Figure 6.22: Sample Section Input File for Fixed Slab Model

The output from the first part of the program is summarized in Figure 6.23. The top shows a schematic of the global geometry, where the nodal numbering, nodal restraints, element connectivity, and loading on the structure based on the "Global Input" file can be visually confirmed. This is followed by the material/section information, which takes the form of a series of stress/strain curves for the materials, and a schematic of a single element that shows the arrangement of reinforcement specified in the "Section Input" file. The images for the second section are not included since they closely resemble those below (no shear reinforcement).

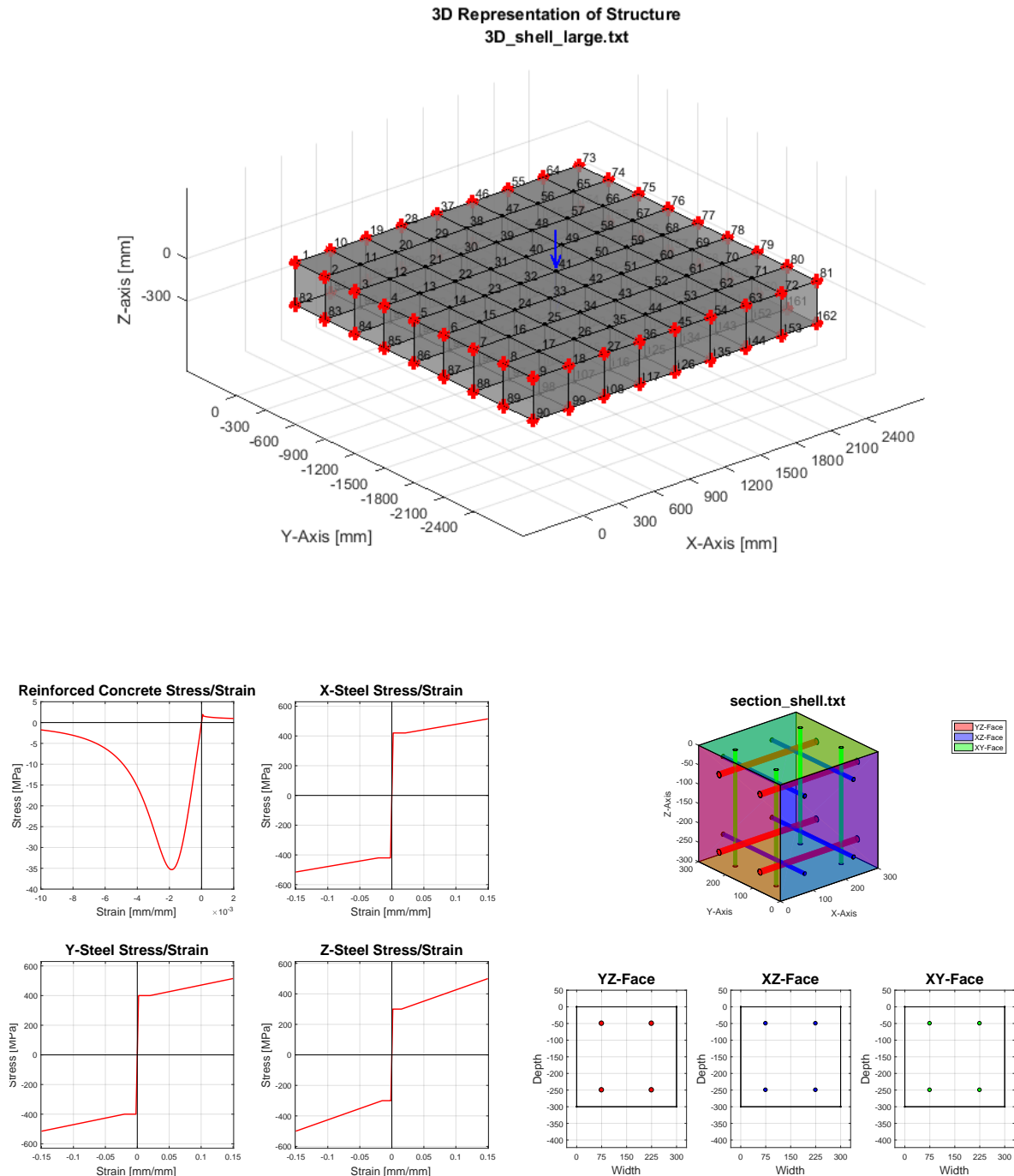


Figure 6.23: Program Output from Structural Analysis Input Files (Slab)

Figure 6.24 shows the output from another sample structural analysis problem, a cantilever beam with torsional loading applied to it.

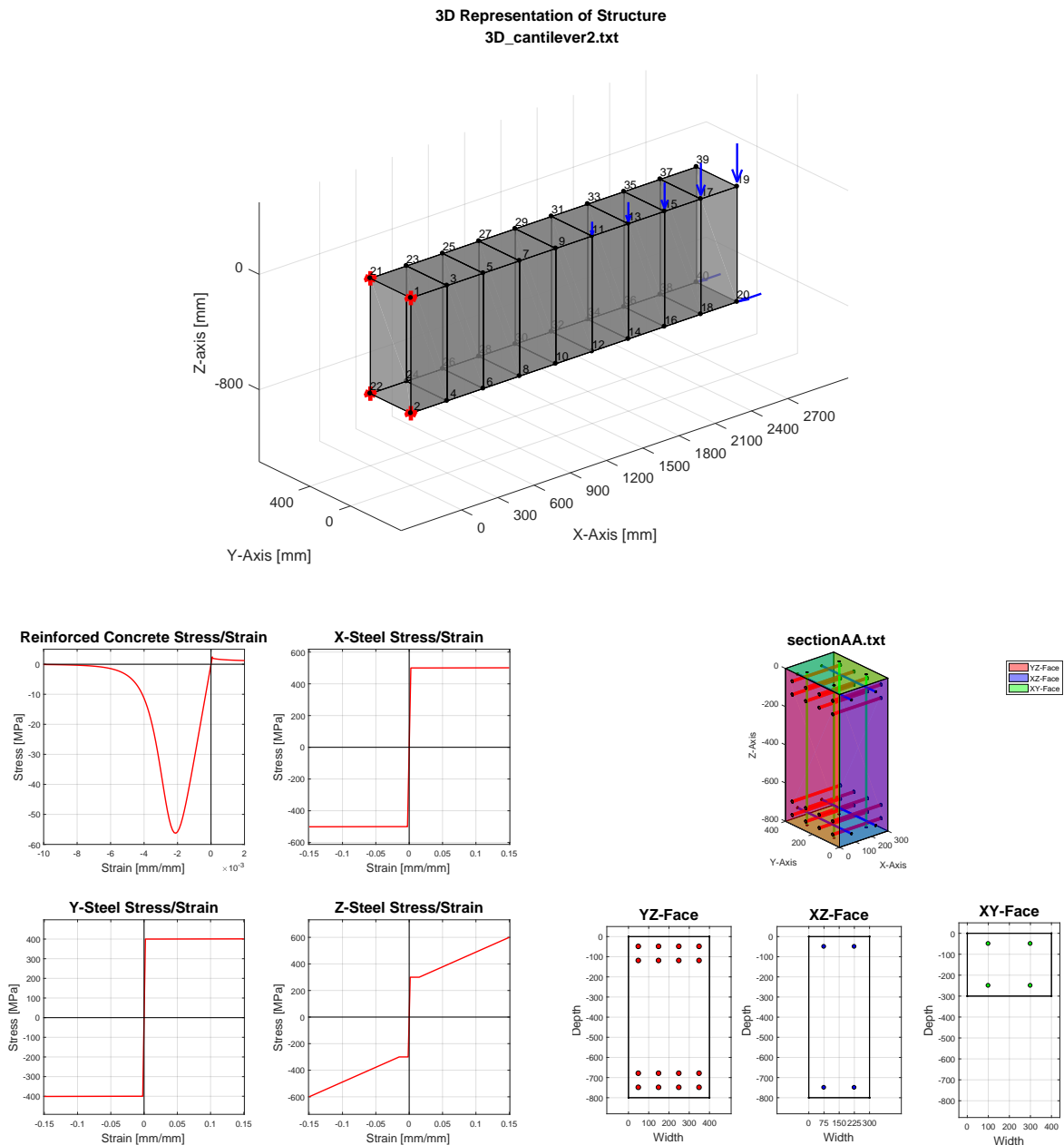


Figure 6.24: Program Output from Structural Analysis Input Files (Beam)

The program also produces two files that present an expanded textual summary of the structure as it has been generated. The "Global Summary" and "Section Summary" files are intended to be an easier way for the user to understand how the structure is defined, since the input text files are dense and sometimes difficult to parse. Examples of these files, for the analysis model of torsional shell specimen ES2, can be found in Appendix E.2.

6.4.3 Structural Analysis and Program Output

The second part of the program deals with performing the specified analysis task. This section corresponds to Step #3 in the main program code structure shown in Appendix D. The operational structure is represented by the flowchart in Figure 6.25, which is a continuation of the flowchart shown in Figure 6.20.

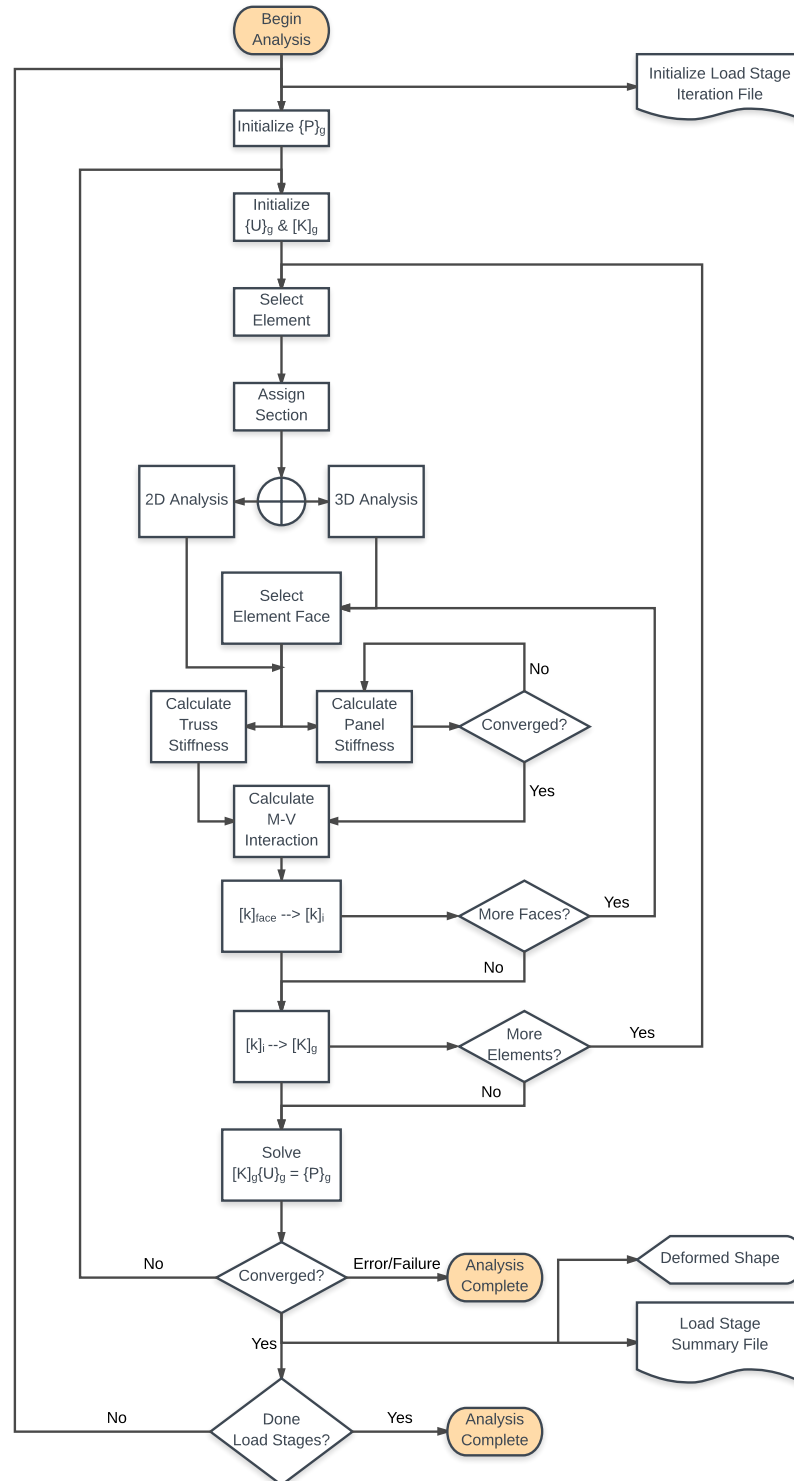


Figure 6.25: Analysis Program Operational Flowchart

For a load stage to be considered completed the analysis must satisfy one of the two global convergence criteria that are set manually by the user. For these analyses, the absolute and relative convergence tolerance in the global displacements is set to 0.005 mm and 0.05% respectively. If the maximum number of iterations is reached or the solution becomes unstable, the structure is considered to have failed and the analysis terminates. After each completed load stage, the program also produces an image of the deformed shape and the location of cracks to assist the user in understanding the failure mechanism. The cracks are simply to indicate how a face of an element is behaving, and should not be taken as a realistic representations of the behaviour. Figure 6.26 Figure 6.27 shows the output from a single load stage in the analysis of the slab and beam respectively, note that the actual output is a 3D plot that can be rotated to better view the structure.

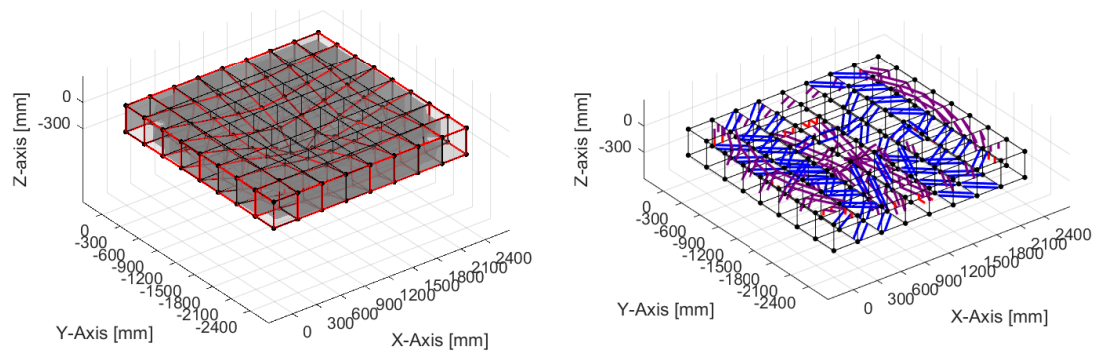


Figure 6.26: *Deformation and Cracking Output at Load Stage for Fixed Slab Model*

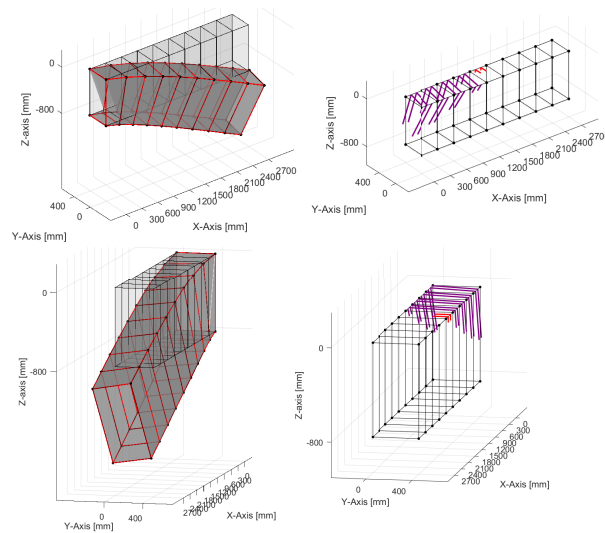


Figure 6.27: *Deformation and Cracking Output at Load Stage for Cantilevered Beam Model*

The program also outputs two text files at each load stage. The "Load Stage Iteration" file is created at the beginning of the load stage and records all the important calculations throughout. The "Load Stage Summary" file on the other hand is created at the end of the load stage and records the high-level behaviour of the model - this is the file that is accessed for post-processing purposes. Examples of these files, for the analysis model of torsional shell specimen ES2, can be found in Appendix E.3.

6.5 Element Verification

As a preliminary verification of the 3d-HyPT element, the two torsion tests that constituted the experimental component of this thesis were modelled using the program described in the previous section. Figure 6.28 shows the finite element mesh generated by the program, which is the same for both tests since the loading and geometry were identical. The test region of the specimens is represented by a 5x5 grid of 3d-HyPT elements, and is globally restrained in three in-plane and three out-of-plane DOFs to provide the necessary stability but still remain statically determinate. Torsion in the model is represented as equal and opposite nodal forces acting along the top and bottom faces (North and South in the experiment), where the resultant moment is taken as the applied torsion. Both models use the same element geometry (230 x 230 x 285 mm), except that ES2 has steel in the Z-direction to represent the T-head reinforcement. The sections are shown in Figure 6.29, and the text files used to generate all the structural inputs are found in Appendix E.1.

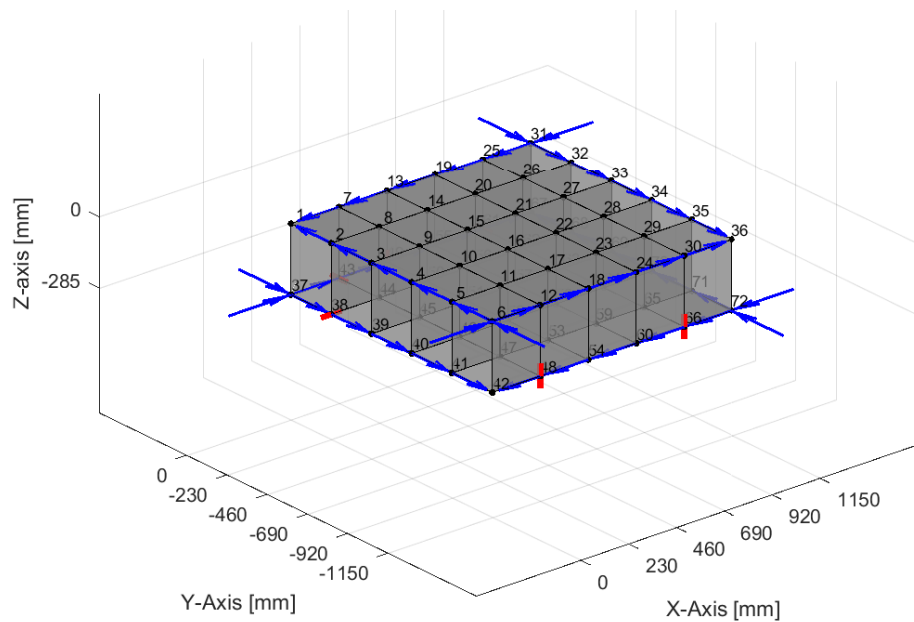


Figure 6.28: *Finite Element Mesh for Torsion Shell Experiments (ES1 & ES2)*

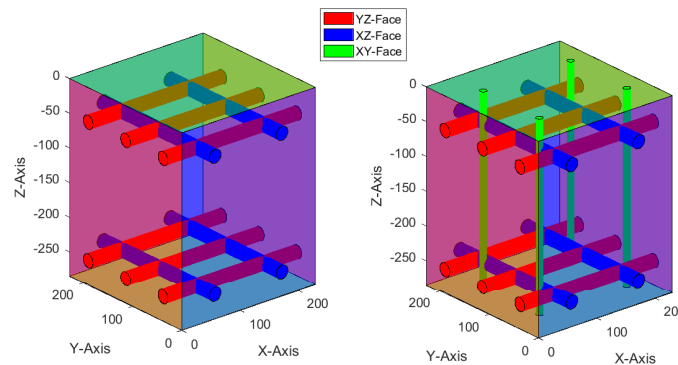


Figure 6.29: *Analysis Element Geometry: ES1 (Left) & ES2 (Right)*

6.5.1 Deformations

Figure 6.30 shows the deformed shape during the analysis of specimen ES2, which closely resembles the double curvature shape associated with pure torsion. The deformations in these images have been magnified to clearly display the progression of deformations, which are similar to the surface deformed shape captured by the LED targets.

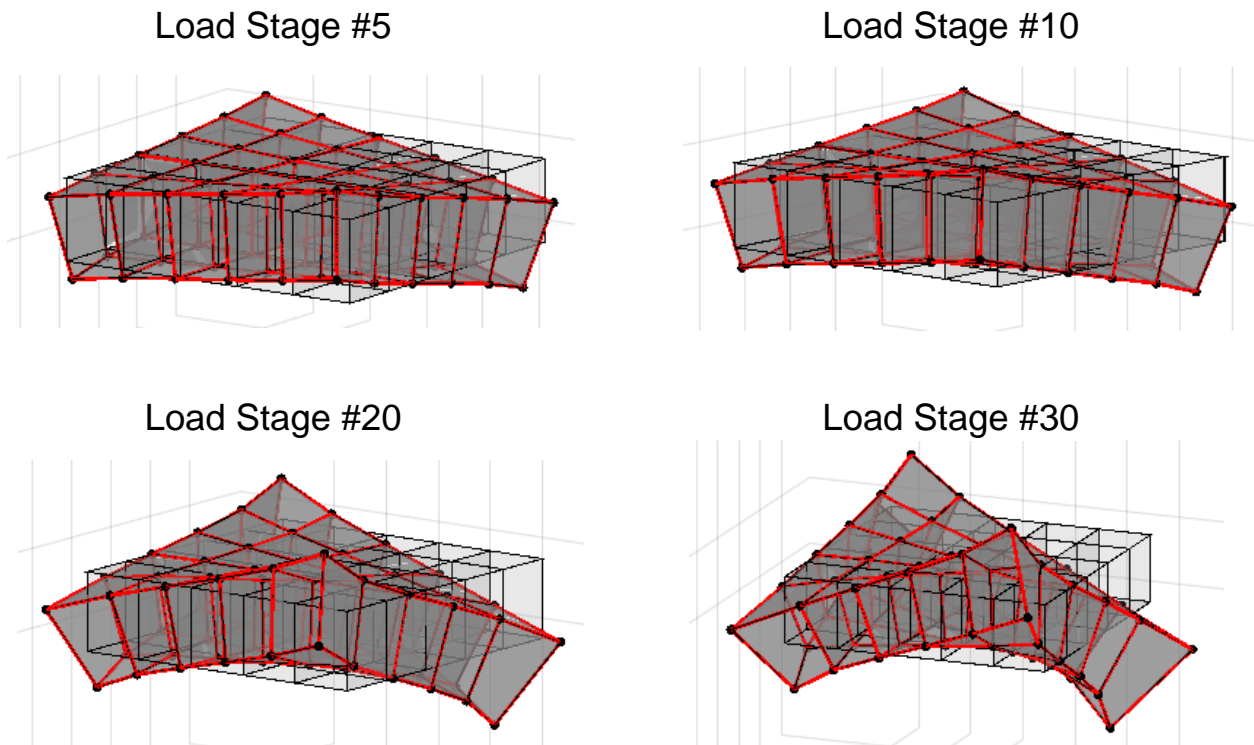


Figure 6.30: *Typical Deformed Shape During the Analysis of a Torsion Shell (Magnified)*

6.5.2 Analysis Comparison

As a preliminary verification study of the element, and to test the functionality of the program, the analysis results for both specimens were post-processed and then compared to their respective experimental data. The following section will discuss the analytical results for the following relationships: torque-twist (Figure 6.31), and out-of-plane shear strain (Figure 6.32). The post-processor is still in development, and hence a detailed look at all the different variables is not currently possible without a significant amount of work beyond the scope of the current project. Another limitation of the program is the fact that it is force-based, meaning that in its current state it does not calculate the post-peak region of a structural analysis problem. Therefore, the comparison plots in this section are only up to the peak response for both the experimental and analytical results.

The torque-twist comparison for both specimens is shown in Figure 6.31. To improve the reliability of the results, the "Program" line is taken as the average of all 25 elements used in each individual model - the top and bottom shear strains are calculated based on the nodal displacements, and are then used to find the twist strain across the element.

The analytical model does an excellent job of predicting the peak torsion, with an Exp./Pred. ratio of 1.09 and 1.04 for ES1 and ES2 respectively. Yet the prediction of the twist strain at the peak torsion is significantly underpredicted, with Exp./Pred. ratios of 1.68 and 1.49. In general, the model matches the pre-cracking behaviour perfectly but is stiffer in the cracked linear portion. Despite the differences in the strength and ductility, it appears that the model captures the shape of the curve before failure - ES1 failing in a more sudden manner, while ES2 has a more ductile response up to its peak due to the T-head reinforcement.

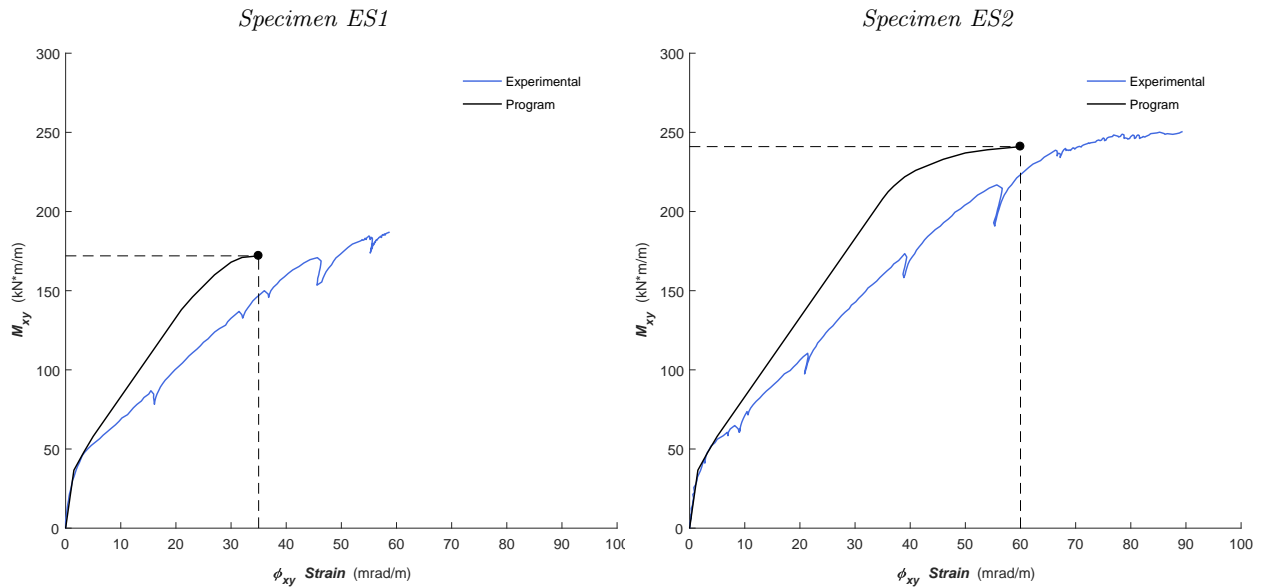


Figure 6.31: Analysis Program Results: Torque-Twist

The out-of-plane shear strain comparison for both specimens is shown in Figure 6.32. There were some inconsistencies in the program results for the elements that were adjacent to the supports, so these outliers were removed from the calculations by only taking the average of the out-of-plane strains for the central elements in both specimens. This was considered a reasonable assumption since the experimental instrumentation being compared to was also located away from the edges of the specimen to avoid disturbed region effects. The relative nodal displacements, read from the "Load Stage Summary" files, between the top and bottom faces of each element were used to calculate the strains in both the XZ and YZ planes.

The analytical model once again shows good agreement with the experimental results, although the values of strain at failure are over and under-predicted for specimens ES1 and ES2 respectively. Yet in both specimens the rapid increase in the out-of-plane shear strains indicates that the peak torsion value is approaching, although the actual strain values calculated are questionable since the convergence of the solution was more difficult during the final load stages (especially for specimen ES1). It was found that the final strain values could vary by up to 20% depending on the magnitude of the load step (increments ranging from 1 kN to 10 kN per load stage were used). Aside from these convergence issues, the cracked linear region of the program results were stable and match the experimental results closely right up to the failure. Specimen ES2, with the T-head shear reinforcement, also exhibited a slightly stiffer response in the cracked linear region than specimen ES1. The rapid increase in the out-of-plane shear strains that precedes the peak torsion is consistent with the failure mode, and observations of significant cover spalling and concrete crushing made during the experiments. It is important to note that only the experimental LP data is used in this comparison, since surface-to-surface strains are consistent with the nodal data generated by the program (as opposed to using the internal strains measured by the EGs). The imposed strain in the Z-direction is also assumed based on the experimental results.

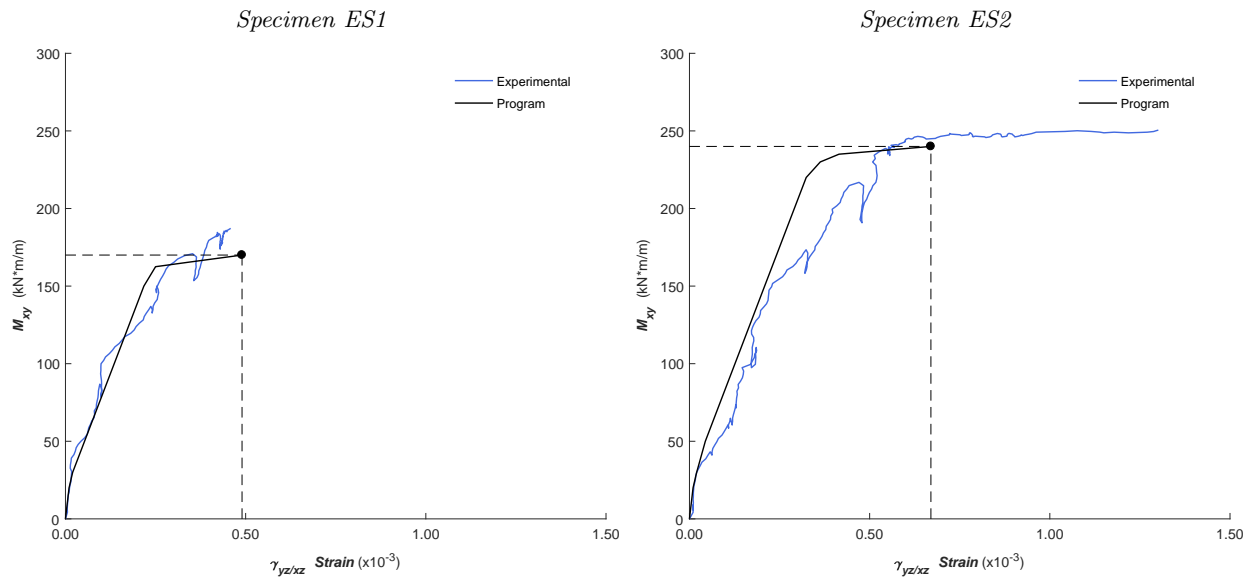


Figure 6.32: Analysis Program Results: Out-of-Plane Shear Strain

Overall, the analysis program that was written to implement the 3d-HyPT element is able to predict some of the main results from the two torsion experiments. An important caveat is that this exercise is only intended as a preliminary proof of concept, and should therefore not be taken as definitive proof that the element is appropriate for all types of shell analyses. The only statement that can be made with confidence at this point is that the 3d-HyPT element is a promising tool for the analysis of shells subjected to torsion. As the post-processor is developed, and more shell experiments are performed, a more in-depth verification study will eventually be conducted.

Chapter 7

Conclusions and Recommendations

The following chapter will restate the research objectives and summarize how they were accomplished. This is followed by a list of the main conclusions divided between the experimental and analytical work, and recommendations for future research work that would build upon the research foundation laid in this thesis.

7.1 Summary of Thesis Objectives

The purpose of this thesis was to develop and present a new rational, and mathematically rigorous, finite element for the nonlinear analysis of reinforced concrete beams and shells. This research was born from the necessity to overcome the computational limitations that exist when working with current analysis paradigms. For example, a typical finite element analysis is formulated by using either several low-powered element or fewer high-powered elements to model a structure. The challenge is that the number of low-powered elements needed for a detailed analysis of a large structure will significantly slow the calculations, while on the other hand relying on complex elements with difficult numerical integration schemes will also lead to a significant computational burden.

The Hybrid Panel-Truss (HyPT) element presents a new approach by relying on the combined actions of simpler subcomponents to represent the complex nonlinearity and deformation patterns inherent in reinforced concrete. The one-dimensional trusses capture the axial and flexural deformations, while the two-dimensional panels capture the shear deformations. Not only is calculating the stiffness matrix explicitly from these subcomponents much less challenging from a computational standpoint, the element itself has also been formulated so that only one is necessary through the depth of a member. Together these two factors lead to a significant numerical simplification, in the context of a stiffness matrix structural analysis solution, by reducing the number of global degrees of freedom necessary in a problem.

The two-dimensional version of the element (2d-HyPT) can be used for the analysis of prismatic reinforced concrete beams and columns subjected to in-plane loads. The three-dimensional version of the element (3d-HyPT) extends this simpler derivation so that the element can be used for the analysis of beams and shells subjected to complex combinations of in-plane and out-of-plane loads. In the process of deriving both versions of the element an experimental program was deemed necessary to gather data on the challenging behaviour associated with pure torsion in shells. Overall, this thesis was structured around accomplishing the following goals:

1. To consolidate the work done to date on the two-dimensional version of the element, and to expand the derivation to include a rigorous membrane formulation based on the MCFT.
2. To validate the two-dimensional element against a series of experimental results.
3. To construct two shell specimens, with and without shear reinforcement, and to load them under pure torsion with a displacement-controlled loading protocol.
4. To derive and validate the three-dimensional version of the element against the torsion experiments.

7.2 Summary of Results and Conclusions

For clarity, the main results and conclusions from the thesis are divided between the physical experiments, and the analytical derivation and verification work.

7.2.1 Experimental

With respect to the experimental program, which consisted of constructing and testing two shell specimens in pure torsion, the following conclusions can be made:

1. A pure torsion loading condition can be recreated in a central test region of a shell by applying equal and opposite moments along the edges of the specimen while orienting the flexural reinforcement at 45° to the loading axis.
2. The displacement-controlled loading protocol established for these tests is a viable means of obtaining useful post-peak data from an experiment.
3. The addition of out-of-plane reinforcement, in the form of T-head bars, significantly improved the strength and ductility of the second shell tested.
4. Out-of-plane strains and through-the-thickness expansion of the specimens are important factors to take into account when modelling torsion in shells.
5. The specimens experienced crushing of the outermost layers of concrete, due to equal and opposite in-plane shear stresses on the front and back faces. Cover spalling initiated the failure and continued in the post-peak region of both tests.

7.2.2 Analytical

With respect to the analytical work, which consisted of deriving and verifying the HyPT element, the following conclusions can be made:

1. The HyPT formulation and derivation has resulted in a robust and accurate tool that can be used to quickly analyze the nonlinear response of large reinforced concrete structures.
2. The 2d-HyPT element can be used to safely predict the failure load of shear critical beams.
3. The 2d-HyPT element can be used to determine the load-deflection response of frames, and can be paired with membrane elements to model joint regions.
4. The 3d-HyPT element can be used to model structures subjected to complex loading conditions.
5. The 3d-HyPT element can be used to predict the torque-twist behaviour of reinforced concrete shells.

7.3 Recommendations for Future Work

The downside of undertaking a research project with tremendous breadth is that the depth of discussion and analysis of certain topics must be sacrificed to allow for the overall completion of the thesis within a reasonable page length. The following section will present a list of topics, which given more time and resources should be explored in detail in the future. For clarity, these recommendations are divided between the experimental and analytical work.

7.3.1 Experimental

The following are a list of ways to build upon the experimental component of this research:

1. The pure torsion experimental program should be expanded to determine the influence that different variables have on the strength and ductility of a shell. A series of specimens should be constructed with variable ratios of longitudinal reinforcement, concrete thicknesses, and concrete strengths.
2. The minimum ratio of transverse reinforcement necessary to guarantee superior strength and ductility should be explicitly determined with an experimental program where several identical shells with variable out-of-plane reinforcement ratios are tested in pure torsion.
3. More information on the out-of-plane deformations associated with reinforced concrete shells should be gathered in the future. The quality of the data gained from the embedded gauges suggests that more should be used to better understand the out-of-plane strains at the center of a shell.

7.3.2 Analytical

The following are a list of ways to build upon the analytical component of this research:

1. Although the 2d-HyPT element was well verified with respect to shear critical reinforced concrete beams, further verification studies should be performed with a focus on flexural failures.
2. Further analysis of large-scale structures and experimental test frames should be performed with the 2d-HyPT element, in conjunction with membranes elements. This procedure should be explicitly explained and the method of linking the different types of elements together should be carefully analyzed.
3. A pre and post-processor should be written to implement the 3d-HyPT element.
4. The derivation of the out-of-plane truss terms used in the 3d-HyPT element should be expressed in a more rigorous manner, rather than relying on experimental curves.
5. To determine its general applicability, the 3d-HyPT element should be used in a detailed verification study similar to what was done with the two-dimensional element in this thesis.

References

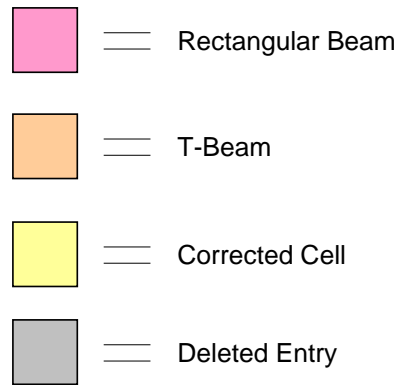
- [1] F. J. Vecchio and M. P. Collins, “The Modified Compression-Field Theory for Reinforced Concrete Elements Subjected to Shear,” *ACI Journal*, vol. 83, no. 2, pp. 219–231, Mar. 1986.
- [2] M. P. Collins, D. Mitchell, P. Adebar, and F. J. Vecchio, “A General Shear Design Method,” *ACI Structural Journal*, vol. 93, no. 1, pp. 36–45, Jan. 1996.
- [3] CSA, “Design of Concrete Structures - Clause 11 - Shear and Torsion,” in *CSA A23.3*, 2004th ed. Canadian Standards Association, 2004, pp. 53–66.
- [4] E. C. Bentz and M. P. Collins, “Development of the 2004 Canadian Standards Association (CSA) A23.3 Shear Provisions for Reinforced Concrete,” *Canadian Journal of Civil Engineering*, vol. 33, no. 5, pp. 521–534, May 2006.
- [5] F. J. Vecchio, E. C. Bentz, and M. P. Collins, “Tools for forensic analysis of concrete structures,” *Computers and Concrete*, vol. 1, no. 1, pp. 1–14, Feb. 2004.
- [6] F. J. Vecchio, “VecTor Analysis Group,” 2011. [Online]. Available: <http://www.civ.utoronto.ca/vector/software.html>
- [7] E. C. Bentz, “Response-2000,” 2000. [Online]. Available: <http://www.ecf.utoronto.ca/~bentz/r2k.htm>
- [8] F. J. Vecchio, “Nonlinear Finite Element Analysis of Reinforced Concrete Membranes,” *ACI Structural Journal*, vol. 86, no. 1, pp. 26–35, Jan. 1989.
- [9] E. C. Bentz, “Sectional Analysis of Reinforced Concrete Members,” PhD, University of Toronto, 2000.
- [10] Intel, “Microprocessor Quick Reference Guide,” 2008. [Online]. Available: <http://www.intel.com/pressroom/kits/quickreffam.htm>
- [11] F. J. Vecchio, “Reinforced Concrete Membrane Element Formulations,” *Journal of Structural Engineering*, vol. 116, no. 3, pp. 730–750, 1990.
- [12] H. C. Huang and E. Hinton, “Lagrangian and Serendipity Plate and Shell Elements Through Thick and Thin,” *Finite Element Methods for Plate and Shell Structures*, vol. 1, pp. 46–61, 1986.
- [13] J. A. Figueiras and D. R. J. Owen, “Analysis of Elasto-Plastic and Geometrically Nonlinear Anisotropic Plates and Shells,” *Finite Element Software for Plates and Shells*, vol. 403, 1984.
- [14] R. D. Cook, D. Malkuk, and M. Plesha, *Concepts and Applications of Finite Element Analysis*. John Wiley & Sons, 1989.
- [15] M. A. Polak and F. J. Vecchio, “Nonlinear Analysis of Reinforced Concrete Shells,” *Journal of Structural Engineering*, vol. 119, no. 12, pp. 3439–3462, 1993.
- [16] T. D. Hrynyk, “Behaviour and Modelling of Reinforced Concrete Slabs and Shells Under Static and Dynamic Loads,” PhD, University of Toronto, 2013.
- [17] T. J. Hughes and M. Cohen, “The Heterosis Finite Element for Plate Bending,” *Computers & Structures*, vol. 9, no. 5, pp. 445–450, Nov. 1978.
- [18] T. Belytschko, J. S.-J. Ong, W. K. Liu, and J. M. Kennedy, “Hourglass Control in Linear and Nonlinear Problems,” *Computer Methods in Applied Mechanics and Engineering*, vol. 43, pp. 251–276, 1984.

- [19] M. P. Collins and D. Mitchell, *Prestressed Concrete Structures*. Toronto, Canada: Response Publications, 1997.
- [20] M. P. Collins and P. Lampert, "Designing for Torsion," in *Structural Concrete Symposium Proceedings*, Toronto, 1971, pp. 38–79.
- [21] M. P. Collins and D. Mitchell, "Shear and Torsion Design of Prestressed and Non-Prestressed Concrete Beams," *Journal of the Prestressed Concrete Institute*, vol. 25, no. 5, pp. 32–100, 1980.
- [22] J. Blaauwendraad and P. C. Hoogenboom, "Stringer Panel Model for Structural Concrete Design," *ACI Structural Journal*, vol. 93, no. 3, pp. 295–305, May 1996.
- [23] L. S. Y. Yeung, "A New Finite Element For Reinforced Concrete Beam Analyses Including Shear," MASC, University of Toronto, 2008.
- [24] A. Cheung, "Influence of Rock Boundary Conditions on Behaviour of Arched and Flat Cemented Paste Backfill Barricade Walls," Ph.D. dissertation, University of Toronto, 2012.
- [25] M. Zaeem, "Nonlinear Finite Element Analysis of the Black River Bridge - A Serviceability Study," MASC, University of Toronto, Toronto, 2013.
- [26] B. Yap, "Modelling Coupling Beams and Coupled Shear Walls," Undergraduate Thesis, University of Toronto, Apr. 2016.
- [27] K.-H. Reineck, E. C. Bentz, B. Fitik, D. A. Kuchma, and O. Bayrak, "ACI-DAFStb Database of Shear Tests on Slender Reinforced Concrete Beams Without Stirrups," *ACI Structural Journal*, vol. 110, no. 5, p. 867, 2013.
- [28] —, "ACI-DAFStb Databases for Shear Tests on Slender Reinforced Concrete Beams with Stirrups," *ACI Structural Journal*, vol. 111, no. 5, 2014.
- [29] K. V. Duong, S. A. Sheikh, and F. J. Vecchio, "Seismic Behavior of Shear-Critical Reinforced Concrete Frame: Experimental Investigation," *ACI Structural Journal*, vol. 104, no. 3, 2007.
- [30] J. Salmon and C. Christopoulos, "Conventional Frame Hysteretic Response," University of Toronto, Tech. Rep., 2017.
- [31] A. Mari, J. M. Bairam, A. Cladera, and E. Oller, "Shear Design and Assessment of Reinforced and Prestressed Concrete Beams Based on a Mechanical Model," *Journal of Structural Engineering*, vol. 142, no. 10, 2016.
- [32] E. C. Bentz, "Membrane-2000," 2000. [Online]. Available: <http://www.ecf.utoronto.ca/~bentz/m2k.htm>
- [33] K. V. Duong, "Seismic behaviour of a shear-critical reinforced concrete frame: an experimental and numerical investigation," Ph.D. dissertation, University of Toronto, 2006.
- [34] G. T. Proestos, "Influence of High-Strength Reinforcing Bars on the Behaviour of Reinforced Concrete Nuclear Containment Structures Subjected to Shear," MASC, University of Toronto, Toronto, 2014.
- [35] G. T. Proestos, G. M. Bae, J. Y. Cho, E. C. Bentz, and M. P. Collins, "Influence of High-Strength Bars on Shear Response of Containment Walls," *ACI Structural Journal*, vol. 113, no. 5, pp. 917–927, Sep. 2016.
- [36] G. M. Bae, J. H. Park, J. Y. Cho, G. T. Proestos, E. C. Bentz, and M. P. Collins, "Investigation of Shear Response of Nuclear Power Plant Wall Elements using High Strength Materials," *IABSE Reports*, vol. 102, no. 30, pp. 867–873, Sep. 2014.
- [37] G. M. Bae, "In-Plane Shear Behaviour of Reinforced Concrete Elements with High-Strength Materials," MASC, Seoul National University, Korea, 2014.
- [38] MTS, *AeroPro Software Reference*, ser. Version 6.20. MTS System Corporation, 2009.
- [39] D. M. Ruggiero, "The Behaviour of Reinforced Concrete Subjected to Reversed Cyclic Shear," PhD, University of Toronto, Toronto, 2015.
- [40] E. C. Bentz, "Shell-2000," 2000. [Online]. Available: <http://www.ecf.utoronto.ca/~bentz/s2k.htm>

A. Shear Critical Beam Databases

The following appendix presents the shear critical beam databases (as published by Reineck et. al.) used in the verification study of the 2d-HyPT element. These data tables presented have been simplified from their original form to show only the columns of data that are necessary to create an appropriate Augustus-II and Response-2000 model.

Certain cells have been highlighted, the legend is shown below:



A.1 No Stirrups - Point Loads

Notation	Nr.	Literature	ID	Modelling		Section Properties				Loading and Geometry					Tension Reinf.					Compression Reinf.				Conc. Comp.		Conc. Tens.		Test Results									
				Load Step	Elc. Size	b	b _w	h	A _c	Z _{c2}	a _p	L	c	a	a/d	d _t	Φ _{st}	A _{st}	r _s	r _w	f _{yt}	d _{c2}	Φ _{c2}	A _{c2}	f _{yc2}	Φ _{sc}	f _c	f _{t,cr,ser}	f _{t,cr,calc}	F	V _{u1} +V _{u2}	V _{u,Rep}	V _{u,F}	V _{u,F}	V _{u,F}		
				kN	mm	mm	mm	mm	mm ²	mm ³	mm	mm	mm	mm	mm	mm	mm	mm ²	%	%	MPa	mm	mm	mm ²	MPa	mm	MPa	MPa	MPa	kN	kN	kN	kN	kN	mm		
Adebar_1989_001_ST1	21	Adebar (1989) +	ST1	10	200	360	360	310	111,600	155	1,625	0	813	2,92	278	20	1,570	1,569	1,569	536	32	20	1,570	536	19	50.1	3,87	4.02	128	129	406	406					
Adebar_1989_002_ST2	22	Adebar;	ST2	10	200	360	360	310	111,600	155	1,625	0	813	2,92	278	20	1,570	1,569	1,569	536	32	20	1,570	536	19	50.1	3,87	4.02	119	120	406	406					
Adebar_1989_003_ST3	23	Collins (1994) +	ST3	10	200	290	290	310	89,900	155	1,625	0	813	2,92	278	20	1,570	1,947	1,947	536	32	20	1,570	536	19	46.9	4.05	3.84	108	109	406	406					
Adebar_1989_005_ST16	25	Adebar;	ST16	10	200	290	290	210	60,900	105	1,625	0	813	4,56	178	20	1,570	3,041	3,041	536	30	20	1,570	536	19	49.1	3.33	3.96	75	76	406	406					
Adebar_1989_007_ST23	27	Collins (1996)	ST23	10	200	290	290	210	89,900	155	1,625	0	813	2,92	278	15	800	0,992	0,992	484	32	15	800	484	19	56.5	5.04	4.24	90	91	406	406					
AhmadKhaloo_1986_001_A1	28	Ahmad;	A1	5	200	127	127	254	32,258	127	2,032	406	813	4,00	203	25	1,013	3,927	3,927	414	13				13	60.0											
AhmadKhaloo_1986_002_A2	29	Khaloo	A2	5	200	127	127	254	32,258	127	1,626	406	610	3,00	203	25	1,013	3,927	3,927	414	13				13	60.0											
AhmadKhaloo_1986_003_A3	30	Poveda (1986)	A3	5	200	127	127	254	32,258	127	1,504	406	549	2,70	203	25	1,013	3,927	3,927	414	13				13	60.0											
AhmadKhaloo_1986_007_A7	34		A7	5	200	127	127	254	32,258	127	2,071	406	832	4,00	208	16	467	1,768	1,768	414	13				13	60.0											
AhmadKhaloo_1986_008_A8	35		A8	5	200	127	127	254	32,258	127	1,655	406	624	3,00	208	16	594	2,248	2,248	414	13				13	60.0											
AhmadKhaloo_1986_013_B1	40		B1	5	200	127	127	254	32,258	127	2,020	406	807	4,00	202	29	1,289	5,034	5,034	414	13				13	66.3											
AhmadKhaloo_1986_014_B2	41		B2	5	200	127	127	254	32,258	127	1,616	406	605	3,00	202	29	1,289	5,034	5,034	414	13				13	66.3											
AhmadKhaloo_1986_015_B3	42		B3	5	200	127	127	254	32,258	127	1,495	406	545	2,70	202	29	1,289	5,034	5,034	414	13				13	66.3											
AhmadKhaloo_1986_019_B7	46		B7	5	200	127	127	254	32,258	127	2,071	406	832	4,00	208	16	594	2,248	2,248	414	13				13	66.3											
AhmadKhaloo_1986_020_B8	47		B8	5	200	127	127	254	32,258	127	1,655	406	624	3,00	208	16	594	2,248	2,248	414	13				13	66.3											
AhmadKhaloo_1986_021_B9	48		B9	5	200	127	127	254	32,258	127	1,530	406	562	2,70	208	16	594	2,248	2,248	414	13				13	66.3											
AhmadKhaloo_1986_025_C1	52	Ahmad;	C1	5	150	127	127	254	32,258	127	1,880	406	737	4,00	184	22	1,552	6,635	6,635	414	13				13	63.6											
AhmadKhaloo_1986_026_C2	53	Khaloo	C2	5	150	127	127	254	32,258	127	1,511	406	552	3,00	184	22	1,552	6,635	6,635	414	13				13	63.6											
AhmadKhaloo_1986_027_C3	54	Poveda (1986)	C3	5	150	127	127	254	32,258	127	1,401	406	497	2,70	184	22	1,552	6,635	6,635	414	13				13	63.6											
AhmadKhaloo_1986_031_C7	58		C7	5	150	127	127	254	32,258	127	2,058	406	826	4,00	207	19	855	3,260	3,260	414	13				13	63.6											
AhmadKhaloo_1986_032_C8	59		C8	5	100	127	127	254	32,258	127	1,645	406	620	3,00	207	19	855	3,260	3,260	414	13				13	63.6											
AhmadKhaloo_1986_033_C9	60		C9	5	150	127	127	254	32,258	127	1,522	406	558	2,70	207	19	855	3,260	3,260	414	13				13	63.6											
AhmadPark_1995_007_B7N	88	Ahmad;	B7N	2	150	102	102	204	20,808	102	1,774	457	659	3,70	178	13	253	1,395	1,395	413	3	6	63	366	13	41.2											
AhmadPark_1995_015_B7H	96	Park;	B7H	2	150	102	102	204	20,808	102	1,774	457	659	3,70	178	13	253	1,395	1,395	413	3	6	63	366	13	75.7											
AhmadPark_1995_016_B8H	97	El-Dash (1995)	B8H	2	150	102	102	204	20,808	102	1,774	457	659	3,70	178	13	253	1,395	1,395	413	3	6	63	366	13	78.4											
AlAlusi_1957_002_12	99	Al-Alusi (1957)	12	1	100	330	76	146	19,194	49	64	1,041	406	318	127	13	253	0,604	2,618	366					6	22.8	1.89	2.31	27	27	159						
AlAlusi_1957_003_11	100		11	1	100	330	76	146	19,194	49	64	1,270	406	432	340	127	13	253	0,604	2,618	366				6	26.2	2.50	2.56	17	18	227						
AlAlusi_1957_004_2	101		2	1	100	330	76	146	19,194	49	64	1,270	406	432	340	127	10	143	0,340	1,473	366				6	25.5	2.23	2.50	14	15	216						
AlAlusi_1957_005_21	102		21	1	100	330	76	151	20,871	50	64	1,270	406	432	340	127	13	253	0,604	2,618	366				6	26.8	2.49	2.60	24	24	216						
AlAlusi_1957_006_15	103		15	1	100	330	76	151	20,871	50	64	1,422	406	508	400	127	13	253	0,604	2,618	366				19	13	253	366	6	22.8	2.30	2.32	17	17	254		
AlAlusi_1957_008_10	105		10	1	100	330	76	146	19,194	49	64	1,422	406	508	400	127	13	253	0,604	2,618	366				6	26.2	2.30	2.56	15	15	254						
AlAlusi_1957_009_4	106		4	1	100	330	76	146	19,194	49	64	1,422	406	508	400	127	10	143	0,340	1,473	366				6	24.2	2.31	2.41	14	14	254						
AlAlusi_1957_010_13	107		13	1	100	330	76	146	19,194	49	64	1,422	406	508	400	127	13	253	0,604	2,618	366				6	26.3	2.27	2.56	17	17	254						
AlAlusi_1957_012_18	109		18	1	100	330	76	146	19,194	49	64	1,549	406	572	450	127	13	253	0,604	2,618	366				6	24.5	2.37	2.44	14	14	286						
AlAlusi_1957_015_7	110		7	1	100	330	76	146	19,194	49	64	1,549	406	572	450	127	13	253	0,604	2,618	366				6	23.0	2.17	2.33	14	14	286						
AlAlusi_1957_016_24	113		24	1	100	330	76	146	19,194	49	64	1,549	406	572	450	127	13	253	0,604	2,618	366				6	26.1	2.44	2.55	15	16	286						
AlAlusi_1957_017_16	114		16	1	100	330	76	151	20,871	50	64	1,549	406	572	450	127	13	253	0,604	2,618	366																

Notation	Nr.	Literature	ID	Modelling		Section Properties					Loading and Geometry					Tension Reinf.					Compression Reinf.		Conc. Comp.		Test Results										
				Load Step	Ele. Size	b	h _w	h	A _c	z _{ca}	d _{sp}	L	c	a/d	d _l	Φ _{st}	A _s	f _{yk}	f _{td}	f _{yk}	f _{cd}	d ₂	Φ _{st2}	A _{s2}	f _{yk2}	Φ _s	f _{cd}	f _{ct,crack}	f _{ct,modul}	F	V _{u,F} +F _{test}	V _{u,Rsp}	V _{u,F} +F	x _c	
																																			mm
Bernhardt_1986_003_S6C	180	Fynboe (1986)	S6C	5	100	150	150	200	30,000	100	2,550	1,750	400	2.52	159	20	628	2,634	2,634	510					79.7	4.77	115	116	116	200					
Bernhardt_1986_004_S9A	181		S9A	5	100	150	150	200	30,000	100	2,550	1,450	550	3.46	159	20	1,257	5,269	5,269	510					79.7	4.77	80	81	81	275					
Bernhardt_1986_005_S9B	182		S9B	5	100	150	150	200	30,000	100	2,550	1,450	550	3.46	159	20	1,257	5,269	5,269	510					79.7	4.77	65	66	66	275					
Bernhardt_1986_006_S9C	183		S9C	5	100	150	150	200	30,000	100	2,550	1,450	550	3.46	159	20	1,257	5,269	5,269	510					79.7	4.77	68	69	69	275					
Bhal_1968_001_B1	184	Bhal (1968)	B1	5	200	240	240	350	84,000	175	38	1,800	38	881	294	300	24	905	1,257	1,257	426	30	20.8	2.44	2.16	70	71	71	480						
Bhal_1968_002_B2	185		B2	5	300	240	240	650	156,000	325	75	3,600	75	1,763	294	600	24	1,810	1,257	1,257	426	30	27.2	2.71	2.62	117	119	119	1,200						
Bhal_1968_003_B3	186		B3	5	400	240	240	950	228,000	475	113	5,400	113	2,644	294	900	24	2,714	1,257	1,257	426	30	25.1	3.02	2.48	162	166	166	1,875						
Bhal_1968_004_B4	187		B4	5	440	240	240	1,250	300,000	625	150	7,200	150	3,525	294	1,200	24	3,619	1,257	1,257	426	30	22.8	2.38	2.31	177	187	187	2,138						
Bhal_1968_005_B5	188		B5	5	300	240	240	650	156,000	325	75	3,600	75	1,763	294	600	24	905	0.628	0.628	426	30	24.2	2.40	2.41	104	107	107	1,022						
Bhal_1968_006_B6	189		B6	5	300	240	240	650	156,000	325	75	3,600	75	1,763	294	600	12	905	0.628	0.628	426	30	22.3	2.94	2.28	112	115	115	853						
Bhal_1968_007_B7	190		B7	5	400	240	240	950	228,000	475	113	5,400	113	2,644	294	900	24	1,357	0.628	0.628	426	30	24.8	2.95	2.46	135	140	140	1,757						
Bhal_1968_008_B8	191		B8	5	400	240	240	950	228,000	475	113	5,400	113	2,644	294	900	12	1,357	0.628	0.628	422	30	25.3	2.28	2.49	123	128	128	1,785						
Bresler_1963_001_0A-1	192	Bresler;	0A-1	10	300	310	310	556	172,374	278	152	3,658	152	1,753	350	461	29	2,579	1,805	1,805	555	19	20.2	2.64	2.12	167	171	171	876						
Bresler_1963_002_0A-2	193	Scoredis (1963)	0A-2	10	370	305	305	561	171,096	281	152	4,572	152	2,210	474	466	29	3,224	2,269	2,269	555	19	21.3	2.89	2.20	178	184	184	716						
Bresler_1963_003_0A-3	194		0A-3	10	520	307	307	556	170,961	278	152	6,401	152	3,124	677	462	29	3,868	2,727	2,727	555	19	35.2	2.76	3.14	189	196	196	1,562						
Cladera_2002_001_H 50/1	195	Cladera,	H 50/1	10	170	200	200	400	80,000	200	75	2,160	75	1,043	290	360	32	1,608	2,234	2,234	500	12	47.5	3.87			100	101	521						
Cladera_2002_003_H 60/1	196		H 60/1	10	170	200	200	400	80,000	200	75	2,160	75	1,043	290	360	32	1,608	2,234	2,234	500	12	58.4	4.29			108	109	521						
Cladera_2002_004_H 75/1	197	Cladera (2002)	H 75/1	10	170	200	200	400	80,000	200	75	2,160	75	1,043	290	360	32	1,608	2,234	2,234	500	12	66.5	4.48			100	101	521						
Cladera_2002_005_H 100/1	198		H 100/1	10	170	200	200	400	80,000	200	75	2,160	75	1,043	290	360	32	1,608	2,234	2,234	500	12	84.6	4.86			118	119	521						
Cao_2000_001_SB 2003/0	199	Cao (2000)	SB 2012/0	25	900	300	300	2,000	600,000	1000	150	10,800	150	5,325	289	1,845	30	8,400	1,518	1,518	436	150	20	2.47	379	418	418	2,663							
Cao_2000_002_SB 2012/0	200		SB 2003/0	25	900	300	300	2,000	600,000	1000	150	10,800	150	5,325	277	1,925	30	2,100	0.364	0.364	436	150	20	2.77	2.65	200	239	239	2,663						
Cederwall_1974_001_734-34	201	Cederwall; Hedman, Losberg (1974)	734-34	5	100	135	135	260	35,100	130	3,000	1,400	800	3.42	234	12	339	1,074	1,074	818		8	101	487	26.9	2.60	41	42	42	400					
Chana_1981_001_2.1a	202	Chana (1981)	2.1a	5	200	203	203	406	82,418	203	40	2,136	40	1,048	300	356	20	1,257	1,739	1,739	478	20	36.5	3.02	3.23	96	96	96	534						
Chana_1981_001_2.1b	204		2.1b	5	200	203	203	406	82,418	203	40	2,136	40	1,048	300	356	20	1,257	1,739	1,739	478	20	36.5	3.02	3.23	97	97	97	534						
Chana_1981_002_2.2a	205		2.2a	5	200	203	203	406	82,418	203	40	2,136	40	1,048	300	356	20	1,257	1,739	1,739	478	20	30.4	2.57	2.84	87	87	87	534						
Chana_1981_002_2.2b	206		2.2b	5	200	203	203	406	82,418	203	40	2,136	40	1,048	300	356	20	1,257	1,739	1,739	478	20	30.4	2.57	2.84	94	94	94	534						
Chana_1981_003_2.3a	207		2.3a	5	200	203	203	406	82,418	203	40	2,136	40	1,048	300	356	20	1,257	1,739	1,739	478	20	33.3	2.75	3.02	99	99	99	534						
Chana_1981_003_2.3b	208		2.3b	5	200	203	203	406	82,418	203	40	2,136	40	1,048	300	356	20	1,257	1,739	1,739	478	20	33.3	2.75	3.02	96	96	96	534						
Chana_1981_004_3.1a	209		3.1a	2	100	100	100	202	20,200	101	24	1,062	24	519	300	177	10	314	1,775	1,775	421	10	22.1	2.63	2.26	24	24	24	266						
Chana_1981_004_3.1b	210		3.1b	2	100	100	100	202	20,200	101	24	1,062	24	519	300	177	10	314	1,775	1,775	421	10	22.1	2.63	2.26	24	24	24	266						
Chana_1981_005_3.2a	211		3.2a	2	100	100	100	202	20,200	101	24	1,062	24	519	300	177	10	314	1,775	1,775	421	10	23.7	2.67	2.38	25	25	25	266						
Chana_1981_005_3.2b	212		3.2b	2	100	100	100	202	20,200	101	24	1,062	24	519	300	177	10	314	1,775	1,775	421	10	23.7	2.67	2.38	26	26	26	266						
Chana_1981_006_3.3a	213		3.3a	2	100	100	100	202	20,200	101	24	1,062	24	519	300	177	10	314	1,775	1,775	421	10	26.1	2.40	2.55	27	27	27	266						
Chana_1981_006_3.3b	214		3.3b	2	100	100	100	202	20,200	101	24	1,062	24	519	300	177	10	314	1,775	1,775	421	10	26.1	2.40	2.55	23	23	23	266						
Chana_1981_007_D1	215		D1	2	100	100	100	202	20,200	101	24	1,062	24	519	300	177	10	314	1,775	1,775	421	10	20.1	2.31	2.11	22	22	22	266						
Chana_1981_008_D2	216		D2	2	100	100	100	202	20,200	101	24	1,062	24	519	300	177	10	314	1,775	1,775	421	10	20.6	2.48	2.15										

Notation	Nr.	Literature	ID	Modelling		Section Properties				Loading and Geometry					Tension Reinf.					Compression Reinf.			Conc. Comp.		Test Results																		
				Load Step	Ele. Size	b	b _w	h	A _c	z _{cg}	d _{sp}	L	c	a	a/d	d _c	Φ _{st}	f _{yk}	f _{yk}	f _{yk}	f _{yk}	f _{yk}	ρ _{st}	ρ _{st}	ρ _{st}	ρ _{st}	ρ _{st}	f _{ct,loc}	f _{ct,med}	F	V _{u,F} †	V _{u,Exp}	V _{u,Exp} †	V _{u,F} †	x _c								
				kN	mm	mm	mm	mm	mm ²	mm	mm	mm	mm	mm	mm	mm	mm ²	%	%	MPa	mm	mm	mm ²	MPa	mm	MPa	MPa	MPa	MPa	MPa	MPa	MPa	MPa	MPa	MPa	kN	kN	kN	kN	kN	mm		
Drangsholt 1990_004_B14	313		B14	5	150	150	150	250	37,500	125	40	2,300	1,058	621	3,000	207	16	1,005	3,238	3,238	485	10	157	16	51.6	3.39	4.10	63	83	311													
Drangsholt 1990_006_B21	315		B21	5	150	150	150	250	37,500	125	40	2,300	974	663	3,000	221	16	603	1,820	1,820	485	10	157	16	75.4	3.94	4.68	68	69	332													
Drangsholt 1990_008_B23	317		B23	5	200	150	150	250	37,500	125	40	2,300	644	828	4,000	207	16	1,005	3,238	3,238	485	10	157	16	75.4	3.94	4.68	78	78	414													
Drangsholt 1990_009_B24	318		B24	5	150	150	150	250	37,500	125	40	2,300	1,058	621	3,000	207	16	1,005	3,238	3,238	485	10	157	16	75.4	3.94	4.68	83	83	311													
Drangsholt 1990_016_B43	320	Drangsholt;	B43	5	200	150	150	250	37,500	125	40	2,300	644	828	4,000	207	16	1,005	3,238	3,238	485	10	157	16	84.0	4.19	4.85	86	87	414													
Drangsholt 1990_017_B44	321	Thorenfeld (1992)	B44	5	150	150	150	250	37,500	125	40	2,300	1,058	621	3,000	207	16	1,005	3,238	3,238	485	10	157	16	84.0	4.19	4.85	107	108	311													
Drangsholt 1990_019_B51	323		B51	5	150	150	150	250	37,500	125	40	2,300	974	663	3,000	221	16	603	1,820	1,820	485	10	157	16	95.3	4.38	5.06	56	57	332													
Drangsholt 1990_021_B53	325		B53	5	200	150	150	250	37,500	125	40	2,300	644	828	4,000	207	16	1,005	3,238	3,238	485	10	157	16	95.3	4.38	5.06	77	78	414													
Drangsholt 1990_022_B54	326		B54	5	150	150	150	250	37,500	125	40	2,300	1,058	621	3,000	207	16	1,005	3,238	3,238	485	10	157	16	95.3	4.38	5.06	78	78	311													
Drangsholt 1990_024_B61	328		B61	5	220	300	300	500	150,000	250	80	4,600	1,948	1,326	3,000	442	32	2,413	1,820	1,820	485	20	628	16	75.4	4.24	4.68	180	186	663													
Drangsholt 1990_026_B63	330		B63	5	270	300	300	500	150,000	250	80	4,600	1,288	1,656	4,000	414	32	4,021	3,238	3,238	485	20	628	16	75.4	4.24	4.68	229	235	828													
Drangsholt 1990_027_B64	331		B64	5	220	300	300	500	150,000	250	80	4,600	2,116	1,242	3,000	414	32	4,021	3,238	3,238	485	20	628	16	75.4	4.24	4.68	281	287	621													
Elzanaty 1986_002_F11	334	Elzanaty;	F11	5	250	178	178	305	54,193	152	3,239	1,080	1,080	4,000	270	19	570	1,188	1,188	434	13	18.3	13	18.3	1.97		44	45	540														
Elzanaty 1986_003_F12	335	Nilson;	F12	5	250	178	178	305	54,193	152	3,219	1,073	1,073	4,000	268	22	1,164	2,440	2,440	434	13	18.3	13	18.3	1.97		53	54	707														
Elzanaty 1986_004_F8	336	Slate (1986)	F8	5	250	178	178	305	54,193	152	3,277	1,092	1,092	4,000	273	13	451	0,930	0,930	434	13	37.6	13	37.6	3.29		45	46	546														
Elzanaty 1986_005_F13	337		F13	5	250	178	178	305	54,193	152	3,239	1,080	1,080	4,000	270	19	570	1,188	1,188	434	13	37.6	13	37.6	3.29		48	49	540														
Elzanaty 1986_006_F14	338		F14	5	250	178	178	305	54,193	152	3,219	1,073	1,073	4,000	268	22	1,164	2,440	2,440	434	13	37.6	13	37.6	3.29		63	65	537														
Elzanaty 1986_007_F1	339		F1	5	250	178	178	305	54,193	152	3,239	1,080	1,080	4,000	270	19	570	1,188	1,188	434	13	63.1	13	63.1	4.40		57	59	564														
Elzanaty 1986_008_F2	340		F2	5	250	178	178	305	54,193	152	3,219	1,073	1,073	4,000	268	22	1,164	2,440	2,440	434	13	63.1	13	63.1	4.40		66	67	547														
Elzanaty 1986_009_F10	341		F10	5	250	178	178	305	54,193	152	3,200	1,067	1,067	4,000	267	25	1,520	3,206	3,206	434	13	63.1	13	63.1	4.40		75	76	533														
Elzanaty 1986_010_F9	342		F9	5	250	178	178	305	54,193	152	3,219	1,073	1,073	4,000	268	22	1,164	2,440	2,440	434	13	76.9	13	76.9	4.71		62	64	537														
Elzanaty 1986_011_F15	343		F15	5	250	178	178	305	54,193	152	3,219	1,073	1,073	4,000	268	22	1,164	2,440	2,440	434	13	66	13	66	4.71		66	68	537														
Elzanaty 1986_015_F6	347		F6	5	400	178	178	305	54,193	152	4,829	1,610	1,610	6,000	268	22	1,164	2,440	2,440	434	13	61.0	13	61.0	4.35		60	62	805														
Feldman 1955_002_L-2	349	Feldman;	L-2	5	150	152	152	305	46,452	152	152	2,438	914	762	3,02	252	29	1,290	3,353	3,353	310	25	19.1	25	19.1	1.61	2.04	76	76	76	544												
Feldman 1955_003_L-2A	350	Siess (1955)	L-2A	5	150	152	152	305	46,452	152	152	2,438	914	762	3,02	252	29	1,290	3,353	3,353	283	25	34.3	25	34.3	2.64	3.09	80	81	497													
Feldman 1955_004_L-3	351		L-3	5	150	152	152	305	46,452	152	152	2,946	914	1,016	4,02	252	29	1,290	3,353	3,353	310	25	25.6	25	25.6	2.14	2.51	53	54	54	648												
Feldman 1955_005_L-4	352		L-4	5	200	152	152	305	46,452	152	152	3,454	914	1,270	5,03	252	29	1,290	3,353	3,353	303	25	23.4	25	23.4	2.14	2.36	51	52	52	940												
Feldman 1955_006_L-5	353		L-5	5	250	152	152	305	46,452	152	152	3,962	914	1,524	6,04	252	29	1,290	3,353	3,353	311	25	25.5	25	25.5	2.39	2.51	51	52	52	1,029												
Feldman 1955_009_L2R	356		L2R	5	150	152	152	305	46,452	152	76	1,524	76	724	2,87	252	29	1,290	3,353	3,353	310	25	19.1	25	19.1	1.61	2.04	75	75	75	686												
Feldman 1955_010_L2aR	357		L2aR	5	150	152	152	305	46,452	152	76	1,524	76	724	2,87	252	29	1,290	3,353	3,353	310	25	34.3	25	34.3	2.64	3.09	93	93	93	362												
Feldman 1955_011_L3R	358		L3R	5	150	152	152	305	46,452	152	76	2,052	76	978	3,87	252	29	1,290	3,353	3,353	310	25	25.6	25	25.6	2.14	2.51	62	62	62	489												
Ferguson 1953_001_A1	359	Ferguson;	A1	2	100	432	402	241	37,097	86	102	1,626	203	711	3,39	210	25	1,013	1,120	4,760	276	6	27.3	6	27.3																		

Notation	Nr.	Literature	ID	Modelling		Section Properties				Loading and Geometry				Tension Reinf.					Compression Reinf.		Conc. Comp.		Test Results									
				Load Step	Ele. Size	b	b _w	h	A _c	z _{ca}	A _{st}	L	c	a/g	d _x	A _{st}	f _y	f _w	f _{cp}	f _{cd}	Φ _{cd}	A ₂	f _{cd2}	Φ _s	f _c	f _{ct,crack}	f _{ct,max}	F	V _{u,F} +F _{top}	V _{u,Exp}	V _{u,F} +F	x _e
Ghannoum_1998_018_H220 (S)	413		H220 (S)	10	100	400	400	220	88,000	110	100	1,450	500	475	2,50	190	20	900	1,184	1,184	433	40	11	200	477	10	56.2	3.14	4.23	106	107	238
Ghannoum_1998_019_H350 (N)	412		H350 (N)	20	200	400	400	350	140,000	175	100	2,063	500	781	2,50	313	25	2,500	2,000	2,000	436	40	11	200	477	10	56.2	3.14	4.23	106	107	238
Ghannoum_1998_020_H350 (S)	414		H350 (S)	15	200	400	400	350	140,000	175	100	2,063	500	781	2,50	313	25	1,500	1,200	1,200	436	40	11	200	477	10	56.2	3.14	4.23	157	159	391
Ghannoum_1998_021_H485 (N)	415		H485 (N)	20	250	400	400	485	194,000	243	100	2,700	500	1,100	2,50	440	30	3,500	1,989	1,989	385	40	11	200	477	10	56.2	3.14	4.23	199	203	550
Ghannoum_1998_022_H485 (S)	416		H485 (S)	20	250	400	400	485	194,000	243	100	2,700	500	1,100	2,50	440	30	2,100	1,193	1,193	385	40	11	200	477	10	56.2	3.14	4.23	199	202	550
Ghannoum_1998_023_H960 (N)	417		H960 (N)	20	350	400	400	960	384,000	480	100	4,945	500	2,223	2,50	889	30	7,000	1,969	1,969	385	40	16	400	444	10	56.2	3.14	4.23	337	350	1,111
Ghannoum_1998_024_H960 (S)	418		H960 (S)	20	350	400	400	960	384,000	480	100	4,945	500	2,223	2,50	889	30	4,200	1,181	1,181	385	40	16	400	444	10	56.2	3.14	4.23	337	329	1,111
Grimm_1997_001_S.1.1	419	Grimm, R. (1997)	S.1.1	5	100	300	300	200	60,000	100	50	1,540	400	570	3.75	153	14	616	1,342	1,342	600	16	87.7	5.80	4.92	10	70	71	273			
Grimm_1997_002_S.1.2	420		S.1.2	5	100	300	300	200	60,000	100	50	1,540	400	570	3.75	152	16	1,005	2,205	2,205	517	16	88.8	3.80	4.94	7	75	76	293			
Grimm_1997_003_S.1.3	421		S.1.3	5	100	300	300	200	60,000	100	50	1,540	400	570	3.90	146	28	1,847	4,217	4,217	487	16	91.3	4.26	4.99	99	99	99	277			
Grimm_1997_004_S.2.2	422	Grimm, R. (1997)	S.2.2	15	200	300	300	400	120,000	200	120	3,260	800	1,230	3.53	348	25	1,963	1,881	1,881	469	16	88.9	3.80	4.95	191	194	615				
Grimm_1997_005_S.2.4	423		S.2.4	15	200	300	300	400	120,000	200	120	3,260	800	1,230	3.75	328	28	3,695	3,755	3,755	487	16	91.7	4.33	5.00	230	233	625				
Grimm_1997_006_S.3.2	424		S.3.2	20	400	300	300	800	240,000	400	250	6,860	1,600	2,630	3.66	718	28	3,695	1,715	1,715	487	16	91.3	4.26	4.99	238	270	1,387				
Grimm_1997_007_S.3.3	425		S.3.3	15	400	300	300	800	240,000	400	250	6,860	1,600	2,630	3.53	746	28	1,847	0,825	0,825	487	16	92.0	5.01	5.00	201	215	1,063				
Grimm_1997_008_S.3.4	426		S.3.4	20	400	300	300	800	240,000	400	250	6,860	1,600	2,630	3.81	690	28	7,389	3,570	3,570	487	16	91.7	4.33	5.00	381	393	1,315				
Grimm_1997_009_S.4.1	427		S.4.1	5	100	300	300	200	60,000	100	50	1,540	400	570	3.73	153	14	616	1,342	1,342	600	16	108.5	5.39	5.29	74	75	309				
Grimm_1997_010_S.4.2	428		S.4.2	10	100	300	300	200	60,000	100	50	1,540	400	570	3.75	152	16	1,005	2,205	2,205	517	16	108.5	5.39	5.29	90	91	293				
Grimm_1997_011_S.4.3	429		S.4.3	10	100	300	300	200	60,000	100	50	1,540	400	570	3.90	146	28	1,847	4,217	4,217	487	16	108.5	5.39	5.29	122	123	208				
Haddadin_1971_001_A1	430	Haddadin, Hong;	A1	10	150	610	178	470	127,419	172	1,905	953	2,50	381	29	2,579	1,110	3,807	517	27.1	2.14	2.62	117	118	476							
Haddadin_1971_002_C1	431	Mattock (1971)	C1	10	250	610	178	470	127,419	172	1,905	953	2,50	381	29	2,579	1,110	3,807	517	23.5	2.48	2.37	87	70	810							
Haddadin_1971_003_E1	432		E1	10	150	610	178	470	127,419	172	1,905	953	2,50	381	29	2,579	1,110	3,807	517	11.5	1.30	1.40	99	101	476							
Haddadin_1971_004_I1	433		I1	10	150	610	178	470	127,419	172	1,905	953	2,50	381	29	2,579	1,110	3,807	517	23.3	2.23	2.35	122	124	476							
Hallgren_1994_001_B90SB5-2-33	434	Hallgren (1994)	B90SB5-2-33	5	100	156	156	232	36,192	116	100	2,000	600	700	3.66	191	12	678	2,272	2,272	651	18	30.4	3.06	2.84	56	57	350				
Hallgren_1994_002_B90SB6-2-33	435		B90SB6-2-33	5	100	156	156	235	36,660	118	100	2,000	600	700	3.61	194	12	678	2,241	2,241	651	18	30.4	3.06	2.84	54	54	350				
Hallgren_1994_003_B90SB9-2-31	436		B90SB9-2-31	5	100	156	156	233	36,348	117	100	2,000	600	700	3.65	192	12	678	2,266	2,266	651	18	28.7	2.88	2.72	49	50	350				
Hallgren_1994_004_B90SB10-2-31	437		B90SB10-2-31	5	100	157	157	234	36,738	117	100	2,000	600	700	3.63	193	12	667	2,202	2,202	651	18	28.7	2.88	2.72	54	54	350				
Hallgren_1994_005_B90SB13-2-86	438		B90SB13-2-86	5	100	163	163	233	37,979	117	100	2,000	600	700	3.65	192	12	678	2,169	2,169	630	18	83.8	6.03	4.85	83	83	350				
Hallgren_1994_006_B90SB14-2-86	439		B90SB14-2-86	5	100	158	158	235	37,130	118	100	2,000	600	700	3.61	194	12	678	2,213	2,213	630	18	83.8	6.03	4.85	77	77	350				
Hallgren_1994_007_B90SB17-2-45	440		B90SB17-2-45	5	100	157	157	232	36,424	116	100	2,000	600	700	3.66	191	12	678	2,258	2,258	630	18	42.5	3.24	3.58	59	60	350				
Hallgren_1994_008_B90SB18-2-45	441		B90SB18-2-45	5	100	155	155	235	36,425	118	100	2,000	600	700	3.61	194	12	678	2,256	2,256	630	18	42.5	3.24	3.58	63	64	350				
Hallgren_1994_009_B90SB21-2-85	442		B90SB21-2-85	5	100	155	155	235	36,425	118	100	2,000	600	700	3.61	194	12	678	2,256	2,256	630	18	82.2	5.40	4.82	69	70	350				
Hallgren_1994_010_B90SB22-2-85	443		B90SB22-2-85	5	100	158	158	234	36,972	117	100	2,000	600	700	3.63	193	12	678	2,225	2,225	630	18	82.2	5.40	4.82	76	76	350				
Hallgren_1994_011_B91SC1-2-62	444		B91SC1-2-62	5	100	156	156	234	36,504	117	100	2,000	600	700	3.63	193	12	678	2,254	2,254	443	18	59.4	4.95	4.31	71	72	350				
Hallgren_1994_012_B91SC2-2-62	445		B91SC2-2-62	5	100	155	155	237	36,735	119	100	2,000	600	700	3.57	192	12	678	2,231	2,231	443	18	59.4	4.95	4.31	70	70	350				
Hallgren_1994_013_B91SC3-2-69	446		B91SC3-2-69	5	100	155	155	235	36,425	118	100	2,000	600	700	3.61	194	12	678	2,256	2,256	443	18	66.7	4.68	4.49	77	77	350				
Hallgren_1994_014_B91SC4-2-69	447		B91SC4-2-69	5	100	156	156	236	36,816	118	100	2,000	600	700	3.59	195	12	678	2,229	2,229	443	18	66.7	4.68	4.49	74	75	350				
Hallgren_1994_015_B91SD1-4-61	448		B91SD1-4-61	5	100	156	156	247	38,532	124	100	2,000	600	700	3.61	194	16	1,206	3,987	3,987	494	18	58.4	4.32	4.29	89	89	350				
Hallgren_1994_016_B91SD2-4-61	449		B91SD2-4-61	5	100	156	156	248	38,688	124	100	2,000	600	700	3.59	195	16	1,206	3,965	3,965	494	18	58.4	4.32	4.29							

Notation	Nr.	Literature	ID	Modelling		Section Properties				Loading and Geometry				Tension Reinf.				Compression Reinf.		Conc. Tems.		Test Results										
				Load Step	Ele. Size	b	b _w	h	A _c	z _{cg}	s _{tp}	L	c	a	a/d	d _s	Φ _s	f _s	f _{yk}	f _{yk}	Φ _s	f _c	f _{ct,tor}	f _{ct,trans}	F	V _{u,3rdStep}	V _{u,Res}	V _{u,lg} +F	x _c			
				kN	mm	mm	mm	mm	mm ²	mm	mm	mm	mm	mm	mm	mm	mm	mm ²	%	%	MPa	mm	mm	MPa	MPa	MPa	MPa	kN	kN	kN	kN	mm
Kani_1967_009_52	494	Kani (1967)	52	2	100	152	152	152	23,226	76	89	1,544	457	544	3,93	138	19	568	2,691	2,691	392	19	22.4	2.29	23	0	272					
Kani_1967_012_55	497		55	2	100	150	150	152	22,916	76	89	1,270	457	406	3,02	135	19	568	2,805	2,805	392	19	22.7	2.21	39	0	203					
Kani_1967_013_56	498		56	2	100	153	153	152	23,342	76	89	1,409	457	476	3,46	137	19	561	2,667	2,667	403	19	24.8	2.46	28	0	238					
Kani_1967_014_57	499		57	2	100	153	153	152	23,342	76	89	1,952	457	747	5,39	139	19	555	2,612	2,612	375	19	24.0	2.40	32	0	374					
Kani_1967_015_58	500		58	2	100	152	152	152	23,226	76	89	1,409	457	476	3,46	138	19	561	2,661	2,661	417	19	24.8	2.46	29	0	238					
Kani_1967_016_59	501		59	2	100	154	154	152	23,535	76	89	1,203	457	373	2,67	140	19	568	2,632	2,632	392	19	24.2	2.42	50	0	186					
Kani_1967_017_60	502		60	2	100	155	155	152	23,613	76	89	1,271	457	407	2,93	139	19	568	2,642	2,642	392	19	24.4	2.43	39	0	203					
Kani_1967_018_81	503		81	5	250	153	153	305	46,761	152	4,170	914	1,628	5,93	274	25	1,161	2,759	2,759	343	19	25.1	2.48	51	0	814						
Kani_1967_020_83	505		83	5	100	156	156	305	47,535	152	2,542	914	814	3,00	271	25	1,161	2,745	2,745	343	19	25.0	2.47	65	0	407						
Kani_1967_021_84	506		84	5	200	151	151	305	46,064	152	3,085	914	1,085	4,00	271	25	1,161	2,835	2,835	342	19	25.0	2.47	55	0	706						
Kani_1967_023_91	508		91	5	250	154	154	305	47,071	152	4,170	914	1,628	6,06	269	25	1,123	2,705	2,705	364	19	25.0	2.47	51	0	814						
Kani_1967_025_93	510		93	5	300	155	155	305	47,226	152	4,441	914	1,763	6,46	273	25	1,123	2,656	2,656	372	19	27.9	2.67	54	0	882						
Kani_1967_027_95	512		95	5	100	153	153	305	46,761	152	2,271	914	678	2,47	275	25	1,161	2,752	2,752	338	19	22.9	2.32	73	0	339						
Kani_1967_028_96	513		96	5	200	153	153	305	46,684	152	3,085	914	1,085	3,94	275	25	1,161	2,756	2,756	335	19	22.9	2.32	56	0	543						
Kani_1967_029_97	514		97	5	200	152	152	305	46,452	152	2,545	914	815	2,95	276	25	1,129	2,681	2,681	366	19	24.8	2.46	62	0	408						
Kani_1967_030_98	515		98	5	100	153	153	305	46,684	152	2,273	914	679	2,47	275	25	1,129	2,685	2,685	366	19	23.8	2.39	76	0	340						
Kani_1967_031_99	516		99	5	100	152	152	305	46,452	152	2,273	914	679	2,50	272	25	1,129	2,726	2,726	366	19	23.8	2.39	77	0	340						
Kani_1967_034_63	519		63	5	400	154	154	610	94,142	305	89	5,356	1,016	2,170	4,00	543	29	2,323	2,771	2,771	352	19	23.8	2.39	93	0	1,085					
Kani_1967_035_64	520		64	5	900	156	156	610	95,226	305	89	9,697	1,016	4,340	8,03	541	29	2,323	2,751	2,751	352	19	23.3	2.35	79	0	2,170					
Kani_1967_036_65	521		65	5	200	150	150	610	91,200	305	89	3,734	1,016	1,359	2,46	552	29	2,329	2,818	2,818	374	19	24.6	2.44	112	0	679					
Kani_1967_037_66	522		66	10	750	156	156	610	95,226	305	89	7,527	1,016	3,255	6,01	541	29	2,323	2,747	2,747	352	19	24.0	2.40	91	0	1,628					
Kani_1967_041_71	526		71	10	400	155	155	610	94,451	305	4,271	1,016	1,628	2,99	544	29	2,245	2,663	2,663	373	19	25.0	2.47	102	0	814						
Kani_1967_043_74	528		74	10	400	152	152	610	92,903	305	4,277	1,016	1,631	3,12	523	29	2,265	2,840	2,840	366	19	24.8	2.46	108	0	815						
Kani_1967_044_75	529		75	10	400	152	152	610	92,903	305	4,277	1,016	1,631	3,11	524	29	2,265	2,836	2,836	367	19	24.9	2.46	108	0	815						
Kani_1967_045_76	530		76	10	200	152	152	610	92,903	305	3,734	1,016	1,359	2,63	518	29	2,265	2,870	2,870	372	19	28.4	2.70	115	0	679						
Kani_1967_046_79	531		79	10	700	153	153	610	93,368	305	8,626	1,016	3,805	6,84	556	29	2,316	2,719	2,719	381	19	23.7	2.38	84	0	1,902						
Kani_1967_048_3042	533		3042	10	400	154	154	1,219	187,664	610	305	7,506	2,032	2,737	2,50	1,095	32	4,555	2,703	2,703	375	19	24.0	2.40	237	0	1,368					
Kani_1967_049_3043	534		3043	10	600	154	154	1,219	187,354	610	254	8,585	2,032	3,277	3,00	1,092	32	4,555	2,714	2,714	376	19	24.6	2.44	165	0	1,638					
Kani_1967_050_3044	535		3044	10	900	152	152	1,219	185,806	610	254	10,759	2,032	4,364	3,98	1,097	32	4,555	2,724	2,724	376	19	27.1	2.62	179	0	2,842					
Kani_1967_051_3045	536		3045	10	900	155	155	1,219	188,903	610	254	12,954	2,032	5,461	5,00	1,092	32	4,568	2,699	2,699	381	19	25.9	2.53	152	0	2,731					
Kani_1967_052_3046	537		3046	1200	155	155	1,219	188,903	610	254	17,394	2,032	7,681	7,00	1,097	32	4,594	2,702	2,702	360	19	24.3	2.42	154	0	3,840						
Kani_1967_053_3047	538		3047	10	1400	155	155	1,219	188,903	610	254	19,548	2,032	8,758	8,00	1,095	32	4,555	2,685	2,685	376	19	24.3	2.42	147	0	4,379					
Kani_1967_054_271	539		271	10	400	611	611	305	186,271	152	4,176	914	1,631	6,07	269	32	4,510	2,746	2,746	377	19	24.6	2.44	217	0	815						
Kani_1967_055_272	540		272	10	300	611	611	305	186,193	152	3,632	914	1,359	5,02	271	32	4,510	2,726	2,726	377	19	24.6	2.44	228	0	679						
Kani_1967_056_273	541		273	10	200	612	612	305	186,580	152	3,089	914	1,087	4,01	271	32	4,510	2,716	2,716	377	19	24.8	2.45	206	0	544						
Kani_1967_057_274	542		274	10	200	612	612	305	186,580	152	2,545	914	815	3,02	270	32	4,510	2,726	2,726	377	19	24.8	2.45	206	0	544						
KaniHuggins_1979_002_266	544		Kani; Huggins; Wittkopp (1979)	266	2	100	153	153	305	46,684	152	2,261	914	673	2,48	272	8	207	0.498	0.498	396	19	15.7	1.76	32	0	337					
KaniHuggins_1979_003_267	545			267	2	150	153	153	305	46,761	152	2,813	914	949	3,53	269	8	213	0.515	0.515	400	19	18.3	2.19	35	0	475					
KaniHuggins_1979_004_268	546			268	2	150	153	153	305	46,684	152	2,546	914	816	2,96	275	8	207	0.491	0.491	396	19	17.7	1.92	27	0	408					
KaniHuggins_1979_007_246	549			246	2	150	153	153	305	46,684	152	2,819	914	952	3,47	274	8	213	0.507	0.507	400	19	22.5	2.48	25	0	476					
KaniHuggins_1979_008_248	550			248	2	100	153	153	305	46,684	152	2,271	914	678	2,41	282	8	213	0.493	0.493	400	19	25.2	2.48	37	0	339					
KaniHuggins_1979_015_179	557			179	2	100	153	153	305	46,684	152	2,271	914	678	2,57	264	8	213	0.526	0.526	400	19	29.9	2.81	34	0	339					
KaniHuggins_1979_016_180	558			180	2	150	153	153	305	46,761	152	2,813	914	949	3,53	269	8	213	0.515	0.515	400	19	32.1	2.95	25	0	475					
KaniHuggins_1979_019_143	561			143	2	150	154	154	305	46,839	152	3,085	914	1,085	3,96	274	10	314	0.744													

Notation	Nr.	Literature	ID	Modelling		Section Properties						Loading and Geometry						Tension Reinf.			Compression Reinf.		Conc. Comp.		Conc. Test Results																		
				Load Step	Ele. Size	b	b _w	h	A _c	z _{cg}	d _{sp}	L	c	a	a/d	d _s	Φ _s	f _{yk}	f _{yk}	f _{yk}	f _{yk}	d _{c2}	Φ _{c2}	A _{c2}	f _{yk2}	Φ _s	f _c	f _{yk,Test}	f _{yk,Mean}	F	V _{u,F} / G _{0p}	V _{u,Exp}	V _{u,Res} + F	x _c									
				kN	mm	mm	mm	mm	mm ²	mm	mm	mm	mm	mm	mm	mm	mm ²	%	%	MPa	mm	mm	mm ²	MPa	mm	MPa	MPa	MPa	MPa	MPa	MPa	MPa	MPa	MPa	MPa	MPa	MPa	MPa					
KaniHuggins_1979_085_36	629	Witkopp (1979)	36	2	150	153	153	305	46,606	152	89	2,819	914	953	3,49	273	16	761	1,823	1,823	491	19	23.7	2.38	52	0	476																
KaniHuggins_1979_087_182	627		182	2	200	155	155	305	47,148	152	3,627	914	1,356	5,05	268	15	748	1,802	1,802	386	19	31.5	2.91	49	0	678																	
KaniHuggins_1979_090_186	632		186	2	150	155	155	305	47,148	152	3,085	914	1,085	3,99	272	15	748	1,780	1,780	394	19	32.7	2.99	55	0	543																	
KaniHuggins_1979_093_191	635		191	2	150	154	154	305	46,839	152	2,545	914	815	2,96	275	16	761	1,801	1,801	497	19	31.6	2.92	53	0	408																	
KaniHuggins_1979_095_193	637		193	2	150	153	153	305	46,761	152	2,271	914	678	2,44	278	16	768	1,803	1,803	352	19	32.2	2.96	57	0	339																	
KaniHuggins_1979_096_194	638		194	2	150	154	154	305	46,916	152	2,542	914	814	2,93	278	16	768	1,797	1,797	352	19	32.2	2.96	51	0	507																	
KaniHuggins_1979_097_195	639		195	2	150	153	153	305	46,684	152	3,085	914	1,085	3,94	275	16	768	1,821	1,821	352	19	32.2	2.96	47	0	443																	
KaniHuggins_1979_099_197	641		197	2	150	150	150	305	45,832	152	2,273	914	679	2,48	274	16	755	1,835	1,835	376	19	33.6	3.04	53	0	340																	
KaniHuggins_1979_104_202	646		202	2	150	154	154	305	46,839	152	4,170	914	1,628	5,97	273	19	1,123	2,680	2,680	377	19	31.5	2.91	50	0	814																	
KaniHuggins_1979_108_206	650		206	2	150	152	152	305	46,452	152	2,273	914	679	2,51	270	19	1,123	2,726	2,726	381	19	32.8	2.99	100	0	340																	
KaniHuggins_1979_110_208	652		208	2	200	157	157	305	47,768	152	3,356	914	1,221	4,44	275	19	1,155	2,679	2,679	379	19	33.3	3.03	60	0	610																	
KaniHuggins_1979_112_210	654	Kani; Huggins;	210	2	150	154	154	305	47,071	152	2,273	914	679	2,50	272	19	1,123	2,675	2,675	381	19	32.8	2.99	79	0	340																	
KaniHuggins_1979_113_211	655	Witkopp (1979)	211	2	200	152	152	305	46,452	152	3,633	914	1,359	5,02	271	25	1,156	2,801	2,801	507	19	32.5	2.97	54	0	680																	
KaniHuggins_1979_114_212	656		212	2	150	155	155	305	47,303	152	2,545	914	815	2,98	273	19	1,129	2,662	2,662	381	19	32.8	2.99	60	0	408																	
KaniHuggins_1979_115_213	657		213	2	200	154	154	305	46,993	152	3,360	914	1,223	4,44	276	19	1,129	2,657	2,657	381	19	34.3	3.09	57	0	612																	
KaniHuggins_1979_116_214	658		214	2	150	153	153	305	46,761	152	2,273	914	679	2,50	272	19	1,129	2,708	2,708	412	19	33.6	3.04	82	0	340																	
KaniHuggins_1979_117_215	659		215	2	150	154	154	305	47,071	152	2,273	914	679	2,48	274	19	1,129	2,673	2,673	412	19	33.6	3.04	66	0	340																	
KaniHuggins_1979_119_709	661		709	2	200	152	152	305	46,452	152	64	3,633	914	1,359	4,87	279	25	1,156	2,717	2,717	379	19	24.4	2.43	52	0	680																
KaniHuggins_1979_120_666	662		666	2	150	155	155	305	47,226	152	64	2,546	914	816	2,95	277	25	1,156	2,697	2,697	348	19	26.9	2.60	63	0	408																
KaniHuggins_1979_121_675	663		675	2	150	152	152	305	46,452	152	64	2,548	914	817	2,95	277	25	1,156	2,740	2,740	378	19	24.2	2.42	57	0	408																
KaniHuggins_1979_122_718	664		718	2	200	152	152	305	46,219	152	64	3,632	914	1,359	4,85	280	25	1,156	2,721	2,721	392	19	24.2	2.41	54	0	679																
KaniHuggins_1979_123_742	665		742	2	200	152	152	305	46,452	152	3,633	914	1,359	5,02	271	25	1,156	2,801	2,801	507	19	32.5	2.97	54	0	680																	
KaniHuggins_1979_124_744	666		744	2	200	152	152	305	46,452	152	3,631	914	1,358	5,05	269	25	1,156	2,820	2,820	465	19	34.2	3.08	52	0	679																	
KaniHuggins_1979_125_746	667		746	2	200	152	152	305	46,452	152	3,629	914	1,357	5,06	268	25	1,156	2,828	2,828	474	19	28.6	2.72	53	0	679																	
KaniHuggins_1979_127_502	669		502	2	150	152	152	305	46,452	152	2,539	914	812	2,83	287	25	1,156	2,643	2,643	373	19	23.0	2.37	50	0	406																	
KaniHuggins_1979_129_504	671		504	2	150	151	151	305	45,987	152	2,542	914	814	2,98	273	25	1,156	2,806	2,806	346	19	23.8	2.39	62	0	407																	
Kawano_1998_001_A-1a	673	Kawano; Watanabe (1998)	A-1a	2	150	105	105	330	34,650	165	2,200	400	900	3,00	300	16	402	1,277	1,277	370	20	22.4	2.28	34	34	34	450																
Kawano_1998_002_A-1b	674		A-1b	2	150	105	105	330	34,650	165	2,200	400	900	3,00	300	16	402	1,277	1,277	370	20	22.4	2.28	30	30	30	450																
Kawano_1998_003_A-2a	675		A-2a	5	250	176	176	570	100,320	285	3,600	600	1,500	3,00	500	16	1,206	1,371	1,371	370	20	24.9	2.46	83	85	85	750																
Kawano_1998_004_A-2b	676		A-2b	5	250	176	176	570	100,320	285	3,600	600	1,500	3,00	500	16	1,206	1,371	1,371	370	20	24.9	2.46	102	104	104	750																
Kawano_1998_005_A-3a	677		A-3a	20	500	350	350	1,050	367,500	525	6,500	800	2,850	3,00	950	25	3,927	1,181	1,181	360	25	19.3	1.97	216	232	232	1,425																
Kawano_1998_006_A-3b	678		A-3b	20	500	350	350	1,050	367,500	525	6,500	800	2,850	3,00	950	25	3,927	1,181	1,181	360	25	19.3	1.97	238	254	254	1,425																
Kawano_1998_007_A-4a	679		A-4a	60	1000	600	600	2,200	1,320,000	1100	13,000	1,000	6,000	3,00	2,000	35	14,432	1,203	1,203	360	40	19.8	2.09	611	721	721	3,000																

A.2 No Stirrups - Distributed Load

Notation	Nr.	Literature	ID	Modelling		Section Properties					Loading and Geometry					Tension Reinf.					Compression Reinf.			Conc. Comp.		Conc. Tens.		Test Results					
				Load Step	Ele. Size	b	b _w	h	A _c	Z _{c2}	a _f	L	c	a	a/d	d _s	Φ _s	A _s	r _s	r _w	f _{yk}	d ₂	Φ _{a2}	A _{s2}	f _{yk2}	Φ _{sc}	f _c	f _{ict, test}	f _{ict, cal}	F	V _{u,f} +B _{sep}	V _{u,Rep}	V _{u,g} + F
				kN	mm	mm	mm	mm	mm ²	mm	mm	mm	mm	mm	mm	mm ²	%	%	MPa	mm	mm	mm ²	MPa	mm	MPa	MPa	MPa	kN	kN	kN	mm		
Feldman 1955 001 D-1	1600	Feldman; Stess (1955)	D-1	20	200	152	152	305	46,452	152	2,794	699	2,77	252	29	1,289	3,351	3,351	295				25	28.4	2.29	2.71	93	60	60	432			
Feldman 1955 002 D-2	1601		D-2	20	200	152	152	305	46,452	152	2,794	699	2,77	252	29	1,289	3,351	3,351	307				25	36.2	2.39	3.20	110	71	71	381			
Feldman 1955 003 D-3	1602		D-3	20	200	152	152	305	46,452	152	3,353	838	3.32	252	29	1,289	3,351	3,351	314				25	30.8	2.66	2.87	94	57	57	457			
Feldman 1955 006 D-6	1603		D-6	20	200	152	152	305	46,452	152	2,794	699	2,77	252	29	1,289	3,351	3,351	310				25	21.4	2.07	2.21	104	62	62	381			
Krefteld 1996 020 2AU	1604	Krefteld;	2AU	20	200	152	152	305	46,452	152	2,438	610	2.40	254	25	507	1,309	1,309	394					18.8		2.01		76	43	44	325		
Krefteld 1996 022 4AU	1605	Thurston (1966)	4AU	20	200	152	152	305	46,452	152	2,438	610	2.40	254	25	1,013	2,618	2,618	273					15.5		1.74		91	52	52	353		
Krefteld 1996 023 5AU	1606		5AU	20	200	152	152	305	46,452	152	2,438	610	2.41	252	29	1,289	3,351	3,351	268					18.2		1.97		110	63	64	352		
Krefteld 1996 026 2CU	1607		2CU	20	200	152	152	305	46,452	152	3,048	762	3.00	254	25	507	1,309	1,309	370					18.4		1.98		54	33	34	302		
Krefteld 1996 027 3CU	1608		3CU	20	200	152	152	305	46,452	152	3,048	762	2.98	256	22	776	1,992	1,992	319					18.1		1.96		72	43	44	607		
Krefteld 1996 028 4CU	1609		4CU	20	200	152	152	305	46,452	152	3,048	762	3.00	254	25	1,013	2,618	2,618	276					18.2		1.96		80	48	49	251		
Krefteld 1996 029 5CU	1610		5CU	20	200	152	152	305	46,452	152	3,048	762	3.02	252	29	1,289	3,351	3,351	224					18.0		1.95		83	50	51	492		
Krefteld 1996 030 6CU	1611		6CU	20	200	152	152	305	46,452	152	3,048	762	3.04	250	32	1,635	4,283	4,283	174					18.2		1.96		78	47	48	466		
Krefteld 1996 031 3EU	1612		3EU	20	200	152	152	305	46,452	152	3,658	914	3.58	256	22	776	1,992	1,992	349					15.2		1.72		62	41	43	409		
Krefteld 1996 032 4EU	1613		4EU	20	200	152	152	305	46,452	152	3,658	914	3.60	254	25	1,013	2,618	2,618	327					17.8		1.94		73	49	50	238		
Krefteld 1996 035 3GU	1614		3GU	20	200	152	152	305	46,452	152	4,267	1,067	4.17	256	22	776	1,992	1,992	379					20.2		2.12		59	42	44	409		
Krefteld 1996 037 5GU	1615		5GU	20	200	152	152	305	46,452	152	4,267	1,067	4.23	252	29	1,289	3,351	3,351	260					18.9		2.02		66	47	49	314		
Krefteld 1996 039 3JU	1616		3JU	20	200	152	152	305	46,452	152	4,877	1,219	4.77	256	22	776	1,992	1,992	379					19.8		2.09		48	37	39	409		
Krefteld 1996 048 4AU	1617		4AU	20	200	152	152	305	46,452	152	2,438	610	2.40	254	25	1,013	2,618	2,618	298					29.3		2.76		117	67	68	276		
Krefteld 1996 049 5AU	1618		5AU	20	200	152	152	305	46,452	152	2,438	610	2.41	252	29	1,289	3,351	3,351	306					29.3		2.76		133	75	76	314		
Krefteld 1996 050 6AU	1619		6AU	20	200	152	152	305	46,452	152	2,438	610	2.43	250	32	1,635	4,283	4,283	278					31.7		2.92		155	88	89	377		
Krefteld 1996 051 4CU	1620		4CU	20	200	152	152	305	46,452	152	3,048	762	3.00	254	25	1,013	2,618	2,618	314					29.9		2.80		97	59	60	213		
Krefteld 1996 052 5CU	1621		5CU	20	200	152	152	305	46,452	152	3,048	762	3.02	252	29	1,289	3,351	3,351	254					29.9		2.80		95	58	59	314		
Krefteld 1996 053 6CU	1622		6CU	20	200	152	152	305	46,452	152	3,048	762	3.04	251	32	1,635	4,278	4,278	249					34.4		3.10		108	65	67	288		
Krefteld 1996 063 4CU	1623		4CU	20	200	152	152	305	46,452	152	3,048	762	3.00	254	25	1,013	2,618	2,618	251					14.7		1.68		71	42	43	569		
Krefteld 1996 067 4EU	1624		4EU	20	200	152	152	305	46,452	152	3,658	914	3.60	254	25	1,013	2,618	2,618	231					11.9		1.43		50	34	35	315		
Leonhardt 1962 007 14/1	1625	Leonhardt;	14/1	20	200	190	190	320	60,800	160	3,000	750	2.75	273	26	1,062	2,047	2,047	465				30	29.9	2.97	2.80	101	64	64	375			
Leonhardt 1962 008 14/2	1626	Walther (1962)	14/2	20	200	190	190	320	60,800	160	3,000	750	2.75	273	26	1,062	2,047	2,047	465				30	29.9	2.97	2.80	101	63	63	400			
Leonhardt 1962 009 15/1	1627		15/1	20	200	190	190	320	60,800	160	4,000	1,000	3.68	272	26	1,062	2,055	2,055	465					30	34.4	3.30	3.09	88	61	61	405		
Leonhardt 1962 010 15/2	1628		15/2	20	200	189	189	320	60,480	160	4,000	1,000	3.66	273	26	1,062	2,058	2,058	465					30	34.4	3.30	3.09	94	68	68	437		
Leonhardt 1962 011 16/1	1629		16/1	20	200	189	189	320	60,800	160	5,000	1,250	4.56	274	26	1,062	2,047	2,047	465					30	31.9	2.59	2.94	88	68	68	436		
Leonhardt 1962 012 16/2	1630		16/2	20	200	189	189	320	60,480	160	5,000	1,250	4.56	274	26	1,062	2,050	2,050	465					30	31.9	2.59	2.94	88	70	70	438		
Regan 1971 001 U/L1	1631	Regan (1971)	U/L1	20	200	152	152	305	46,360	153	3,366	841	3.18	265	16	1,206	2,995	2,995	630				16	397	427	19	32.6	0.00	2.98	110	64	64	508
Shioya 1989 005 UB-10-1.3-0	1632	Shioya (1989)	UB-10-1.3-0	20	200	300	300	240	72,000	120	2,000	500	2.50	200	16	804	1,340	1,340	353				5	17.7	1.89	1.93	79	47	47	282			
Shioya 1985 003 2-3	1633	Shioya (1989);	2-3	20	200	300	300	655	196,500	328	7,200	1,800	3.00	600	6	679	0.377	0.377	440					10	18.7	1.63	2.00	94	72	72	1,000		
Shioya 1985 004 2-4	1634	Shioya, Nojiri,	2-4	20	200	500	500	1,200	600,000	600	12,000	3,000	3.00	1,000	10	2,199	0.440	0.440	370					10	24.8	1.85	2.46	151	157	157	1,600		
Shioya 1985 005 2-5	1635	Akiyama (1985)	2-5	20	200	500	500	1,200	600,000	600	12,000	3,000	3.00	1,000	10	2,199	0.440	0.440	370					25	19.5	2.01	2.07	178	170	170	1,800		
Shioya 1985 006 2-6	1636		2-6	20	200	1,000	1,000	2,100	2,100,000	1050	24,000	6,000	3.00	2,000	16	8,042	0.402	0.402	370					25	26.1	2.46	2.55	924	539	539	4,133		
Shioya 1985 007 2-7	1637		2-7	20	200	1,500	1,500	3,140	4,710,000	1570	36,000	9,000	3.00	3,000	25	17,671	0.393	0.393	360					25	21.9	1.97	2.25	1,890	1,103	1,103	6,000		
Shioya 1989 004 3-4	1638	Shioya (1989)	3-4	20	200	300	300	655	196,500	328	7,200	1,800	3.00	600	6	679	0.377	0.377	440														

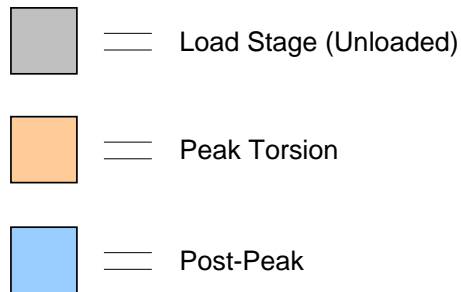
A.3 Stirrups - Point Loads

1	2	3	4	5	6	7 Section properties						8 Loading and Geometry						9 Tension Reinf.						10 Compression Reinf.						11 Conc. Comp.		12 Test Results									
						Modelling	Load Step		Ele. Size		b	b _h	h	A _s	Z _{xx}	Δ	L	c	a	a _d	d _s	Δ _s	A _s	f _t	f _{ck}	f _{yk}	f _{yk}	f _{yk}	f _{yk}	f _{yk}	f _{yk}	f _{yk}	f _{yk}	f _{yk}	f _{yk}	f _{yk}	f _{yk}	F _u	V _u	V _u	V _u
1	2	3	4	5	6	7	8	9	10	11	12	13	14	15	16	17	18	19	20	21	22	23	24	25	26	27	28	29	30	31	32	33	34	35	36	37	38				
Notation	Nr.	Literature	ID			kn	mm	mm	mm	mm	mm	mm	mm	mm	mm	mm	mm	mm	mm	mm	mm	mm	mm	mm	mm	mm	mm	mm	mm	mm	mm	mm	mm	mm	mm	mm	mm	mm	mm	mm	
Almad_1996_001_NHW-3	19	Almad_1996_006_NHW-3	NNW-3	2	200	127	127	254	32,258	127	32	1,189	32	594	32	203	19	1,140	4,531	4,531	421	38	13	253	421	6	63	0.691	324	19	39					3.39	87	87	87		
Almad_1996_008_NHW-3b	23	Almad_1996_009_NHW-4	NHW-3b	2	200	127	127	254	32,258	127	32	1,189	32	578	292	198	19	1,140	4,531	4,531	421	38	13	253	421	6	63	0.654	324	19	87					4.96	108	108	108		
Angelakos_1999_001_DBI330M	40	Angelakos D. Collins P. (1999)	DBI330M	2	200	300	300	1,000	300,000	500	76	5,400	76	2,662	2,883	925	30	1,400	9,505	9,505	550	75	15	400	483	10	71	0.079	508	30	30					2.78	256	266	266		
Aparicio_1997_001_VHA	45	Aparicio Calavera del Pozo (1997)	VHA	2	200	585	75	800	277,821	421	12,000	0	2,400	3,411	704	20	7,640	1,855	14,470	500	12	653	500	12	226	1,774	500	42								3.56	887	895	895		
Bernhardt_1986_002_S7 A	58	Bernhardt_1986_002_S7 B	S7 A	2	200	150	150	200	30,000	100	2,550	1,450	550	3,42	161	20	1,257	5,203	5,203	500	8	101	427	7	67	0.447	427	78								4.77	140	141	141		
Bernhardt_1986_005_S8 B	60	Bernhardt_1986_005_S8 B	S8 B	2	200	150	150	200	30,000	100	2,550	1,450	550	3,42	161	20	1,257	5,203	5,203	500	8	101	427	7	67	0.447	427	78								4.77	150	151	151		
Bhal_1968_001_B1S	62	Bhal_1968_002_B2S	B1S	2	200	240	240	350	84,000	175	180	3,000	180	810	2,700	300	24	905	1,257	1,257	426	25	10	157	443	6	57	0.147	441	30	26					2.26	246	248	248		
Bhal_1968_003_B3S	64	Bhal_1968_004_B4S	B3S	2	200	240	240	350	84,000	175	180	3,000	180	810	2,700	300	24	905	1,257	1,257	426	25	10	157	443	6	57	0.147	441	30	24					2.39	233	248	250		
Bresler_1963_001_A-1	111	Bresler_1963_001_A-1	A-1	2	200	307	307	361	112,522	281	152	3,658	152	1,753	3,76	466	29	2,579	1,800	1,800	555	51	13	253	346	6	63	0.098	326	19	23					2.57	223	234	237		
Bresler_1963_007_C-1	117	Bresler_1963_007_C-1	C-1	2	200	155	155	200	30,000	100	2,550	1,450	550	3,42	161	20	1,257	5,203	5,203	500	8	101	427	7	67	0.447	427	78								4.77	150	151	151		
Caldera_2002_001_H 50/2	123	Caldera_2002_002_H 40/3	H50/2	2	200	200	200	400	80,000	200	75	2,160	75	1,043	2,953	353	32	1,608	2,278	2,278	500	35	8	101	540	6	57	0.109	530	12	47					3.87	178	179	179		
Caldera_2002_004_H 50/4	125	Caldera_2002_004_H 60/2	H50/4	2	200	200	200	400	80,000	200	75	2,160	75	1,043	2,953	353	32	1,608	2,278	2,278	500	37	8	101	540	6	57	0.141	530	12	47					3.87	246	247	247		
Caldera_2002_007_H 75/2	132	Caldera_2002_010_H 100/2	H75/2	2	200	200	200	400	80,000	200	75	2,160	75	1,043	2,953	353	32	1,608	2,278	2,278	500	35	8	101	540	6	57	0.141	530	12	65					4.48	200	205	205		
Cederwall_1974_003_T34-46	137	Cederwall Hedman Loberg (1974)	T34-46	2	200	139	139	260	36,100	130	3,000	1,800	600	2,56	234	12	339	1,043	1,043	818	8	101	540	6	57	0.407	437	29							2.66	96	97	97			
Gabrielson_1993_006_HS1	208	Gabrielson_1993_007_HS2	HS1	1	200	200	200	322	64,400	161	2,050	450	800	3,08	260	16	1,608	1,093	1,093	666	8	101	0.430	522	77	2.60	4.73	77	2.60	4.73	77	2.60	4.73	77	2.60	4.73	77	2.60	4.73	200	251
Gabrielson_1993_009_HPS1	209	Gabrielson_1993_009_HPS2	HS2	1	200	200	200	322	64,400	161	2,050	450	800	3,08	260	16	1,608	1,093	1,093	666	8	101	0.430	522	77	2.60	4.73	77	2.60	4.73	77	2.60	4.73	77	2.60	4.73	77	2.60	4.73	200	201
Gabrielson_1993_009_HPS2	211	Gabrielson_1993_009_HPS2	HPS2	2	200	200	200	287	57,400	144	1,300	250	424	2,25	166	16	1,608	3,574	3,574	666	8	101	0.335	522	97	3.20	5.14	97	3.20	5.14	97	3.20	5.14	97	3.20	5.14	97	3.20	5.14	305	306
Gudis_1963_001_V	213	Gudis Radogna (1963)	V	2	200	250	80	400	59,300	200	76	2,464	635	914	2,97	308	22	776	0.431	1,418	584	22	6	113	491	6	57	0.707	491	15	32					2.92	123	124	124		
Guralnik_1960_004_IB-2R	217	Guralnik_1960_005_IC-1R	IB-2R	2	200	584	178	387	110,161	140	76	2,464	635	914	2,97	308	22	776	0.431	1,418	584	22	6	113	491	6	57	0.244	529	16	16					1.42	1.65	1.60	142		
Guralnik_1960_006_IC-2R	218	Guralnik_1960_008_ID-2R	IC-1R	2	200	584	178	387	110,161	140	76	2,464	635	914	2,97	308	22	776	0.431	1,418	584	22	6	113	491	6	57	0.244	529	16	16					2.16	2.92	2.92	412		
Guralnik_1960_008_ID-2R	221	Guralnik_1960_008_ID-2R	IC-2R	2	200	584	178	387	110,161	140	76	2,464	635	914	2,97	308	22	776	0.431	1,418	584	22	6	113	491	6	57	0.244	529	16	16					2.16	2.92	2.92	227		
Hamadi_1976_002_G1-2	243	Hamadi (1976), Hamadi, Regan (1980)	G1-2	2	200	300	120	400	86,300	134	75	2,160	75	1,213	3,46	300	20	1,257	0.718	2,992	400	12	452	350	6	57	0.377	320	20	24					2.29	218	220	218			
Heeger_2003_001_NSC-3R	247	Heeger, J. Gortz, S. Will N(2001)	NSC-3R	2	200	220	180	500	100,000	242	3,000	1,500	333	450	25	2,945	2,975	2,626	532	8	101	0.539	314	67	4.51	6.7	67	4.51	6.7	4.51	6.7	4.51	6.7	4.51	6.7	4.51	6.7	4.51	6.7	4.51	429
Heeger_2003_002_NSC-3R	248	Heeger, J. Gortz, S. Will N(2001)	NSC-3R	2	200	220	180	500	100,000	242	3,000	1,500	333	450	25	2,945	2,975	2,626	532	8	101	0.539	314	67	4.51	6.7	67	4.51	6.7	4.51	6.7	4.51	6.7	4.51	6.7	4.51	6.7	4.51	6.7	4.51	429
Johnson_1939_002_B2-04	250	Johnson, Cox (1939)	B2-04	2	200	305	305	338	103,064	161	2,743	914	914	300	305	16	764	0.822	0.822	416	6	63	0.102	276	19	21										2.07	100	103	103		
Johnson_1939_009_T3-1	257	Johnson_1939_010_T3-1	T3-1	2	200	305	305	337	102,718	169	2,743	914	914	300	305	16	726	0.781	0.781	444	6	63	0.102	276	19	21										2.09	102	104	104		
Johnson_1989_001_1	259	Johnson_1989_002_2	T3-1	2	200	305	305	337	102,718	169	2,743	914	914	300	305	16	726	0.781	0.781	444	6	63	0.102	276	19	21										2.09	102	104	104		
Johnson_1989_005_5	263	Johnson_1989_005_5	T3-1	2	200	305	305	337	102,718	169	2,743	914	914	300	305	16	726	0.781	0.781	444	6	63	0.102	276	19	21										2.09	102	104	104		
Kong_1997_001_S1-1	358	Kong_1997_002_S1-2	B2-04	2	200	305	305	338	103,064	161	2,743	914	914	300	305	16	764	0.822	0.822	416	6	63	0.102	276	19	21										2.07	100	103	103		
Kong_1997_002_S1-2	359	Kong_1997_003_S1-3	S1-																																						

B. AeroPro Experimental Data

The following appendix presents the data recorded by the various types of instrumentation, processed through the AeroPro software, during the pure torsion shell experiments. Since the data was sampled at 10 Hz, the initial unfiltered number of data rows per test was unwieldy (approx. 200,000 rows). To make the analysis tasks more manageable this was reduced to the approximately 800 data rows per test presented here. In the interest of keeping the appendix compact, the excel sheets have been stitched together with columns across the page, to be read from top to bottom and from left to right.

Certain cells have been highlighted, the legend is shown below:



B.1 Specimen ES1

Actuators

Table with columns for NAME, UNIT, and ROW# for actuators. It contains multiple rows of data for various actuators, including their units and row identifiers.

Figure B.1: ES1 Experimental Data Forces

LVDTs

Table with columns for NAME, UNIT, and various sensor data points (NH, HT, NV, ND, NW, SH, ST, SV, SW, SD, SOW) for three different rows of sensors. Each row contains multiple columns of numerical data.

Figure B.2: ES1 Experiment Data (LVDTs)

LPs

Table with columns NAME UNIT, LP1, LP2, LP3, LP4, LP5, LP6, LP7, LP8, LP9, LP10, LP11, LP12, LP13, LP14, LP15 and corresponding numerical data for various LPs.

Figure B.3: ES1 Experimental Data (LPs - Part 1/4)

South SGs

Table with 4 main sections: NAME UNIT ROW# and NAME UNIT ROW#. Each section contains columns for S1 through S13 and corresponding values. The table lists experimental data for various South SGs, organized into four distinct blocks.

Figure B.8: ES1 Experimental Data (South SGs)

B.2 Specimen ES2

Actuators

NAME	Row	N ₁	N ₂	N ₃	N ₄	N ₅	N ₆	N ₇	N ₈	N ₉	N ₁₀	N ₁₁	N ₁₂	N ₁₃	N ₁₄	N ₁₅	N ₁₆	N ₁₇	N ₁₈	N ₁₉	N ₂₀	N ₂₁	N ₂₂	N ₂₃	N ₂₄	N ₂₅	N ₂₆	N ₂₇	N ₂₈	N ₂₉	N ₃₀	N ₃₁	N ₃₂	N ₃₃	N ₃₄	N ₃₅	N ₃₆	N ₃₇	N ₃₈	N ₃₉	N ₄₀	N ₄₁	N ₄₂	N ₄₃	N ₄₄	N ₄₅	N ₄₆	N ₄₇	N ₄₈	N ₄₉	N ₅₀	N ₅₁	N ₅₂	N ₅₃	N ₅₄	N ₅₅	N ₅₆	N ₅₇	N ₅₈	N ₅₉	N ₆₀	N ₆₁	N ₆₂	N ₆₃	N ₆₄	N ₆₅	N ₆₆	N ₆₇	N ₆₈	N ₆₉	N ₇₀	N ₇₁	N ₇₂	N ₇₃	N ₇₄	N ₇₅	N ₇₆	N ₇₇	N ₇₈	N ₇₉	N ₈₀	N ₈₁	N ₈₂	N ₈₃	N ₈₄	N ₈₅	N ₈₆	N ₈₇	N ₈₈	N ₈₉	N ₉₀	N ₉₁	N ₉₂	N ₉₃	N ₉₄	N ₉₅	N ₉₆	N ₉₇	N ₉₈	N ₉₉	N ₁₀₀	N ₁₀₁	N ₁₀₂	N ₁₀₃	N ₁₀₄	N ₁₀₅	N ₁₀₆	N ₁₀₇	N ₁₀₈	N ₁₀₉	N ₁₁₀	N ₁₁₁	N ₁₁₂	N ₁₁₃	N ₁₁₄	N ₁₁₅	N ₁₁₆	N ₁₁₇	N ₁₁₈	N ₁₁₉	N ₁₂₀	N ₁₂₁	N ₁₂₂	N ₁₂₃	N ₁₂₄	N ₁₂₅	N ₁₂₆	N ₁₂₇	N ₁₂₈	N ₁₂₉	N ₁₃₀	N ₁₃₁	N ₁₃₂	N ₁₃₃	N ₁₃₄	N ₁₃₅	N ₁₃₆	N ₁₃₇	N ₁₃₈	N ₁₃₉	N ₁₄₀	N ₁₄₁	N ₁₄₂	N ₁₄₃	N ₁₄₄	N ₁₄₅	N ₁₄₆	N ₁₄₇	N ₁₄₈	N ₁₄₉	N ₁₅₀	N ₁₅₁	N ₁₅₂	N ₁₅₃	N ₁₅₄	N ₁₅₅	N ₁₅₆	N ₁₅₇	N ₁₅₈	N ₁₅₉	N ₁₆₀	N ₁₆₁	N ₁₆₂	N ₁₆₃	N ₁₆₄	N ₁₆₅	N ₁₆₆	N ₁₆₇	N ₁₆₈	N ₁₆₉	N ₁₇₀	N ₁₇₁	N ₁₇₂	N ₁₇₃	N ₁₇₄	N ₁₇₅	N ₁₇₆	N ₁₇₇	N ₁₇₈	N ₁₇₉	N ₁₈₀	N ₁₈₁	N ₁₈₂	N ₁₈₃	N ₁₈₄	N ₁₈₅	N ₁₈₆	N ₁₈₇	N ₁₈₈	N ₁₈₉	N ₁₉₀	N ₁₉₁	N ₁₉₂	N ₁₉₃	N ₁₉₄	N ₁₉₅	N ₁₉₆	N ₁₉₇	N ₁₉₈	N ₁₉₉	N ₂₀₀	N ₂₀₁	N ₂₀₂	N ₂₀₃	N ₂₀₄	N ₂₀₅	N ₂₀₆	N ₂₀₇	N ₂₀₈	N ₂₀₉	N ₂₁₀	N ₂₁₁	N ₂₁₂	N ₂₁₃	N ₂₁₄	N ₂₁₅	N ₂₁₆	N ₂₁₇	N ₂₁₈	N ₂₁₉	N ₂₂₀	N ₂₂₁	N ₂₂₂	N ₂₂₃	N ₂₂₄	N ₂₂₅	N ₂₂₆	N ₂₂₇	N ₂₂₈	N ₂₂₉	N ₂₃₀	N ₂₃₁	N ₂₃₂	N ₂₃₃	N ₂₃₄	N ₂₃₅	N ₂₃₆	N ₂₃₇	N ₂₃₈	N ₂₃₉	N ₂₄₀	N ₂₄₁	N ₂₄₂	N ₂₄₃	N ₂₄₄	N ₂₄₅	N ₂₄₆	N ₂₄₇	N ₂₄₈	N ₂₄₉	N ₂₅₀	N ₂₅₁	N ₂₅₂	N ₂₅₃	N ₂₅₄	N ₂₅₅	N ₂₅₆	N ₂₅₇	N ₂₅₈	N ₂₅₉	N ₂₆₀	N ₂₆₁	N ₂₆₂	N ₂₆₃	N ₂₆₄	N ₂₆₅	N ₂₆₆	N ₂₆₇	N ₂₆₈	N ₂₆₉	N ₂₇₀	N ₂₇₁	N ₂₇₂	N ₂₇₃	N ₂₇₄	N ₂₇₅	N ₂₇₆	N ₂₇₇	N ₂₇₈	N ₂₇₉	N ₂₈₀	N ₂₈₁	N ₂₈₂	N ₂₈₃	N ₂₈₄	N ₂₈₅	N ₂₈₆	N ₂₈₇	N ₂₈₈	N ₂₈₉	N ₂₉₀	N ₂₉₁	N ₂₉₂	N ₂₉₃	N ₂₉₄	N ₂₉₅	N ₂₉₆	N ₂₉₇	N ₂₉₈	N ₂₉₉	N ₃₀₀	N ₃₀₁	N ₃₀₂	N ₃₀₃	N ₃₀₄	N ₃₀₅	N ₃₀₆	N ₃₀₇	N ₃₀₈	N ₃₀₉	N ₃₁₀	N ₃₁₁	N ₃₁₂	N ₃₁₃	N ₃₁₄	N ₃₁₅	N ₃₁₆	N ₃₁₇	N ₃₁₈	N ₃₁₉	N ₃₂₀	N ₃₂₁	N ₃₂₂	N ₃₂₃	N ₃₂₄	N ₃₂₅	N ₃₂₆	N ₃₂₇	N ₃₂₈	N ₃₂₉	N ₃₃₀	N ₃₃₁	N ₃₃₂	N ₃₃₃	N ₃₃₄	N ₃₃₅	N ₃₃₆	N ₃₃₇	N ₃₃₈	N ₃₃₉	N ₃₄₀	N ₃₄₁	N ₃₄₂	N ₃₄₃	N ₃₄₄	N ₃₄₅	N ₃₄₆	N ₃₄₇	N ₃₄₈	N ₃₄₉	N ₃₅₀	N ₃₅₁	N ₃₅₂	N ₃₅₃	N ₃₅₄	N ₃₅₅	N ₃₅₆	N ₃₅₇	N ₃₅₈	N ₃₅₉	N ₃₆₀	N ₃₆₁	N ₃₆₂	N ₃₆₃	N ₃₆₄	N ₃₆₅	N ₃₆₆	N ₃₆₇	N ₃₆₈	N ₃₆₉	N ₃₇₀	N ₃₇₁	N ₃₇₂	N ₃₇₃	N ₃₇₄	N ₃₇₅	N ₃₇₆	N ₃₇₇	N ₃₇₈	N ₃₇₉	N ₃₈₀	N ₃₈₁	N ₃₈₂	N ₃₈₃	N ₃₈₄	N ₃₈₅	N ₃₈₆	N ₃₈₇	N ₃₈₈	N ₃₈₉	N ₃₉₀	N ₃₉₁	N ₃₉₂	N ₃₉₃	N ₃₉₄	N ₃₉₅	N ₃₉₆	N ₃₉₇	N ₃₉₈	N ₃₉₉	N ₄₀₀	N ₄₀₁	N ₄₀₂	N ₄₀₃	N ₄₀₄	N ₄₀₅	N ₄₀₆	N ₄₀₇	N ₄₀₈	N ₄₀₉	N ₄₁₀	N ₄₁₁	N ₄₁₂	N ₄₁₃	N ₄₁₄	N ₄₁₅	N ₄₁₆	N ₄₁₇	N ₄₁₈	N ₄₁₉	N ₄₂₀	N ₄₂₁	N ₄₂₂	N ₄₂₃	N ₄₂₄	N ₄₂₅	N ₄₂₆	N ₄₂₇	N ₄₂₈	N ₄₂₉	N ₄₃₀	N ₄₃₁	N ₄₃₂	N ₄₃₃	N ₄₃₄	N ₄₃₅	N ₄₃₆	N ₄₃₇	N ₄₃₈	N ₄₃₉	N ₄₄₀	N ₄₄₁	N ₄₄₂	N ₄₄₃	N ₄₄₄	N ₄₄₅	N ₄₄₆	N ₄₄₇	N ₄₄₈	N ₄₄₉	N ₄₅₀	N ₄₅₁	N ₄₅₂	N ₄₅₃	N ₄₅₄	N ₄₅₅	N ₄₅₆	N ₄₅₇	N ₄₅₈	N ₄₅₉	N ₄₆₀	N ₄₆₁	N ₄₆₂	N ₄₆₃	N ₄₆₄	N ₄₆₅	N ₄₆₆	N ₄₆₇	N ₄₆₈	N ₄₆₉	N ₄₇₀	N ₄₇₁	N ₄₇₂	N ₄₇₃	N ₄₇₄	N ₄₇₅	N ₄₇₆	N ₄₇₇	N ₄₇₈	N ₄₇₉	N ₄₈₀	N ₄₈₁	N ₄₈₂	N ₄₈₃	N ₄₈₄	N ₄₈₅	N ₄₈₆	N ₄₈₇	N ₄₈₈	N ₄₈₉	N ₄₉₀	N ₄₉₁	N ₄₉₂	N ₄₉₃	N ₄₉₄	N ₄₉₅	N ₄₉₆	N ₄₉₇	N ₄₉₈	N ₄₉₉	N ₅₀₀	N ₅₀₁	N ₅₀₂	N ₅₀₃	N ₅₀₄	N ₅₀₅	N ₅₀₆	N ₅₀₇	N ₅₀₈	N ₅₀₉	N ₅₁₀	N ₅₁₁	N ₅₁₂	N ₅₁₃	N ₅₁₄	N ₅₁₅	N ₅₁₆	N ₅₁₇	N ₅₁₈	N ₅₁₉	N ₅₂₀	N ₅₂₁	N ₅₂₂	N ₅₂₃	N ₅₂₄	N ₅₂₅	N ₅₂₆	N ₅₂₇	N ₅₂₈	N ₅₂₉	N ₅₃₀	N ₅₃₁	N ₅₃₂	N ₅₃₃	N ₅₃₄	N ₅₃₅	N ₅₃₆	N ₅₃₇	N ₅₃₈	N ₅₃₉	N ₅₄₀	N ₅₄₁	N ₅₄₂	N ₅₄₃	N ₅₄₄	N ₅₄₅	N ₅₄₆	N ₅₄₇	N ₅₄₈	N ₅₄₉	N ₅₅₀	N ₅₅₁	N ₅₅₂	N ₅₅₃	N ₅₅₄	N ₅₅₅	N ₅₅₆	N ₅₅₇	N ₅₅₈	N ₅₅₉	N ₅₆₀	N ₅₆₁	N ₅₆₂	N ₅₆₃	N ₅₆₄	N ₅₆₅	N ₅₆₆	N ₅₆₇	N ₅₆₈	N ₅₆₉	N ₅₇₀	N ₅₇₁	N ₅₇₂	N ₅₇₃	N ₅₇₄	N ₅₇₅	N ₅₇₆	N ₅₇₇	N ₅₇₈	N ₅₇₉	N ₅₈₀	N ₅₈₁	N ₅₈₂	N ₅₈₃	N ₅₈₄	N ₅₈₅	N ₅₈₆	N ₅₈₇	N ₅₈₈	N ₅₈₉	N ₅₉₀	N ₅₉₁	N ₅₉₂	N ₅₉₃	N ₅₉₄	N ₅₉₅	N ₅₉₆	N ₅₉₇	N ₅₉₈	N ₅₉₉	N ₆₀₀	N ₆₀₁	N ₆₀₂	N ₆₀₃	N ₆₀₄	N ₆₀₅	N ₆₀₆	N ₆₀₇	N ₆₀₈	N ₆₀₉	N ₆₁₀	N ₆₁₁	N ₆₁₂	N ₆₁₃	N ₆₁₄	N ₆₁₅	N ₆₁₆	N ₆₁₇	N ₆₁₈	N ₆₁₉	N ₆₂₀	N ₆₂₁	N ₆₂₂	N ₆₂₃	N ₆₂₄	N ₆₂₅	N ₆₂₆	N ₆₂₇	N ₆₂₈	N ₆₂₉	N ₆₃₀	N ₆₃₁	N ₆₃₂	N ₆₃₃	N ₆₃₄	N ₆₃₅	N ₆₃₆	N ₆₃₇	N ₆₃₈	N ₆₃₉	N ₆₄₀	N ₆₄₁	N ₆₄₂	N ₆₄₃	N ₆₄₄	N ₆₄₅	N ₆₄₆	N ₆₄₇	N ₆₄₈	N ₆₄₉	N ₆₅₀	N ₆₅₁	N ₆₅₂	N ₆₅₃	N ₆₅₄	N ₆₅₅	N ₆₅₆	N ₆₅₇	N ₆₅₈	N ₆₅₉	N ₆₆₀	N ₆₆₁	N ₆₆₂	N ₆₆₃	N ₆₆₄	N ₆₆₅	N ₆₆₆	N ₆₆₇	N ₆₆₈	N ₆₆₉	N ₆₇₀	N ₆₇₁	N ₆₇₂	N ₆₇₃	N ₆₇₄	N ₆₇₅	N ₆₇₆	N ₆₇₇	N ₆₇₈	N ₆₇₉	N ₆₈₀	N _{681</}
------	-----	----------------	----------------	----------------	----------------	----------------	----------------	----------------	----------------	----------------	-----------------	-----------------	-----------------	-----------------	-----------------	-----------------	-----------------	-----------------	-----------------	-----------------	-----------------	-----------------	-----------------	-----------------	-----------------	-----------------	-----------------	-----------------	-----------------	-----------------	-----------------	-----------------	-----------------	-----------------	-----------------	-----------------	-----------------	-----------------	-----------------	-----------------	-----------------	-----------------	-----------------	-----------------	-----------------	-----------------	-----------------	-----------------	-----------------	-----------------	-----------------	-----------------	-----------------	-----------------	-----------------	-----------------	-----------------	-----------------	-----------------	-----------------	-----------------	-----------------	-----------------	-----------------	-----------------	-----------------	-----------------	-----------------	-----------------	-----------------	-----------------	-----------------	-----------------	-----------------	-----------------	-----------------	-----------------	-----------------	-----------------	-----------------	-----------------	-----------------	-----------------	-----------------	-----------------	-----------------	-----------------	-----------------	-----------------	-----------------	-----------------	-----------------	-----------------	-----------------	-----------------	-----------------	-----------------	-----------------	-----------------	-----------------	------------------	------------------	------------------	------------------	------------------	------------------	------------------	------------------	------------------	------------------	------------------	------------------	------------------	------------------	------------------	------------------	------------------	------------------	------------------	------------------	------------------	------------------	------------------	------------------	------------------	------------------	------------------	------------------	------------------	------------------	------------------	------------------	------------------	------------------	------------------	------------------	------------------	------------------	------------------	------------------	------------------	------------------	------------------	------------------	------------------	------------------	------------------	------------------	------------------	------------------	------------------	------------------	------------------	------------------	------------------	------------------	------------------	------------------	------------------	------------------	------------------	------------------	------------------	------------------	------------------	------------------	------------------	------------------	------------------	------------------	------------------	------------------	------------------	------------------	------------------	------------------	------------------	------------------	------------------	------------------	------------------	------------------	------------------	------------------	------------------	------------------	------------------	------------------	------------------	------------------	------------------	------------------	------------------	------------------	------------------	------------------	------------------	------------------	------------------	------------------	------------------	------------------	------------------	------------------	------------------	------------------	------------------	------------------	------------------	------------------	------------------	------------------	------------------	------------------	------------------	------------------	------------------	------------------	------------------	------------------	------------------	------------------	------------------	------------------	------------------	------------------	------------------	------------------	------------------	------------------	------------------	------------------	------------------	------------------	------------------	------------------	------------------	------------------	------------------	------------------	------------------	------------------	------------------	------------------	------------------	------------------	------------------	------------------	------------------	------------------	------------------	------------------	------------------	------------------	------------------	------------------	------------------	------------------	------------------	------------------	------------------	------------------	------------------	------------------	------------------	------------------	------------------	------------------	------------------	------------------	------------------	------------------	------------------	------------------	------------------	------------------	------------------	------------------	------------------	------------------	------------------	------------------	------------------	------------------	------------------	------------------	------------------	------------------	------------------	------------------	------------------	------------------	------------------	------------------	------------------	------------------	------------------	------------------	------------------	------------------	------------------	------------------	------------------	------------------	------------------	------------------	------------------	------------------	------------------	------------------	------------------	------------------	------------------	------------------	------------------	------------------	------------------	------------------	------------------	------------------	------------------	------------------	------------------	------------------	------------------	------------------	------------------	------------------	------------------	------------------	------------------	------------------	------------------	------------------	------------------	------------------	------------------	------------------	------------------	------------------	------------------	------------------	------------------	------------------	------------------	------------------	------------------	------------------	------------------	------------------	------------------	------------------	------------------	------------------	------------------	------------------	------------------	------------------	------------------	------------------	------------------	------------------	------------------	------------------	------------------	------------------	------------------	------------------	------------------	------------------	------------------	------------------	------------------	------------------	------------------	------------------	------------------	------------------	------------------	------------------	------------------	------------------	------------------	------------------	------------------	------------------	------------------	------------------	------------------	------------------	------------------	------------------	------------------	------------------	------------------	------------------	------------------	------------------	------------------	------------------	------------------	------------------	------------------	------------------	------------------	------------------	------------------	------------------	------------------	------------------	------------------	------------------	------------------	------------------	------------------	------------------	------------------	------------------	------------------	------------------	------------------	------------------	------------------	------------------	------------------	------------------	------------------	------------------	------------------	------------------	------------------	------------------	------------------	------------------	------------------	------------------	------------------	------------------	------------------	------------------	------------------	------------------	------------------	------------------	------------------	------------------	------------------	------------------	------------------	------------------	------------------	------------------	------------------	------------------	------------------	------------------	------------------	------------------	------------------	------------------	------------------	------------------	------------------	------------------	------------------	------------------	------------------	------------------	------------------	------------------	------------------	------------------	------------------	------------------	------------------	------------------	------------------	------------------	------------------	------------------	------------------	------------------	------------------	------------------	------------------	------------------	------------------	------------------	------------------	------------------	------------------	------------------	------------------	------------------	------------------	------------------	------------------	------------------	------------------	------------------	------------------	------------------	------------------	------------------	------------------	------------------	------------------	------------------	------------------	------------------	------------------	------------------	------------------	------------------	------------------	------------------	------------------	------------------	------------------	------------------	------------------	------------------	------------------	------------------	------------------	------------------	------------------	------------------	------------------	------------------	------------------	------------------	------------------	------------------	------------------	------------------	------------------	------------------	------------------	------------------	------------------	------------------	------------------	------------------	------------------	------------------	------------------	------------------	------------------	------------------	------------------	------------------	------------------	------------------	------------------	------------------	------------------	------------------	------------------	------------------	------------------	------------------	------------------	------------------	------------------	------------------	------------------	------------------	------------------	------------------	------------------	------------------	------------------	------------------	------------------	------------------	------------------	------------------	------------------	------------------	------------------	------------------	------------------	------------------	------------------	------------------	------------------	------------------	------------------	------------------	------------------	------------------	------------------	------------------	------------------	------------------	------------------	------------------	------------------	------------------	------------------	------------------	------------------	------------------	------------------	------------------	------------------	------------------	------------------	------------------	------------------	------------------	------------------	------------------	------------------	------------------	------------------	------------------	------------------	------------------	------------------	------------------	------------------	------------------	------------------	------------------	------------------	------------------	------------------	------------------	------------------	------------------	------------------	------------------	------------------	------------------	------------------	------------------	------------------	------------------	------------------	------------------	------------------	------------------	------------------	------------------	------------------	------------------	------------------	------------------	------------------	------------------	------------------	------------------	------------------	------------------	------------------	------------------	------------------	------------------	------------------	------------------	------------------	------------------	------------------	------------------	------------------	------------------	------------------	------------------	------------------	------------------	------------------	------------------	------------------	------------------	------------------	------------------	------------------	------------------	------------------	-----------------------

LVDTs

Table with columns for NAME, UNIT, and various sensor parameters (NHB, NHT, NVE, NVW, NDV, NDVW, SHB, SHT, SVE, SVW, SDV, SDVW) for three different rows of data.

Figure B.10: ES2 Experimental Data (LVDTs)

LPs

Table with columns NAME UNIT, LP1-LP15, and rows of experimental data points.

Table with columns NAME UNIT, LP1-LP15, and rows of experimental data points.

Figure B.11: Experimental Data (LPs - Part 1/2)

Table with columns: NAME, LP1, LP2, LP3, LP4, LP5, LP6, LP7, LP8, LP9, LP10, LP11, LP12, LP13, LP14, LP15, ROW #. Contains experimental data for various test cases.

Table with columns: NAME, LP1, LP2, LP3, LP4, LP5, LP6, LP7, LP8, LP9, LP10, LP11, LP12, LP13, LP14, LP15, ROW #. Contains experimental data for various test cases.

Figure B.12: ES2 Experimental Data (LPs - Part 2)

EGs

Table with columns: NAME UNIT, EG_1B, EG_1G, EG_1W, EG_2B, EG_2G, EG_2W, EG_3B, EG_3G, EG_3W, EG_4B, EG_4G, EG_4W. Rows contain numerical data for various units and EG categories.

Table with columns: NAME UNIT, EG_1B, EG_1G, EG_1W, EG_2B, EG_2G, EG_2W, EG_3B, EG_3G, EG_3W, EG_4B, EG_4G, EG_4W. Rows contain numerical data for various units and EG categories.

Figure B.13: ES2 Experimental Data (EGs - Part 1/2)

North SGs

Table with columns: NAME, UNIT, N1, N2, N3, N4, N5, N6, N7, N8, N9, N10, N11, N12, N13, N14, N15, N16, N17, N18, N19, N20, N21, N22, N23, N24, N25, N26, N27, N28, N29, N30, N31, N32, N33, N34, N35, N36, N37, N38, N39, N40, N41, N42, N43, N44, N45, N46, N47, N48, N49, N50, N51, N52, N53, N54, N55, N56, N57, N58, N59, N60, N61, N62, N63, N64, N65, N66, N67, N68, N69, N70, N71, N72, N73, N74, N75, N76, N77, N78, N79, N80, N81, N82, N83, N84, N85, N86, N87, N88, N89, N90, N91, N92, N93, N94, N95, N96, N97, N98, N99, N100. Rows include data for various aircraft models like 141879, 141880, etc.

Table with columns: NAME, UNIT, N1, N2, N3, N4, N5, N6, N7, N8, N9, N10, N11, N12, N13, N14, N15, N16, N17, N18, N19, N20, N21, N22, N23, N24, N25, N26, N27, N28, N29, N30, N31, N32, N33, N34, N35, N36, N37, N38, N39, N40, N41, N42, N43, N44, N45, N46, N47, N48, N49, N50, N51, N52, N53, N54, N55, N56, N57, N58, N59, N60, N61, N62, N63, N64, N65, N66, N67, N68, N69, N70, N71, N72, N73, N74, N75, N76, N77, N78, N79, N80, N81, N82, N83, N84, N85, N86, N87, N88, N89, N90, N91, N92, N93, N94, N95, N96, N97, N98, N99, N100. Rows include data for various aircraft models like 141879, 141880, etc.

Figure B.15: E2 Experimental Data (North SGs)

South SGs

Table with 4 columns of data, each containing NAME, UNIT, and ROW# headers followed by numerical values for various parameters.

Figure B.16: ES2 Experimental Data (South SGs)

C. LED Load Stage Grids

The following appendix presents the LED element grids for the mohr's circle variables calculated at each load stages for both shell specimens. In the body of the thesis only the element grids at the peak torsion was shown to conserve space.

For reference, the load stages in each test occur at the following torsion values:

ES1		ES2	
$[\frac{kN \cdot m}{m}]$		$[\frac{kN \cdot m}{m}]$	
M_{xy}		M_{xy}	
LS 1	86.8	LS 1	64.8
LS 2	168.8	LS 2	110.5
Peak	187.2	LS 3	173.4
LS 3	182.9	LS 4	214.7
LS 4	170.4	Peak	250.5
LS 5	147.9	LS 5	219.6
LS 6	101.8	LS 6	138.9

C.1 Specimen ES1

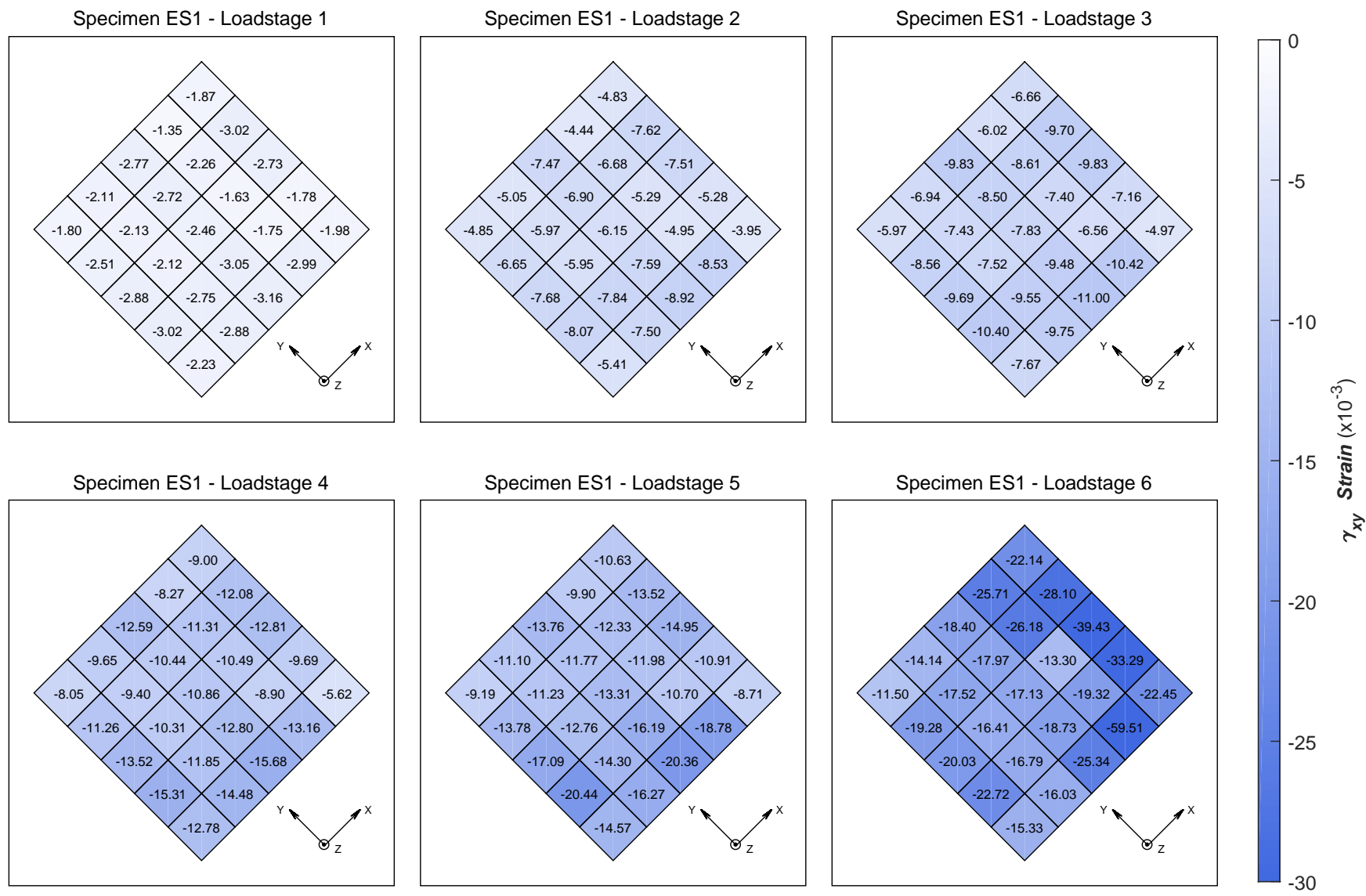


Figure C.1: ES1 In-Plane (XY) Shear Strain at Load Stages

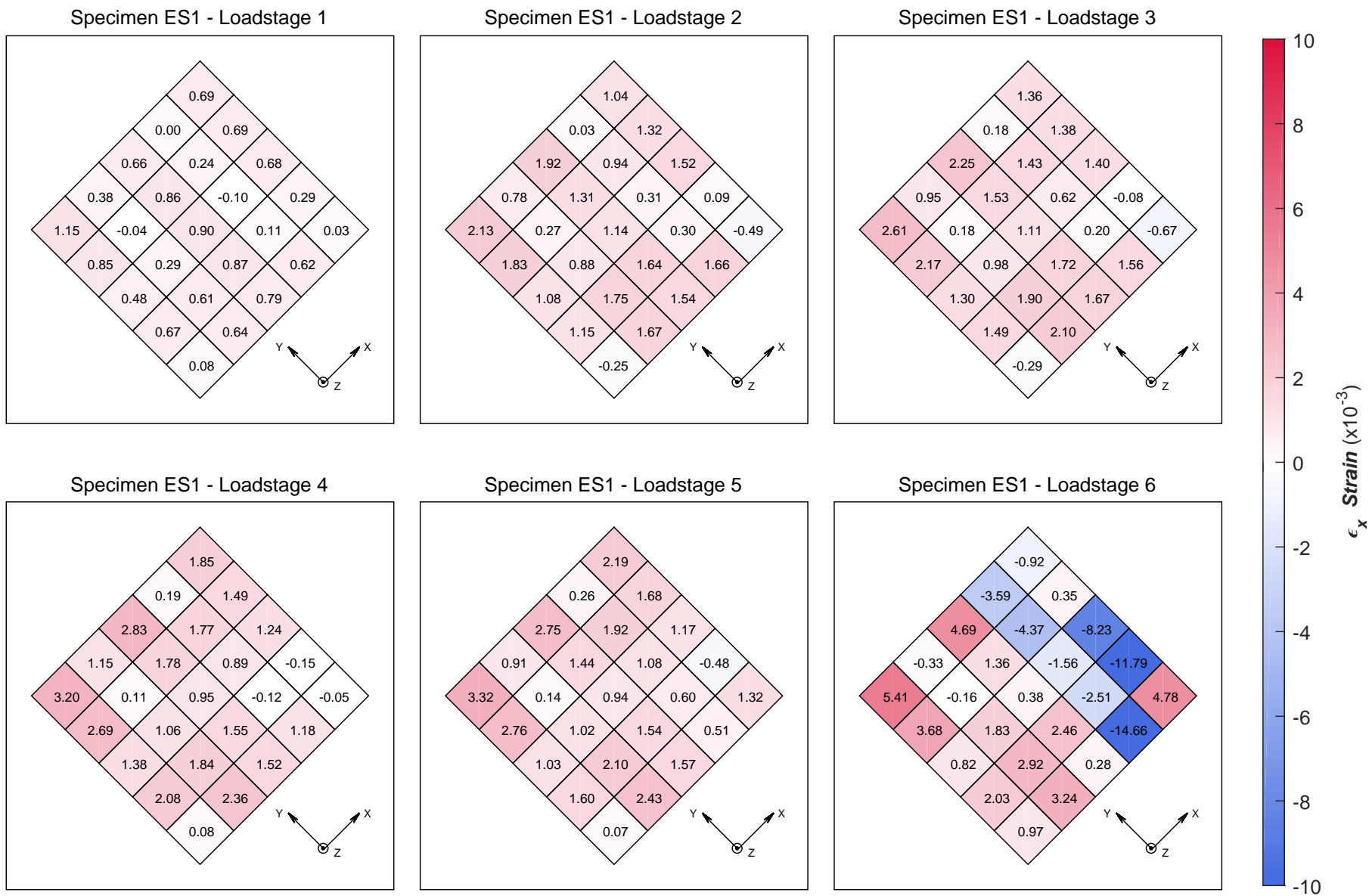


Figure C.2: ES1 X-Direction Strain at Load Stages

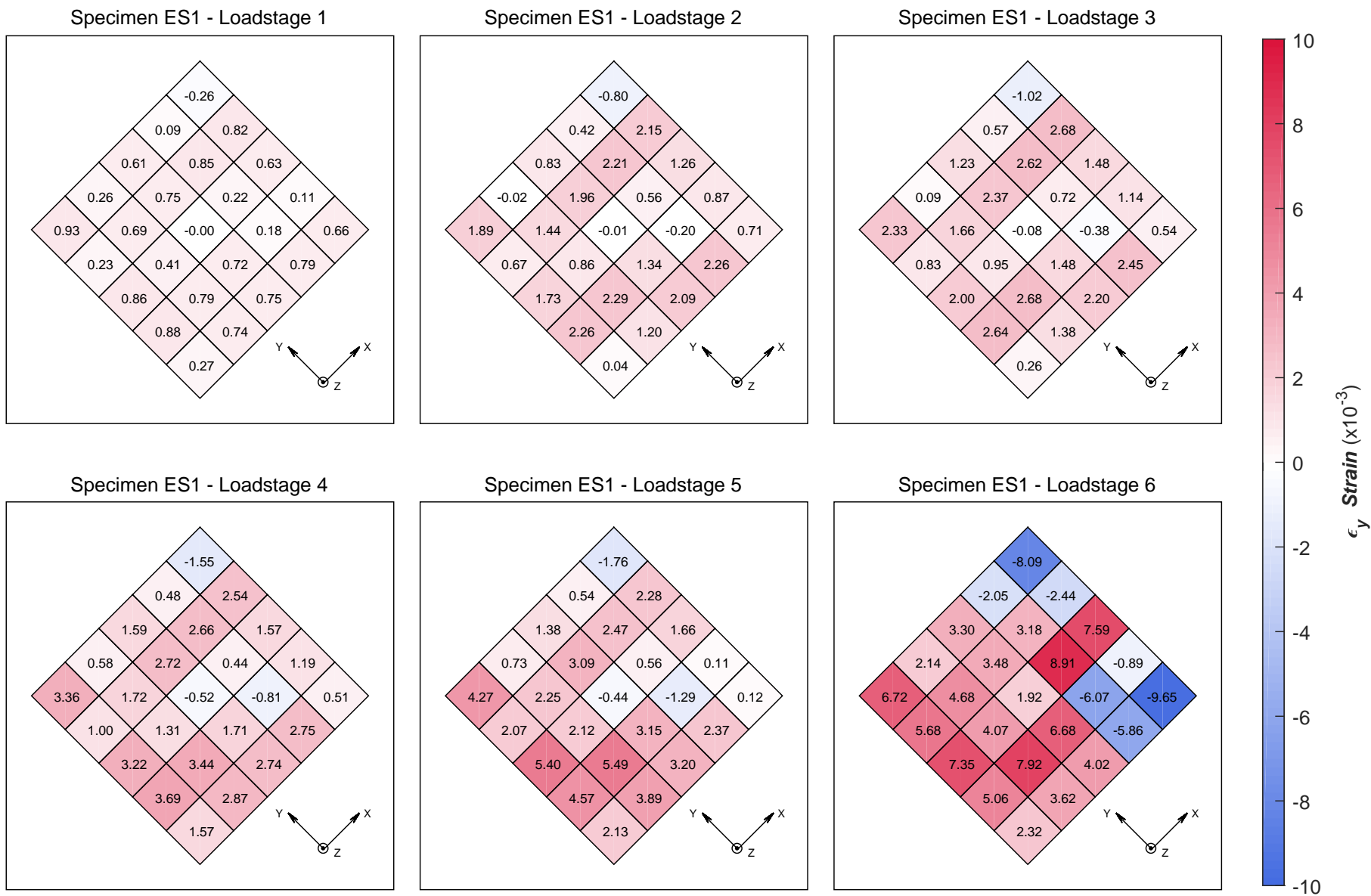


Figure C.3: ES1 Y-Direction Strain at Load Stages

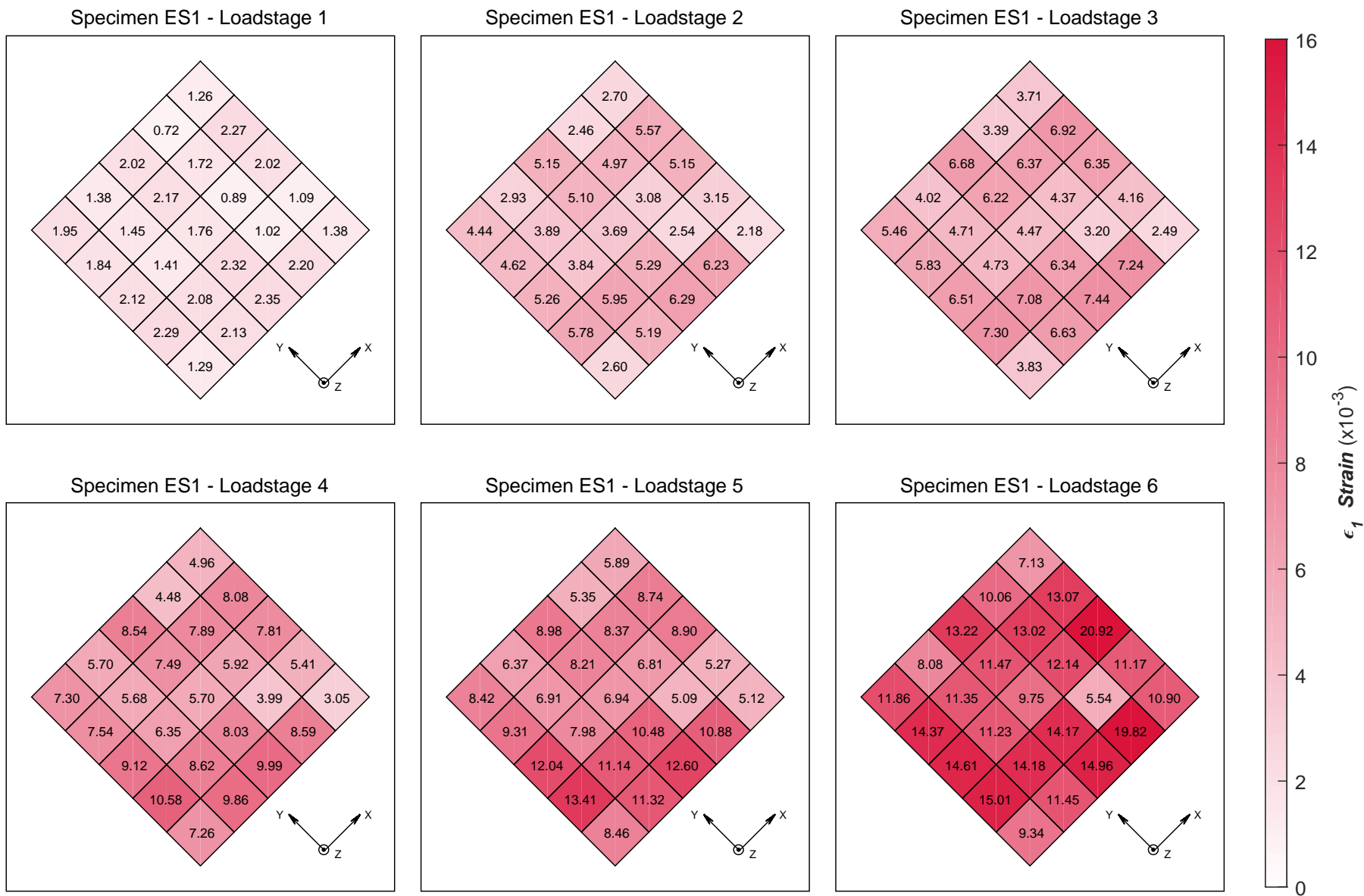


Figure C.4: ES1 Principal Tensile Strain at Load Stages

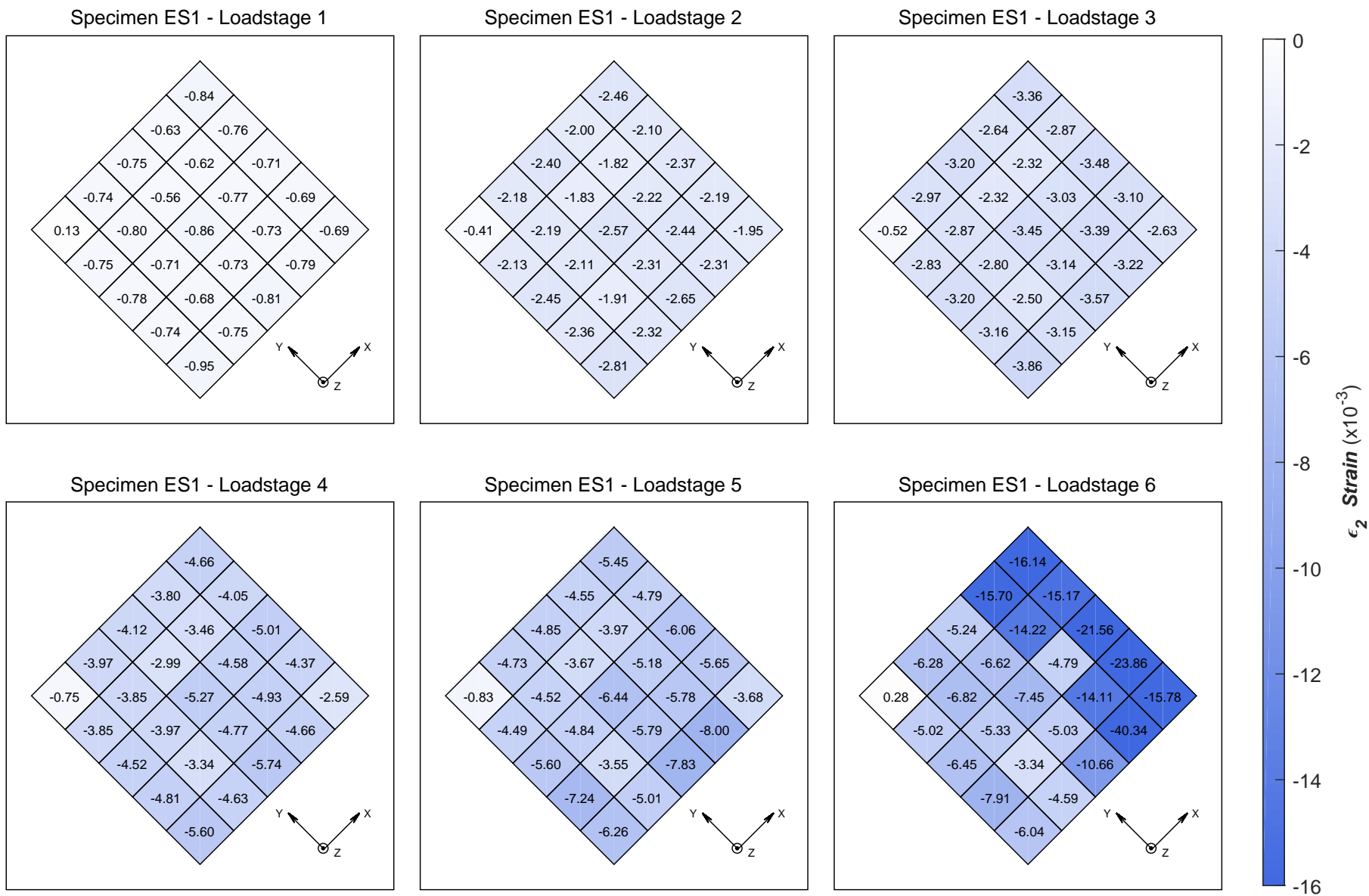


Figure C.5: ES1 Principal Compressive Strain at Load Stages

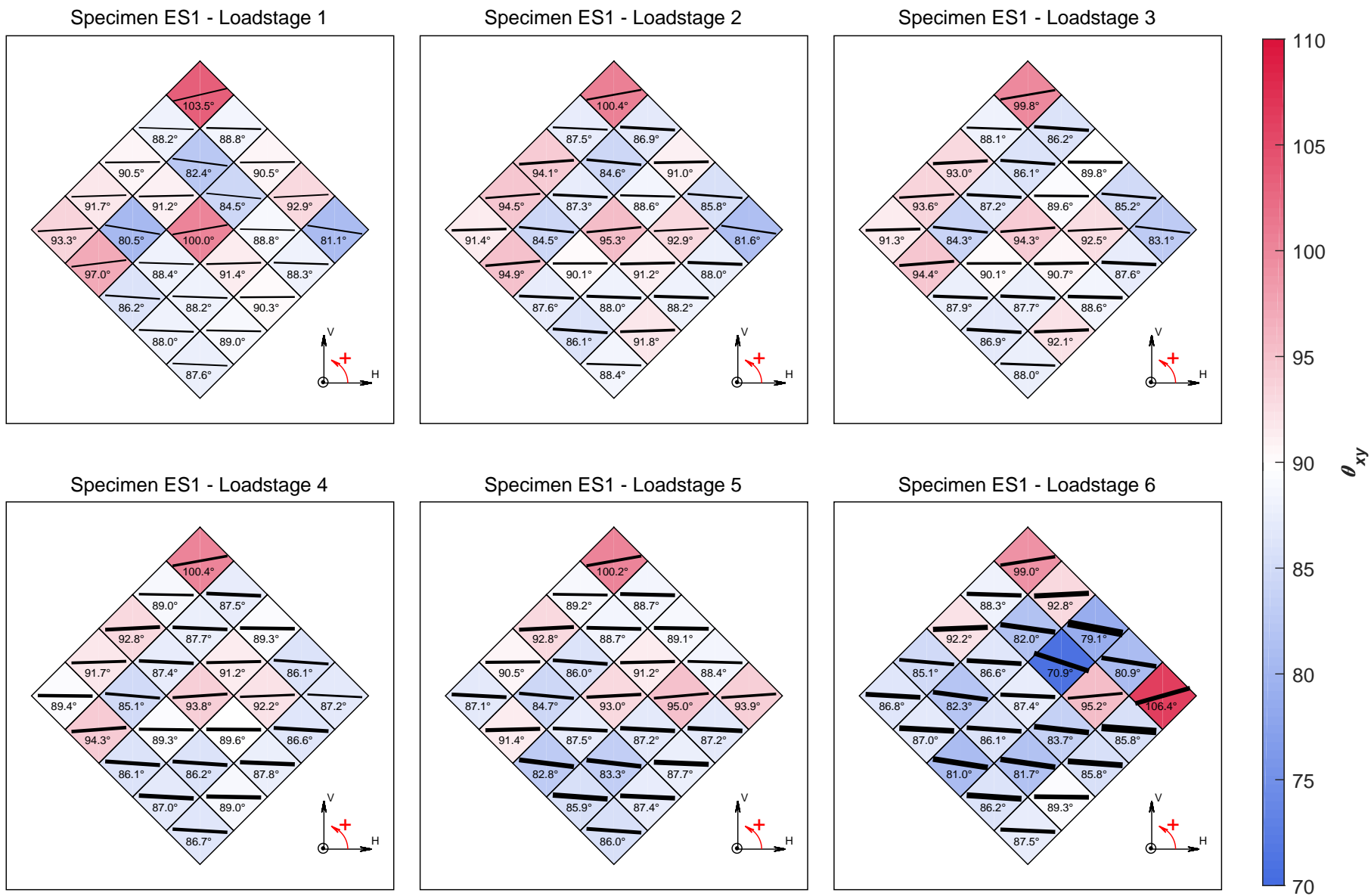


Figure C.6: ES1 Angle of Principal Strain (CCW+) at Load Stages

C.2 Specimen ES2

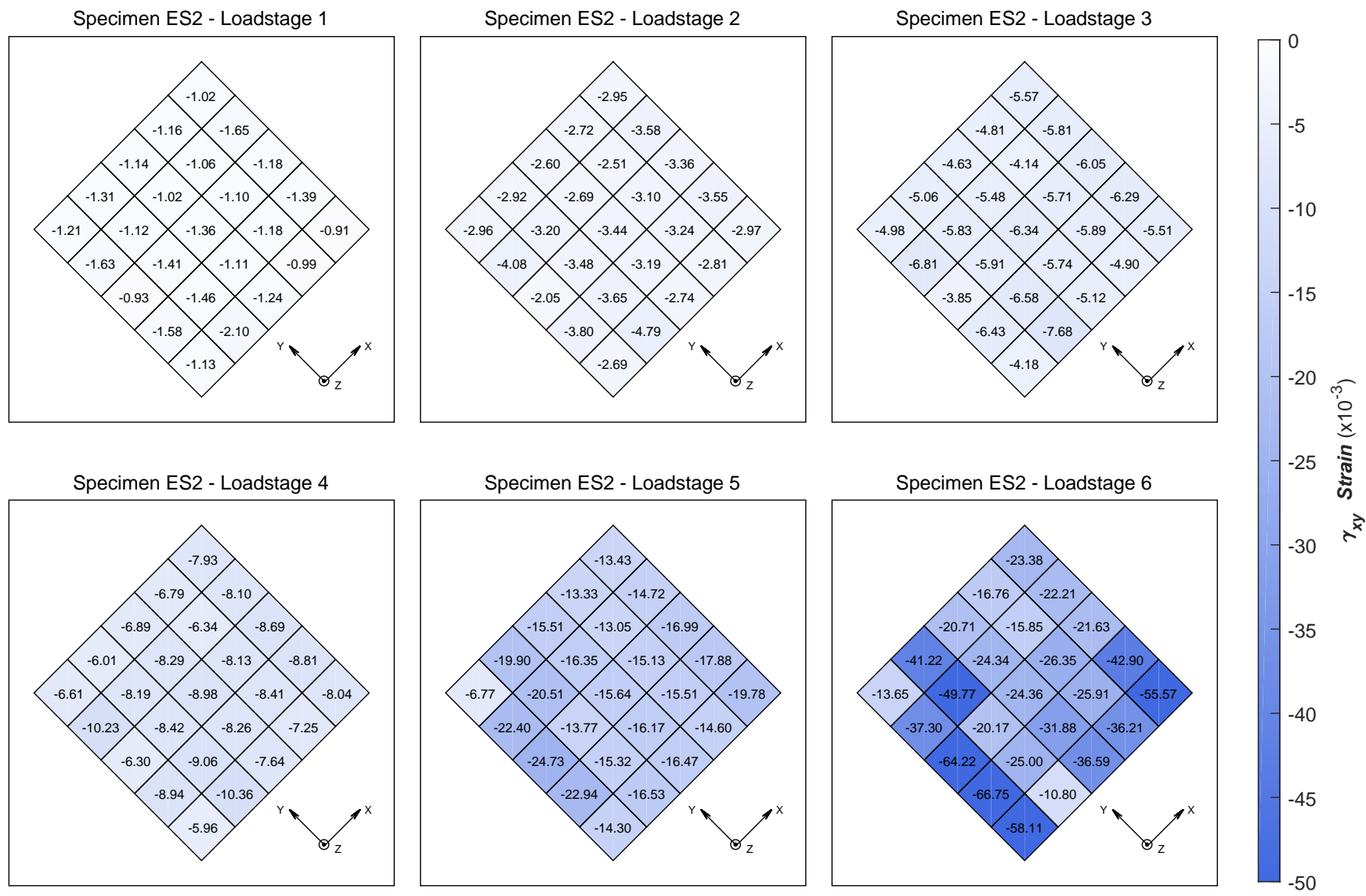


Figure C.7: ES2 In-Plane (XY) Shear Strain at Load Stages

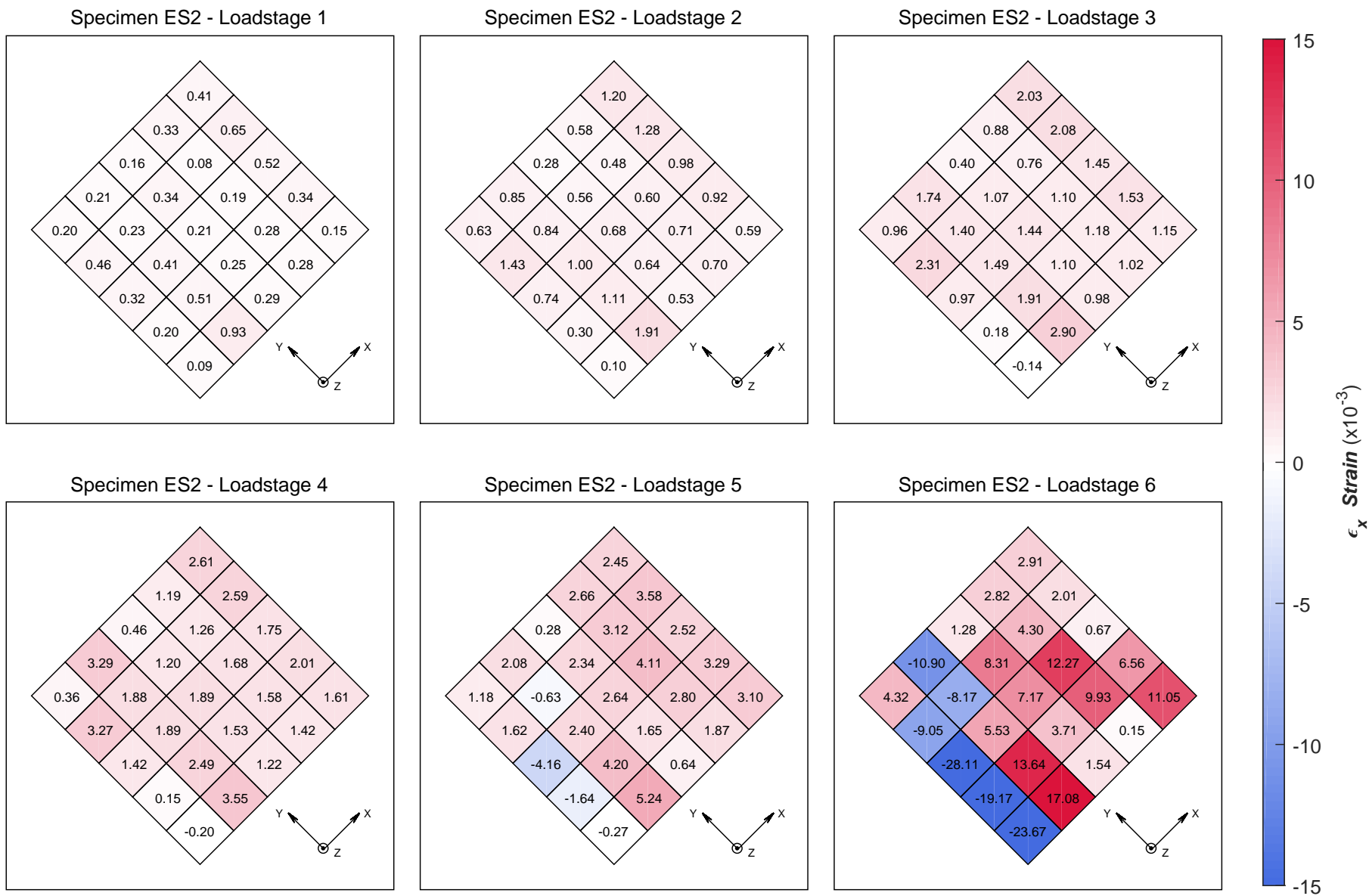


Figure C.8: ES2 X-Direction Strain at Load Stages

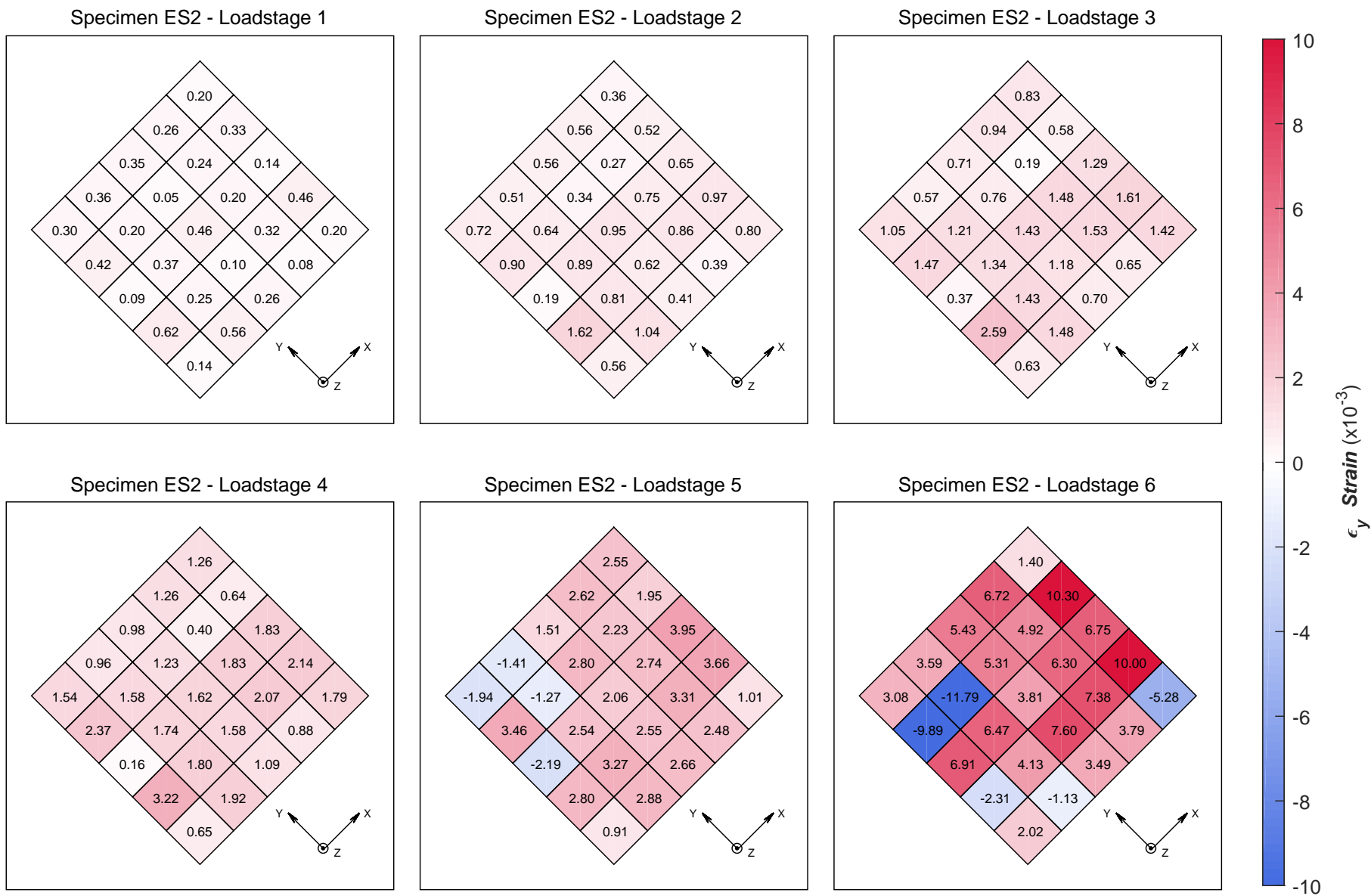


Figure C.9: ES2 Y-Direction Strain at Load Stages

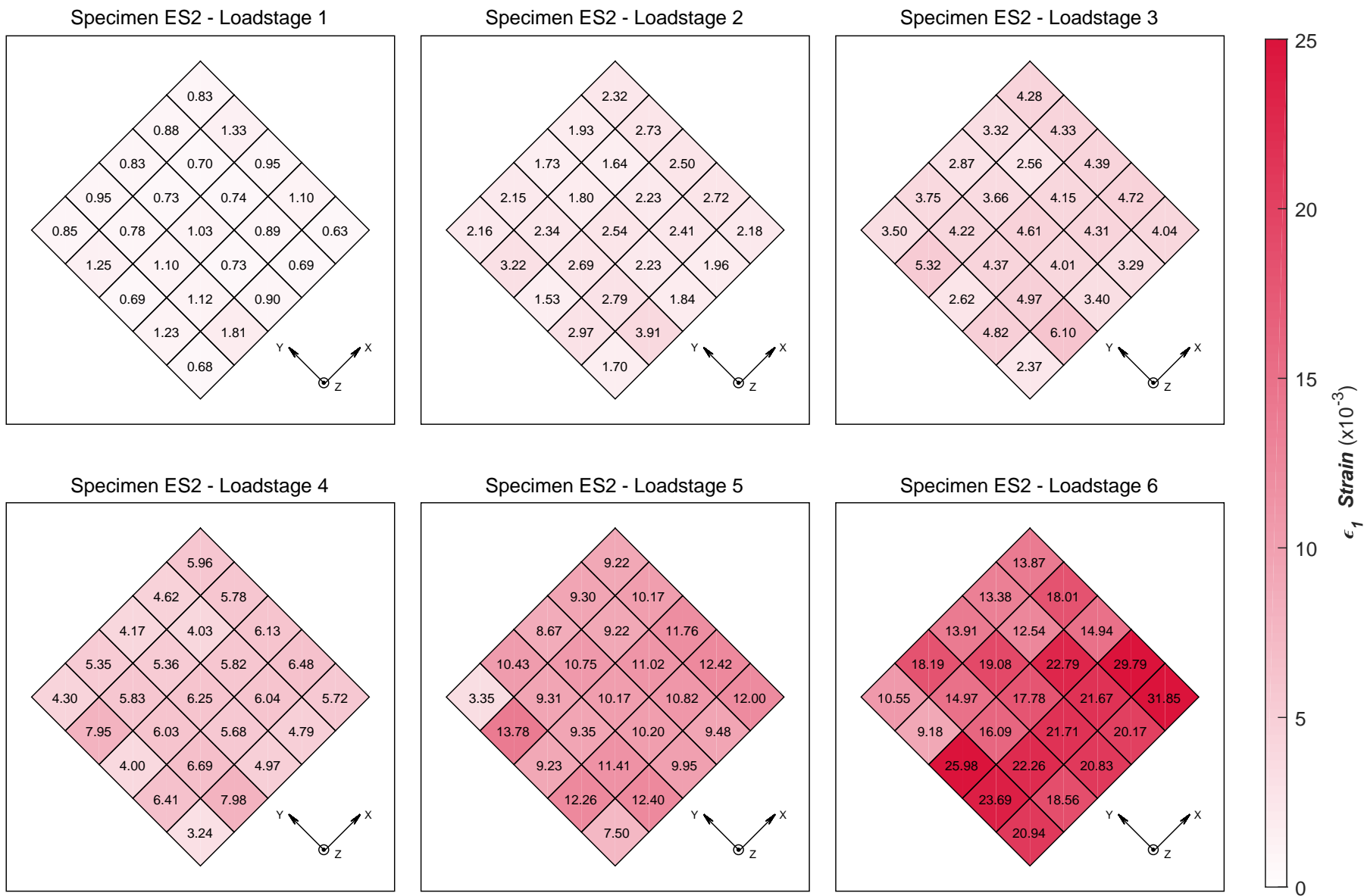


Figure C.10: ES2 Principal Tensile Strain at Load Stages

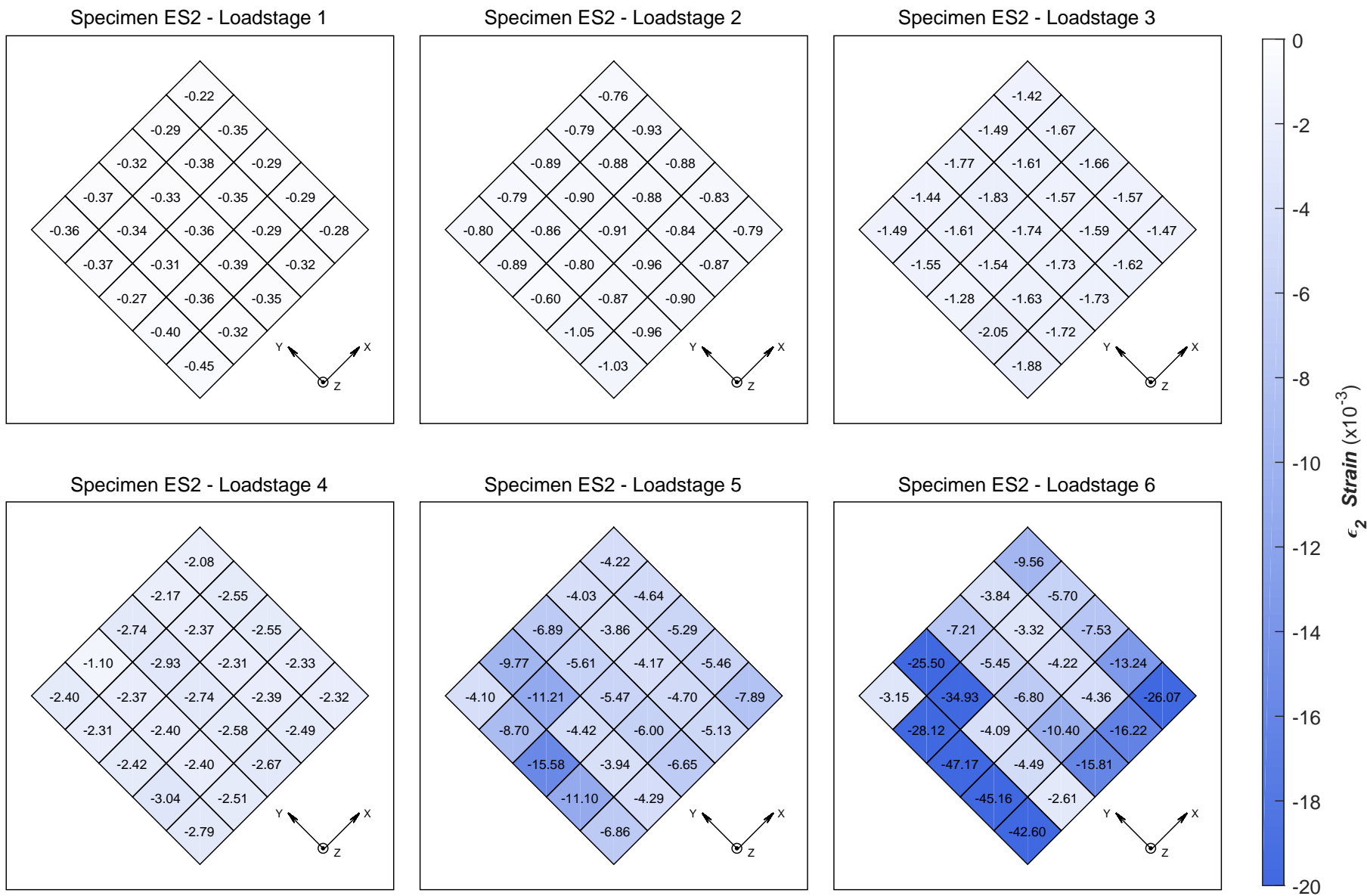


Figure C.11: ES2 Principal Compressive Strain at Load Stages

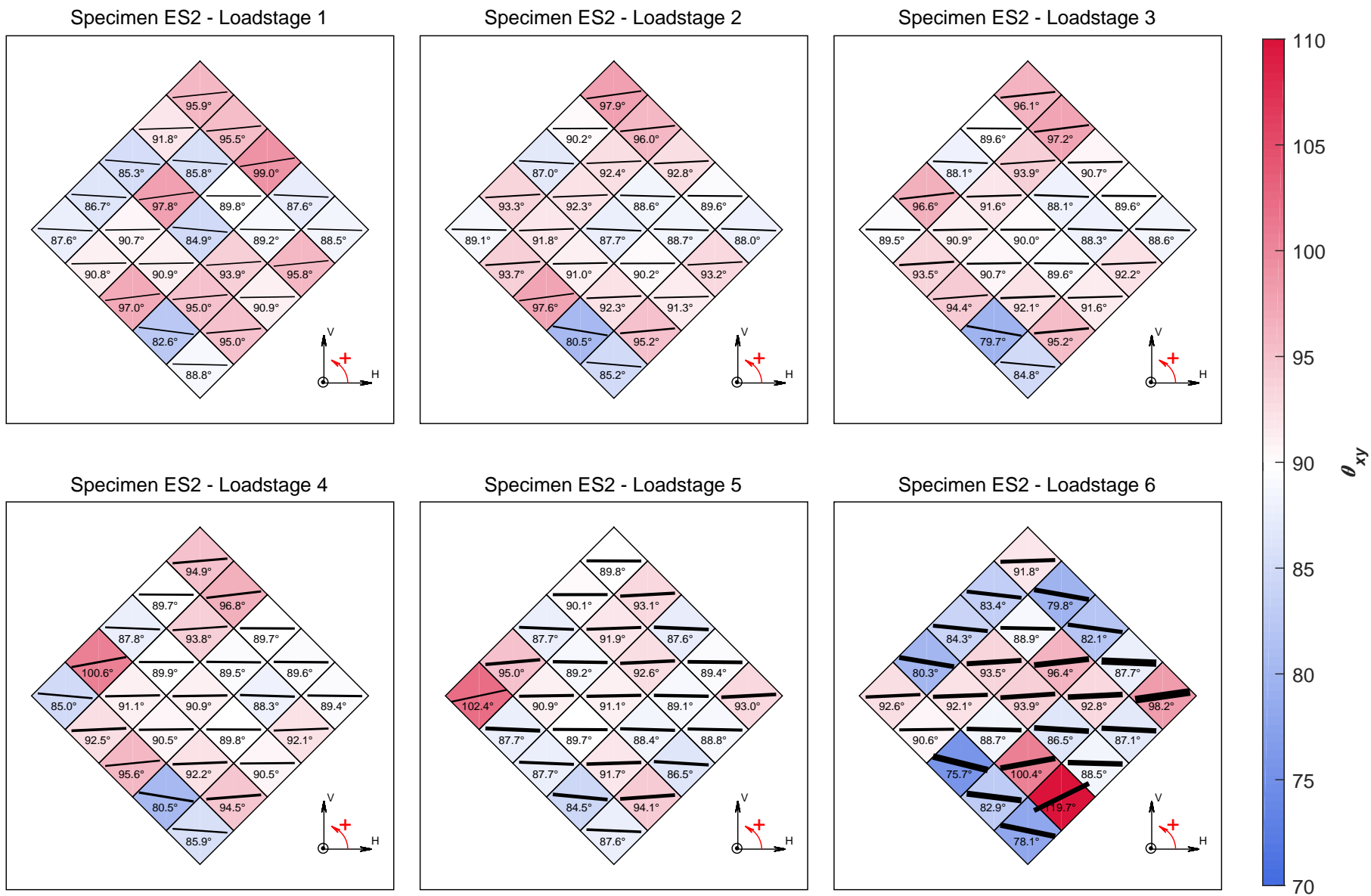


Figure C.12: ES2 Angle of Principal Strain (CCW+) at Load Stages

D. Analysis Program: Main Code Structure

The following appendix presents the skeleton code for the program written in MATLAB to implement the HyPT element formulation.

```

clearvars; close all; clc;

O = IO; % INPUT/OUTPUT CLASS

O.file_g = '3D_shell_large.txt'; % Name of Global File
O.directory(O.file_g) % Create File Directory

%%%%%%%%%%%%%%%%%%%%%%%%%%%%%%%%%%%%%%%%%%%%%%%%%%%%%%%%%%%%%%%%%%%%%%%%
% STEP #1 : READ THE GLOBAL TEXT FILE %
% - Define the Type of Problem (2D or 3D) %
% - Define the # of Sections Types and text file names %
% - Node/Restraint/Element/Loading Information %
%%%%%%%%%%%%%%%%%%%%%%%%%%%%%%%%%%%%%%%%%%%%%%%%%%%%%%%%%%%%%%%%%%%%%%%%
fprintf( '*****\n' )
fprintf( 'STEP #1: DEFINE THE PROBLEM\n' )
fprintf( '*****\n' )

%%% GLOBAL PROBLEM CLASS %%%
G = R_Global(O); % GLOBAL CLASS

G.read_file % Read Text File
G.read_file_node % Save Node Data
G.read_file_restraint % Save Restraint Data
G.read_file_load % Save Load Data
G.read_file_beam % Save Element Data

%%%%%%%%%%%%%%%%%%%%%%%%%%%%%%%%%%%%%%%%%%%%%%%%%%%%%%%%%%%%%%%%%%%%%%%%
% STEP #2 : READ THE SECTION TEXT FILES %
% - Loop depends on how many sections defined in problem %
% - Read information about the reinforced concrete section %
% - Read information about the material properties of section %
%%%%%%%%%%%%%%%%%%%%%%%%%%%%%%%%%%%%%%%%%%%%%%%%%%%%%%%%%%%%%%%%%%%%%%%%
fprintf( '*****\n' )
fprintf( 'STEP #2: DEFINE CONCRETE SECTION & MATERIAL PROPERTIES\n' )
fprintf( '*****\n' )

S = R_Section(G.sec_num,O); % SECTION CLASS
M = R_Material(G.sec_num,O); % MATERIAL CLASS

for x=1:G.sec_num
    %%%% SECTION CLASS %%%%
    S(x).read_file(G,G.sec_name{x}) % Read Text File
    S(x).read_reinforcement % Read X,Y,Z-Reinforcement
    S(x).calc_tstiff % Calc. Tension Stiffening
    S(x).calc_rho % Calc. Reinforcement Ratios
    S(x).plot(G) % Plot Section

    %%%% MATERIAL CLASS %%%%
    M(x).read_file(G.sec_name{x}) % Read Text File
    M(x).calc_xsteel % X-Steel Comp. & Tens.
    M(x).calc_ysteel % Y-Steel Comp. & Tens.
    M(x).calc_zsteel % Z-Steel Comp. & Tens.
    M(x).calc_comp % Concrete Comp. Curve
    M(x).calc_tens % Concrete Tens. Curve
    M(x).plot % Plot Material Curves
end

O.file_summary_G(G) % Global Summary File
O.file_summary_SM(G,S,M) % Sec./Mat Summary File
G.plot(S,0) % Display Structure

```

Figure D.1: MATLAB Main File Code (Part 1/3)

```

%%%%%%%%%%%%%%%%%%%%%%%%%%%%%%%%%%%%%%%%%%%%%%%%%%%%%%%%%%%%%%%%%%%%%%%%%%%%%%
% STEP #3 : ASSEMBLE & SOLVE GLOBAL STIFFNESS MATRIX
% - 1st Loop = Load Stage (Initialize {p})
% - 2nd Loop = Iteration (Initialize [K] & {u})
% - 3rd Loop = Element Stiffnesses
% - Iterate until Global Convergence Achieved
%%%%%%%%%%%%%%%%%%%%%%%%%%%%%%%%%%%%%%%%%%%%%%%%%%%%%%%%%%%%%%%%%%%%%%%%%%%%%%
fprintf( '\n*****\n' )
fprintf( 'STEP #3: ASSEMBLE & SOLVE GLOBAL STIFFNESS MATRIX\n' )
fprintf( '*****\n' )

%%%%%%%%%%%%%%%%%%%%%%%%%%%%%%%%%%%%%%%%%%%%%%%%%%%%%%%%%%%%%%%%%%%%%%%%%%%%%%
% STEP #3a: APPLIED LOADS
% - Load Stage Loop
% - Initialize {p}
% - Initialize 'Solver' class (wipe all previous)
%%%%%%%%%%%%%%%%%%%%%%%%%%%%%%%%%%%%%%%%%%%%%%%%%%%%%%%%%%%%%%%%%%%%%%%%%%%%%%
for i = 1:G.num_step

    fprintf( '\nLOADSTAGE #%d: %s\n' ,i,O.file_g)
    O.file_loadstage(G,i) % Make Load Stage Files

    C = Crack(G,O); % CRACK CLASS
    K = Solver(O); % SOLVER CLASS

    K.initialize_p(G,i) % Init. Load Vector

    %%%%%%%%%%%%%%%%%%%%%%%%%%%%%%%%%%%%%%%%%%%%%%%%%%%%%%%%%%%%%%%%%%%%%%%%%%%
    % STEP #3b: GLOBAL CONVERGENCE & SOLVE
    % - Global Solution Iteration Loop
    % - Initialize [K] & {u}
    % - Iterate until Absolute OR Relative Criteria Satisfied
    %%%%%%%%%%%%%%%%%%%%%%%%%%%%%%%%%%%%%%%%%%%%%%%%%%%%%%%%%%%%%%%%%%%%%%%%%%%
    while ((K.error1 >= K.max_error1) && (K.error2 >= K.max_error2)) &&
        (K.count <= K.max_iter)

        fprintf( 'Iteration #2d --- \n' , K.count)
        O.file_iter1(K.count,K.error1) % Load Stage Header

        K.initialize_k(G) % Init. Global Stiffness
        K.initialize_u(G) % Init. Disp. Vector

        %%%%%%%%%%%%%%%%%%%%%%%%%%%%%%%%%%%%%%%%%%%%%%%%%%%%%%%%%%%%%%%%%%%%%%%%%%%
        % STEP #3c : ELEMENT STIFFNESS
        % - Global Matrix Assembly Loop (Sum element contributions)
        % - Numbers of Face (2D = 1, 3D = 6)
        % - Element Matrix Assembly Loop (Truss + Panel + Crack)
        %%%%%%%%%%%%%%%%%%%%%%%%%%%%%%%%%%%%%%%%%%%%%%%%%%%%%%%%%%%%%%%%%%%%%%%%%%%
        for j = 1:G.tot_elem

            x = K.select_section(G,j); % Select Material/Section

            for k = 1:K.num_faces

                K.select_face(G,k,j) % Select the Face
                O.file_iter2(G,K,j,k) % Element/Face Iter. Header
            end
        end
    end
end

```

Figure D.2: MATLAB Main File Code (Part 2/3)


```

%%%%%%%%%%%%%%%%%%%%%%%%%%%%%%%%%%%%%%%%%%%%%%%%%%%%%%%%%%%%%%%%%%%%%%%%%% TRUSS CLASS %%%%%%%%%%%%%%%%%%%%%%%%%%%%%%%%%%%%%%%%%%%%%%%%%%%%%%%%%%%%%%%%%%%%%%%%%%%
T = Truss(O); % TRUSS CLASS
T.face_define(S(x),M(x),K,G.type) % Assign Face Variables
T.concrete(M(x)) % Concrete Contribution
T.steel(M(x),G.type) % Steel Contribution
T.assemble % Assemble Stiffness Terms
T.dv_solve % Find Force Centroid
T.crack_calc(M(x),K.face); % Flexural Cracking

%%%%%%%%%%%%%%%%%%%%%%%%%%%%%%%%%%%%%%%%%%%%%%%%%%%%%%%%%%%%%%%%%%%%%%%%%% MCFT CLASS %%%%%%%%%%%%%%%%%%%%%%%%%%%%%%%%%%%%%%%%%%%%%%%%%%%%%%%%%%%%%%%%%%%%%%%%%%%
P = MCFT(O,T); % PANEL CLASS
P.face_define(S(x),M(x),K.face) % Assign Face Variables

while ((P.error1 >= P.max_error1) &&
      ((P.error2 >= P.max_error2) || (P.error3 >= P.max_error3)) ) &&
      (P.count <= P.max_iter)

    P.strain_vector(K.face_u) % MCFT Strain Input
    P.strain_p % Principal Strains
    P.rotation_mat % Rotation Matrix
    P.stress_steel % Steel Stresses
    P.stress_conc_comp(M(x)) % Concrete Compression
    P.stress_conc_tens(M(x)) % Concrete Tension
    P.shear_crack(M(x),j,k) % Shear on Crack
    P.assemble_D % Secant Moduli
    P.next_iteration % Next Iteration Terms
end

P.assemble(M(x),G.type) % Assmeble Panel Terms

%%%%%%%%%%%%%%%%%%%%%%%%%%%%%%%%%%%%%%%%%%%%%%%%%%%%%%%%%%%%%%%%%%%%%%%%%% CRACK CLASS %%%%%%%%%%%%%%%%%%%%%%%%%%%%%%%%%%%%%%%%%%%%%%%%%%%%%%%%%%%%%%%%%%%%%%%%%%%
C.record_g_crk(j,K.count,P.crack) % Face Cracked?
C.record_shr_crk(j,k,P) % Shear Cracking
C.record_flex_crk(j,k,T) % Flexural Cracking

C.VM_disturbed(G,S(x)) % Disturbed Region?
C.VM_interaction(P,G,T,j) % Assemble M-V Terms

K.k_face(k,T.k1,P.k1,C.k1) % Assemble All K-terms
end

K.k_element(G.type,K.num_faces) % Add to Element Stiffness
K.k_global(G) % Add to Global Stiffness
end

%%%%%%%%%%%%%%%%%%%%%%%%%%%%%%%%%%%%%%%%%%%%%%%%%%%%%%%%%%%%%%%%%%%%%%%%%%
% STEP #3b: GLOBAL CONVERGENCE & SOLVE %
% - [K]{u} = {p} %
% - Partition Stiffness Matrix Based on Restrained DOFs %
% - Compare Global Displacements to Previous Step %
% - Calculate Relative and Absolute Errors, if diverging = terminate %
%%%%%%%%%%%%%%%%%%%%%%%%%%%%%%%%%%%%%%%%%%%%%%%%%%%%%%%%%%%%%%%%%%%%%%%%%%

K.partition(G) % Partition Matrix
K.solve(G) % Solve Stiffness Problem
K.loop_check(G) % Check Global Convergence
K.next_iteration(G) % Prepare Next Iter.
end

O.file_summary_LS(G,K,C,i) % Load Stage Summary File
end

```

Figure D.3: MATLAB Main File Code (Part 3/3)

E. Analysis Program: Input/Output Files

E.1 Input Text Files for Shell Torsion Analysis

```

////////////////////////////////////////////////////////////////////////////////////////////////////////////////////////////////
// Name:      Edvard Bruun
// Project:   Shell Specimen (ES1 and ES2)
// Created:   September 14th, 2016
// Updated:   July 1st, 2017
//
//
////////////////////////////////////////////////////////////////////////////////////////////////////////////////////////////////

// Global file must be in same directory as the program

// FORMAT: Type = '2D' or '3D' (If 2D then ignore Y-data)
//          Number of Name Entries Must Match # of Sections Precisely
//          Enter the exact text file name to read
// NOTES : No Empty Lines in this list
//          Section names must be one word
//          For Multiple Sections, Add Additional Name Rows
-INPUT FILE-
Type      = 3D
Sections  = 1
Name      = section_specimen.txt
-INPUT FILE END-

// FORMAT: [X_Start (mm), Y_Start (mm), Z_Start (mm)] / [#_nodes, d_node#, d_x, d_y, d_z] / [#_lines, d_node#, d_x, d_y, d_z] /
// NOTES : White space is not important so long as information lies between ' / '
//          Start a line with '/' if you want it to not be read
//          If '2D' Problem then the Y-data will be ignored
-NODE LIST-
0 0      0 / 6 6 230 0 0 / 6 1 0 -230 0 /
0 0 -285 / 6 6 230 0 0 / 6 1 0 -230 0 /
-NODE LIST END-

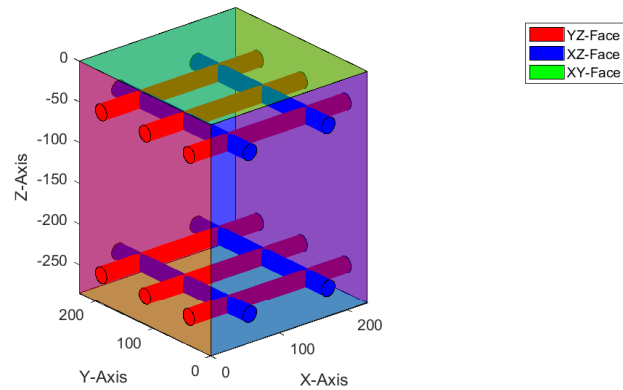
// FORMAT: [node #] / [X_restrain (0 | 1 | 2), Y_restrain (0 | 1 | 2), Z_restrain (0 | 1 | 2)] / [#_Restrains d_node#]
// NOTES : 0 = Unrestrained
//          1 = Fully Restrained
//          2 = Conditionally Restrained (Not Implemented)
-RESTRAINT LIST-
//OUT OF PLANE
49 / 0 0 1 / 1 1 /
48 / 0 0 1 / 1 1 /
66 / 0 0 1 / 1 1 /
//
// IN PLANE
38 / 1 0 0 / 1 1 /
43 / 0 1 0 / 1 1 /
61 / 0 1 0 / 1 1 /
-RESTRAINT LIST END-

// FORMAT: [node #] / [X_Load, Y_Load, Z_Load] / [#_Loads, d_node#, d_Fx, d_Fy, d_Fz ] / [Constant Toggle] / #_steps d_Fx d_Fy d_Fz /
// NOTES : 1 = Constant - ON
//          0 = Constant - OFF
//          Loads on Repeating Nodes are Cumulative
-LOAD LIST-
//
// Top Corner Nodes
1 / -45000 45000 0 / 1 1 0 0 0 / 0 / 300 -5000 5000 0 /
31 / -45000 -45000 0 / 1 1 0 0 0 / 0 / 300 -5000 -5000 0 /
6 / 45000 45000 0 / 1 1 0 0 0 / 0 / 300 5000 5000 0 /
36 / 45000 -45000 0 / 1 1 0 0 0 / 0 / 300 5000 -5000 0 /
// Top Sides
2 / 0 45000 0 / 4 1 0 0 0 / 0 / 300 0 5000 0 /
32 / 0 -45000 0 / 4 1 0 0 0 / 0 / 300 0 -5000 0 /
7 / -45000 0 0 / 4 6 0 0 0 / 0 / 300 -5000 0 0 /
12 / 45000 0 0 / 4 6 0 0 0 / 0 / 300 5000 0 0 /
//
// Bot Corner Nodes
72 / -45000 45000 0 / 1 1 0 0 0 / 0 / 300 -5000 5000 0 /
42 / -45000 -45000 0 / 1 1 0 0 0 / 0 / 300 -5000 -5000 0 /
67 / 45000 45000 0 / 1 1 0 0 0 / 0 / 300 5000 5000 0 /
37 / 45000 -45000 0 / 1 1 0 0 0 / 0 / 300 5000 -5000 0 /
// Bot Sides
68 / 0 45000 0 / 4 1 0 0 0 / 0 / 300 0 5000 0 /
38 / 0 -45000 0 / 4 1 0 0 0 / 0 / 300 0 -5000 0 /
48 / -45000 0 0 / 4 6 0 0 0 / 0 / 300 -5000 0 0 /
43 / 45000 0 0 / 4 6 0 0 0 / 0 / 300 5000 0 0 /
//
-LOAD LIST END-

// FORMAT: [N_1, N_2, N_3, N_4] [N_5, N_6, N_7, N_8] / [Section File Name] / [#_Elements, d_node#] / [#_lines d_node#] /
// NOTES : Front (XZ-Face) defined first - Left nodes first followed by right nodes
//          Back (YZ-Face) defined next - Left nodes first followed by right nodes (ONLY IF 3D)
//          Last Entry Section is only for 3D (not possible to do lines of elements in 2D)
-BEAM LIST-
//
2 38 8 44 1 37 7 43 / section_specimen.txt / 5 6 / 5 1 /
//
-BEAM LIST END-

```

Figure E.1: Global Input File for Specimen ES1 and ES2 Models



```

////////////////////////////////////////////////////////////////////////////////////////////////////////////////////////////////
// Name:      Edvard Bruun
// Project:   Experimental Shells (ES1)
// Created:   Semptember 14th, 2016
// Updated:   July 1st, 2017
//
// Do Not Include Empty Rows Between Titles
// Do Not Change Title Names
//
////////////////////////////////////////////////////////////////////////////////////////////////////////////////////////////////

// Unknown = 0 (Use Default Value)
-MATERIAL-
Concrete Comp. Str. [MPa] = 30.4
Concrete Tens. Str. [MPa] = 0
Poisson Ratio      = 0.15
Aggregate Size     [mm]  = 10
X-Steel Yield      [MPa] = 509
X-Steel Ultimate   [MPa] = 636
X-Steel Modulus    [MPa] = 147000
Y-Steel Yield      [MPa] = 509
Y-Steel Ultimate   [MPa] = 636
Y-Steel Modulus    [MPa] = 147000
Z-Steel Yield      [MPa] = 0
Z-Steel Ultimate   [MPa] = 0
Z-Steel Modulus    [MPa] = 0

// All Units in 'mm'
// 2D Problem: X = Element Length, Y = Section Width, Z = Section Height
// 3D Problem: X = Length in X-Dir, Y = Length in Y-Dir, Z = Out-of-Plane Thickness
-GEOMETRY-
X-width      = 230
Y-width      = 230
Z-width      = 285
Clear Cover  = 25
Filename     = section_specimen.txt

// 1 Row:      bot_layers = 1 / rebar_size = 25      / num_bars = 7      / d = 572      /
// 1+ Row:     bot_layers = 3 / rebar_size = 25 20 15 / num_bars = 7 3 3 / d = 572 500 400 /
// No Rebar:   bot_layers = 0 /
// Use '/' Between Inputs, Whitespace on Both Sides

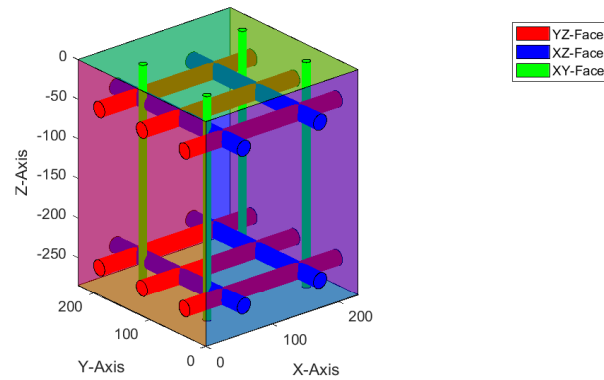
// 'd' is Measured From Top of Section (i.e. Towards Negative Z-dir)
-X-REINFORCEMENT-
xy-inclination = 0
xz-inclination = 0
bot_layers = 1 / rebar_size = 20 / num_bars = 3 / d = 250 /
top_layers = 1 / rebar_size = 20 / num_bars = 3 / d = 50 /

// 'd' is Measured From Top of Section (i.e. Towards Negative Z-dir)
-Y-REINFORCEMENT-
yx-inclination = 90
yz-inclination = 0
bot_layers = 1 / rebar_size = 20 / num_bars = 2 / d = 250 /
top_layers = 1 / rebar_size = 20 / num_bars = 2 / d = 50 /

// 'd' is Measured From Left of Section (i.e. Towards Positive X-dir)
-Z-REINFORCEMENT-
zx-inclination = 90
zy-inclination = 90
bot_layers = 1 / rebar_size = 10 / num_bars = 0 / d = 250 /
top_layers = 1 / rebar_size = 10 / num_bars = 0 / d = 50 /

```

Figure E.2: Section Input File for Specimen ES1



```

////////////////////////////////////////////////////////////////////////////////////////////////////////////////////////////////
// Name:      Edvard Bruun
// Project:   Experimental Shells (ES2)
// Created:   September 14th, 2016
// Updated:   July 1st, 2017
//
// Do Not Include Empty Rows Between Titles
// Do Not Change Title Names
//
////////////////////////////////////////////////////////////////////////////////////////////////////////////////////////////////

// Unknown = 0 (Use Default Value)
-MATERIAL-
Concrete Comp. Str. [MPa] = 37.6
Concrete Tens. Str. [MPa] = 0
Poisson Ratio       = 0.15
Aggregate Size      [mm] = 10
X-Steel Yield       [MPa] = 509
X-Steel Ultimate    [MPa] = 636
X-Steel Modulus     [MPa] = 147000
Y-Steel Yield       [MPa] = 509
Y-Steel Ultimate    [MPa] = 636
Y-Steel Modulus     [MPa] = 147000
Z-Steel Yield       [MPa] = 474
Z-Steel Ultimate    [MPa] = 657
Z-Steel Modulus     [MPa] = 213000

// All Units in 'mm'
// 2D Problem: X = Element Length, Y = Section Width, Z = Section Height
// 3D Problem: X = Length in X-Dir, Y = Length in Y-Dir, Z = Out-of-Plane Thickness
-GEOMETRY-
X-width      = 230
Y-width      = 230
Z-width      = 285
Clear Cover  = 25
Filename     = section_specimenb.txt

// 1 Row:   bot_layers = 1 / rebar_size = 25      / num_bars = 7      / d = 572      /
// 1+ Row:  bot_layers = 3 / rebar_size = 25 20 15 / num_bars = 7 3 3 / d = 572 500 400 /
// No Rebar: bot_layers = 0 /
// Use '/' Between Inputs, Whitespace on Both Sides

// 'd' is Measured From Top of Section (i.e. Towards Negative Z-dir)
-X-REINFORCEMENT-
xy-inclination = 0
xz-inclination = 0
bot_layers = 1 / rebar_size = 20 / num_bars = 3 / d = 250 /
top_layers = 1 / rebar_size = 20 / num_bars = 3 / d = 50 /

// 'd' is Measured From Top of Section (i.e. Towards Negative Z-dir)
-Y-REINFORCEMENT-
yx-inclination = 90
yz-inclination = 0
bot_layers = 1 / rebar_size = 20 / num_bars = 2 / d = 250 /
top_layers = 1 / rebar_size = 20 / num_bars = 2 / d = 50 /

// 'd' is Measured From Left of Section (i.e. Towards Positive X-dir)
-Z-REINFORCEMENT-
zx-inclination = 90
zy-inclination = 90
bot_layers = 1 / rebar_size = 10 / num_bars = 2 / d = 200 /
top_layers = 1 / rebar_size = 10 / num_bars = 2 / d = 50 /

```

Figure E.3: Section Input File for Specimen ES2

E.2 Analysis Summary Output Files for Torsion Specimen ES2

```

GLOBAL PROBLEM SUMMARY

Type of Problem      = 3D
Number of Sections  = 1
---section_specimenb.txt

***** NODE DATA *****
Num. Nodes = 72

      [mm]      [mm]      [mm]
Node  X-Coord  Y-Coord  Z-Coord
1      0         0         0
2      0        -230      0
3      0        -460      0
4      0        -690      0
5      0        -920      0
6      0       -1150      0
7     230         0         0
8     230        -230      0
9     230        -460      0
10    230        -690      0
11    230        -920      0
12    230       -1150      0
13    460         0         0
14    460        -230      0
15    460        -460      0
16    460        -690      0
17    460        -920      0
18    460       -1150      0
19    690         0         0
20    690        -230      0
21    690        -460      0
22    690        -690      0
23    690        -920      0
24    690       -1150      0
25    920         0         0
26    920        -230      0
27    920        -460      0
28    920        -690      0
29    920        -920      0
30    920       -1150      0
31   1150         0         0
32   1150        -230      0
33   1150        -460      0
34   1150        -690      0
35   1150        -920      0
36   1150       -1150      0
37     0         0       -285
38     0        -230      -285
39     0        -460      -285
40     0        -690      -285
41     0        -920      -285
42     0       -1150      -285
43    230         0       -285
44    230        -230      -285
45    230        -460      -285
46    230        -690      -285
47    230        -920      -285
48    230       -1150      -285
49    460         0       -285
50    460        -230      -285
51    460        -460      -285
52    460        -690      -285
53    460        -920      -285
54    460       -1150      -285
55    690         0       -285
56    690        -230      -285
57    690        -460      -285
58    690        -690      -285
59    690        -920      -285
60    690       -1150      -285
61    920         0       -285
62    920        -230      -285
63    920        -460      -285
64    920        -690      -285
65    920        -920      -285
66    920       -1150      -285
67   1150         0       -285
68   1150        -230      -285
69   1150        -460      -285
70   1150        -690      -285
71   1150        -920      -285
72   1150       -1150      -285

```

Figure E.4: Global Summary Output File for Specimen ES2 (Part 1/2)

```

***** RESTRAINT DATA *****
Num. Restrained Nodes = 6
Num. Restrained DOFs = 6

Node   X-Res   Y-Res   Z-Res
38      1       0       0
43      0       1       0
48      0       0       1
49      0       0       1
61      0       1       0
66      0       0       1

***** LOAD DATA *****
Num. Loaded Nodes = 40
Num. Load Stages = 300

Node   [1/0]   [N]     [N]     [N]     [N]     [N]     [N]
Constant X-Load  Y-Load  Z-Load  X+      Y+      Z+
1       0     -45000  45000   0     -5000   5000   0
2       0       0     45000   0      0       5000   0
3       0       0     45000   0      0       5000   0
4       0       0     45000   0      0       5000   0
5       0       0     45000   0      0       5000   0
6       0     45000  45000   0      5000   5000   0
7       0    -45000   0      0     -5000   0       0
12      0     45000   0      0      5000   0       0
13      0    -45000   0      0     -5000   0       0
18      0     45000   0      0      5000   0       0
19      0    -45000   0      0     -5000   0       0
24      0     45000   0      0      5000   0       0
25      0    -45000   0      0     -5000   0       0
30      0     45000   0      0      5000   0       0
31      0    -45000  -45000  0     -5000  -5000   0
32      0       0    -45000  0      0     -5000   0
33      0       0    -45000  0      0     -5000   0
34      0       0    -45000  0      0     -5000   0
35      0       0    -45000  0      0     -5000   0
36      0     45000  -45000  0      5000  -5000   0
37      0     45000  -45000  0      5000  -5000   0
38      0       0    -45000  0      0     -5000   0
39      0       0    -45000  0      0     -5000   0
40      0       0    -45000  0      0     -5000   0
41      0       0    -45000  0      0     -5000   0
42      0    -45000  -45000  0     -5000  -5000   0
43      0     45000   0      0      5000   0       0
48      0    -45000   0      0     -5000   0       0
49      0     45000   0      0      5000   0       0
54      0    -45000   0      0     -5000   0       0
55      0     45000   0      0      5000   0       0
60      0    -45000   0      0     -5000   0       0
61      0     45000   0      0      5000   0       0
66      0    -45000   0      0     -5000   0       0
67      0     45000   45000   0      5000   5000   0
68      0       0     45000   0      0      5000   0
69      0       0     45000   0      0      5000   0
70      0       0     45000   0      0      5000   0
71      0       0     45000   0      0      5000   0
72      0    -45000  45000   0     -5000   5000   0

***** ELEMENT DATA *****
Num. Elements = 25

F = Front Face
B = Back Face
L = Left Side
R = Right Side

[Node 1] [Node 2] [Node 3] [Node 4] [Node 5] [Node 6] [Node 7] [Node 8]
Element  F-LT   F-LB   F-RT   F-RB   B-LT   B-LB   B-RT   B-RB   Section Name
1         2     38     8      44     1     37     7     43   section_specimenb.txt
2         8     44    14     50     7     43    13     49   section_specimenb.txt
3        14     50    20     56    13     49    19     55   section_specimenb.txt
4        20     56    26     62    19     55    25     61   section_specimenb.txt
5        26     62    32     68    25     61    31     67   section_specimenb.txt
6         3     39     9      45     2     38     8     44   section_specimenb.txt
7         9     45    15     51     8     44    14     50   section_specimenb.txt
8        15     51    21     57    14     50    20     56   section_specimenb.txt
9        21     57    27     63    20     56    26     62   section_specimenb.txt
10       27     63    33     69    26     62    32     68   section_specimenb.txt
11        4     40    10     46     3     39     9     45   section_specimenb.txt
12       10     46    16     52     9     45    15     51   section_specimenb.txt
13       16     52    22     58    15     51    21     57   section_specimenb.txt
14       22     58    28     64    21     57    27     63   section_specimenb.txt
15       28     64    34     70    27     63    33     69   section_specimenb.txt
16        5     41    11     47     4     40    10     46   section_specimenb.txt
17       11     47    17     53    10     46    16     52   section_specimenb.txt
18       17     53    23     59    16     52    22     58   section_specimenb.txt
19       23     59    29     65    22     58    28     64   section_specimenb.txt
20       29     65    35     71    28     64    34     70   section_specimenb.txt
21        6     42    12     48     5     41    11     47   section_specimenb.txt
22       12     48    18     54    11     47    17     53   section_specimenb.txt
23       18     54    24     60    17     53    23     59   section_specimenb.txt
24       24     60    30     66    23     59    29     65   section_specimenb.txt
25       30     66    36     72    29     65    35     71   section_specimenb.txt

```

Figure E.5: Global Summary Output File for Specimen ES2 (Part 2/2)

```

SECTION AND MATERIAL SUMMARY

Type of Problem      = 3D
Number of Sections  = 1

-----
                          Material Data
-----
Curve Increment      = 1.000e-04

Steel Model          = Trilinear
Concrete Comp Model = Popovics
Concrete Tens Model = 1986-Large

Rebar Table
[mm] [mm^2]
Diam. Area
  5     35
 10    100
 11    100
 12    110
 13    130
 14    150
 15    200
 16    200
 17    230
 18    250
 19    280
 20    300
 21    350
 22    380
 23    415
 24    450
 25    500
 26    530
 27    570
 28    615
 29    660
 30    700
 31    750
 32    800
 33    850
 34    900
 35   1000
 45   1500
 55   2500

-----
                          section_specimenb.txt
-----
X-dim      = 230 [mm]
Y-dim      = 230 [mm]
Z-dim      = 285 [mm]
Clear Cover = 25 [mm]

Concrete Comp. Strength (f'c) = 30.0 [MPa]
Concrete Comp. Strain (e'c)  = -1.960e-03 [mm/mm]
Concrete Tens. Strength (f'cr) = 1.807 [MPa]
Concrete Tens. Strain (e'cr)  = 7.206e-05 [mm/mm]
Concrete Uncracked Modulus (Ec) = 25084 [MPa]
Concrete Poisson Ratio       = 0.150
Concrete Aggregate Size      = 10 [mm]

X-Steel Modulus = 200000 [MPa]
X-Steel Yield   = 500.0 [MPa] @ 2.500e-03 [mm/mm]
X-Steel Rupture = 575.0 [MPa] @ 1.500e-01 [mm/mm]
X-Reinf Ratio   = 2.746%

Y-Steel Modulus = 200000 [MPa]
Y-Steel Yield   = 500.0 [MPa] @ 2.500e-03 [mm/mm]
Y-Steel Rupture = 575.0 [MPa] @ 1.500e-01 [mm/mm]
Y-Reinf Ratio   = 1.831%

Z-Steel Modulus = 200000 [MPa]
Z-Steel Yield   = 300.0 [MPa] @ 1.500e-03 [mm/mm]
Z-Steel Rupture = 500.0 [MPa] @ 1.500e-01 [mm/mm]
Z-Reinf Ratio   = 0.756%

```

Figure E.6: Section Summary Output File for Specimen ES2

E.3 Sample Load Stage Output Files for Torsion Specimen ES2

Note: This represents a small component of the "Load Stage Iteration" file generated during Load Stage #31 for the analysis of ES2. This particular excerpt shows the results of the program calculations for the Truss, Panel, and Interaction Terms for Iteration #3, Element #5, and face XZ-1.

```

Problem Type          = 3D
Num. Nodes           = 72

Num. Restrained Nodes = 6
Num. Loaded Nodes     = 40
Number of Elements   = 25

Number of Load Stages = 300
Max Iter. (Per Stage) = 50
Max Abs. Error (Per Stage) = 0.050 %
Max Rel. Error (Per Stage) = 0.050 [mm]

-----
GLOBAL ITERATION #1
-----
LAST ITERATION ERROR = N/A
-----
.
(Remove Other Iteration Calcs)
.
-----
GLOBAL ITERATION #2
-----
LAST ITERATION ERROR = 100.00%
-----
.
(Remove Other Iteration Calcs)
.
-----
GLOBAL ITERATION #3
-----
LAST ITERATION ERROR = 8035.41%
-----
.
(Remove Other Element Calcs)
.
-----
ELEMENT 5/25
FACE XZ-1 --- 1/6
-----

TRUSS BAR START
-----
e_bot = -4.171e-05
e_top = 1.407e-05
slope = -1.957e-07
Concrete Stiffness Component

Steel Stiffness Component
---Top Rebar Layer: 1
---Bot Rebar Layer: 1

CONCRETE RESULTS
k_t [N/mm] = 1.196499e+06
k_bt [N/mm] = 5.993717e+05
k_tb [N/mm] = 5.993717e+05
k_b [N/mm] = 1.196497e+06

TOP STEEL RESULTS
k_t [N/mm] = 1.620165e+05
k_bt [N/mm] = 3.447161e+04
k_tb [N/mm] = 3.447161e+04
k_b [N/mm] = 7.334384e+03

BOT STEEL RESULTS
k_t [N/mm] = 3.593851e+03
k_bt [N/mm] = 2.567036e+04
k_tb [N/mm] = 2.567036e+04
k_b [N/mm] = 1.833597e+05

COMPLETE TRUSS STIFFNESS
k_t [N/mm] = 1.362110e+06
k_bt [N/mm] = 6.595137e+05
k_tb [N/mm] = 6.595137e+05
k_b [N/mm] = 1.387191e+06

-----
TRUSS BAR END

CRACK FACE = no

DEPTH = 0.00

```

Figure E.7: Load Stage Iteration File (Excerpt) for Specimen ES2 (Part 1/2)


```

MFCT PANEL START: Iteration #1
-----
Input Stresses
s1 = 0.000 [MPa]
s2 = 0.000 [MPa]
s3 = 0.000 [MPa]
Input Strains
e1 = 7.034e-06 [mm/mm]
e2 = 0.000e+00 [mm/mm]
e3 = -8.339e-06 [mm/mm]
Principle Direction Values
Mohr Circle (Quadrant 1)
Principal Strain (e1_p) = 8.97e-06 [mm/mm]
Principal Strain (e2_p) = -1.94e-06 [mm/mm]
Concrete (ec1_p) = 8.97e-06 [mm/mm]
Concrete (ec2_p) = -1.94e-06 [mm/mm]
Principal Angle (theta_p) = -24.93 [deg]
Steel-1 Angle (theta_2n) = -24.93 [deg]
Steel-2 Angle (theta_2n) = -114.93 [deg]
Steel Stresses & Strains
Strain: 1-Steel = 7.03e-06 [mm/mm]
Stress: 1-Steel = 1.03 [MPa]
Strain: 2-Steel = -1.00e-35 [mm/mm]
Stress: 2-Steel = -0.00 [MPa]
Concrete Compressive Stresses
B-Factor = 0.48
e_p = -9.359e-04 [mm/mm]
f_p = -14.48 [MPa]
e_c2 = -1.938e-06 [mm/mm]
f_c2 = -0.06 [MPa]
Concrete Tensile Stresses
Cracked (yes/no) = no
Secant Moduli
Ec1 = 25205 [MPa]
Ec2 = 30902 [MPa]
Es1 = 147000 [MPa]
Es2 = 200000 [MPa]
Gc = 13882 [MPa]
Output Stresses
s1 = 0.204 [MPa]
s2 = 0.000 [MPa]
s3 = -0.109 [MPa]
Output Strains
e1 = 7.034e-06 [mm/mm]
e2 = 3.045e-07 [mm/mm]
e3 = -8.339e-06 [mm/mm]
MFCT PANEL START: Iteration #2
-----
Input Stresses
s1 = 0.204 [MPa]
s2 = 0.000 [MPa]
s3 = -0.109 [MPa]
Input Strains
e1 = 7.034e-06 [mm/mm]
e2 = 3.045e-07 [mm/mm]
e3 = -8.339e-06 [mm/mm]
Principle Direction Values
Mohr Circle (Quadrant 1)
Principal Strain (e1_p) = 9.03e-06 [mm/mm]
Principal Strain (e2_p) = -1.69e-06 [mm/mm]
Concrete (ec1_p) = 9.03e-06 [mm/mm]
Concrete (ec2_p) = -1.69e-06 [mm/mm]
Principal Angle (theta_p) = -25.55 [deg]
Steel-1 Angle (theta_2n) = -25.55 [deg]
Steel-2 Angle (theta_2n) = -115.55 [deg]
Steel Stresses & Strains
Strain: 1-Steel = 7.03e-06 [mm/mm]
Stress: 1-Steel = 1.03 [MPa]
Strain: 2-Steel = 3.05e-07 [mm/mm]
Stress: 2-Steel = 0.06 [MPa]
Concrete Compressive Stresses
B-Factor = 0.44
e_p = -8.570e-04 [mm/mm]
f_p = -13.25 [MPa]
e_c2 = -1.688e-06 [mm/mm]
f_c2 = -0.05 [MPa]
Concrete Tensile Stresses
Cracked (yes/no) = no
Secant Moduli
Ec1 = 25205 [MPa]
Ec2 = 30903 [MPa]
Es1 = 147000 [MPa]
Es2 = 200000 [MPa]
Gc = 13882 [MPa]
Output Stresses
s1 = 0.204 [MPa]
s2 = 0.000 [MPa]
s3 = -0.109 [MPa]
Output Strains
e1 = 7.034e-06 [mm/mm]
e2 = 3.098e-07 [mm/mm]
e3 = -8.339e-06 [mm/mm]
Secant Shear Modulus = 10959 [MPa]
-----
MCFT PANEL END
SHEAR-MOMENT INTERACTION START
-----
Shear-Moment Term = 'ND'
-----
SHEAR-MOMENT INTERACTION END

.
(Remove Other Face Calcs)
.
-----
.
(Remove Other Element Calcs)
.
-----
GLOBAL ITERATION #4
-----
.
.
.

```

Figure E.8: Load Stage Iteration File (Excerpt) for Specimen ES2 (Part 2/2)

Note: This represents a reduced "Load Stage Summary" file generated at the end of load stage #31 for the analysis of ES2 - only the first and last entry in the node/element lists is shown.

```

Problem Type      = 3D
Num. Nodes       = 72

Num. Restrained Nodes = 6
Num. Loaded Nodes  = 40
Number of Elements = 25

Number of Load Stages = 100
Max Iter. (Per Stage) = 50
Max Abs. Error (Per Stage) = 0.050 %
Max Rel. Error (Per Stage) = 0.050 [mm]

-----
GLOBAL SUMMARY
LOADSTAGE #31
-----

***** ERROR DATA *****
Maximum Relative Error

[mm]
Iteration  Rel. Error  Abs Error  Node  DOF  Direction
1          100.000%  0.039     1     1     X
2          8035.410%  0.000    21    62     Z
3         -3151.925%  0.046    61   181     X
4           759.789%  0.001    60   180     Y
5          2014.577%  0.023    43   127     X
6          3270.205%  0.126     2     5     Z
7          -977.435%  0.007    69   207     Y
8          1634.161%  0.001    57   171     Y
9          -843.356%  0.072     6    16     X
10         1887.582%  0.000    13    38     Z
11         6208.785%  0.001    57   171     Y
12         1460.501%  0.023    43   127     X
13         -34223.359%  0.008    14    42     Y
14          771.438%  0.002    52   155     Z
15         -2815.980%  0.093     2     4     X
16         1867.439%  0.002    60   180     Y
17         2965.499%  0.039    39   116     Z
18         13048.385%  0.038     6    16     X
19          9993.195%  0.149    40   119     Z
20         -22805.869%  0.000    18    53     Z
21          1005.640%  0.004    55   165     Y

Maximum Absolute Error

[mm]
Iteration  Abs Error  Node  DOF  Direction
1          0.208    72   215     Z
2          0.104    72   215     Z
3          0.116    72   214     X
4          0.085    72   214     X
5          0.052    12    34     X
6          0.133     4    10     X
7          0.130     1     2     Z
8          0.050    72   214     X
9          0.088     5    14     Z
10         0.068     6    17     Z
11         0.098     1     2     Z
12         0.129    42   125     Z
13         0.069    72   214     X
14         0.073    18    52     X
15         0.121    37   110     Z
16         0.117    37   110     Z
17         0.067     6    17     Z
18         0.058     1     2     Z
19         0.157     6    17     Z
20         0.109     6    16     X
21         0.041    36   106     X

***** NODE DISPLACEMENT DATA *****
Num. Nodes = 72

[mm] [mm] [mm]
Node  X-Coord  Y-Coord  Z-Coord
1     -0.074   0.147  -0.175
.
72    -0.399   0.019  -0.437

***** NODAL FORCE DATA *****

[N] [N] [N]
Node  X-Load  Y-Load  Z-Load
1     -35000  35000    0
.
72    -35000  35000    0

***** CRACK INFORMATION *****
Track the Global Cracking of the Structure (Every Iteration)
If anything cracks = yes

I# 1  I# 2  I# 3  I# 4  I# 5  I# 6  I# 7  I# 8  I# 9  I#10  I#11  I#12  I#13  I#14  I#15  I#16  I#17  I#18  I#19  I#20  I#21
Ele # 1  no  yes  yes  yes  yes  yes  yes  yes  yes  yes  yes  yes  yes  yes  yes  yes  yes  yes  yes  yes
.
Ele # 25  no  yes  yes  yes  yes  yes  yes  yes  yes  yes  yes  yes  yes  yes  yes  yes  yes  yes  yes  yes

***** SHEAR CRACKING *****
If a panel cracks = yes
This is only for the Final Iteration

Face:  XZ-1  XZ-2  YZ-1  YZ-2  XY-1  XY-2
Ele # 1  no  no  no  no  no  yes
.
Ele # 25  no  no  no  no  no  yes

Rotation of Principal Plane (CCW = +)

Face:  XZ-1  XZ-2  YZ-1  YZ-2  XY-1  XY-2
Ele # 1  -84.2  88.6  4.5  22.3  58.2  -65.9
.
Ele # 25  -88.6  84.2  -22.3  -4.5  58.2  -65.9

***** FLEXURAL/AXIAL CRACKING *****
If a panel cracks = top/bot
(Looks at which face is more in tension)
This is only for the Final Iteration

Face:  XZ-1  XZ-2  YZ-1  YZ-2  XY-1  XY-2
Ele # 1  no  no  top  no  no  no
.
Ele # 25  no  no  no  top  no  no

Depth of Neutral Axis
(Location in Global Coordinate System)

Face:  XZ-1  XZ-2  YZ-1  YZ-2  XY-1  XY-2
Ele # 1  0.0  0.0  -68.9  0.0  0.0  0.0
.
Ele # 25  0.0  0.0  0.0  -68.9  0.0  0.0
    
```

Figure E.9: Load Stage Summary File (Reduced) for Specimen ES2